

University of Strathclyde
Department of Mechanical Engineering

Non-Keplerian Orbits for Low-Thrust Propulsion
by
Shahid Baig

A thesis presented in fulfilment of the requirements
for the degree of Doctor of Philosophy

2009

Copyright Statement

This thesis is the result of the author's original research. It has been composed by the author and has not been previously submitted for examination which has led to the award of a degree. The copyright of this thesis belongs to the author under the terms of the United Kingdom Copyright Acts as qualified by University of Strathclyde Regulation 3.50. Due acknowledgement must always be made of the use of any material contained in, or derived from, this thesis.

Acknowledgements

I would like to thank my supervisor Professor Colin McInnes for all of his help throughout the last three years. This thesis would not be possible without his assistance. Furthermore, I am also thankful to Dr. Thomas Waters and Dr. James Biggs for useful discussions on periodic orbits. I would also like to thank all of my family (especially my parents and my wife) and friends for their support. Moreover, I am grateful to the National Centre for Physics, Quaid-i-Azam University Islamabad for funding my work.

Abstract

Low thrust propulsion such as solar electric and solar sail propulsion are being considered to enhance or enable future space missions. This thesis generates new non-Keplerian orbits for solar electric propulsion, solar sail propulsion and a hybrid of sail/solar electric propulsion by utilising continuous low-thrust acceleration.

For solar electric propulsion, the idea to generate periodic orbits has been extended from linear to non-linear order, and thus shows the feasibility of artificial halo orbits in the circular restricted three-body problem. Stable and unstable artificial halo orbits using solar electric propulsion are found around artificial equilibrium points in the forbidden regions for a solar sail.

The recent idea of a hybrid sail/solar electric spacecraft to reduce orbital transfer time in the solar system has been extended to generate new artificial equilibrium points in the Sun-Earth circular restricted three-body problem. Notably, it was found that the hybrid sail can be used to generate artificial equilibria in the forbidden regions for a pure solar sail. The hybrid sail also shows a potential application for a polar (Earth) observer mission. Moreover, it is shown that the hybrid sail can be stabilised around unstable artificial equilibrium points by orienting the thruster system while keeping the sail orientation fixed to ease the control issues of actuating a large sail.

For solar sail propulsion, a novel family of displaced non-Keplerian orbits (light-levitated geostationary orbits) are demonstrated in the Earth-sail two-body problem to prove the disputed claim of Forward that such orbits exist. A collocation scheme with inequality path constraints was found to be the most promising

approach to generate such displaced geostationary orbits in the full non-linear problem. However, only modest displacement geostationary orbits can exist.

Contents

1	Introduction	1
1.1	The Circular Restricted Three-body Problem	2
1.1.1	Equations of Motion	2
1.1.2	Location of Lagrange Points	4
1.1.3	Jacobi's Integral	6
1.2	Periodic and Quasi-Periodic Orbits	6
1.3	Low-Thrust Propulsion System	11
1.3.1	Electric Propulsion System	11
1.3.1.1	Electrothermal thruster	12
1.3.1.2	Electrostatic thruster	12
1.3.1.3	Electromagnetic thruster	14
1.3.2	Solar Sail Propulsion	15
1.3.2.1	Solar Sail Model and Performance Parameters	15
1.3.2.2	Recent Advances in Solar Sail Technology	19
1.3.3	Hybrid Sail	20
1.4	Literature Review of NKO and Thesis Objectives	21
1.4.1	NKO and the Circular Restricted Three-Body Problem	22
1.4.1.1	Artificial Equilibria and Halo orbits	22
1.4.1.2	Applications of Artificial Equilibria	25
1.4.1.3	Displaced NKO for the Non-Autonomous Solar Sail Problem	27

1.4.2	NKO and the Two-Body Problem	29
1.5	Thesis Layout	32
1.6	Papers Published	33
2	Artificial Halo Orbits for Low-Thrust Propulsion Spacecraft	34
2.1	Equations of Motion	35
2.2	Linearised System	38
2.3	Nonlinear Approximations	40
2.4	Differential Correction and Low-Thrust Halo Orbits	47
2.5	Stable Low-Thrust Halo orbits	51
2.6	Conclusions	55
3	Artificial Three-Body Equilibria for Hybrid Low-Thrust Propulsion	58
3.1	Partially Reflecting Hybrid Sail Model	59
3.1.1	Dimensional Force Model	59
3.1.2	Non-dimensional Acceleration Model	61
3.2	Equations of Motion and Artificial Equilibria	63
3.2.1	Minimisation of SEP Acceleration at $t=0$	67
3.2.2	Equilibria Options During Mission Life	69
3.2.2.1	Option 1	70
3.2.2.2	Option 2	71
3.3	Linear Stability Analysis for the Hybrid Sail	72
3.3.1	Linearised System	72
3.3.2	Stability Analysis at $t_0 = 0$	74
3.4	Evaluation of Hybrid Sail Performance	78
3.4.1	Pure Sail	79
3.4.2	Pure SEP	79
3.4.3	Hybrid Sail	81
3.5	Conclusions	88

4	Control of Hybrid Sail at an Equilibrium Point	89
4.1	Controllability of the Hybrid Sail	90
4.2	Linear State-Feedback Control	92
4.3	Conclusions	96
5	Levitated Geostationary Orbits	99
5.1	Equations of Motion	100
5.2	Linearised Equations	104
5.3	Accommodating the Nonlinearities	109
5.3.1	Hermite Simpson Method	110
5.3.2	Statement of Problem	111
5.3.3	Newton's Method and the Analytical Jacobian Matrix	113
5.3.4	Illustrative Examples	115
5.4	Linear Analysis with Seasonal Effects	120
5.4.1	Direction of the Sun-line	120
5.4.2	Linearised Solution	122
5.5	Illustrative Examples at Summer Solstice	124
5.6	Application: Solar Power Transmission from Space	127
5.7	Equilibria in ECEF-Frame and Solar Power Satellite System	129
5.8	Conclusions	131
6	Periodic Orbits Around a Geostationary Point	133
6.1	Collocation Method with no Inequality Path Constraints	133
6.2	Differential Corrector Method	136
6.2.1	Linear Periodic Solution for z -Equation	136
6.2.2	Symmetry in the Equations of Motion	140
6.2.3	Differential Corrector for Periodic Solution	141
6.3	Conclusions	144

7 Conclusion	148
7.1 Chapter 2	148
7.2 Chapter 3 and Chapter 4	149
7.3 Chapter 5 and Chapter 6	150
7.4 Future Work	151
A Linearized Solution	152
A.1 Eigenvector for Centre Eigenvalue	152
A.2 Bounded solution for δx and δy	153
B Hybrid sail acceleration due to SRP with TFSC	154
B.1 Nondimensional solar sail acceleration due to SRP with TFSC . . .	154
B.2 Matrix K in Eq.(3.35)	155
C Jacobian Matrix	158

List of Figures

1.1	Geometry of the restricted-three body problem. The primary masses m_1 and m_2 are at rest in a synodic rotating reference frame (x, y, z) with origin at centre of mass (CM) and with fixed separation R	3
1.2	Lagrange points of the circular restricted three body problem with $\mu = 0.1$. The only parameter of the system is μ ($\mu = 3.0032 \times 10^{-6}$ for the Sun-Earth system, $\mu = 1.215 \times 10^{-2}$ for the Earth-Moon system).	5
1.3	Linear-order L_1 Lyapunov orbit ($A_x(5000 \text{ km})$) in the Sun-Earth system.	7
1.4	Linear-order L_2 Lissajous orbit ($A_x(6000 \text{ km}), A_z(15000 \text{ km})$) in the Sun-Earth system.	8
1.5	Third-order L_1 halo orbit ($A_z(120,000 \text{ km})$) in the Sun-Earth system. Halo orbits do not exist at linear order.	9
1.6	Solar radiation force on an ideal solar sail. The vector \mathbf{u} is normal to the sail surface.	16
1.7	(a) The (ideal) sail characteristic thrust $F_c = m_0 a_c = 2P_0 A_S$ vs sail length (b) Characteristic acceleration vs sail length for $\sigma_S = 10 \text{ g/m}^2$ and different payload masses m_{pl}	18
1.8	Sail segments fully deployed by (a) NASA/ATK space system (b) NASA/L'Grade system and (c) ESA/DLR joint programme.	19
1.9	Solar sail configuration with Solar Electric Propulsion [54].	20

1.10	Contours of sail lightness number $\beta_0 = (1) 0.05(2) 0.10(3) 0.15(4) 0.30$ in the xz -plane for (a) an ideal solar sail and (b) a realistic partially reflecting sail with sail reflectivity 0.9. No artificial equilibrium solutions exist in the gray region.	26
2.1	Definition of coordinate system and low-thrust spacecraft in a periodic halo orbit about an artificial equilibrium point beyond L_2	36
2.2	Zero velocity curves in the Sun-Earth system for (a) energy values of the L_1 and (b) energy values of the L_2 point . For the classical case $\mathbf{a}_T = (0, 0, 0)$ (dashed contour lines) and for the low-thrust system $\mathbf{a}_T = (0.0001, 0, 0)$ (solid contour lines).	37
2.3	Lissajous trajectory at AEP $\mathbf{r}_0 = [1.02 \ 0 \ 0]^T$ (beyond L_2) in the Sun-Earth system. $A_x = A_z = 2.3396 \times 10^{-5}(3500 \text{ km})$ and $\phi_{xy} = \phi_z = 0$ are chosen for illustration purposes. The AEP needs $\mathbf{a}_T = (-0.0512, 0, 0)$	40
2.4	Period of artificial halo orbit vs AEPs selected at x_0 near to (a) L_1 and (b) L_2 points in the Sun-Earth system. The dotted curve shows the low-thrust acceleration required at x_0 to create AEPs while the solid line shows the orbit period. $\mathbf{a}_T = 0$ at L_1 and L_2	43
2.5	Zero and second order frequencies vs AEPs selected at x_0 near to (a) L_1 and (b) L_2 points in the Sun-Earth system.	44
2.6	The minimum x-amplitude to have artificial halo orbits vs AEPs selected at x_0 near to (a) L_1 and (b) L_2 points.	45
2.7	Orbit period versus AEPs selected at x_0 near to (a) L_1 and (b) L_2 points with various A_z values: $A_z(125, 000)$ km for the black dashed-line, $A_z(3 \times 125, 000)$ km for the gray solid-line, and $A_z(7 \times 125, 000)$ km for the black solid-line.	46

2.8	Artificial halo orbits are shown in gray around artificial L_1 points ($n = 1$) with low thrust acceleration vectors $\mathbf{a}_T = (\pm 0.01, 0, 0)$ and $\mathbf{a}_T = (\pm 0.02, 0, 0)$. The classical halo orbit is also shown (3rd dark black orbit). All periodic orbits have the same $A_z = 8.3557 \times 10^{-4}$ (125,000 km).	48
2.9	Artificial halo orbits are shown in gray around artificial L_2 points ($n = 3$) with low thrust acceleration vectors $\mathbf{a}_T = (\pm 0.01, 0, 0)$ and $\mathbf{a}_T = (\pm 0.02, 0, 0)$. The classical halo orbit is also shown (3rd dark black orbit). All periodic orbits have the same $A_z = 8.3557 \times 10^{-4}$ (125,000 km).	49
2.10	Artificial periodic halo orbits in the Sun-Earth system around AEP $\mathbf{r}_0 = (1.01134, 0, 0)$ with $\mathbf{a}_T = (-0.01, 0, 0)$ pointing towards the Sun. The first five periodic orbits are generated by using an initial guess from Lindstedt-Poincaré. Large amplitude periodic orbits are produced using the continuation method with $\Delta T_{1/2} = -0.02$. The dashed line is the stable halo orbit.	52
2.11	The half-period of classical halo orbits about L_2 is shown by the dashed line, and the half-period of artificial halo orbits about AEP $\mathbf{r}_0 = (1.01134, 0, 0)$ is shown by the solid line.	53
2.12	Classical halo orbits about L_2 shown by the dashed line, and artificial halo orbits about AEP $\mathbf{r}_0 = (1.01134, 0, 0)$ with low-thrust acceleration $\mathbf{a}_T = (-0.01, 0, 0)$ shown by the solid line. Heavy dots on both curves corresponds to stable halo orbits.	53
2.13	Stable orbit around AEP $\mathbf{r}_0 = (1.01134, 0, 0)$ with low-thrust acceleration $\mathbf{a}_T = (-0.01, 0, 0)$ maintain halo shape for 25 years.	56
3.1	Solar radiation pressure force model for a specularly reflecting hybrid sail. The solar electric propulsion thruster is also shown.	60

3.2	Maximum cone angle for a hybrid sail (5% TFSC area relative to total area) is less than that for a pure sail (with no TFSC area) . . .	62
3.3	Definition of coordinate system and hybrid sail using two low-thrust propulsion systems.	63
3.4	Definition of cone and clock angles for vectors \mathbf{n} , \mathbf{m} and \mathbf{a}_{gc} in frame F_b	65
3.5	Required low thrust acceleration from SEP at $\mathbf{r}_0 = [1.005 \ 0.005 \ 0.005]^T$ as a function of the sail pitch angle α and sail clock angle δ for a sail with $\beta_0 = 0.03$. Minimum $a_T = 0.0269$ at optimal angles $(\alpha^*(0), \delta^*(0)) = (40.23^\circ, 39.46^\circ)$	66
3.6	Thrust acceleration contours a_T in the xz-plane. Values 0.02, 0.03 shown by dotted lines for the pure SEP system and shown by solid lines for the hybrid sail. ∓ 23.5 deg are the angles of the polar axis of the Earth (dashed lines) with respect to the normal to the ecliptic plane at summer and winter solstices.	68
3.7	Regions I-IV in the Sun-Earth three-body system are classified according to the stability of artificial equilibria for a hybrid sail. 1, 2 and 3 represent contours of $D = 0$, $p_0 = 0$ and $p_1 = 0$ respectively. .	76
3.8	Variation in the roots $\kappa_1, \kappa_2, \kappa_3$ of cubic Eq. (3.45) due to decrease of hybrid sail mass. The root κ_3 corresponds to a saddle point. The AEP $\mathbf{r}_0 = [0.99558 \ 0 \ 0.01016]^T$ is chosen for illustration, the hybrid sail has initial mass $m_0 = 500$ kg and $\beta_0 = 0.03$	77
3.9	Thrust acceleration magnitude required from pure SEP and hybrid sail (at $t = 0$) at artificial equilibrium points above L_1 along the Earth's polar axis (north pole at summer solstice).	78

3.10	Spacecraft initial (wet) mass required for an AEP for a 100 kg payload for a polar observer mission (above L_1). Five-year mission lifetime is considered for a pure SEP and hybrid sail. Initial mass variation for a pure and hybrid sail with sail assembly loading equal to a) 14.1 g/m ² b) 10 g/m ² and c) 5 g/m ² are also shown. The vertical line shows that the pure sail cannot be placed along the polar axis below 0.015 AU.	83
3.11	Hybrid sail during mission life stationed at polar distance 0.01831 AU along the polar axis above L_1 : a) SRP acceleration magnitude b) Pitch angle.	86
3.12	Hybrid sail during mission life stationed at polar distance 0.01831 AU along the polar axis above L_1 : (a) ion thruster force, and b) ion thruster firing angle with respect to the sail normal.	87
4.1	SEP system pointing angles α_T and γ_T defined in frame F_b allowing pitch and yaw control. The frame F_b is defined in section 3.2. . . .	90
4.2	Open loop control: histories of (a) states and (b) control effort for initial condition $\delta\mathbf{X}(0) = [0.001, 0.001, 0.001, 0.0, 0.0, 0.001]$ and $t_f = 2.55\pi$	93
4.3	Finite horizon LQR control: histories of (a) states (the dashed line is the linear system, and the solid line is the nonlinear system) and (b) control effort for initial condition $\delta\mathbf{X}(0) = [0.001, 0.001, 0.001, 0.0, 0.0, 0.001]$ and $t_f = 10\pi$ (mission lifetime). Weighted matrices $S(t_f) = \rho_1 I_6 = 0_{6 \times 6}$, $Q = I_6$ and $R = \rho_2 I_2 = 10^{-4} I_2$ are chosen.	95
4.4	Finite horizon LQR control: histories of (a) states (the dashed line is the linear system, and the solid line is the nonlinear system) and (b) control effort for initial condition $\delta\mathbf{X}(t_0) = [0.001, 0.001, 0.001, 0.0, 0.0, 0.001]$ perturbed at $t_0 = 5\pi$ and $t_f = 10\pi$ (mission lifetime). Weighting matrices are $S(t_f) = \rho_1 I_6 = 0_{6 \times 6}$, $Q = I_6$ and $R = \rho_2 I_2 = 10^{-4} I_2$. . .	97

4.5	Finite horizon LQR control: histories of (a) states (the dashed line is the linear system, and the solid line is the nonlinear system) and (b) control effort for initial condition $\delta\mathbf{X}(0) = [0.001, 0.001, 0.001, 0.001, 0.001, 0.001]$ and $t_f = 10\pi$ (mission lifetime). Weighting matrices are $S(t_f) = \rho_1 I_6 = 0_{6 \times 6}$, $Q = I_6$ and $R = \rho_2 I_2 = 10^{-4} I_2$	98
5.1	Two coordinate systems ECI (x_I, y_I, z_I) and ECEF (x_e, y_e, z_e) are shown. A solar sail on a displaced orbit above the equatorial plane around a geostationary point at r_{gs} , where the sun line $\hat{\mathbf{S}}$ is assumed to be in the Earth equatorial plane.	101
5.2	The sail pitch α is defined with respect to the Earth equatorial plane, while the yaw angle δ is defined with respect to the Sun-line in the equatorial plane, where the Sun-line $\hat{\mathbf{S}}$ is in the equator plane.	103
5.3	Displaced solar sail orbits of period $T = 2\pi/\Omega^*$ around a geostationary point. The solar sails are pitched at $\alpha^* = 35.264^\circ$ on each orbit. For the solid-line orbit at $\zeta^0 = 0.000237168$ (10 km), the gray-line orbit at $\zeta^0 = 0.000355752$ (15 km) and the dashed-line orbit at $\zeta^0 = 0.000474336$ (20 km), the sails require a characteristic acceleration $a_0^* = 0.000616181$ (0.138 mms^{-2}), $a_0^* = 0.000924272$ (0.207 mms^{-2}) and $a_0^* = 0.00123236$ (0.276 mms^{-2}) respectively.	107
5.4	Displaced orbits of period $T = 2\pi/\Omega^*$. (a) The two orbits are at the same displacement $\zeta^0 = 0.000237168$ (10 km) for a sail with $a_0 = 0.001561$ (0.35 mms^{-2}). The sail is pitched at angle $\alpha_1 = 8.95^\circ$ for the dashed-line orbit and at an angle $\alpha_2 = 65.92^\circ$ for the solid-line orbit so that $\cos^2 \alpha_1 \sin \alpha_1 = \cos^2 \alpha_2 \sin \alpha_2$ (b) For a sail with a_0 (0.138 mms^{-2}), multiple orbits are shown at different displacements ζ^0 by varying the pitch angle at 60° (the gray solid-line orbit), 55° (the black solid-line orbit), 35.264° (the black dashed-line orbit), 25° (the gray dashed-line orbit).	108

5.5	i^{th} segment for Hermite-Simpson transcription.	111
5.6	A sail with characteristic acceleration 0.328 mms^{-2} shows a displaced periodic orbits of period $T = 2\pi/\Omega^*$ around a geostationary point (a) in the ECEF frame (b) in the ECI frame (the black solid line orbit is a non-Keplerian orbit from the collocation scheme and the gray solid line orbit is the Keplerian geostationary orbit) and (c) control history.	117
5.7	Displaced periodic orbits using a high performance sail with a characteristic acceleration of 6 mms^{-2} (a) in the ECEF frame (b) in the ECI frame and (c) the control history.	119
5.8	The Sun-line $\hat{\mathbf{S}}$ is shown at an arbitrary angle ϕ above the Earth's equatorial plane. $\hat{\mathbf{S}}'$ is the projection of the Sun-line in the Earth's equatorial plane. The angle Ω^*t is in the Earth's equatorial plane and the angle ϕ is out of the Earth's equatorial plane. The angle ϕ is assumed constant over one orbit period.	121
5.9	10 km levitated displaced periodic orbits for a sail with characteristic acceleration $a_0 = 0.002795$ (0.626 mms^{-2}) at the summer solstice (dashed-line orbit with $\alpha = 70^\circ$), winter solstice (solid-line black orbit with $\alpha = 73^\circ$) and at autumn/spring equinoxes (gray orbit with $\alpha = 72.65^\circ$).	123
5.10	At the summer solstice (worst-case scenario), displaced periodic orbits for a sail with a characteristic acceleration 6 mms^{-2} (a) in the ECEF frame (b) in the ECI frame and (c) the control history (right).	125

5.11	(a) The two solar sails are pitched at $\alpha = \pm 45^\circ$ on displaced orbits (the solid-line orbits) at a levitation distance $\zeta^0 = \pm 2$ km. The microwave energy generator-transmitter is orbiting (the dashed-line orbit) in the Earth's equatorial plane and is placed in centre of the system. All three orbits have the same period $T = 2\pi/\Omega^*$ and in-plane acceleration a_p (b) orbits from the linear analysis (sails on displaced orbits with a_0 (0.03 mms^{-2}) (i.e., a_p ($0.010635 \text{ mms}^{-2}$) on all orbits)) and the non-linear analysis illustrating the SPS concept in ECEF-frame at the equinoxes (c) sail pitch angle history.	128
5.12	(a) Light-levitated cylindrical orbit at +2 km (b) history of sail pitch angle α and Sun's declination angle ϕ over one year (c) component of sail acceleration parallel to Earth's equatorial plane $a_p = a_0 \cos^2 \alpha \cos(\alpha + \phi)$	130
6.1	(a) Dashed-line represent flat linearised displaced periodic orbit at distance of 10 km above the Earth's equatorial plane. The solid-line is a periodic solution of Eq. (5.22) around a geostationary point, however it is not a displaced orbit. Both orbits have the same period $T = 2\pi/\Omega^*$ and sail characteristic acceleration 0.138 mms^{-2} (b) periodic orbits x - y projection.	135
6.2	The dashed-line and solid line are control history of the linear and nonlinear periodic orbits of Fig. 6.1 respectively.	135
6.3	Projections of periodic orbits ($a_0(0.05 \text{ mms}^{-2})$) around a geostationary point in the ECEF-rotating frame. Dashed line is the linearised orbit and solid line is the nonlinear orbit from the differential corrector.	142

6.4	Projections of periodic orbits ($a_0(0.1 \text{ mms}^{-2})$) around a geostationary point in the ECEF-rotating frame. Dashed line is the linearised orbit and solid line is the nonlinear orbit from the differential corrector.	143
6.5	Nonlinear periodic orbits of period $T = 2\pi/\Omega^*$ around a geostationary point in the ECEF-rotating frame with $\alpha^* = 35.264^\circ$ and different a_0 parameters: a_0 (0.215 mms^{-2}) for the thin solid-line, a_0 (0.335 mms^{-2}) for the thick solid-line, and a_0 (0.425 mms^{-2}) for the dashed-line. The thick solid-line and dashed-line orbits are generated using the continuation method while the thin solid line orbit is obtained using the differential corrector method.	145
6.6	A sail with characteristic acceleration 0.425 mms^{-2} (a) the periodic orbit in the ECEF-frame and (b) sail control history obtained using the collocation scheme. The linearised periodic orbit, shown by the dashed-line, is an initial guess for the collocation scheme.	146

List of Tables

1.1	Parameters of the linearised solution at $L_{1,2}$ of the Sun-Earth system.	8
2.1	Initial condition for stable orbits with $\mathbf{a}_T = (-0.01, 0, 0)$ which corresponds to a low-thrust acceleration 0.0593 mms^{-2} and low-thrust force 30 mN for a 500 kg spacecraft.	54
3.1	Mass breakdown for three different propulsion systems for a spacecraft stationed at a polar distance 0.01831 AU along the polar axis above L_1 . A fixed payload mass and fixed mission life of 5 years is assumed in the case of pure SEP and the hybrid sail.	84
5.1	ΔV budget to generate displaced NKO using pure a SEP system. The displaced NKO with period τ_e is chosen above and synchronous with a geostationary point at r_{gs}	131

Nomenclature

- A_S sail area (not including thin film area)
- A_{TF} thin film area
- A_T total hybrid sail area, $= A_S + A_{TF}$
- a_{ref} dimensional reference acceleration in the three-body problem,
 $= 0.00593 \text{ m/s}^2$ in the Sun-Earth system
- \mathbf{a}_{gc} non-dimensional acceleration vector required to balance gravitational and centrifugal force
- a_{gc} magnitude of vector \mathbf{a}_{gc} , $a_{gc} = |\mathbf{a}_{gc}|$
- \acute{a}_{gc} dimensional acceleration required to balance gravitational and centrifugal force,
 $= a_{\text{ref}} \times a_{gc}$
- \mathbf{a}_{SS} acceleration vector due to solar radiation pressure from (ideal) sail
- \mathbf{a}_S non-dimensional acceleration vector due to solar radiation pressure from (realistic) sail
- a_s magnitude of vector \mathbf{a}_S , $a_s = |\mathbf{a}_S|$
- \mathbf{a}_T non-dimensional thrust acceleration vector from electric propulsion system
- a_T magnitude of vector \mathbf{a}_T , $a_T = |\mathbf{a}_T|$
- \acute{a}_T dimensional thrust acceleration from electric propulsion system,
 $= a_{\text{ref}} \times a_T$
- a_r dimensional reference acceleration in the two-body problem,
 $= 0.224208 \text{ m/s}^2$ for a spacecraft/sail at geostationary orbit around the Earth
- a_0 non-dimensional (ideal) sail characteristic acceleration
- a_c dimensional sail characteristic acceleration, $= a_r \times a_0$
- $\mathbf{C}_{b/a}$ transformation matrix from F_a to F_b frame
- c speed of light, $= 3 \times 10^8 \text{ m/s}$
- \mathbf{F}_S dimensional force from sail due to solar radiation pressure, N
- \mathbf{F}_T dimensional thrust force from electric propulsion system, N
- G universal gravitational constant, $= 6.672 \times 10^{-11} \text{ N m}^2/\text{kg}^2$

g_0	gravity acceleration at the Earth's surface, = 9.80665 m/s ²
L_s	solar luminosity, = 3.856×10^{26} W
m	instantaneous mass of spacecraft
m_1	mass of the Sun
m_2	mass of the Earth
\mathbf{n}	unit vector normal to (realistic) sail surface and directed away from the Sun
p_i	i^{th} polynomial coefficient of cubic equation, ($i = 0 - 2$)
R_1	dimensional distance between the Sun and spacecraft
r_1	non-dimensional distance between the Sun and spacecraft
\mathbf{r}	position vector of spacecraft with respect to center of mass of the two primaries
\mathbf{r}	position vector of solar sail with respect to center of the Earth in ECEF-frame
\tilde{r}_S	sail film reflectivity
\tilde{r}_{TF}	thin film reflectivity
\mathbf{u}	unit vector normal to (ideal) sail surface and directed away from the Sun
\mathbf{u}	= (α_T, δ_T) gimbal angles defining thruster's orientation (pitch and yaw angles)
Δt	time step
\mathcal{T}	thrust force magnitude from electric propulsion system, $\mathcal{T} = \mathbf{F}_T $
T	orbit period
α	solar sail pitch angle
δ	solar sail clock angle (or yaw angle)
ω	dimensional angular velocity of rotating frame, = $\sqrt{\frac{G(m_1+m_2)}{R^3}}$ s ⁻¹
$\boldsymbol{\omega}$	non-dimensional angular velocity vector in rotating frame
σ^*	critical sail loading parameter, = 1.53×10^{-3} kg/m ²
τ_m	mission lifetime
<i>Superscript</i>	
T	Transpose

Abbreviations

AEPs	artificial equilibrium points
CRTBP	circular restricted three-body problem
ERTBP	elliptical restricted three-body problem
ECI	Earth-centred inertial
ECEF	Earth-centred earth-fixed
NEA	near Earth asteroid
NEXT	NASA's evolutionary Xenon thruster
NKO	non-Keplerian orbits
PPU	power processor unit
SEP	solar electric propulsion
SRP	solar radiation pressure
TFSC	thin film solar cells

Chapter 1

Introduction

Section 1.1 describes the dynamical model of the circular restricted three-body problem and the locations of the five Lagrange points therein. The only integral of the circular restricted three-body problem, Jacobi's integral, is also derived. The various families of orbits i.e., periodic and quasi periodic orbits around the Lagrange points for the classical case (a spacecraft under the gravitational force of the primaries with no propulsion), and their applications for space science missions are discussed in section 1.2. In this thesis three types of low-thrust propulsion systems are used to generate non-Keplerian orbits (NKO). These low-thrust propulsion systems, solar electric propulsion, solar sail and a combination of solar electric propulsion and solar sail to form a hybrid propulsion system are discussed in section 1.3. The key performance parameters for a solar electric propulsion system and solar sail propulsion are also discussed. Among the solar electric propulsion systems, electrostatic thrusters are discussed in detail as these thrusters can be selected for the hybrid sail configuration.

In section 1.4, a literature review for non-Keplerian orbits in the restricted three-body problem and two-body problem is provided. Moreover, three key research objectives for the thesis are also outlined. Section 1.5 provides the thesis layout. The conference and journal papers published by the author are provided in the last section of this chapter.

1.1 The Circular Restricted Three-body Problem

The circular restricted three-body problem (CRTBP) is one of the long standing problems in celestial mechanics, originally formulated by Leonard Euler in 1772. It describes the motion of an infinitesimal mass under the gravitational influence of two massive bodies in circular motion about their common center of mass. Although termed ‘three-body’, in reality the restricted problem is a one-body problem of infinitesimal mass m , since the motion of the two massive bodies is known; pure Keplerian circular motion. The CRTBP does not have an analytical closed-form solution as six integrals of motion are required, while only one integral of motion, *Jacobi’s integral*, is available. Let m_1 and m_2 denote the two massive bodies, referred to as the primary masses. The main assumption is that

$$m \ll m_2 < m_1$$

so that the third body does not influence the motion of the primary masses. In orbital dynamics, this assumption can be used to model the motion of any spacecraft in the Earth-Moon system or Sun-Earth system for example.

The next sub-section describes the equations of motion of the CRTBP in non-dimensional units. The equilibrium points of these equations of motion are discussed in Sec. 1.1.2, and the only scalar constant of the CRTBP, Jacobi’s integral, is given in Sec. 1.1.3.

1.1.1 Equations of Motion

The restricted three-body problem is usually modelled in a reference frame rotating with angular speed $\omega = \sqrt{\frac{G(m_1+m_2)}{R^3}}$ defined by the orbital motion of the primaries, where R is the distance between the primaries. The origin of this frame, illustrated in Fig. 1.1, is at the center of the two primaries. The x -axis lies along the two primaries, the z -axis is perpendicular to the orbit plane, parallel to the angular

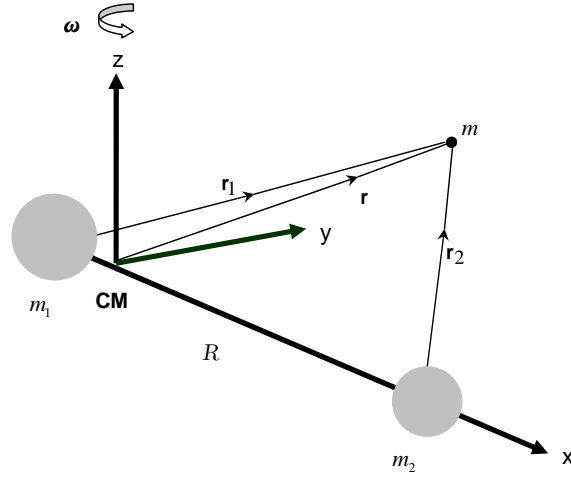


Figure 1.1: Geometry of the restricted-three body problem. The primary masses m_1 and m_2 are at rest in a synodic rotating reference frame (x, y, z) with origin at centre of mass (CM) and with fixed separation R .

velocity vector, and the y -axis completes the right-handed coordinate system. The system is made non-dimensional by taking the units of length, mass and time such that the distance between the primaries R , the product of gravitational constant G and the sum of the masses of the primaries, $G(m_1 + m_2)$, and the period of the primaries are 1, 1 and 2π respectively.

Define the mass ratio $\mu = \frac{m_2}{m_1 + m_2}$, then m_1 is located at $(-\mu, 0, 0)$ and m_2 is located at $(1 - \mu, 0, 0)$ with respect to the center of mass. If $\mathbf{r} = [x \ y \ z]^T$ denotes the position vector of the mass m relative to the center of mass, then the position vector of the mass m with respect to the primaries m_1 and m_2 is given by

$$\mathbf{r}_1 = [x + \mu \ y \ z]^T, \quad \mathbf{r}_2 = [x - (1 - \mu) \ y \ z]^T$$

The equations of motion of the mass m can now be written in the following non-dimensional form

$$\ddot{\mathbf{r}} + 2 \boldsymbol{\omega} \times \dot{\mathbf{r}} + \boldsymbol{\omega} \times (\boldsymbol{\omega} \times \mathbf{r}) = \mathbf{a}_g \quad (1.1)$$

where $\boldsymbol{\omega} \parallel \hat{z}$ (see Fig. 1.1), and the gravitational acceleration \mathbf{a}_g on the mass m is

given by

$$\mathbf{a}_g = -\frac{1-\mu}{r_1^3}\mathbf{r}_1 - \frac{\mu}{r_2^3}\mathbf{r}_2$$

where in non-dimensional units $Gm_2 = \mu$ and $Gm_1 = 1 - \mu$. The component form of the equations of motion Eq. (1.1) are given by

$$\ddot{x} - 2\dot{y} = x - \frac{1-\mu}{r_1^3}(x+\mu) - \frac{\mu}{r_2^3}(x-(1-\mu)) = \frac{\partial V}{\partial x} \quad (1.2)$$

$$\ddot{y} + 2\dot{x} = y \left(1 - \frac{1-\mu}{r_1^3} - \frac{\mu}{r_2^3} \right) = \frac{\partial V}{\partial y} \quad (1.3)$$

$$\ddot{z} = z \left(-\frac{1-\mu}{r_1^3} - \frac{\mu}{r_2^3} \right) = \frac{\partial V}{\partial z} \quad (1.4)$$

where the pseudo-potential V , which is sum of the centrifugal and gravitational potential is given by

$$V = \frac{1}{2}(x^2 + y^2) + \left(\frac{1-\mu}{r_1} + \frac{\mu}{r_2} \right)$$

These nonlinear, coupled ordinary differential Eqs. (1.2-1.4) cannot be solved in closed form. Numerical integration shows that there exist periodic solutions, but that the majority of solutions are chaotic [89].

1.1.2 Location of Lagrange Points

The Lagrange points are equilibrium points where the infinitesimal mass m will be at rest relative to the rotating frame so that $\dot{x} = \ddot{x} = \dot{y} = \ddot{y} = \dot{z} = \ddot{z} = 0$. Substituting these conditions in Eqs. (1.2-1.4) to obtain equilibrium points, it can be seen that

$$\frac{\partial V}{\partial x} = \frac{\partial V}{\partial y} = \frac{\partial V}{\partial z} = 0$$

It is easy to see from Eq. (1.4) that in order to set $\frac{\partial V}{\partial z} = 0$, one must have $z = 0$, that is, all the equilibrium points lie in the $x - y$ plane. Therefore, two conditions $\frac{\partial V}{\partial x} = \frac{\partial V}{\partial y} = 0$ are left to find the equilibrium points.

Substituting $r_1 = r_2 = 1$ in Eqs. (1.2-1.3), it can be seen that both equations are satisfied i.e, $\frac{\partial V}{\partial x} = \frac{\partial V}{\partial y} = 0$, which results in the *triangular* Lagrange points L_4

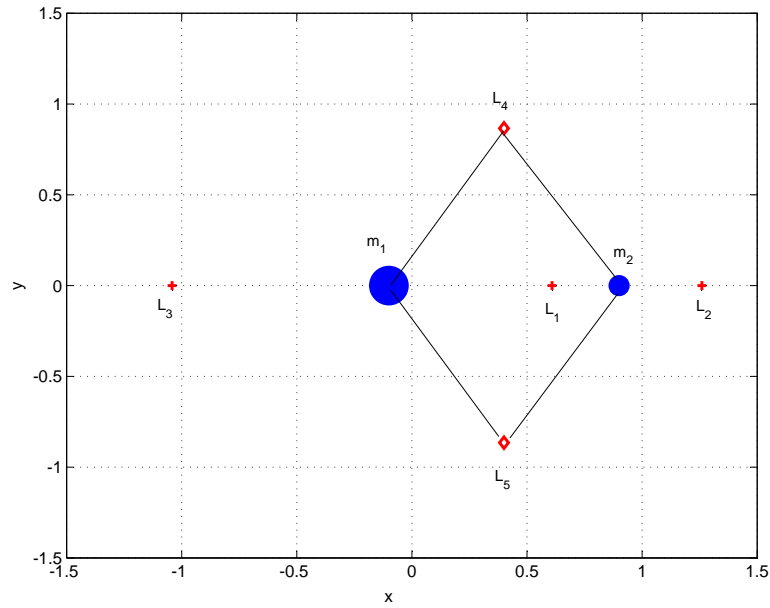


Figure 1.2: Lagrange points of the circular restricted three body problem with $\mu = 0.1$. The only parameter of the system is μ ($\mu = 3.0032 \times 10^{-6}$ for the Sun-Earth system, $\mu = 1.215 \times 10^{-2}$ for the Earth-Moon system).

and L_5 at $(1/2 - \mu, \sqrt{3}/2, 0)$ and $(1/2 - \mu, -\sqrt{3}/2, 0)$ respectively. Now, substituting $y = z = 0$ in Eqs. (1.3-1.4) implies $\frac{\partial V}{\partial y} = \frac{\partial V}{\partial z} = 0$, and so finally a quintic equation in x is solved to satisfy $\frac{\partial V}{\partial x} = 0$ (see Eq. 1.2), which results in the *collinear* Lagrange points for the three real roots $x(L_1)$, $x(L_2)$ and $x(L_3)$. These points L_1, \dots, L_5 are shown in Fig. 1.2 in the rotating frame.

The Lagrange points have great utility for space science missions. Current missions such as the SOHO spacecraft use the Earth-Sun L_1 point to observe the Sun continuously. The collinear points are unstable, therefore a spacecraft in the vicinity of these points needs active control. The triangular points will be linearly stable provided that $\mu \leq 0.0385209$, a condition that is true for all bodies in the solar system [102].

1.1.3 Jacobi's Integral

Jacobi's integral is the only scalar constant constraining the motion of the infinitesimal mass (spacecraft) in the circular restricted three-body problem. To derive Jacobi's constant, Eqs. (1.2-1.4) can be re-written in vector form as

$$\ddot{\mathbf{r}} + 2\boldsymbol{\omega} \times \dot{\mathbf{r}} = \nabla V \quad (1.5)$$

Taking the scalar product with $\dot{\mathbf{r}} = \mathbf{v}$, it can be seen that

$$\mathbf{v} \cdot \dot{\mathbf{v}} + 2\mathbf{v} \cdot (\boldsymbol{\omega} \times \mathbf{v}) = \mathbf{v} \cdot \nabla V = \frac{d\mathbf{r}}{dt} \cdot \frac{\partial V}{\partial \mathbf{r}}$$

Since V is a function of position and not explicitly of time, then

$$\frac{d\left[\frac{1}{2}\mathbf{v}^T \mathbf{v}\right]}{dt} = \frac{dV}{dt}$$

which is an exact differential and so integration yields Jacobi's constant C as

$$C(\mathbf{r}, \mathbf{v}) = \frac{1}{2}\mathbf{v}^T \mathbf{v} - V(\mathbf{r}) \quad (1.6)$$

According to Poincaré [45], an infinite number of periodic orbits exist in the 3-body problem. These are natural periodic orbits in the 3-body problem and are generated numerically since no closed form solutions of Eq. (1.1) exist. Notably, no propulsion system is required to generate these natural orbits. Some useful orbits for space science missions are discussed in next section.

1.2 Periodic and Quasi-Periodic Orbits

This section describes periodic and quasi-periodic orbits around the Lagrange points $L_{1,2}$ (see section 1.1.2) in the Sun-Earth system. One way to generate periodic orbits from the nonlinear equations of motion is to first generate periodic solutions of the corresponding linearised equations. Then, the bounded solution

of the linearised equations around the Lagrange points are found to be

$$\delta x = -A_x \cos(w_{xy}t + \phi_{xy}) \quad (1.7)$$

$$\delta y = kA_x \sin(w_{xy}t + \phi_{xy}) \quad (1.8)$$

$$\delta z = A_z \sin(w_z t + \phi_z) \quad (1.9)$$

where δx , δy and δz are position components relative to the Lagrange points [75]. The parameters A_x and A_z are the amplitude, and ϕ_{xy} and ϕ_z are the phase angles, with w_{xy} and w_z the in and out of plane frequencies.

The linearised solution in Eqs. (1.7-1.9) will describe:

1. 2-D periodic orbit if we restrict the motion in the plane i.e., $\delta z = 0$ in Eq. (1.9). Then Eqs. (1.7-1.8) illustrate a 2-D *Lyapunov* orbit.
2. 3-D quasi-periodic orbit if w_{xy}/w_z is an irrational number. This orbit is usually referred to as *Lissajous* trajectory.
3. 3D periodic orbit if w_{xy}/w_z is a rational number.

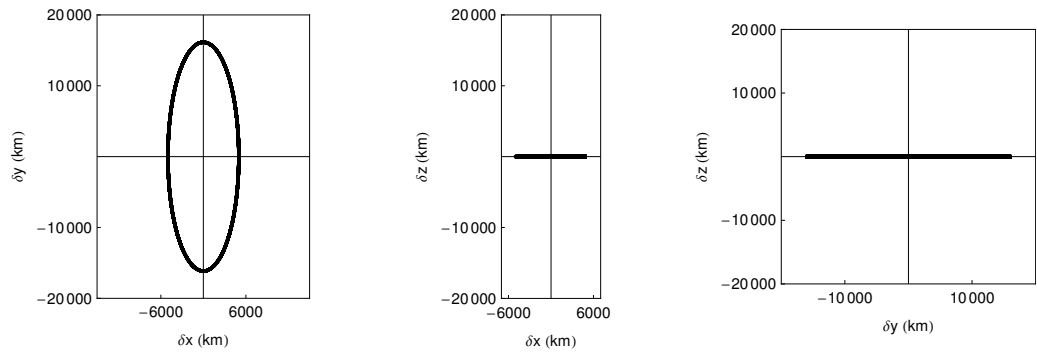


Figure 1.3: Linear-order L_1 Lyapunov orbit ($A_x(5000 \text{ km})$) in the Sun-Earth system.

Fig. 1.3 shows a *Lyapunov* orbit around L_1 in the plane. The Lyapunov orbit is characterised by one parameter A_x and is symmetric about the x -axis.

Values of w_{xy} and w_z at $L_{1,2}$ (see Table 1.1) are such that the ratio w_{xy}/w_z is an irrational number, therefore, three-dimensional motion is a *Lissajous* trajectory.

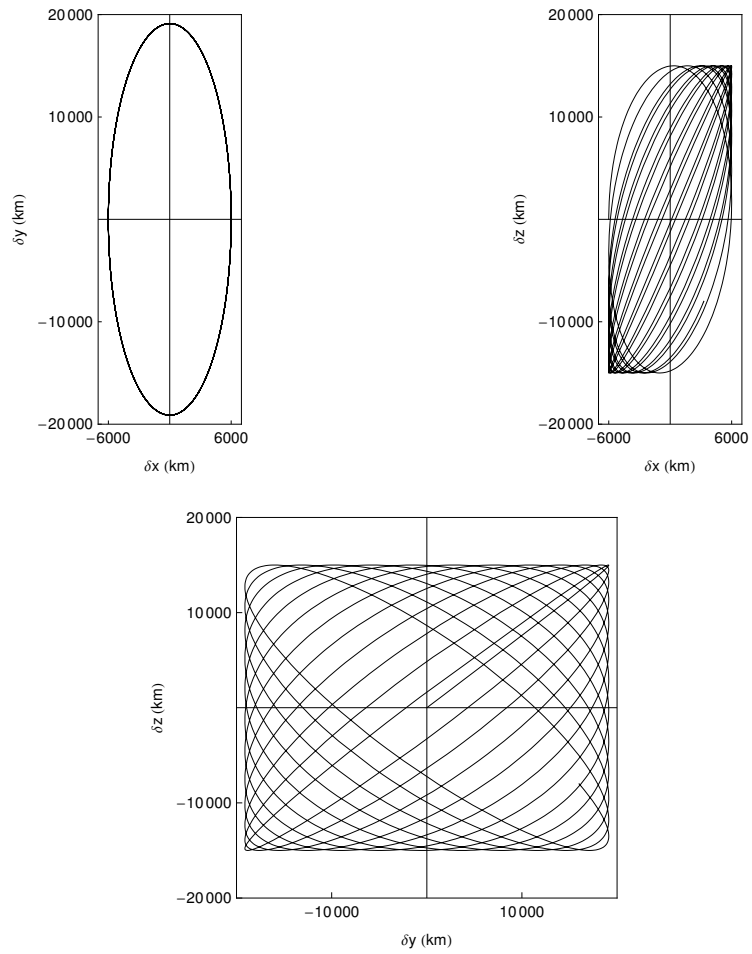


Figure 1.4: Linear-order L_2 Lissajous orbit ($A_x(6000 \text{ km})$, $A_z(15000 \text{ km})$) in the Sun-Earth system.

Table 1.1: Parameters of the linearised solution at $L_{1,2}$ of the Sun-Earth system.

Parameter	Value at L_1	Value at L_2
w_{xy}	2.08645	2.05701
w_z	2.01521	1.98507
k	3.22927	3.18723

The Lissajous trajectory is not a closed path or a periodic orbit. A Lissajous orbit around L_2 is shown in Fig. 1.4 at linear order. The Lissajous orbit is characterised by two parameters A_x (or A_y) and A_z . The Lagrange point L_2 lies on the night side of the Earth, and is therefore an ideal location for space-based astronomy. The European Space Agency GAIA mission [79] will use a large amplitude Lissajous- L_2 orbit without eclipse (as viewed from Earth along the x -axis) for 5-years.

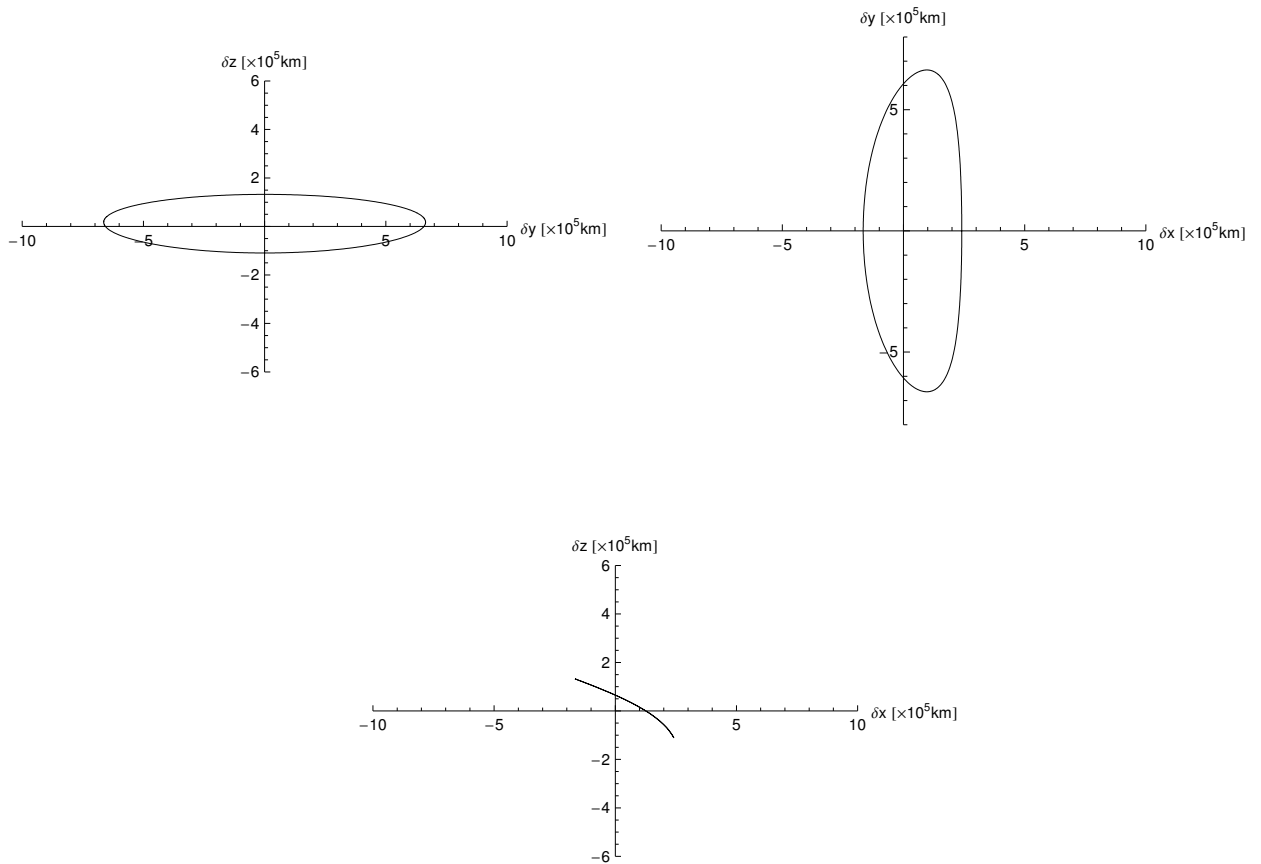


Figure 1.5: Third-order L_1 halo orbit ($A_z(120,000 \text{ km})$) in the Sun-Earth system. Halo orbits do not exist at linear order.

A special case exists where the ratio w_{xy}/w_z is a rational number and becomes equal to one when the amplitude of the orbit is large so that the nonlinear terms of Eq. (1.1) are significant. Then, a 3-D *halo* orbit is formed. A certain combination

of amplitudes exists for the generation of halo orbits provided that the in-plane amplitude A_x of the orbit becomes greater than some minimum amplitude A_{xmin} , i.e., ($A_x > A_{xmin}$). Fig. 1.5 shows a halo orbit around L_1 . The halo orbit is characterised by one parameter, usually A_z , and is symmetric about the xz -plane. From the Lagrange point L_1 of the Sun-Earth system, a spacecraft has an uninterrupted view of the Sun and Earth. The ISEE-3 and SOHO mission spacecraft both used halo orbits ($A_z = 120,000$ km) around L_1 [23]. The spacecraft is not placed at the L_1 point as the Sun is a powerful radio source, therefore any signal from the spacecraft would be overwhelmed. Therefore, a spacecraft must orbit L_1 in a halo orbit which keeps it a few degrees away from the Sun-line.

The linear and third order analytic approximations of Lyapunov and halo orbits are shown in Fig. 1.3 and Fig. 1.5 respectively. These approximations are used as an initial guess to determine the periodic solution of the full non-linear system Eq.(1.1), and necessary corrections to this initial guess are made using a differential corrector scheme [90]. Whereas for Lissajous orbits, the analytic approximation (first or third-order) is used as an initial guess, the quasi-periodic motion in the full non-linear system is determined using a two-level differential corrector scheme [42].

In this section non-Keplerian orbits in the classical case are generated in the vicinity of the Lagrange points $L_{1,2}$. These periodic orbits (Lyapunov, Lissajous and halo) are unstable. Low-thrust propulsion has important roles for these periodic orbits. Firstly, low-thrust propulsion can be used to stabilise such orbits [12, 50]. Secondly, low thrust propulsion can be used to generate such orbits around points other than the classical Lagrange points, as will be seen later. However, we will first discuss what types of low-thrust propulsion system exist.

1.3 Low-Thrust Propulsion System

This section describes low-thrust propulsion systems such as *solar electric propulsion* which utilises propellant efficiently and *solar sail propulsion* system which uses no propellant. In the final subsection, a hybrid propulsion concept is also discussed.

The use of solar electric propulsion as a primary propulsion system has been flight tested, For example, the NASA Deep Space-1 mission, launched in 1998, used the NSTAR (NASA Solar Electric Propulsion Technology Application Readiness) ion engine, and ESA's SMART-1 spacecraft used a Hall-effect thruster as primary propulsion, launched in September 2003. For solar sail propulsion a flight test was attempted in June 2005 (Cosmos-1 mission) by the Planetary Society. However, the mission aims for Cosmos-1, to demonstrate the first controlled-flight using solar photons, was not completed due to launch failure. In fact, a controlled flight of solar sail propulsion has yet to be flown. However, sail technologies to support future missions are progressing.

1.3.1 Electric Propulsion System

More than 160 satellites have used an electric propulsion system in some form. Electric propulsion systems consist of a power source (solar or nuclear), a thruster system (including power conditioning) and propellant management (storage and delivery) subsystem. This sub-section describes the different categories of electric propulsion systems. In particular, electrostatic thrusters which can be used for the hybrid sail configuration (see section 1.3.3) are considered.

Electric propulsion has a higher specific impulse I_{sp} than chemical propulsion, and therefore provides lower propellant consumption over long periods. Specific impulse is defined as the thrust per unit weight of propellant flow at sea level, thus

$$I_{sp} = \mathcal{T} / \dot{m}g_0 = v_e / g_0 \quad (1.10)$$

where $\mathcal{T} = \dot{m}v_e$ is the engine thrust, \dot{m} is the mass flow rate of the propellant and $g_0 = 9.81 \text{ m/s}^2$ is the gravitational acceleration constant at sea level. Other performance characteristics of electric propulsion systems are the thruster efficiency (η_e), specific mass (k_e) and thruster lifetime [17].

Thruster efficiency (η_e) is defined as the jet power $P_j = 1/2\dot{m}v_e^2$ in the exhaust of the electric propulsion system divided by the electrical power P_e input to the thruster

$$\eta_e = \frac{P_j}{P_e} = \frac{1/2\dot{m}v_e^2}{P_e} \Rightarrow P_e = \frac{\dot{m}(I_{sp}g_0)^2}{2\eta_e} \quad (1.11)$$

The specific mass k_e is defined as the ratio of power processor and propulsion system mass to the power P_e input to the thruster. Higher η_e and lower k_e is desired for an effective electric propulsion system.

Electric propulsion systems are classified into three classes i.e., electro-thermal, electrostatic and electromagnetic systems.

1.3.1.1 Electrothermal thruster

Electro-thermal thrusters such as resistojets and arcjets thrusters heat the propellant (commonly Hydrazine (N_2H_4)) by electrical resistance or electric discharge respectively, with the heated propellant expanded through a nozzle. Resistojet/arcjet systems are widely used for attitude control and for north-south station-keeping on commercial communication satellites. Electrothermal thrusters will not be considered further in this thesis, as these thrusters are not applicable ($I_{sp} < 1000$ s) for applications to NKO.

1.3.1.2 Electrostatic thruster

Electrostatic thrusters use an applied electric field to accelerate positive ions. Both grided ion engines (NASA 30-cm NSTAR-engine) and Hall-effect thrusters (ESA's SMART-1 spacecraft) are electrostatic thrusters. Other examples of grided ion thruster are the UK-10 (10 cm exit diameter) that provides a maximum thrust of 25

mN ($I_{sp} = 3345$ s, $P_{e,max} = 660$ W, and $\eta_e = 60\%$), and the RIT-10 thruster system that provides a maximum thrust of 15 mN ($I_{sp} = 3467$ s, $P_{e,max} = 585$ W, and $\eta_e = 64\%$) [30].

In gridded ion thrusters, the working fluid (Xenon) is ionized by stripping off electrons, and then the positive ions are accelerated to a very high exhaust velocity by means of an electrostatic field created between two perforated grids held at high voltage. Positively charged ions are emitted at high exhaust velocity of order 30 km/s. In the Hall thruster (loosely speaking a gridless ion engine), an axial electric field E and radial magnetic field B is generated which confines the electrons (generated by an external cathode) to drift azimuthally along the $E \times B$ direction in the discharge channel. The propellant ions, created by ionization of a rotating plasma of electrons, are accelerated electrostatically (ions are too heavy to be effected by B) and exit the thruster at high velocity to produce thrust. To prevent a build up of charge on the spacecraft, the positively charged ions at exit are electrically neutralised by ejecting electrons.

If an ion of mass m_i having a total charge of q passes through an electric potential difference Φ , an energy balance gives

$$\frac{1}{2}m_i v_e^2 = q\Phi \Rightarrow v_e = \sqrt{\frac{2q\Phi}{m_i}} \quad (1.12)$$

To throttle the engine, the control parameters are the voltage Φ and propellant flow rate \dot{m} . Φ is the beam voltage for the gridded ion engine and discharge voltage for the Hall-effect thruster [18]. The specific impulse and thrust-to-power ratio are obtained using Eq. (1.12) and can be written as

$$I_{sp} = \frac{v_e}{g_0} = \frac{1}{g_0} \sqrt{\frac{2q}{m_i}} \sqrt{\Phi} \quad (1.13)$$

$$\frac{\mathcal{T}}{P_e} = \frac{\dot{m}v_e}{J\Phi} = \frac{\dot{m}v_e}{\frac{q}{m_i}\dot{m}\Phi} = \sqrt{\frac{2m_i}{q\Phi}} \quad (1.14)$$

where J is the beam current. Xenon is used as a propellant in both thruster systems since Xenon ions have a large mass to charge ratio (m_i/q). When throttling down the engine, if the voltage Φ is kept fixed, then Eq.(1.13) shows that I_{sp} will be

fixed. The changing \dot{m} will cause a change of P_e (see Eq.(1.11)), and thus thrust level $\mathcal{T} = \dot{m}v_e$. The state-of-art throttle-able NSTAR gridded ion engine was designed for a life of 1 year and at full power $P_{e,max} = 2.3$ kW processed 83 kg propellant. However, the maximum throughput capability of the NSTAR ion engine is assumed to be 130 kg without engine wearout [14]. Recently, the NSTAR flight spare engine has demonstrated a lifetime of 3.5 years (the longest life of any rocket engine) and processed 235 kg propellant [43]. However, the next generation system (NEXT) has a larger propellant throughput capability (450 kg), higher input power (6.9 kW), thrust (240 mN), and a lightweight gimbal mechanism giving 18° thruster pitch/yaw [49]. Briefly, the life of an ion thruster is limited by progressive grid/thruster component erosion from ion impingement, so that large propellant throughput capability per engine is a technologically challenging requirement.

Gridded ion thrusters can be considered for non-Keplerian orbits. Firstly, the gridded ion thruster has a greater specific impulse I_{sp} (> 3000 s) than electrothermal thrusters I_{sp} (< 1000 s) and Hall-effect thrusters I_{sp} ($\simeq 1600$ s), but Hall thrusters provide more thrust \mathcal{T} at a given input power P_e than the ion thruster. Secondly, ion thrusters have greater efficiency ($> 65\%$) and lifetime (2 – 3 years) than the Hall-effect thruster efficiency (around 50%) and lifetime (8000 h). Thirdly, ion thrusters have a narrower beam angle (typically 20°) than the Hall-effect thruster, which will be important for the hybrid sail concept described later in section 1.3.3.

1.3.1.3 Electromagnetic thruster

The electromagnetic thruster uses the electromagnetic forces generated in a very high-current plasma discharge to accelerate ionized propellant and produce thrust. The pulsed plasma thruster (PPT) is a pulsed mode electromagnetic thruster using a solid propellant (Teflon). Recently a lightweight (total mass = 2 kg) micro-PPT module with a thrust level of 150μ N (Peak power = 20 W, $I_{sp}=500$ s and $\eta_e = 5\%$) has been proposed for solar sails as a secondary attitude control system [100].

1.3.2 Solar Sail Propulsion

A solar sail consists of a large, lightweight reflector and uses momentum exchange with solar photons to generate thrust. The photon pressure P exerted on a perpendicular surface is given by [64]

$$P = \frac{W}{c} \quad (1.15)$$

where c is the speed of light ($3 \times 10^8 \text{m/s}$), and W is the energy flux across the surface at a distance R_1 from the Sun

$$W = \frac{L_s}{4\pi R_1^2} = \frac{L_s}{4\pi R_E^2} \left(\frac{R_E}{R_1}\right)^2 = W_E \left(\frac{R_E}{R_1}\right)^2 \quad (1.16)$$

where L_s is the solar Luminosity ($3.856 \times 10^{26} \text{ W}$) and W_E (1368 W/m^2) is the energy flux at R_E , the mean distance of the Earth from the Sun. Substituting Eq. (1.16) into Eq. (1.15), it can be seen that

$$P = \frac{W_E}{c} \left(\frac{R_E}{R_1}\right)^2 = P_0 \left(\frac{R_E}{R_1}\right)^2 \quad (1.17)$$

where $P_0 = 4.563 \times 10^{-6} \text{ N/m}^2$ is the solar radiation pressure at 1 astronomical unit (AU).

1.3.2.1 Solar Sail Model and Performance Parameters

An ideal solar sail (perfect reflecting surface) experiences an incident force equal to the reflected force. The force on a sail area A_S due to the incident solar radiation is given by

$$\mathbf{F}_i = PA_S \cos \alpha \hat{\mathbf{r}}_1 \quad (1.18)$$

where α is the sail pitch angle defined as the angle between the sail normal \mathbf{u} and the incident radiation direction $\hat{\mathbf{r}}_1$. $A_S \cos \alpha$ is the projected sail area along the incident-radiation direction. The force on the sail surface due to the reflected solar radiation is given by

$$\mathbf{F}_r = PA_S \cos \alpha (-\mathbf{s}) \quad (1.19)$$

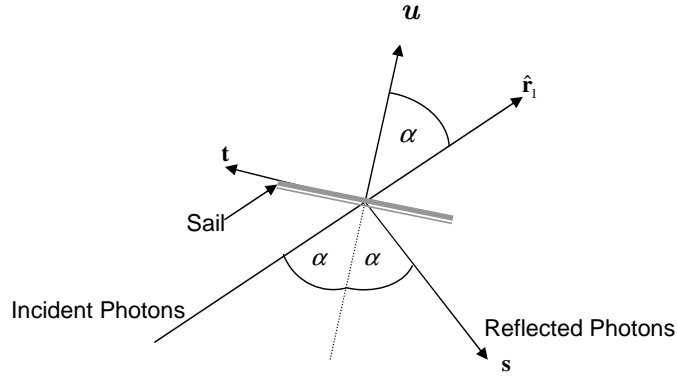


Figure 1.6: Solar radiation force on an ideal solar sail. The vector \mathbf{u} is normal to the sail surface.

where \mathbf{s} is the specular reflection direction. The total force on the ideal sail is therefore given by

$$\mathbf{F}_S = \mathbf{F}_i + \mathbf{F}_r = PA_S \cos \alpha (\hat{\mathbf{r}}_1 - \mathbf{s}) \quad (1.20)$$

From Fig. 1.6, it can be seen that

$$\hat{\mathbf{r}}_1 - \mathbf{s} = (\cos \alpha \mathbf{u} - \sin \alpha \mathbf{t}) - (-\cos \alpha \mathbf{u} - \sin \alpha \mathbf{t}) = 2 \cos \alpha \mathbf{u} \quad (1.21)$$

where \mathbf{t} is in the transverse direction normal to \mathbf{u} . Therefore, the total force is given by

$$\mathbf{F}_S = 2PA_S \cos^2 \alpha \mathbf{u} \quad (1.22)$$

and the force is directed normal to the sail surface.

The solar sail performance is defined by the sail characteristic acceleration. The sail characteristic acceleration a_c is defined as the acceleration experienced by the sail due to solar radiation pressure at 1 AU when oriented perpendicular to the Sun ($\alpha = 0$). From Eq. (1.22), a_c is given by

$$a_c = \frac{2P_0 A_S}{m_0} = \frac{2P_0}{\sigma_T} \quad (1.23)$$

where m_0 is the total mass of the solar sail and $\sigma_T = m_0/A_S$ is the total sail loading. The sail mass m_0 consists of the payload mass m_{pl} and sail structural

mass m_S . Therefore, the sail characteristic acceleration a_c can be written as

$$a_c = \frac{2P_0 A_S}{m_{pl} + m_S} \Rightarrow A_S = \frac{m_{pl}}{\frac{2P_0}{a_c} - \sigma_S} \quad (1.24)$$

where $\sigma_S = m_S/A_S$ is the sail assembly loading, and is a key technology parameter. The sail assembly loading is a measure of the sail film thickness and structural design. For a 100×100 m sail, a sail assembly loading of $10 - 14$ g/m² is estimated based on developing sail technologies [22, 31, 93]. Eq. (1.24) shows that as σ_S reduces, the required sail area A_S decreases for a given payload mass m_{pl} and sail characteristic acceleration a_c . Fig. 1.7a shows the sail characteristic thrust $F_c = m_0 a_c$ generated with the length of a square sail. The Fig. 1.7b shows the design space using Eq. (1.24) for a fixed sail assembly loading of $\sigma_S = 10$ g/m², and the maximum a_c achievable with zero payload mass is 0.9126 mms⁻². The solar sail acceleration $\mathbf{a}_{SS} = \frac{\mathbf{F}_S}{m_0}$ can be derived using Eq. (1.22) and Eq. (1.17) as

$$\mathbf{a}_{SS} = a_c \left(\frac{R_E}{R_1} \right)^2 \cos^2 \alpha \mathbf{u} \quad (1.25)$$

The solar sail acceleration \mathbf{a}_{SS} will become zero at $\alpha = \alpha_{max} = \pi/2$ when the sail is edge-wise to the Sun.

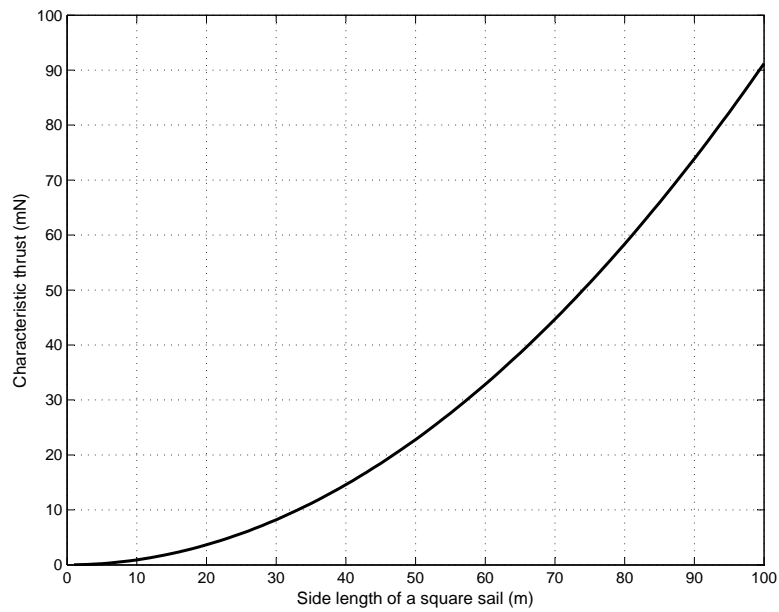
Another equivalent performance parameter is the sail lightness number β_0 , and is defined as the ratio of the sail acceleration when oriented normal to the Sun and the Sun's gravitational acceleration Gm_1/R_1^2 so that

$$\beta_0 = \frac{a_c \left(\frac{R_E}{R_1} \right)^2}{Gm_1/R_1^2} = \frac{a_c}{Gm_1/R_E^2} = \frac{a_c}{5.93 \text{ mms}^{-2}} = \frac{2P_0/\sigma_T}{5.93 \text{ mms}^{-2}} = \frac{\sigma^*}{\sigma_T} \quad (1.26)$$

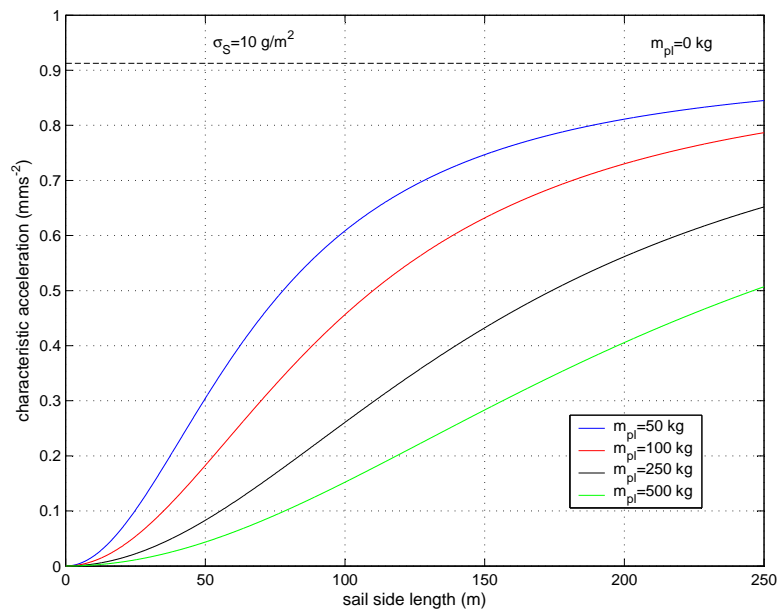
where $\sigma^* = 2P_0/5.93 \text{ mms}^{-2} = 1.53 \times 10^{-3} \text{ kg/m}^2$ is the critical sail loading.

So far an ideal sail has been assumed. However, a real sail will be Aluminium coated on front side (for high reflectivity) and Chromium coated on back side (for high emissivity due to thermal constraints), therefore only one side of the sail can be directed towards the Sun. The sail characteristic acceleration for a real sail can be written as [22]

$$a_c = \frac{2P_0 A_S \eta}{m_{pl} + m_S} \Rightarrow a_c = \frac{2P_0 \eta}{m_{pl}/A_S + \sigma_S} \quad (1.27)$$

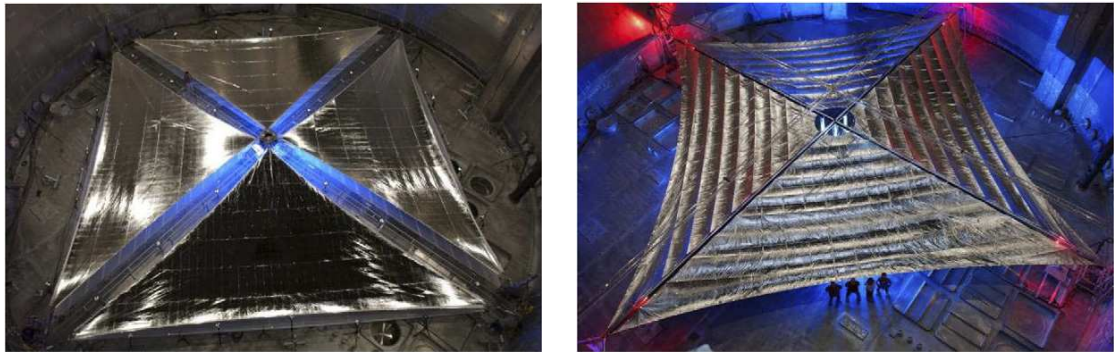


(a)



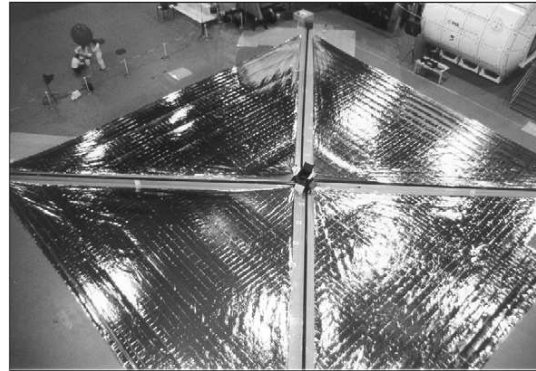
(b)

Figure 1.7: (a) The (ideal) sail characteristic thrust $F_c = m_0 a_c = 2P_0 A_S$ vs sail length (b) Characteristic acceleration vs sail length for $\sigma_S = 10 \text{ g/m}^2$ and different payload masses m_{pl} .



(a)

(b)



(c)

Figure 1.8: Sail segments fully deployed by (a) NASA/ATK space system (b) NASA/L'Grade system and (c) ESA/DLR joint programme.

where $\eta = 0.90815$ for a Al/Cr-coated solar sail.

1.3.2.2 Recent Advances in Solar Sail Technology

This section describes current solar sail development programmes. NASA's In-Space Propulsion Technology (ISP) programme is progressing to mature solar sail technologies to enable or enhance near and mid-term space science missions. Two different 20-m square solar sails with four segments were designed and fabricated by ATK space systems and L'Grade Inc [44]. These two sails successfully completed ground deployment tests under space environment and vacuum conditions at the

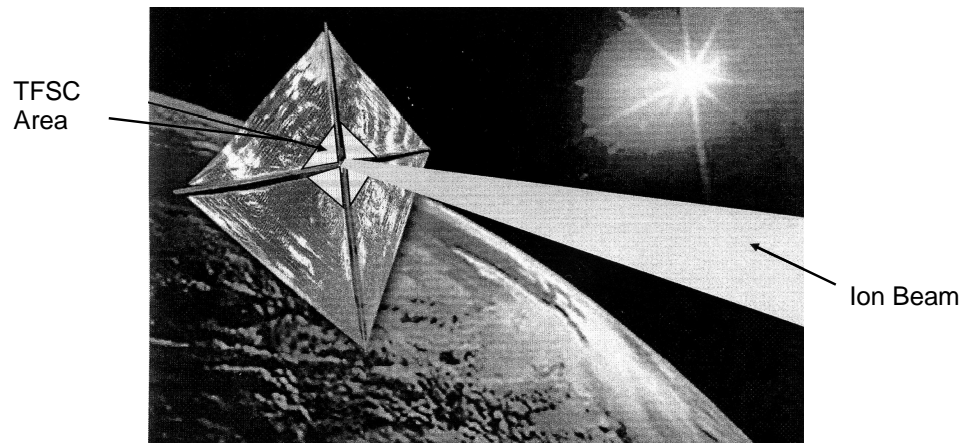


Figure 1.9: Solar sail configuration with Solar Electric Propulsion [54].

NASA Glenn Research Centre in 2005, as shown in Fig. 1.8(a-b). The European Space Agency ESA/DLR also deployed a 20-m sail as shown in Fig. 1.8(c). The sail comprised four segments with four different sail membranes ($12\ \mu\text{m}$ Mylar, $4.0\ \mu\text{m}$ polyethylen-naphthalate and two segments of $7.5\ \mu\text{m}$ Kapton) [53].

ATK space systems used Al-coated (front side) $2.5\ \mu\text{m}$ CP1 (Clear Plastic) as the sail membrane and proposed a 3-axis attitude control system (ACS) comprising a sliding mass along the boom with spreader bars, and micro-PPT at the boom tip as secondary propulsion. L'Grade Inc. used Al-coated (front side) and Chromium coated (backside) $2\ \mu\text{m}$ Mylar as the sail membrane and a 3-axis attitude control system provided by 4 vanes at the tips of the booms. Another option for ACS could be to shift the centre-of-mass from the centre-of-pressure using a two-axis gimballed control boom with a tip-mounted payload/bus.

1.3.3 Hybrid Sail

Solar electric propulsion and solar sail propulsion can be combined to enhance their performance. Such a hybrid of sail/solar electric propulsion (SEP) spacecraft is termed a hybrid sail, and its configuration is shown in Fig. 1.9.

The idea of the hybrid sail was first proposed by Leipold and Götz [54] who

assume a square sail with an SEP thruster attached to the sail centre, with part of the sail area at the sail center covered by flexible thin film solar cells (TFSC). The thruster may be mounted on a gimbal for pitch/yaw control of the SEP system. The SEP system may be jettisoned after fuel depletion. TFSC can act as a power source for the SEP system and other subsystems of the hybrid sail. TFSC technology has many advantages over state-of-the-art wafer based solar cell technology including high power to mass ratio, low costs and good resistance against radiation. To qualify TFSC for future space use, flight experiments are being planned in Low Earth orbit and Medium Earth orbit [34]. Leipold and Götz [54] and recently Mengali and Quarta [71] in their studies show that the hybrid sail has the attractive feature of reducing mission time with respect to a pure sail and a pure SEP system respectively for many heliocentric transfers.

1.4 Literature Review of NKO and Thesis Objectives

In this section the literature for non-Keplerian Orbits (NKO) using low-thrust propulsion will be reviewed . Furthermore, this section will also outline the thesis objectives. The literature for non-Keplerian orbits using low-thrust propulsion is classified into two and three-body problems.

The well known conic section Keplerian orbits exist in the two-body gravitational problem. Low thrust propulsion systems can be used to modify these Keplerian orbits into non-Keplerian orbits. In fact families of non-Keplerian orbits can be generated in this way. Although low-thrust propulsion systems other than solar sails can be used for NKO, the solar sail is well suited for non-Keplerian orbits since propellantless propulsion can enable longer mission lifetime. The development of sail technologies to enable these NKO is in progress. The Geostorm mission (NASA) and Geosail mission (ESA) are key near-term missions that will

use solar sail NKO. Non-Keplerian orbits are a principal driver for developing near term solar sails.

1.4.1 NKO and the Circular Restricted Three-Body Problem

In the circular restricted three-body problem, the gravitational forces of the two primaries and the centripetal force on a spacecraft in a rotating frame are balanced at the Lagrange points (see section 1.1.2). Therefore, in the neighborhood of the Lagrange points the thrust from low-thrust propulsion can play a significant role. The literature for halo orbits in the circular restricted three-body problem is firstly discussed.

1.4.1.1 Artificial Equilibria and Halo orbits

Before discussing artificial halo orbits, ‘classical’ halo orbits are reviewed. Around the collinear Lagrange points, ‘classical’ halo orbits have been studied extensively, for example Farquhar [24], Farquhar and Kamel [25], Breakwell and Brown [13], Richardson [82], Howell [41], Thurman and Worfolk [90] and Cielaszyk and Wie [20]. In fact, Farquhar [24] first proposed a halo orbit around L_2 in the Earth-Moon system for continuous communication between the Earth and the far-side of the Moon. Since the Earth views the same side of the Moon, a communication network is necessary and a single spacecraft in a halo orbit can communicate with the far-side of the Moon. Notably, Richardson [81, 82] used the method of Lindstedt-Poincaré to obtain a third-order analytical approximation of (unstable) periodic halo orbits in a simple, high-precision and straightforward manner (approximation of a periodic orbit shown in Fig. 1.5). Stable halo orbits were found by Breakwell and Brown around L_2 in the Earth-Moon system [13], and later on by Howell [41] for a wide range of mass ratios around all the three collinear Lagrange points in an extensive numerical study.

Artificial equilibrium points (AEPs) are similar to Lagrange points and can be generated if a continuous acceleration is available from a low-thrust propulsion system such as a solar sail, solar electric propulsion system or hybrid system. The continuous acceleration from these propulsion systems can cancel any residual acceleration at the AEP, and so can generate a static equilibrium point, or a periodic orbit around the AEP if the linearised eigenvalue spectrum of the Jacobian around the AEP contains at least one centre.

McInnes et al. [68] show that continuous surfaces of AEPs can be generated in the CRTBP for a solar sail propulsion system, but only in certain allowed regions. These AEPs are characterised by the sail lightness number and sail orientation. The linearised eigenvalue spectrum for a solar-sail around AEPs contains at least one centre, so linear periodic orbits can be generated or the Lindstedt Poincaré method can be applied. McInnes [60] and Baoyin and McInnes [1], describe halo orbits around AEPs on the line joining the two primaries in the solar sail three-body problem. However, McInnes [60] describes stable regions of halo orbits around unstable AEPs, when the amplitude of the halo orbit becomes large. Waters and McInnes [94] generate unstable ‘artificial’ halo orbits in the solar-sail CRTBP about AEPs which are high above the ecliptic plane but normal to the Sun-Earth line. By choosing AEPs above the ecliptic plane, Waters and McInnes [94] found periodic orbits at linear order due to the coupling of the linearised out-of-the plane dynamics with the linearised in-plane dynamics in contrast to the classical case. Therefore, the linear solution can be used as an initial guess to numerically continue to large amplitude halo orbits without using the Lindstedt Poincaré method. Since these halo orbits are unstable, Waters and McInnes [95, 97] used an optimal controller to stabilise the sail onto unstable halo orbits using variation in the sail’s orientation. Waters and McInnes [95] also show that for an arbitrary fixed point in three-dimensional space (away from the Sun-line) the linearised eigenvalue spectrum does not contain a centre, therefore the Lindstedt-Poincaré method fails to generate periodic orbits. The authors first assigned

eigenvalues to the controller (pole-placement method) using single variable control based on the Center Manifold Theorem¹, and then used this controller to generate periodic orbits. The linearised eigenvalue spectrum of the AEP has a negative eigenvalue (stable mode) and positive eigenvalue (unstable mode), which means that there is one trajectory going towards the fixed point (stable manifold) and one departing (unstable manifold). Like equilibrium points, periodic orbits have stable and unstable modes (corresponding to eigenvalues of the Monodromy matrix) which describe trajectories that wind onto and off the periodic orbit and represent the stable and unstable manifolds of the periodic orbit. Waters and McInnes [96] show that for a solar sail in the CRTBP there are equilibrium points that admit homoclinic paths (i.e, the unstable and stable manifolds intersect and thus the equilibrium points are self-connected fixed points). Moreover, halo orbits about such equilibrium points inherit the homoclinic nature of the equilibrium point (a behaviour of periodic orbits not observed in the classical Sun-Earth case). For a solar sail, all of these ‘artificial’ halo orbits around AEPs, in and above the ecliptic plane, are in the allowed/accessible volume of space.

Morimoto et al. [73] find AEPs in the CRTBP for a solar electric or nuclear electric low-thrust propulsion system. These AEPs are characterised by the thrust acceleration magnitude and thrust orientation. In particular, *marginally stable* regions, in addition to unstable regions of AEPs, are found that differ from the solar sail problem which has only unstable regions of AEPs. Marginally stable regions are similar to L_4 and L_5 but are closer to the Earth. Therefore, Morimoto et al. [73] suggest that the telecommunications link budget for a spacecraft in such marginally stable regions will be less than that for L_4 and L_5 . Morimoto et al. [72] also find *resonant* periodic orbits with a constant, continuous acceleration at linear order around the *marginally stable* AEPs along the axis joining the primary

¹If the linearised eigenvalue spectrum about a fixed point consists of a centre (pure imaginary eigenvalues) and stable mode (negative and real eigenvalue), then the nonlinear dynamics is governed by the centre.

bodies.

It is concluded from the above review that the existence of halo orbits (unstable and stable halo orbits about unstable AEPs) for solar electric propulsion has not been discussed in the literature. Only resonant periodic orbits at linear order are shown [72] in the marginally stable region where large acceleration is required since the marginally stable regions are far away from L_2 . The *first objective* of this thesis is therefore to demonstrate the existence of such halo orbits, especially in the forbidden/inaccessible volume of space for a solar sail and in the neighborhood of the Lagrange points L_1 and L_2 .

1.4.1.2 Applications of Artificial Equilibria

Two approaches exist in the literature to generate displaced NKO using low-thrust propulsion. In the first approach, artificial equilibria (fixed points) are generated using low-thrust propulsion in a rotating frame, and these artificial equilibria will describe a displaced NKO when viewed from an inertial frame. In the second approach, the displaced NKO are generated directly in the rotating frame. For the circular restricted Sun-Earth problem (an autonomous dynamical system) both approaches are used to generate displaced NKO [2, 36], while for the circular restricted Earth-Moon problem (a non-autonomous system for a solar sail) the second approach is the only choice.

This section reviews the literature for the first approach i.e., generating artificial equilibria using low-thrust propulsion in a rotating frame.

For an ideal solar sail, Forward [29] and McInnes [64, 68] first suggested the application of artificial equilibria in the Sun-Earth rotating frame. Forward [29] proposed fixed points (artificial equilibria) high above the ecliptic plane towards the night-side of the Earth for high latitude communications and McInnes [64, 68] proposed artificial equilibria towards the day-side of the Earth for real-time polar imaging (a polar observer mission). Both are examples of one-year NKO in the Sun-Earth three-body problem. McInnes [62] in subsequent studies finds for a

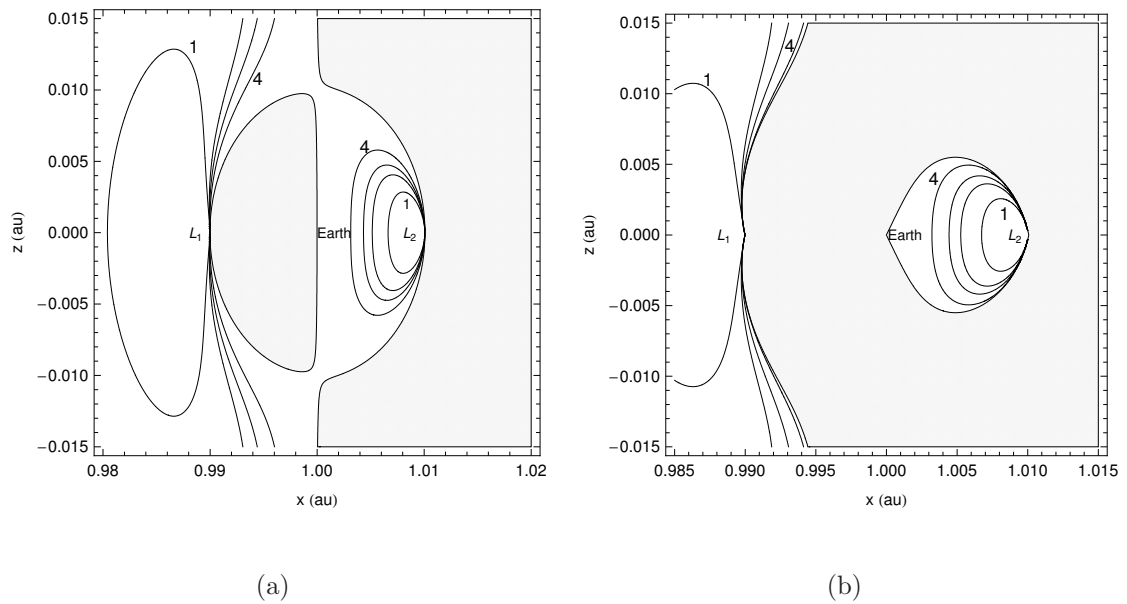


Figure 1.10: Contours of sail lightness number $\beta_0 = (1) 0.05(2) 0.10(3) 0.15(4) 0.30$ in the xz -plane for (a) an ideal solar sail and (b) a realistic partially reflecting sail with sail reflectivity 0.9. No artificial equilibrium solutions exist in the gray region.

realistic, partially reflecting sail where the thrust vector is no longer strictly normal to the sail surface, a reduction in the volume of possible artificial equilibrium solutions attached to the natural L_1 and L_2 Lagrange points (see Fig.1.10). The significant reduction in volume about L_2 suggests that a realistic sail cannot be used for night-side communications along the polar axis as was proposed by Forward [29] for an ideal sail. Morrow et al. [74] also carried out an analysis for a solar sail hovering in close proximity to an asteroid and found AEP solutions in Hill's problem, similar to the restricted three-body problem.

Missions have been proposed that use solar sails to generate AEPs in and above the ecliptic plane. The NASA/NOAA (National Oceanic and Atmospheric Administration) Geostorm warning mission is an application of solar sail equilibria in the ecliptic plane sunward of L_1 and requires a sail assembly loading of 14 g/m^2 and sail size of order $100 \times 100 \text{ m}$ [93]. NOAA interest [21] in the polar observer mission [29, 64] uses an application of sail equilibria out of the ecliptic plane.

However, for a polar observer mission, a sail with the same sail assembly loading as for the Geostorm mission and a payload mass of 100 kg needs a rather large sail (180×180 m). The deployment and control of such a large solar sail will be technologically difficult. Improvements in two key sail design parameters, a decrease in the sail assembly loading and an increase in sail size are being developed [31].

For an SEP system, where reaction mass provides a low thrust propulsive force, Morimoto et al. [73] find artificial equilibrium points in the CRTBP. The SEP system can be used to generate artificial equilibria in the forbidden regions of the ideal/real sail problem. However, continuous acceleration from an SEP system at AEPs for several years will require a large mass of propellant, unlike a sail which is a true propellantless system.

The *second objective* of this thesis is therefore to investigate the properties of artificial equilibria by combining solar sail and solar electric propulsion (hybrid sail, see section 1.3.3) for applications that are technologically difficult using either of these low thrust propulsion systems alone. Furthermore, the objective is to investigate the use of the hybrid sail for displaced NKO (i.e., artificial equilibria in the Sun-Earth rotating frame) extending the hybrid sail proposal by Leipold and Götz [54] for orbital transfers in solar system.

1.4.1.3 Displaced NKO for the Non-Autonomous Solar Sail Problem

Although this thesis considers periodic orbits in the *circular-restricted* three-body problem using low-thrust propulsion, recent literature has also focused on the *elliptical-restricted* three-body problem (ERTBP) using low-thrust propulsion [8–11, 37]. In the ERTBP, the two primaries move in elliptical orbits about their centre of mass while the assumption that $m \ll m_2 < m_1$ still holds (see section 1.1). A useful coordinate system to use for equilibria and periodic orbits in the ERTBP, is a *rotating and pulsating coordinate system* in which the locations of primaries and Lagrange points are fixed. Baoyin and McInnes [3] reconsider AEP solutions

for a solar sail in the ERTBP and find equilibrium points exist only within the ecliptic plane. However, the authors find that when the eccentricity of the orbit of the primary bodies is small (like the Sun-Earth system), out-of-ecliptic equilibria can be achieved with active control. The dynamical system in the ERTBP is non-autonomous, therefore, periodic orbits of integer multiples of 1 year can only be found. Biggs et al. [10] generate 1 year periodic orbits for a sail with characteristic acceleration $a_c = 0.3 \text{ mms}^{-2}$ (or $\beta_0 = 0.05$) (a near-term sail) in the ERTBP high above the ecliptic plane. The authors start from the 1 year orbit for a sail in the CRTBP (i.e. $e = 0$) [94] and then used the eccentricity e as a continuation parameter to find 1 year orbits in the ERTBP until they generate the desired 1 year orbit for the Sun-Earth system ($e = 0.0167$). This 1 year orbit remains unstable in both the CRTBP and ERTBP cases. The orbit is in the accessible region for a sail (far from Earth) and therefore can provide polar images. Biggs et al. [9] also proposed tracking this orbit in the ERTBP using variation in the sail's orientation, and they find that maintaining the sail on the orbit generated using the ERTBP will cause less tracking error than an orbit generated in the CRTBP. Recently, starting from 1 year periodic orbits in the ERTBP, Biggs and McInnes [8] found a family of one year periodic orbits (with different amplitudes) above L_1 by choosing the sail pitch angle as a continuation parameter for a fixed $\beta_0 = 0.05$. Furthermore, the authors choose some orbits from this family to show that a formation can be used for remote sensing of the Earth's North pole.

Although this thesis considers the displaced NKO analysis in the circular-restricted Sun-Earth system, recent interest has emerged in the Earth-Moon CRTBP. McInnes [61] first investigated displaced elliptical NKO at linear order above L_2 using a solar sail (with a constant sail-orientation) in the rotating frame of the Earth-Moon three-body system. The dynamics are non-autonomous since the direction of the Sun-line is varying in the rotating frame. The author demonstrated that a sail with $a_c = 0.2 \text{ mms}^{-2}$ is displaced above L_2 (i.e., $z = 3500 \text{ km}$) and can be used for lunar far side and polar communications with the Earth. Later, Simo

and McInnes [61, 86] show that such displaced NKO exist at linear-order above all of the Lagrange points L_1, L_2, \dots, L_5 in the Earth-Moon restricted three-body problem. In the full-nonlinear time-varying problem at low displacement above L_3, L_4 and L_5 , a reference displaced NKO can be generated by choosing a set of initial conditions with a fixed sail-attitude [86]. However, for an orbit above L_2 in the full-nonlinear time-varying problem, Simo and McInnes [85] proposed a hybrid system with SEP thrusters tracking the displaced NKO generated at linear-order using only a fixed-attitude sail. In fact, the thruster system is used to cancel the non-linearities in the non-linear dynamics, and thus will force linear dynamics. Recently, Ozimek et. al. generated displaced NKO below L_1 and L_2 , and below the lunar south pole in the full-nonlinear time-varying problem by varying the sail attitude through a collocation scheme. They suggested that these displaced NKO can be used for continuous constant communication with the lunar south pole using a single spacecraft with $a_c = 0.58 - 1.70 \text{ mms}^{-2}$ rather than two spacecraft as proposed earlier [35].

1.4.2 NKO and the Two-Body Problem

This section reviews the literature for artificial equilibria/displaced NKO generated using low-thrust propulsion in the two-body problem.

For low-thrust spacecraft, McInnes [66] investigated families of circular orbits displaced above the central body by generating artificial equilibria in a rotating frame of arbitrary angular velocity (a free parameter which in turn also determines the orbit period). In particular, a displaced orbit above and synchronous with Saturn's ring system is proposed for high-resolution imaging. However, a large acceleration is required for the displaced orbit due to the large gravitational parameter of Saturn. Lu and Love [57] proposed hovering (artificial equilibria) over an asteroid generated by using continuous low-thrust propulsion as a means to modify the orbit of an Earth-threatening asteroids/NEA (Near Earth Asteroid). To generate such artificial equilibria, two canted thrusters are required to

avoid engine exhaust plume impingement on the NEA surface. Recently, McInnes [65] proposed a low-thrust spacecraft in a displaced NKO, rather than artificial equilibria, as a method of gravitational coupling. The thruster system in such a displaced NKO need not be canted for certain orbit parameters (i.e., displacement and orbit radius). Wie [99] suggested that such a displaced NKO can be used more efficiently (i.e., provide larger deflection ΔV) by flying multiple small spacecraft rather than a single large spacecraft. Wie [99] also proposed static equilibria using solar sails due to its propellantless nature and the absence of the impingement problem on the NEA surface.

For a solar sail system, McInnes and Simmons [69] found families of Sun-centered circular displaced NKO (orbit period as a free parameter) for solar physics applications, and one year orbits synchronous with the Earth for space weather missions. McInnes and Simmons [70] also find families of planet-centered circular NKO behind the planet in the anti-Sun direction to observe the full 3D structure of the geomagnetic tail. More explicitly, McInnes and Simmons [69, 70] formulate two-body dynamics in the rotating frame to look for artificial equilibria and obtain NKO when viewed in an inertial frame.

The planet Mercury has a very small J_2 -term (nearly zero oblateness), therefore Leipold and Wagner [55] and Leipold et. al. [52] suggested that thrust normal to the osculating orbit plane around Mercury can be used to generate forced Sun-synchronous conditions (the rate of the line of longitude of the ascending node of the orbit is equal to the rate of Mercury around the Sun). A solar sail with a characteristic acceleration $a_c = 0.25 \text{ mms}^{-2}$ (which becomes 2.65 mms^{-2} at Mercury perigee and 1.15 mms^{-2} at Mercury apogee) is proposed in an elliptical NKO around Mercury for remote sensing. McInnes et al. [16] suggested the Geosail mission for observing the geomagnetic tail of the Earth using a solar sail. An elliptical orbit (10×30 Earth Radii) around Earth within the ecliptic plane is chosen with the apse-line along the Sun-Earth line. A simple steering law to keep the sail normal parallel to apsidal-line causes Sun-synchronous apse line rotation

i.e., at a mean rate of $0.9865^\circ/\text{day}$ with a small characteristic acceleration of $a_c = 0.136 \text{ mms}^{-2}$, thus providing continuous coverage of the geomagnetic tail.

A controversial geostationary displaced NKO using a solar sail was first suggested by Forward [27, 28]. A satellite in geostationary orbit has continuous communication with a point on the ground since both the satellite and ground station move with the same (Earth) angular velocity, thus greatly simplifying the ground antenna tracking problem. Orbital positions on geostationary orbit (a single orbit) are defined by longitude and a station-keeping box of order $75 \times 75 \text{ km}$ or $150 \times 150 \text{ km}$ is assigned with respect to its original central (longitude) position [59], within which the satellite is maintained. However, various slots (longitudes) along geostationary orbit are already crowded. In order to increase the number of slots over a particular longitude, Forward [27, 28] first proposed the idea to ‘levitate’ a spacecraft above or below the nominal geostationary orbit. Forward tried to achieve ‘equilibrium’ in the Earth fixed rotating frame to form a NKO in an inertial frame. By tilting the solar sail, Forward [27, 28] uses a component of the sail acceleration perpendicular to the Earth’s equatorial plane to ‘levitate’ the sail above or below the Earth’s equatorial plane. However, Fischer and Haerting [26], in their paper ‘Why light-levitation geostationary cylindrical orbits are not feasible’, and later Kolk [91] claim such light-levitation is not possible, as the component of sail acceleration neglected by Forward [27, 28] parallel to the Earth’s equatorial plane does not allow for ‘equilibrium’.

The *third* objective of thesis is therefore to prove the assertion of Forward [27, 28] that displaced geostationary NKO exist using solar sail propulsion. The neglected parallel component of sail acceleration can be compensated for such that displaced geostationary orbits can be shown to exist for the same three cases as considered by Forward [27, 28] i.e., autumn/spring equinoxes, summer solstice and the worst-case of winter solstice.

1.5 Thesis Layout

In this thesis, three new kinds of NKO are proposed using low thrust propulsion. In Chapter 2, halo orbits about artificial equilibrium points near to the Sun-Earth Lagrange points L_1 and L_2 in the circular restricted three-body problem are generated, where the third body is a spacecraft with solar electric propulsion. The periodic orbit analysis of solar electric propulsion at linear order is extended to *nonlinear order* using the Lindstedt-Poincaré method to find solutions of third-order, and a differential corrector method is used to generate solutions for the full nonlinear problem. The selected artificial equilibrium points inside L_1 and beyond L_2 allow for halo orbits that are not accessible with solar sail propulsion. Stable artificial halo orbits are also computed using a continuation method, and such stable orbits are demonstrated with a reasonably small low-thrust acceleration pointing towards the Sun.

Chapter 3 proposes a new concept of creating artificial equilibrium points in the circular restricted three-body problem, where the third body uses a hybrid of solar sail and solar electric propulsion. This idea is important in that it extends the hybrid sail concept, originally proposed to reduce orbital transfer time, to use at equilibrium points. However, the hybrid sail equilibria require throttling of the electric propulsion system and the AEPs of interest are unstable.

In Chapter 4, the hybrid sail is stabilised about unstable AEPs using the solar electric propulsion gimbal pitch/yaw angles while keeping the sail at a fixed attitude to ease the control issues for a large sail. Robustness against injection errors is also demonstrated.

In Chapter 5, a novel analysis of displaced geostationary orbits in the Earth-sail two-body problem is presented. The analysis resolves a long standing controversy in orbital dynamics by demonstrating both analytically and numerically (using a collocation scheme with inequality path constraints) that displaced geostationary orbits can exist. However, only modest displaced geostationary orbits are shown

due to the large parallel component of the sail acceleration in the equatorial plane.

In Chapter 6, periodic orbits around geostationary points in the Earth-sail two-body problem are presented. However, these are not true displaced geostationary orbits. A comparison of periodic orbits obtained using a differential corrector scheme is also made with the periodic orbits computed using the collocation scheme.

In Chapter 7, some concluding remarks are made along with some recommendations for future research.

1.6 Papers Published

The results presented in this thesis have been published in one conference paper and two international peer reviewed journals (AIAA Journal of Guidance, Control and Dynamics; Celestial Mechanics and Dynamical Astronomy), and one paper has been submitted for publication to the AIAA Journal of Guidance, Control and Dynamics. These papers are listed below:

- S. Baig and C. R. McInnes. Artificial Three-Body Equilibria for Hybrid Low-Thrust Propulsion. *Journal of Guidance, Control and Dynamics*, 31(6):1644-1655, November-December 2008.
- S. Baig and C. R. McInnes. Artificial Halo Orbits for Low-Thrust Spacecraft. *Celestial Mechanics and Dynamical Astronomy*, 104(4):321-335, August 2009.
- S. Baig and C. R. McInnes. Light Levitated Geostationary Cylindrical Orbits are Feasible. submitted to *Journal of Guidance, Control and Dynamics*, August 2009.
- S. Baig and C. R. McInnes. Artificial Three-Body Equilibria for Hybrid Low-Thrust Propulsion and Stabilization *59th IAC Congress, Glasgow, Scotland, UK. IAC-08.C1.3.1*, September 29-October 3, 2008.

Chapter 2

Artificial Halo Orbits for Low-Thrust Propulsion Spacecraft

This chapter aims to extend the analysis of Morimoto et al.'s orbits [72] for low-thrust spacecraft at linear order to non-linear order (i.e., halo orbits). Thus, the feasibility of halo orbits will be shown in the Sun-Earth system about artificial equilibrium points (AEPs) which can be generated using low-thrust propulsion spacecraft. In particular, the existence of halo orbits about unstable AEPs inside L_1 and beyond L_2 are shown where a solar sail cannot be placed so that low-thrust propulsion, such as solar electric propulsion, is the only option to generate artificial halo orbits around these points inaccessible to a solar sail. Stable halo orbits for low-thrust spacecraft about unstable AEPs are also shown using the orbit half period as a continuation parameter.

This chapter is arranged as follows. In the next two sections the equations of motion and periodic orbits at linear order are outlined for a low-thrust system in the CRTBP as given by Morimoto et al. [72], as required for analysis of the nonlinear system. However, it is shown that the system admits a constant of motion since the equations of motion not explicitly dependent on time (see Sect. 2.1).

In addition, the linear order solution for the low-thrust system is derived in a new compact manner (see Sect. 2.2). Halo orbits are computed analytically and numerically about AEPs for low-thrust propulsion systems using the Lindstedt-Poincaré and differential corrector method in Sect. 2.3 and Sect. 2.4 respectively. In Sect. 2.5, stable halo orbits for low-thrust propulsion spacecraft are shown around unstable artificial equilibrium point beyond L_2 .

2.1 Equations of Motion

The dynamical model of the CRTBP and the synodic coordinate frame (see Sect. 1.1.1) is chosen to describe a low-thrust spacecraft in the gravitational influence of the Sun-Earth system. A synodic coordinate frame i.e., co-rotating with the two primary masses m_1 and m_2 at constant angular velocity $\boldsymbol{\omega}$ with origin at their center of mass is shown in Fig. 2.1. The units are chosen to set the product of the gravitational constant and the sum of the primary masses, the distance between the primaries, and the magnitude of the angular velocity of the rotating frame to be unity as described in Section 1.1.1. In Fig. 2.1, \mathbf{r}_1 and \mathbf{r}_2 are the position vectors of the spacecraft with respect to m_1 and m_2 , respectively, with

$$\mathbf{r}_1 = [x + \mu \quad y \quad z]^T, \quad \mathbf{r}_2 = [x - (1 - \mu) \quad y \quad z]^T$$

where we denote $\mathbf{r} = [x \ y \ z]^T$ as the position vector of the low-thrust spacecraft relative to the center of mass. The non-dimensional equation of motion of a low-thrust spacecraft in the rotating frame of reference is given by

$$\ddot{\mathbf{r}} + 2 \boldsymbol{\omega} \times \dot{\mathbf{r}} = \nabla V + \mathbf{a}_T \equiv \mathbf{F} \quad (2.1)$$

where V is the effective potential given by

$$V = \frac{1}{2}(x^2 + y^2) + \left(\frac{1 - \mu}{r_1} + \frac{\mu}{r_2} \right) \quad (2.2)$$

The vector \mathbf{a}_T is the acceleration due to the low-thrust propulsion system. At an equilibrium point $\ddot{\mathbf{r}}$ and $\dot{\mathbf{r}}$ vanish, so an equilibrium point is a zero of \mathbf{F} i.e.,

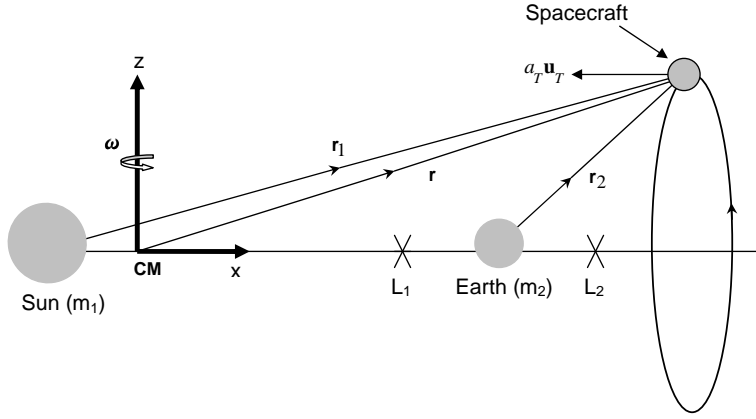


Figure 2.1: Definition of coordinate system and low-thrust spacecraft in a periodic halo orbit about an artificial equilibrium point beyond L_2 .

$\mathbf{F}(\mathbf{r}_0) = \mathbf{0}$. Thus, a nonequilibrium point \mathbf{r}_0 in the rotating frame is changed into an artificial equilibrium point with low-thrust acceleration vector \mathbf{a}_T satisfying the following condition

$$-\nabla V = \mathbf{a}_T(\mathbf{r}_0) = a_T \mathbf{u}_T \quad (2.3)$$

where the magnitude and direction of the low-thrust acceleration is given by

$$\begin{aligned} a_T &= |\nabla V(\mathbf{r}_0)| \\ \mathbf{u}_T &= -\frac{\nabla V}{|\nabla V|} \end{aligned} \quad (2.4)$$

Taking the dot product on both sides of Eq. (2.1) with $\dot{\mathbf{r}} = \mathbf{v}$, it is found that

$$\mathbf{v} \cdot \dot{\mathbf{v}} + 2\mathbf{v} \cdot (\boldsymbol{\omega} \times \mathbf{v}) - \mathbf{v} \cdot \mathbf{a}_T = \mathbf{v} \cdot \nabla V = \frac{d\mathbf{r}}{dt} \cdot \frac{\partial V}{\partial \mathbf{r}}$$

or

$$\frac{d \left[\frac{1}{2} \mathbf{v}^T \mathbf{v} - \mathbf{a}_T^T \mathbf{r} \right]}{dt} = \frac{dV}{dt}$$

Therefore, the Jacobi constant for the low-thrust system is given by

$$\mathcal{C}(\mathbf{r}, \mathbf{v}) = \frac{1}{2} \mathbf{v}^T \mathbf{v} - \mathbf{a}_T^T \mathbf{r} - V(\mathbf{r}) \quad (2.5)$$

For the correct initial conditions, the spacecraft will move on a periodic orbit around an artificial equilibrium point \mathbf{r}_0 with constant continuous acceleration \mathbf{a}_T satisfying Eq. (2.4), and having constant of motion \mathcal{C} .

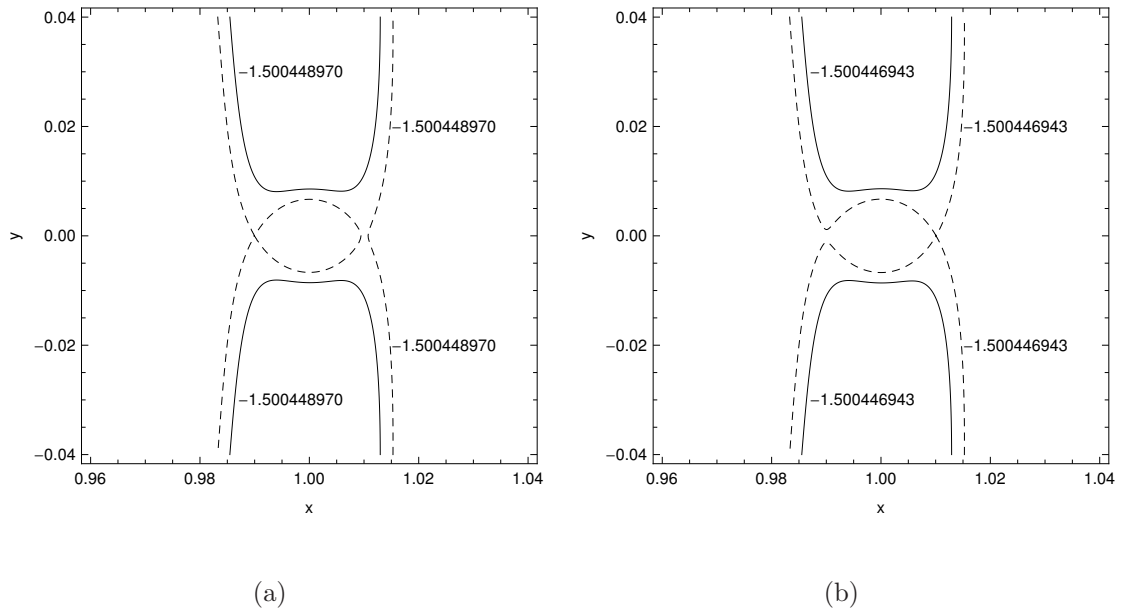


Figure 2.2: Zero velocity curves in the Sun-Earth system for (a) energy values of the L_1 and (b) energy values of the L_2 point . For the classical case $\mathbf{a}_T = (0, 0, 0)$ (dashed contour lines) and for the low-thrust system $\mathbf{a}_T = (0.0001, 0, 0)$ (solid contour lines).

The classical case (with no propulsion) is Hamiltonian and time independent, so an energy integral of motion exists and this energy is defined by Eq. (2.5) with $\mathbf{a}_T = (0, 0, 0)$ (see Eq. (1.6)). In the Sun-Earth system, the energies of the spacecraft at rest at L_1 and L_2 (i.e., $-V(\mathbf{r}_{L_1})$ and $-V(\mathbf{r}_{L_2})$) are -1.500448970 and -1.500446943 respectively.

Fig. 2.2 shows that the classical case contours are closed for energy values at the L_1 and L_2 points (see dashed contour lines). However, in the case of a low-thrust system for $\mathbf{a}_T = (0.0001, 0, 0)$ and contours with the same energy values (see solid contour lines), the contours at L_1 and L_2 points are opened, permitting the spacecraft to escape from the Sun-Earth system.

2.2 Linearised System

A linear system $\delta\dot{\mathbf{X}} = A\delta\mathbf{X}$ in the vicinity of an equilibrium point \mathbf{r}_0 is obtained by perturbing the nonlinear system Eq. (2.1) such that $\mathbf{r} \rightarrow \mathbf{r}_0 + \delta\mathbf{r}$, where $\mathbf{r}_0 = (x_0, 0, 0)$, $\delta\mathbf{r} = (\delta x, \delta y, \delta z)^T$ and $\delta\mathbf{X} = (\delta\mathbf{r}, \delta\dot{\mathbf{r}})^T$. The attitude of the low-thrust system \mathbf{u}_T is not perturbed so as to restrict the stability analysis in the sense of Lyapunov. Furthermore, \mathbf{a}_T is fixed with respect to the perturbation $\delta\mathbf{r}$ i.e., $\frac{\partial \mathbf{a}_T}{\partial \mathbf{r}} = 0$. Then, the Jacobian matrix A is given by

$$A = \begin{pmatrix} 0_3 & I_3 \\ M & \Omega \end{pmatrix} \quad (2.6)$$

where I_3 is the 3×3 unity matrix. Moreover,

$$M = \left. \frac{\partial \nabla V}{\partial \mathbf{r}} \right|_{\mathbf{r}_0} = \begin{pmatrix} a & 0 & 0 \\ 0 & b & 0 \\ 0 & 0 & e \end{pmatrix}, \quad \Omega = \begin{pmatrix} 0 & 2 & 0 \\ -2 & 0 & 0 \\ 0 & 0 & 0 \end{pmatrix}$$

and

$$a = 2c + 1, \quad b = 1 - c, \quad e = -c$$

with

$$c(x_0, \mu) = \frac{\mu}{|x_0 + \mu - 1|^3} + \frac{1 - \mu}{|x_0 + \mu|^3} > 0$$

as $\mu > 0$ and $1 - \mu > 0$. In Eq. (2.6), the z equation is decoupled from the x and y equations for the AEP \mathbf{r}_0 chosen on the x -axis (or in the $x - y$ ecliptic plane), so the out of ecliptic plane equation of motion is given by

$$\delta\ddot{z} + c\delta z = 0$$

which has a simple harmonic solution $\delta z = A_z \sin(w_z t + \phi_z)$, where $w_z = \sqrt{c}$. The characteristic polynomial for the x, y linearised system Eq. (2.6) rewritten in matrix form

$$\begin{pmatrix} \delta\dot{x} \\ \delta\dot{y} \\ \delta\ddot{x} \\ \delta\ddot{y} \end{pmatrix} = \begin{pmatrix} 0 & 0 & 1 & 0 \\ 0 & 0 & 0 & 1 \\ a & 0 & 0 & 2 \\ 0 & b & -2 & 0 \end{pmatrix} \begin{pmatrix} \delta x \\ \delta y \\ \delta\dot{x} \\ \delta\dot{y} \end{pmatrix} \quad (2.7)$$

is given by

$$p(\lambda) = \lambda^4 + (2 - c)\lambda^2 + (1 + c - 2c^2)$$

By letting $\alpha = \lambda^2$, then the roots of $p(\alpha) = 0$ are as follows

$$\alpha_1 = \frac{c - 2 + \sqrt{9c^2 - 8c}}{2}, \quad \alpha_2 = \frac{c - 2 - \sqrt{9c^2 - 8c}}{2} \quad (2.8)$$

AEPs where $c(x_0, \mu) > 1$ are considered (the unstable region) and not the marginally stable region (where $8/9 \leq c(x_0, \mu) < 1$) [73], then $9c^2 - 8c > (c - 2)^2$. From Eq. (2.8), then $\alpha_1 > 0$ and $\alpha_2 < 0$. So the eigenvalues spectrum of Eq. (2.7) consists of a saddle and center $\{\pm i\lambda_1, \pm\lambda_r\}$, where $\lambda_1 = w_{xy} = \sqrt{-\alpha_2}$ and $\lambda_r = \sqrt{\alpha_1}$.

Let $\mathbf{u}_1 + i\mathbf{w}_1$ be an eigenvector of the linearised Eq. (2.7) corresponding to eigenvalue $i\lambda_1$ (see Appendix A.1) and let \mathbf{v}_1 and \mathbf{v}_2 be the eigenvectors corresponding to eigenvalues $+\lambda_r$ and $-\lambda_r$. Then, the generalised solution of Eq. (2.7) is given by [5]

$$\begin{pmatrix} \delta x \\ \delta y \\ \delta \dot{x} \\ \delta \dot{y} \end{pmatrix} = \cos(w_{xy}t)[A\mathbf{u}_1 + B\mathbf{w}_1] + \sin(w_{xy}t)[B\mathbf{u}_1 - A\mathbf{w}_1] \quad (2.9)$$

$$+ Ce^{\lambda_r t}\mathbf{v}_1 + De^{-\lambda_r t}\mathbf{v}_2$$

where

$$\mathbf{u}_1 = (0, (a + w_{xy}^2), 2w_{xy}^2, 0)^T, \quad \mathbf{w}_1 = (-2w_{xy}, 0, 0, w_{xy}(a + w_{xy}^2))^T$$

$C = 0$ and $D = 0$ switch off the real modes to obtain bound solutions for δx and δy (see Appendix A.2). Finally, the three-dimensional bound solution to the linear problem Eq. (2.6) can be written as

$$\begin{aligned} \delta x &= -A_x \cos(w_{xy}t + \phi_{xy}), & \delta y &= kA_x \sin(w_{xy}t + \phi_{xy}), \\ \delta z &= A_z \sin(w_z t + \phi_z) \end{aligned} \quad (2.10)$$

with $k = \frac{a + w_{xy}^2}{2w_{xy}}$. For the AEPs in this chapter, the ratio of the in-plane w_{xy} and out of plane frequency w_z is not a rational number, so a quasi-periodic Lissajous trajectory can be obtained as shown in Fig. 2.3.

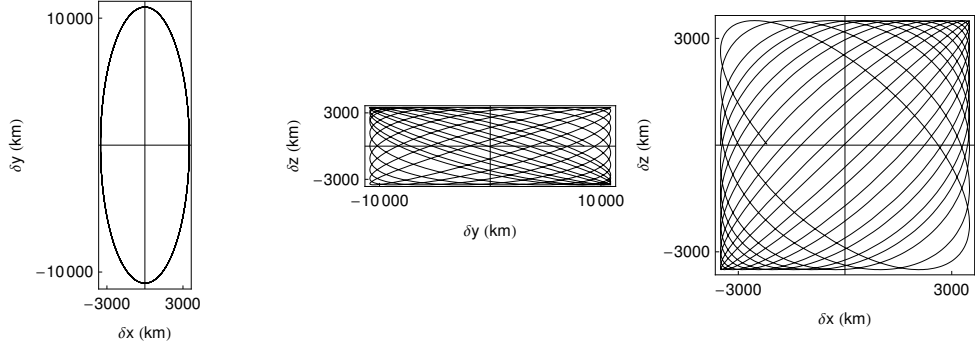


Figure 2.3: Lissajous trajectory at AEP $\mathbf{r}_0 = [1.02 \ 0 \ 0]^T$ (beyond L_2) in the Sun-Earth system. $A_x = A_z = 2.3396 \times 10^{-5}$ (3500 km) and $\phi_{xy} = \phi_z = 0$ are chosen for illustration purposes. The AEP needs $\mathbf{a}_T = (-0.0512, 0, 0)$.

2.3 Nonlinear Approximations

The Lindstedt-Poincaré method is used to find periodic approximations to the equations of motion Eq. (2.1). In the CRTBP literature, Lindstedt-Poincaré [82, 90] is used quite extensively to force the two linear frequencies (w_{xy} and w_z) to be equal by contributing nonlinear terms if the amplitudes A_x and A_z of the linear solution are large enough. The method is based on the assumption that if the nonlinearities are small, then the frequency of the periodic solution to the nonlinear system is a perturbation of the frequency of a periodic solution to the linear system. Therefore, the nonlinearity alters the frequency from w_{xy} to $w_{xy}w$, where

$$w = 1 + \epsilon w_1 + \epsilon^2 w_2 + \dots \quad (2.11)$$

This frequency correction allows the removal of secular terms through determination of w_i during the development of the approximate periodic solution about AEPs.

A Taylor series expansion of \mathbf{F} to third-order [4] about AEP \mathbf{r}_0 is found by making the transformation $\mathbf{r} \rightarrow \mathbf{r}_0 + \delta\mathbf{r}$, so the system of nonlinear equations is

obtained

$$\begin{aligned} \delta\ddot{\mathbf{r}} + 2\boldsymbol{\omega} \times \delta\dot{\mathbf{r}} = & \mathbf{F}(\mathbf{r}_0) + \left(\delta\mathbf{r}^T \cdot \left[\frac{\partial}{\partial \mathbf{r}} \right] \right) \nabla V \Big|_{\mathbf{r}=\mathbf{r}_0} + \frac{1}{2!} \left(\delta\mathbf{r}^T \cdot \left[\frac{\partial}{\partial \mathbf{r}} \right] \right)^2 \nabla V \Big|_{\mathbf{r}=\mathbf{r}_0} \\ & + \frac{1}{3!} \left(\delta\mathbf{r}^T \cdot \left[\frac{\partial}{\partial \mathbf{r}} \right] \right)^3 \nabla V \Big|_{\mathbf{r}=\mathbf{r}_0} + O(\delta\mathbf{r}^4) \end{aligned}$$

where it is assumed that $\frac{\partial \mathbf{a}_T}{\partial \mathbf{r}}$, $\frac{\partial^2 \mathbf{a}_T}{\partial \mathbf{r}^2}$ etc., are all zero. In component form the equations of motion through third-order are given by

$$\begin{aligned} \delta\ddot{x} - 2\delta\dot{y} - (2c + 1)\delta x &= 3C(2\delta x^2 - \delta y^2 - \delta z^2) \\ &+ 4D\delta x(2\delta x^2 - 3\delta y^2 - 3\delta z^2) + O(\delta\mathbf{r}^4) \\ \delta\dot{y} + 2\delta\dot{x} + (c - 1)\delta y &= -6C\delta x\delta y \\ &- 3D\delta y(4\delta x^2 - \delta y^2 - \delta z^2) + O(\delta\mathbf{r}^4) \\ \delta\ddot{z} + w_{xy}^2\delta z &= -6C\delta x\delta z - 3D\delta z(4\delta x^2 - \delta y^2 - \delta z^2) \\ &+ O(\delta\mathbf{r}^4) + \Delta\delta z \end{aligned} \tag{2.12}$$

where $C = \frac{V_{xxx}|_{\mathbf{r}=\mathbf{r}_0}}{12}$ and $D = \frac{V_{xxxx}|_{\mathbf{r}=\mathbf{r}_0}}{48}$ are evaluated at the AEP $\mathbf{r}_0 = (x_0, 0, 0)$. Note that to force the linearized z-equation to the form $\delta\ddot{z} + w_{xy}^2\delta z = 0$, the term $\Delta = w_{xy}^2 - c = w_{xy}^2 - w_z^2$ ($\Delta = O(A_z^2) = O(\epsilon^2)$) should be considered on the right-hand-side of the z-equation in higher-order approximation (the linear periodic solution given in Eq. (2.10) with w_z replaced by w_{xy} and acts as a first approximation).

The following relations exist to switch off the secular terms which appear as a result of method of successive approximations in the inhomogeneous part of the system of equations of order $O(\epsilon^2)$ and $O(\epsilon^3)$.

$$\begin{aligned} w_1 = 0, \quad w_2 = s_1 A_x^2 + s_2 A_z^2 \\ l_1 A_x^2 + l_2 A_z^2 + \Delta = 0, \quad \phi_z = \phi_{xy} + n\pi/2 \quad n = 1, 3 \end{aligned}$$

The expressions for s_i, l_i are given in Ref. [90]. The closed orbit corresponding to these constraints is a halo orbit. Northern halo orbits, whose maximum out-of-plane component is above the ecliptic plane, are obtained corresponding to the

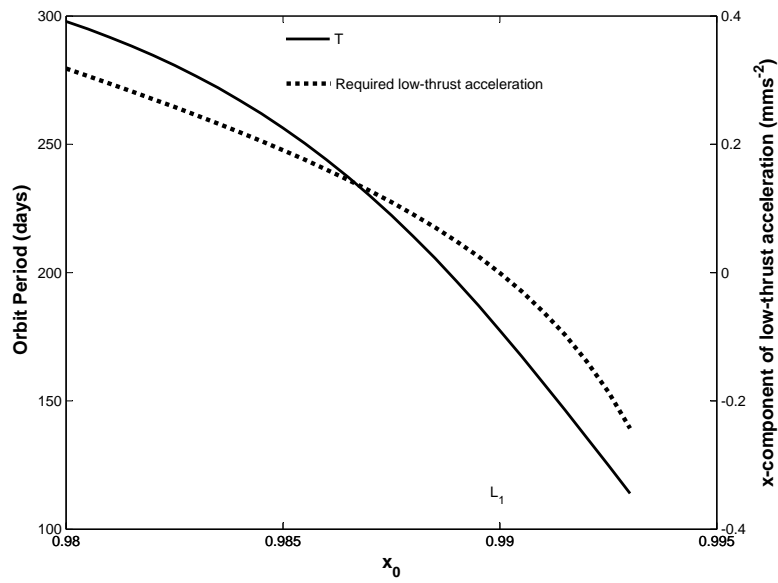
solution $n = 1$ and $n = 3$ about AEPs near L_1 and L_2 respectively. The period of the orbit can be found from the amplitude-frequency relation $T = 2\pi/w_{xy}w$, where $w = 1 + s_1A_x^2 + s_2A_z^2$. The minimum in-plane amplitude $A_{xmin} = \sqrt{|\Delta/l_1|}$ required to have a halo orbit can be derived from the above amplitude-constraint relation by substituting $A_z = 0$. The complete third-order successive approximation solution of Eq. (2.12) using the Lindstedt-Poincaré method is given by [90]

$$\begin{aligned}
\delta x(t) &= -A_x \cos \tau_1 + a_{21}A_x^2 + a_{22}A_z^2 + (a_{23}A_x^2 + \zeta a_{24}A_z^2) \cos 2\tau_1 \\
&\quad + (a_{31}A_x^3 + \zeta a_{32}A_xA_z^2) \cos 3\tau_1 \\
\delta y(t) &= kA_x \sin \tau_1 + (b_{21}A_x^2 + \zeta b_{22}A_z^2) \sin 2\tau_1 + (b_{31}A_x^3 + \zeta b_{32}A_xA_z^2) \sin 3\tau_1 \\
&\quad + (b_{33}A_x^3 + b_{34}A_xA_z^2 + \zeta b_{35}A_xA_z^2) \sin \tau_1 \\
\delta z(t) &= (-1)^{(n-1)/2} A_z \cos \tau_1 + (-1)^{(n-1)/2} d_{21}A_xA_z(\cos 2\tau_1 - 3) \\
&\quad + (-1)^{(n-1)/2} (d_{32}A_zA_x^2 - d_{31}A_z^3) \cos 3\tau_1
\end{aligned} \tag{2.13}$$

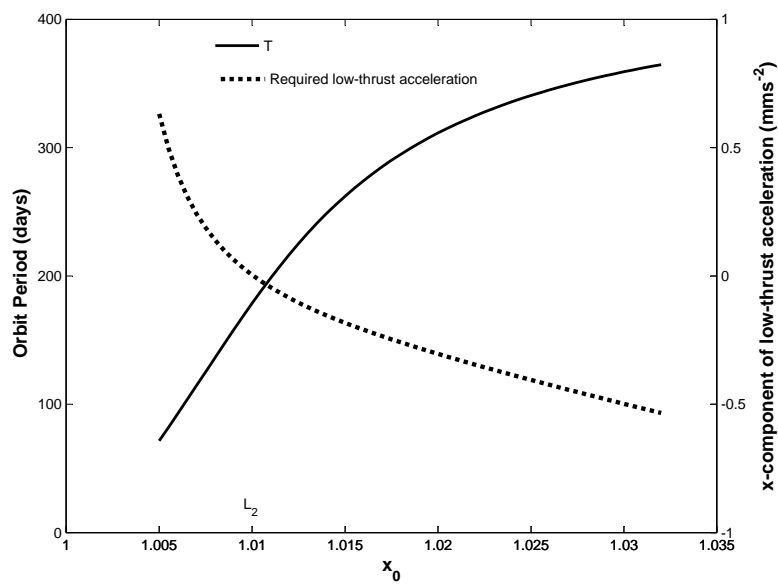
where $\zeta = (-1)^n$ and $\tau_1 = w_{xy}wt + \phi$. The constants s_i, l_i, a_{ij}, b_{ij} and d_{ij} involve C, D, k and w_{xy} which in turn ultimately depend on \mathbf{r}_0 and μ . Note that the numerical values of these constants will be different from that given in [82, 90] due to the different scaling system chosen in the non-dimensionalisation (see Sect. 2.1). In Eq. (2.13) the expression for $\delta y(t)$ also contains the third-order correction to the amplitude of $\sin \tau_1$ by Thurman and Worfolk [90] in Richardson's original solution [82]. This correction allows faster convergence of the differential corrector algorithm.

Fig. 2.4 shows that the magnitude of the low-thrust acceleration \mathbf{a}_T is zero at L_1 and L_2 and increases to convert a nonequilibrium point at x_0 away from L_1 and L_2 into an equilibrium point. Artificial L_1 and L_2 points are chosen that require a maximum $a_T \approx 0.05$ (0.296 mms^{-2}) and $a_T \approx 0.1$ (0.593 mms^{-2}), which corresponds to a thrust of 150 mN and 300 mN for a 500 kg spacecraft. For points inside L_1 and beyond L_2 , the direction of \mathbf{a}_T is sunward, so these periodic artificial halo orbits with a given z -amplitude cannot be generated with a solar sail.

Fig. 2.4 also shows that the period $T = \frac{2\pi}{(1+w_2)w_{xy}}$ of these artificial halo orbits

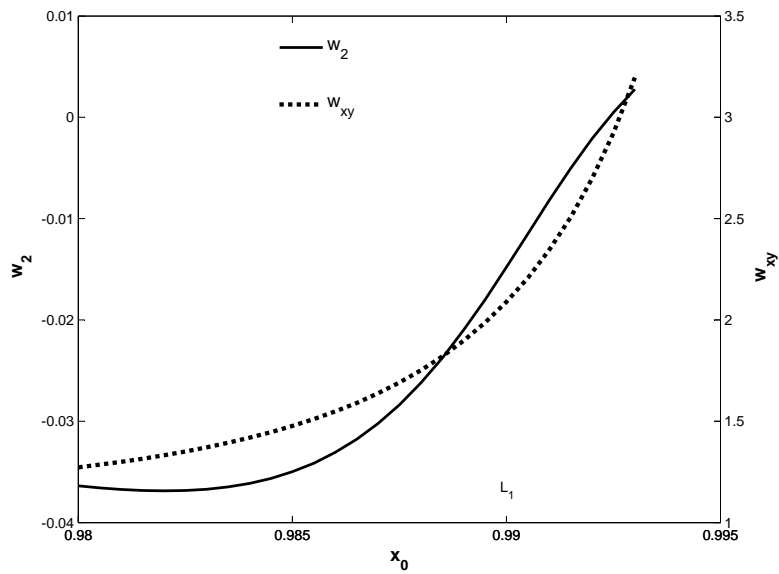


(a)

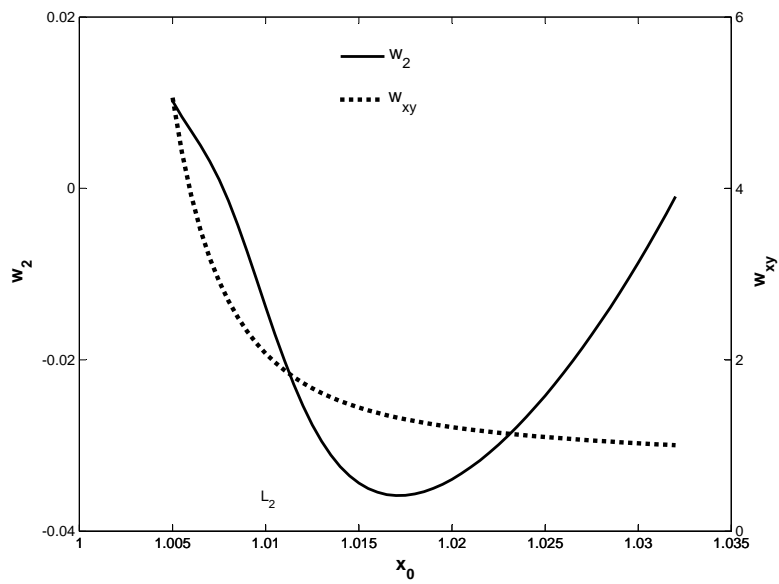


(b)

Figure 2.4: Period of artificial halo orbit vs AEPs selected at x_0 near to (a) L_1 and (b) L_2 points in the Sun-Earth system. The dotted curve shows the low-thrust acceleration required at x_0 to create AEPs while the solid line shows the orbit period. $a_T = 0$ at L_1 and L_2 .

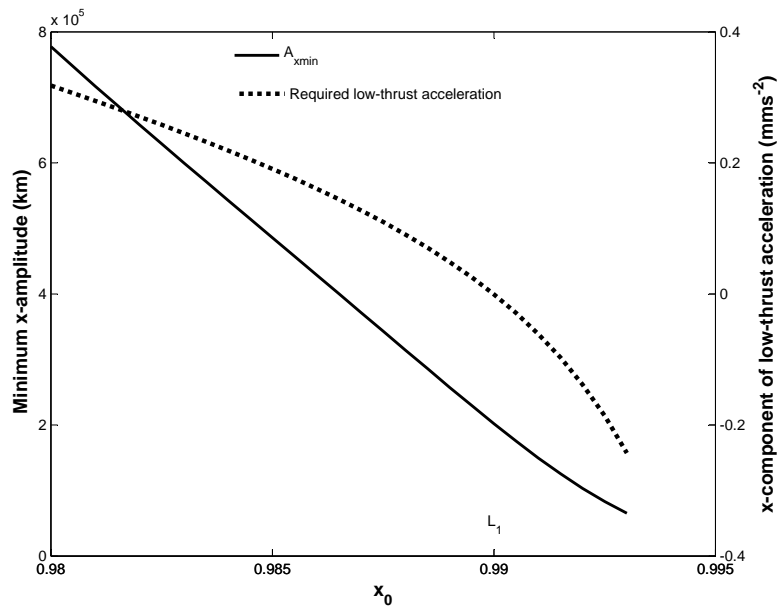


(a)

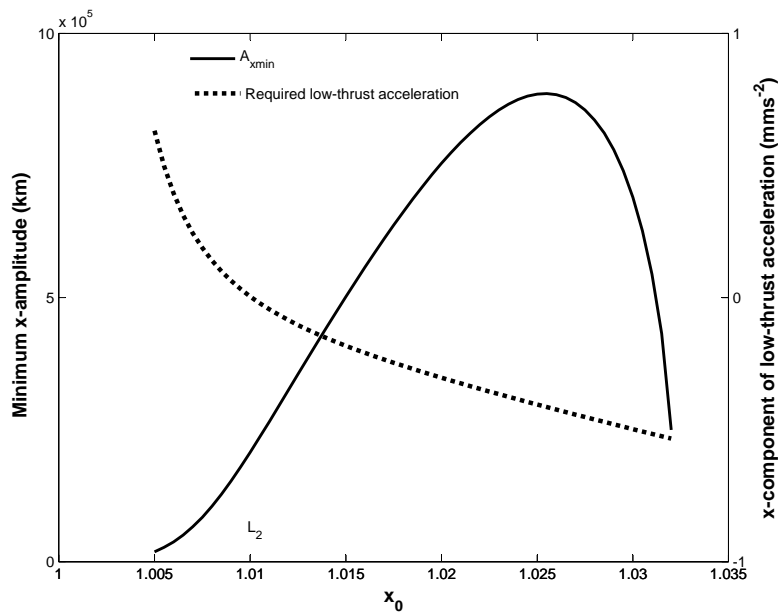


(b)

Figure 2.5: Zero and second order frequencies vs AEPs selected at x_0 near to (a) L_1 and (b) L_2 points in the Sun-Earth system.

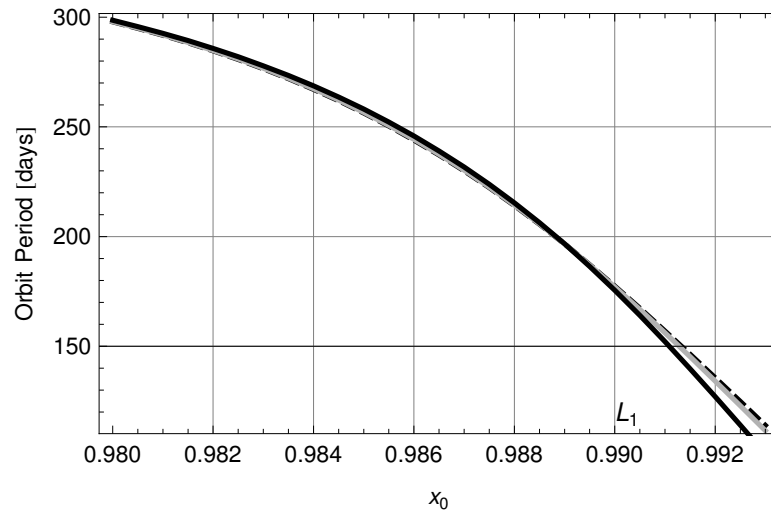


(a)

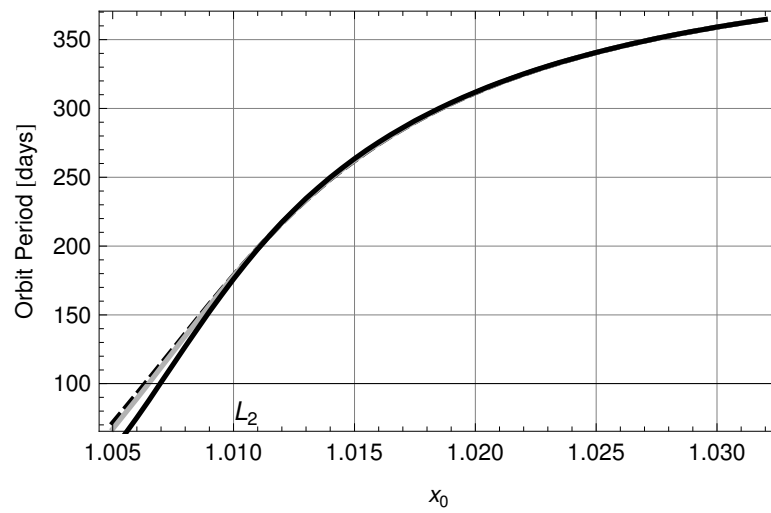


(b)

Figure 2.6: The minimum x-amplitude to have artificial halo orbits vs AEPs selected at x_0 near to (a) L_1 and (b) L_2 points.



(a)



(b)

Figure 2.7: Orbit period versus AEPs selected at x_0 near to (a) L_1 and (b) L_2 points with various A_z values: $A_z(125,000)$ km for the black dashed-line, $A_z(3 \times 125,000)$ km for the gray solid-line, and $A_z(7 \times 125,000)$ km for the black solid-line.

follow the inverse behaviour of the zero order frequency w_{xy} (see Fig. 2.5). Fig. 2.5 shows that the second order frequency correction to the zero order term is very small, or approximately a maximum $< 3.5\%$ frequency correction to the zero order solution (as $w_1 = 0$) for $A_z = 8.3557 \times 10^{-4}$ (125,000 km). Fig. 2.5 also shows that the correction can increase/decrease the period. Fig. 2.6 shows that the minimum amplitude $A_{xmin} = \sqrt{|\frac{\Delta}{l_1}|}$ beyond artificial L_2 points first increases then decreases when a_T exceeds ≈ 0.07 (0.415 mms^{-2}), as at this point the rate at which $\sqrt{\Delta}$ decreases becomes more than the rate at which $\frac{1}{\sqrt{|l_1|}}$ increases. Although in Figs. (2.4-2.5) A_z is chosen with 125,000 km, the effect of A_z on the second order frequency correction w_2 , and so period T is relatively small where the initial guess from Lindstedt-Poincaré valid (see Fig. 2.7).

2.4 Differential Correction and Low-Thrust Halo Orbits

The initial guess from the Lindstedt-Poincaré analysis can be used to integrate the full nonlinear system of equations Eq. (2.1) along with the constant low-thrust acceleration \mathbf{a}_T to generate periodic orbits around AEP \mathbf{r}_0 . The trajectory will not close as the Lindstedt-Poincaré method generates (periodic) solutions that are approximations to the periodic solutions of the full nonlinear equations of motion.

The nonlinear equations of motion Eq. (2.1) with constant \mathbf{a}_T are symmetric under the transformation $y \rightarrow -y$ and $t \rightarrow -t$, so this symmetry about the xz -plane with a time-reversal suggests periodic orbits need to be determined for a half period $T_{1/2}$ only. Let $\mathbf{X}_0 = (x_0, 0, z_0, 0, \dot{y}_0, 0)$ be initial data from Lindstedt-Poincaré, so the spacecraft leaves perpendicularly from the $y = 0$ plane. On the first return to the $y = 0$ plane, its state is

$$\mathbf{X}(T_{1/2}) = (\tilde{x}, 0, \tilde{z}, \dot{\tilde{x}}, \dot{\tilde{y}}, \dot{\tilde{z}})$$

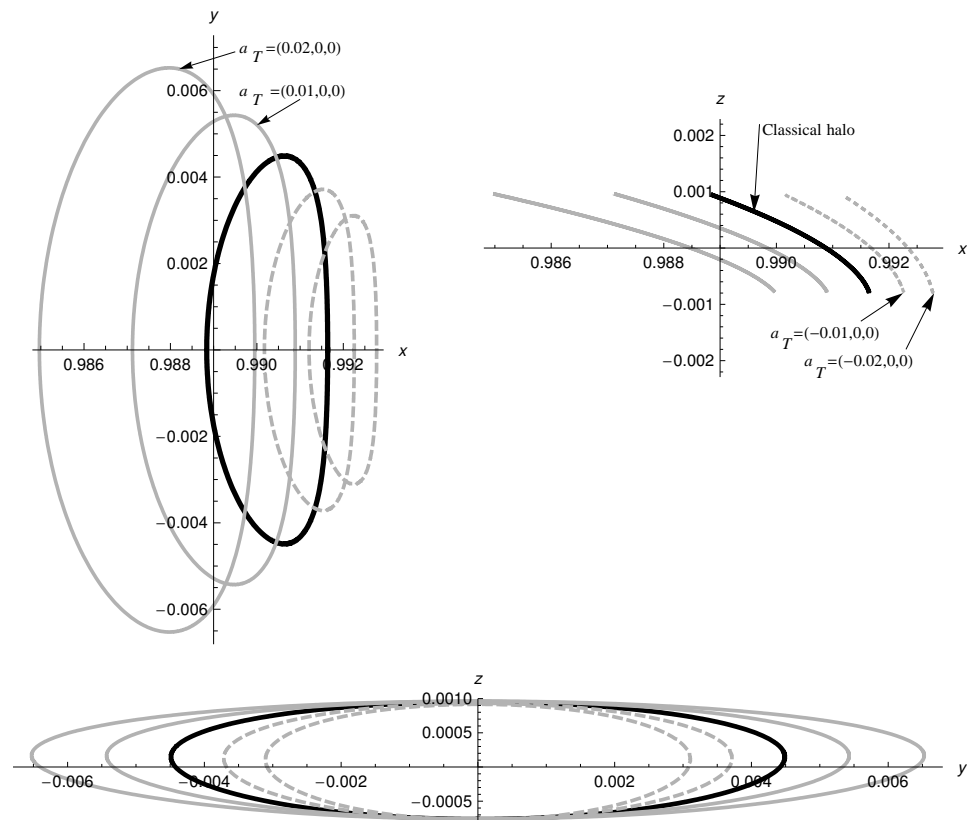


Figure 2.8: Artificial halo orbits are shown in gray around artificial L_1 points ($n = 1$) with low thrust acceleration vectors $\mathbf{a}_T = (\pm 0.01, 0, 0)$ and $\mathbf{a}_T = (\pm 0.02, 0, 0)$. The classical halo orbit is also shown (3rd dark black orbit). All periodic orbits have the same $A_z = 8.3557 \times 10^{-4}$ (125,000 km).

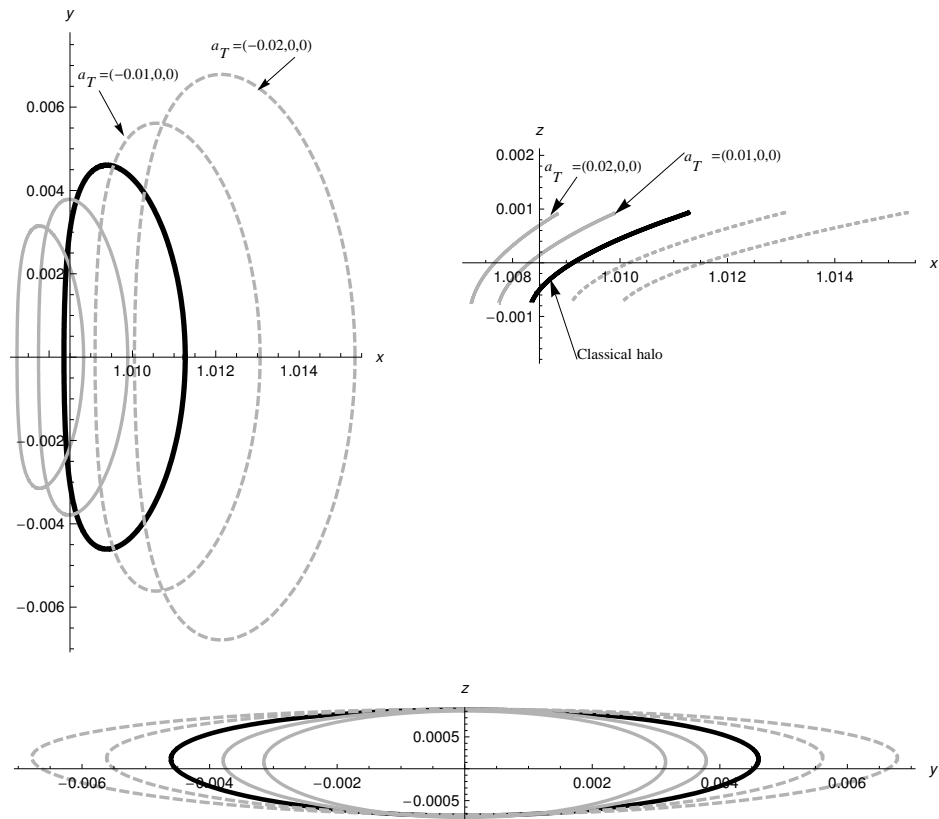


Figure 2.9: Artificial halo orbits are shown in gray around artificial L_2 points ($n = 3$) with low thrust acceleration vectors $\mathbf{a}_T = (\pm 0.01, 0, 0)$ and $\mathbf{a}_T = (\pm 0.02, 0, 0)$. The classical halo orbit is also shown (3rd dark black orbit). All periodic orbits have the same $A_z = 8.3557 \times 10^{-4}$ (125,000 km).

so a periodic solution exists when $\dot{\tilde{x}} = \dot{\tilde{z}} = 0$.

Let $\bar{\mathbf{X}}(t)$ represent the reference solution (known) corresponding to \mathbf{X}_0 . This solution can be used to relate the solution of the perturbed initial state $\Delta\mathbf{X}_0$ from the reference solution at $t = 0$ to its deviation in the final state from the reference solution at $T_{1/2} + \Delta T_{1/2}$ by

$$\Delta\mathbf{X}(T_{1/2} + \Delta T_{1/2}) = \frac{\partial\mathbf{X}(T_{1/2}, \mathbf{X}_0)}{\partial\mathbf{X}_0} \Delta\mathbf{X}_0 + \dot{\mathbf{X}}(T_{1/2}) \Delta T_{1/2} \quad (2.14)$$

The matrix $\frac{\partial\mathbf{X}}{\partial\mathbf{X}_0} = \Phi$ is the state transition matrix evaluated along the reference solution $\bar{\mathbf{X}}(t)$. To make $\dot{\tilde{x}} = \dot{\tilde{z}} = 0$ at $y = 0$, x_0 , \dot{y}_0 , $T_{1/2}$ are varied iteratively by corrections Δx_0 , $\Delta\dot{y}_0$ and $\Delta T_{1/2}$ while keeping z_0 fixed. These corrections can be calculated from Eq. (2.14) explicitly as follows

$$\begin{pmatrix} \Delta x_0 \\ \Delta\dot{y}_0 \\ \Delta T_{1/2} \end{pmatrix} = \begin{pmatrix} \phi_{21} & \phi_{25} & \dot{y} \\ \phi_{41} & \phi_{45} & \ddot{x} \\ \phi_{61} & \phi_{65} & \ddot{z} \end{pmatrix}_{t=T_{1/2}}^{-1} \begin{pmatrix} 0 - y \\ 0 - \dot{\tilde{x}} \\ 0 - \dot{\tilde{z}} \end{pmatrix} \quad (2.15)$$

where ϕ_{ij} are elements of the matrix Φ at $T_{1/2}$. The full state transition matrix Φ is computed by integrating the following variational equations

$$\dot{\Phi} = A(t)\Phi, \quad \Phi(0) = I_6 \quad (2.16)$$

along with the nonlinear system $\dot{\mathbf{X}} = \mathbf{f}(\mathbf{X})$ at each iteration for the corrected initial conditions. In the above equation, $A(t) = \frac{\partial\mathbf{f}}{\partial\mathbf{X}}$ is the Jacobian of \mathbf{f} with respect to \mathbf{X} .

Figs. (2.8-2.9) show numerically generated periodic halo orbits as explained above. The gray orbits are artificial periodic halo orbits around artificial L_1 points (see Fig. 2.8) and artificial L_2 points (see Fig. 2.9) for low-thrust acceleration values $a_T = 0.01$ and $a_T = 0.02$ with the same A_z . The dashed gray orbits have a low-thrust acceleration vector pointing towards the Sun, so a solar sail cannot generate these periodic artificial halo orbits.

2.5 Stable Low-Thrust Halo orbits

So far artificial halo orbits around unstable AEPs have been considered. The instability of AEPs implies that artificial halo orbits around these points will also be unstable. However, a continuation method may be used to generate families of periodic orbit with large amplitude and move beyond the region where the linear terms dominate (i.e., saddle behaviour), so regions of stable halo orbits with low-thrust propulsion may be found.

Given a known periodic solution of Eq. (2.1) with a known initial condition \mathbf{X}_0 and parameter of interest (for example A_z), then the continuation method computes the new initial condition to have a periodic orbit for a given fixed new parameter ($A_z + \Delta A_z$). The continuation method, particularly relating to classical halo orbits is discussed in [41, 47]. Usually the z -amplitude A_z is used as a continuation parameter and when it reaches an extreme value, the continuation parameter is changed from A_z to A_x . In this chapter, the half period $T_{1/2}$ is chosen as a continuation parameter when an initial guess from the Lindstedt-Poincaré (third-order approximations) does not give convergence in the differential corrector scheme (e.g., $A_z = 0.08453$ ($10 \times 125,000$ km) for the AEP $\mathbf{r}_0 = (1.01134, 0, 0)$). It is found that $T_{1/2}$ as a continuation parameter at large amplitude provides better convergence accuracy than A_z and A_x , the conventional continuation parameters.

For an accurate given periodic orbit $(\mathbf{X}_0, T_{1/2})$, the half period is changed from $T_{1/2}$ to $T'_{1/2} = T_{1/2} + \Delta T_{1/2}$. Then $(\mathbf{X}_0, T'_{1/2})$ is used as initial values for integrating Eq. (2.1) and keep the period fixed at $T'_{1/2}$. For a fixed period $T'_{1/2}$, the second term on the right-hand-side of Eq. (2.14) vanishes, and so the correction in the initial condition $\Delta \mathbf{X}_0$ can be calculated as

$$\Delta \mathbf{X}_0 = \left. \frac{\partial \mathbf{X}(T'_{1/2}, \mathbf{X}_0)}{\partial \mathbf{X}_0} \right|^{-1} \Delta \mathbf{X}(T'_{1/2}) \quad (2.17)$$

In particular, to ensure y, \dot{x}, \dot{z} are zero at $T'_{1/2}$, x_0, \dot{y}_0 and z_0 are varied iteratively by corrections $\Delta x_0, \Delta \dot{y}_0$ and Δz_0 . These corrections can be calculated from Eq. (2.17)

as follows

$$\begin{pmatrix} \Delta x_0 \\ \Delta \dot{y}_0 \\ \Delta z_0 \end{pmatrix} = \begin{pmatrix} \phi_{21} & \phi_{25} & \phi_{23} \\ \phi_{41} & \phi_{45} & \phi_{43} \\ \phi_{61} & \phi_{65} & \phi_{63} \end{pmatrix}_{t=T'_{1/2}}^{-1} \begin{pmatrix} 0 - y \\ 0 - \dot{x} \\ 0 - \dot{z} \end{pmatrix} \quad (2.18)$$

where ϕ_{ij} are elements of the matrix Φ at $T'_{1/2}$.

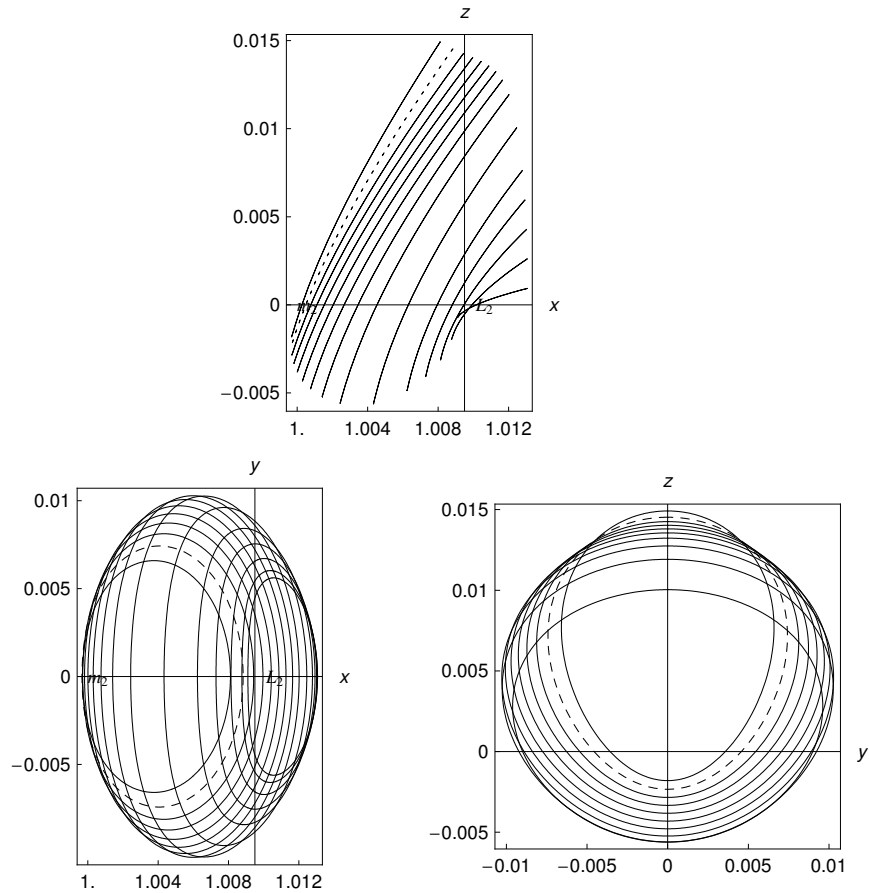


Figure 2.10: Artificial periodic halo orbits in the Sun-Earth system around AEP $\mathbf{r}_0 = (1.01134, 0, 0)$ with $\mathbf{a}_T = (-0.01, 0, 0)$ pointing towards the Sun. The first five periodic orbits are generated by using an initial guess from Lindstedt-Poincaré. Large amplitude periodic orbits are produced using the continuation method with $\Delta T_{1/2} = -0.02$. The dashed line is the stable halo orbit.

Fig. 2.10 shows a family of halo orbits about AEPs beyond L_2 . The period corresponding to this family of orbits (solid line) is shown in Fig. 2.11. For compar-

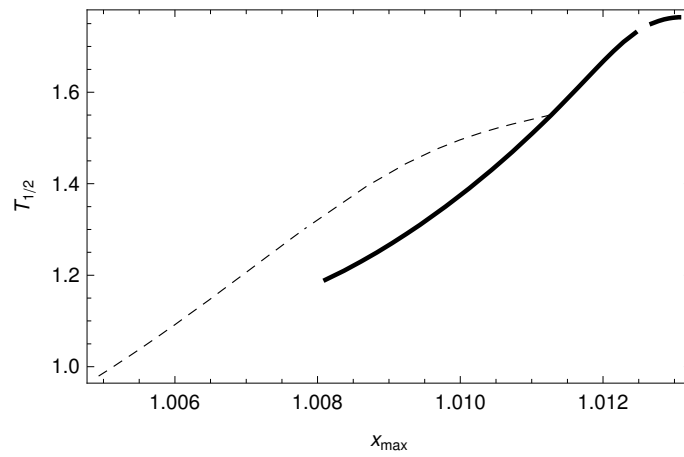


Figure 2.11: The half-period of classical halo orbits about L_2 is shown by the dashed line, and the half-period of artificial halo orbits about AEP $\mathbf{r}_0 = (1.01134, 0, 0)$ is shown by the solid line.

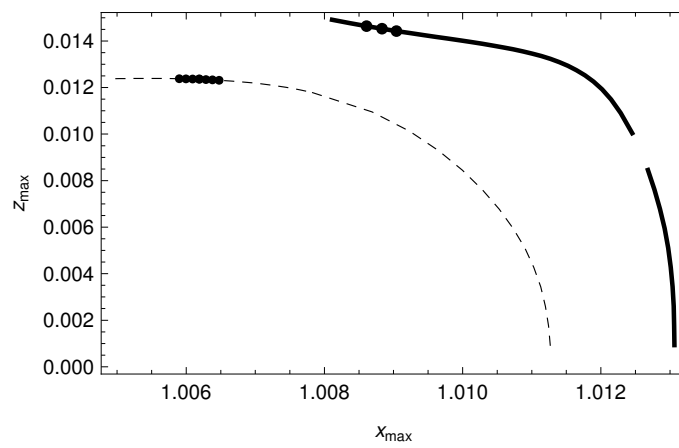


Figure 2.12: Classical halo orbits about L_2 shown by the dashed line, and artificial halo orbits about AEP $\mathbf{r}_0 = (1.01134, 0, 0)$ with low-thrust acceleration $\mathbf{a}_T = (-0.01, 0, 0)$ shown by the solid line. Heavy dots on both curves corresponds to stable halo orbits.

Table 2.1: Initial condition for stable orbits with $\mathbf{a}_T = (-0.01, 0, 0)$ which corresponds to a low-thrust acceleration 0.0593 mms^{-2} and low-thrust force 30 mN for a 500 kg spacecraft.

$x_0 (\times 10^8 \text{ km})$	$z_0 (\times 10^6 \text{ km})$	$\dot{y}_0 (\times 10^2 \text{ m/s})$	$T_{1/2}$ (days)	\mathcal{C}
1.509505487164924	2.158391940114810	-4.177777862144087	73.8218469	-1.49000437
1.509191101130694	2.173171517835050	-4.076979879730191	72.6592201	-1.49000439
1.508857610708376	2.189749813954399	-3.966248219678315	71.4965932	-1.49000442

ison, the period of classical halo orbits about L_2 is also shown. Fig. 2.12 shows the same family of orbits (see first plot in Fig. 2.10) characterised by their maximum x -value x_{max} and maximum z -value z_{max} . Switching from the Lindstedt-Poincaré analysis at $x_{max} = 1.0126$ to the continuation method with $\Delta T_{1/2} = -0.02$ causes a gap in the artificial halo orbits curves (see Figs. 2.11-2.12). However, halo orbits exist in the gap and can be shown by choosing a smaller $\Delta T_{1/2}$.

According to Floquet theory, the first order or linear stability of periodic orbits is described by the eigenvalues of the monodromy matrix $\Phi(T)$. Let the nonlinear system Eq. (2.1) be written as $\dot{\mathbf{X}} = \mathbf{f}(\mathbf{X})$. Since the trace of the Jacobian $\frac{\partial \mathbf{f}}{\partial \mathbf{X}} = 0$ [see Eq. (2.6)], eigenvalues of the monodromy matrix occur in reciprocal pairs [15]. The system is autonomous, so it has $+1$ as an eigenvalue for a periodic orbit [98]. Thus, two of the eigenvalues of the monodromy matrix are unity because of the reciprocal pair condition, and the stability of the periodic orbit is given by the complex conjugate eigenvalues on the unit circle in the complex plane. Thus, for stable periodic orbits, the spectrum of the monodromy matrix is described by

$$\{1, 1, \lambda_i, \bar{\lambda}_i, \lambda_j, \bar{\lambda}_j\} \quad (2.19)$$

i.e., modulus of all the eigenvalues lie on the unit circle. However, if all $|\lambda_i| = 1$ that does not provide the stability information of the nonlinear system. Therefore, the nonlinear stability is tested by numerically integrating the nonlinear system of equations and the periodic orbit keeps a halo shape for large integration times. However, for artificial unstable periodic orbits, the eigenvalue spectrum of the

monodromy matrix is given by

$$\{1, 1, \lambda_r, 1/\lambda_r, \lambda_i, \bar{\lambda}_i\} \quad (2.20)$$

The initial condition for stable artificial periodic orbits is given in Table 2.1. In the Sun-Earth system, the low-thrust acceleration 0.0593 mm/s^2 corresponds to 30 mN thrust for a 500 kg spacecraft. Assuming $I_{sp} = 3200 \text{ s}$ and propellant mass fraction of 50%, the propellant will be consumed within 11.5 years. However, these stable orbits can maintain a halo shape for larger integration times i.e., 25 years (see Fig. 2.13). Stable halo orbits (shown by dots in Fig. 2.12) about L_2 are between the L_2 point and the Earth, while artificial stable orbits in the case of low-thrust propulsion about AEP $\mathbf{r}_0 = (1.01134, 0, 0)$ are closer to L_2 . The stable halo orbits can also be found by choosing A_x as a continuation parameter with a tolerance of $\frac{|\dot{x}|+|\dot{z}|}{2} < 10^{-7}$ and the orbit ($A_z(17.5 \times 125,000 \text{ km})$) maintains halo shape for 7 years only (a good tolerance 10^{-9} is obtained by choosing $T_{1/2}$ as a continuation parameter and the orbit is shown in Fig.2.13). Although the existence of stable halo orbits for low-thrust propulsion spacecraft is shown around unstable AEP, an in-depth stability analysis could be performed [51, 92], but is left to future work.

2.6 Conclusions

The possibility of generating halo orbits using a near-term electric propulsion system has been shown in the circular restricted three-body problem around nonequilibrium points by changing these points into equilibrium points with low-thrust acceleration. In particular, halo orbits around nonequilibrium points inside L_1 and beyond L_2 that require the low-thrust acceleration to be directed sunward are shown to be feasible with such low-thrust propulsion. It is therefore impossible for solar sails to generate these artificial halo orbits. We have also shown that we may fine tune the initial data provided by the Lindstedt-Poincaré method, for

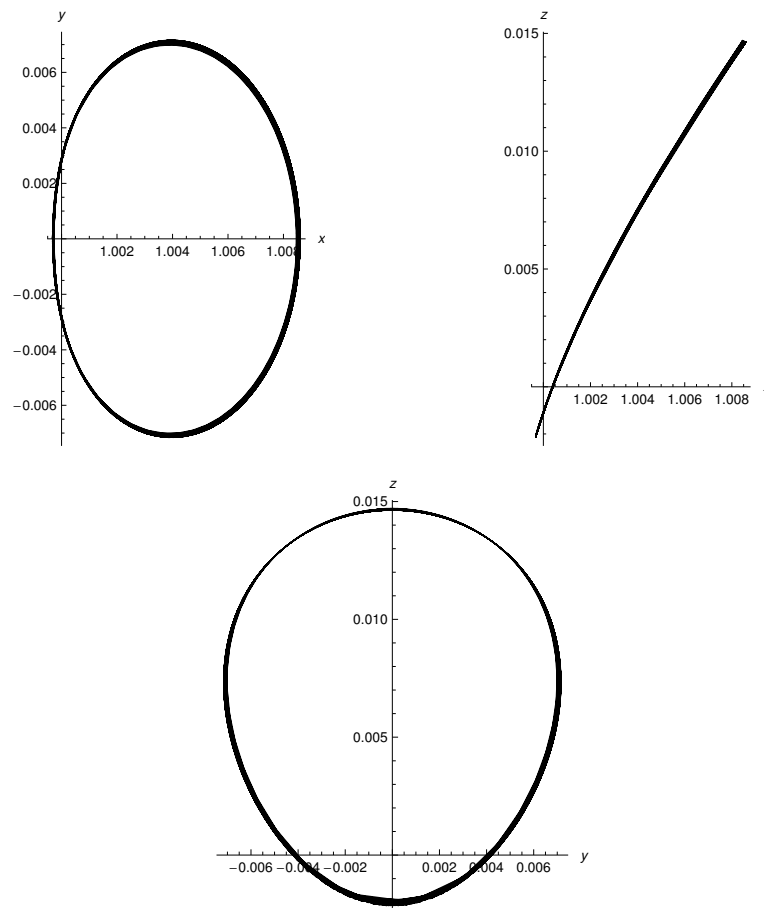


Figure 2.13: Stable orbit around AEP $\mathbf{r}_0 = (1.01134, 0, 0)$ with low-thrust acceleration $\mathbf{a}_T = (-0.01, 0, 0)$ maintain halo shape for 25 years.

the integration of the nonlinear equations of motion with constant continuous low-thrust acceleration, to produce closed orbits around artificial equilibrium point using a differential corrector. Both the period and minimum amplitude of halo orbits about artificial equilibrium points inside L_1 decreases with an increase in low-thrust acceleration. The halo orbits about artificial equilibrium points beyond L_2 in contrast show an increase in period with an increase in low-thrust acceleration. However, the minimum amplitude first increases and then decreases after the thrust acceleration exceeds 0.415 mm/s^2 . Stable low-thrust halo orbits for a point beyond L_2 are also found using a continuation method, while the continuation parameter is chosen as the half-period of the halo orbit. These stable halo orbits are realisable with solar electric propulsion and found to be towards L_2 , while the classical stable halo orbits around L_2 are approximately halfway between the Earth and L_2 .

Chapter 3

Artificial Three-Body Equilibria for Hybrid Low-Thrust Propulsion

This chapter proposes a new concept for creating artificial equilibrium points in the circular restricted three-body problem using a hybrid sail i.e., with both SEP and solar sail propulsion. The work aims to investigate the use of a hybrid sail for artificial equilibrium points that are technologically difficult with either of these propulsion systems alone. The hybrid sail has freedom in specifying the sail lightness number, then minimising the required thrust acceleration from the solar electric propulsion thruster while satisfying the equilibrium condition. The stability analysis of such artificial equilibrium points uses a linear method which results in a linear time varying (mass) system. The freezing time method then provides unstable and marginally stable regions for hybrid solar sail artificial equilibria. Three propulsion systems (solar electric propulsion, solar sail and hybrid sail) have been compared with a given payload mass and mission life for a polar Earth observation mission. For a near-term sail assembly loading, for the hybrid sail a substantially lower propellant mass is found compared with solar electric propulsion and lower sail length with respect to a solar sail, and a lower total

initial spacecraft mass.

In the next section the force model for a partially reflecting hybrid sail is described. The solar radiation pressure (SRP) and SEP accelerations are normalised with respect to a reference acceleration and are used in Sect. 3.2 to describe the equations of motion of a hybrid sail in the CRTBP. In Sect. 3.2, for a hybrid sail the required SEP acceleration is minimised for a given sail lightness number while satisfying the equilibrium condition. Two strategies are discussed in Sect. 3.2.2 to maintain the equilibrium condition. In Sect. 3.3, because of the slowly time varying (mass) linear system, the freezing time method is used to determine the stability of AEPs of a hybrid sail in the Sun-Earth CRTBP. Section 3.4 compares the performance of the hybrid sail relative to a pure sail and a pure SEP system for a polar Earth observer mission. Finally, conclusions are presented in Sec. 3.5.

3.1 Partially Reflecting Hybrid Sail Model

3.1.1 Dimensional Force Model

The hybrid sail configuration is adopted from Leipold and Götz [54] as described in the section 1.3.3. They developed a hybrid sail force model that takes different reflectivities for the sail and TFSC area for their magnitude, but leaves the thrust direction acting normal to the sail surface. This chapter considers a hybrid sail model which has a SRP force component along the sail surface (non-ideal reflectivity) and so the total SRP force is no longer normal to sail surface.

The solar radiation pressure at a distance R_1 from the Sun (see Eq.(1.15)) is given by

$$P = \frac{L_s}{4\pi R_1^2 c} \quad (3.1)$$

The unit vectors normal to and transverse to the hybrid sail surface are defined by \mathbf{n} and \mathbf{t} respectively, as shown in Figure 3.1. The direction of incident photons is described by $\hat{\mathbf{r}}_1 = \cos \alpha \mathbf{n} - \sin \alpha \mathbf{t}$ and so the SRP force due to the incident photons

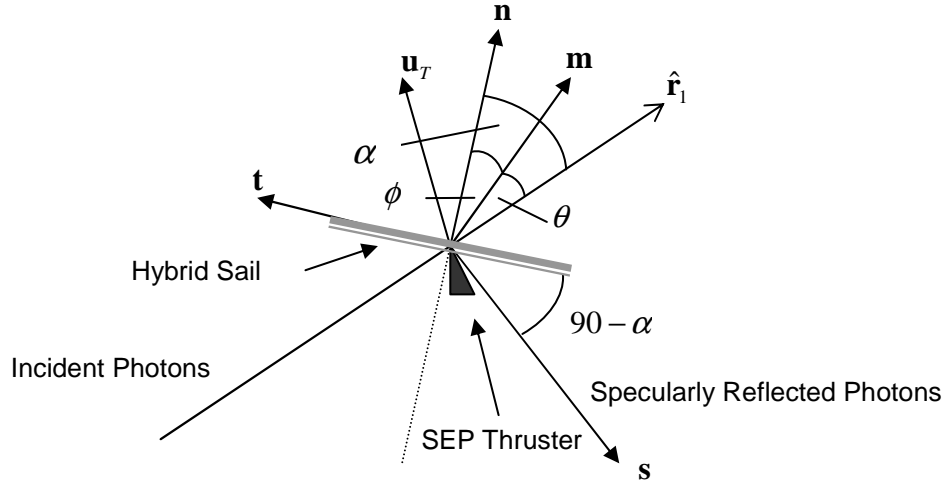


Figure 3.1: Solar radiation pressure force model for a specularly reflecting hybrid sail. The solar electric propulsion thruster is also shown.

is then

$$\mathbf{F}_i = PA_T \cos \alpha (\hat{\mathbf{r}}_1) \quad (3.2)$$

where $A_T \cos \alpha$ is the projected area in the direction of the incident photons. Specular reflection (no diffuse reflection and thermal re-emission) is assumed from both TFSC area A_{TF} and sail area A_S . The force on the hybrid sail due to the reflected photons is then

$$\mathbf{F}_r = \tilde{r}_S PA_S \cos \alpha (-\mathbf{s}) + \tilde{r}_{TF} PA_{TF} \cos \alpha (-\mathbf{s}) \quad (3.3)$$

where \tilde{r}_S is the sail film reflectivity and \tilde{r}_{TF} is the thin film reflectivity. The unit vector $\mathbf{s} = -\cos \alpha \mathbf{n} - \sin \alpha \mathbf{t}$ defines the direction of the specularly reflected photons. The total force \mathbf{F}_S exerted on the hybrid sail due to incident and reflected photons is therefore

$$\mathbf{F}_S = \mathbf{F}_i + \mathbf{F}_r = F_n \mathbf{n} + F_t \mathbf{t} \quad (3.4)$$

with

$$\begin{aligned} F_n &= (\hat{\mathbf{r}}_1 \cdot \mathbf{n})^2 [(1 + \tilde{r}_S) PA_S + (1 + \tilde{r}_{TF}) PA_{TF}] \\ F_t &= (\hat{\mathbf{r}}_1 \cdot \mathbf{n})(\hat{\mathbf{r}}_1 \cdot \mathbf{t}) [(1 - \tilde{r}_S) PA_S + (1 - \tilde{r}_{TF}) PA_{TF}] \end{aligned}$$

where $\hat{\mathbf{r}}_1 \cdot \mathbf{n} = \cos \alpha$ and $\hat{\mathbf{r}}_1 \cdot \mathbf{t} = -\sin \alpha$, and so the SRP force on the hybrid sail \mathbf{F}_S will now act in direction \mathbf{m} as shown in Figure 3.1.

The force due to the SEP thruster placed at the centre of the sail, as shown in Figure 3.1, is given by

$$\mathbf{F}_T = \mathcal{T} \mathbf{u}_T \quad (3.5)$$

where the unit vector \mathbf{u}_T denotes the thrust direction.

The total thrust provided by the hybrid sail due to the SRP and the SEP thruster can be obtained from the sum of Eqs. (3.4) and (3.5).

3.1.2 Non-dimensional Acceleration Model

The hybrid sail model is considered in the Sun-Earth CRTBP and is made non-dimensional by choosing the units as discussed in section 1.1.1. Thus, the non-dimensional unit of acceleration corresponds to $a_{\text{ref}} = \omega^2 R = 0.00593 \text{ m/s}^2$ in the Sun-Earth system.

To obtain the acceleration \mathbf{a}_S due to SRP for a hybrid sail in non-dimensional form, which will be used in the equations of motion of the hybrid sail described in the next section, Eq. (3.4) is divided by mass m and dimensional reference acceleration $\omega^2 R$, then re-arranging (see Appendix B.1) it is found that

$$\mathbf{a}_S = a_s \mathbf{m} = \frac{1}{2} \beta_0 \frac{m_0}{m} \frac{1 - \mu}{r_1^2} g(\hat{\mathbf{r}}_1 \cdot \mathbf{n})^2 \mathbf{n} + \frac{1}{2} \beta_0 \frac{m_0}{m} \frac{1 - \mu}{r_1^2} h(\hat{\mathbf{r}}_1 \cdot \mathbf{n})(\hat{\mathbf{r}}_1 \cdot \mathbf{t}) \mathbf{t} \quad (3.6)$$

where

$$\begin{aligned} g &= (1 + \tilde{r}_S) - \frac{A_{TF}}{A_T} (\tilde{r}_S - \tilde{r}_{TF}) \\ h &= (1 - \tilde{r}_S) + \frac{A_{TF}}{A_T} (\tilde{r}_S - \tilde{r}_{TF}) \end{aligned}$$

and m_0 is the initial mass of hybrid sail and $\beta_0 = \frac{\sigma^*}{(\frac{m_0}{A_T})}$ is defined as the dimensionless lightness number. The acceleration model for a non-ideal pure sail [62] is easily recovered from Eq. (3.6) when the sail mass is constant $m = m_0$ and $\tilde{r}_{TF} = \tilde{r}_S$.

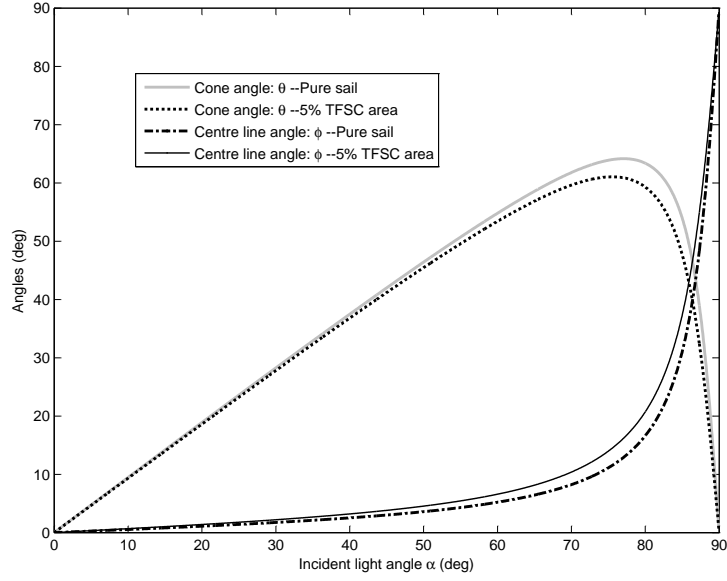


Figure 3.2: Maximum cone angle for a hybrid sail (5% TFSC area relative to total area) is less than that for a pure sail (with no TFSC area)

For a given m_0 , β_0 and TFSC fractional area with respect to total area, the *magnitude* of acceleration due to SRP acting on the hybrid sail increases with the decrease of the hybrid sail mass m and may be written as

$$a_s = \frac{1}{2} \beta_0 \frac{m_0}{m} \frac{1 - \mu}{r_1^2} \cos \alpha \sqrt{g^2 \cos^2 \alpha + h^2 \sin^2 \alpha} \quad (3.7)$$

The offset angle between \mathbf{m} and \mathbf{n} , usually called the centre-line angle ϕ , (see Figure 3.1) can be obtained from Eq. (3.6) by dividing the ratio of transverse and normal accelerations as

$$\tan \phi = \frac{h}{g} \tan \alpha \quad (3.8)$$

The actual *direction* of the SRP acceleration for a hybrid sail is defined by the cone angle θ . Using the relation $\alpha = \theta + \phi$ and Eq. (3.8), the cone angle θ can be written as

$$\tan \theta = \frac{(g - h) \tan \alpha}{g + h \tan^2 \alpha} \quad (3.9)$$

Assuming a reflectivity for a typical aluminised sail film $\tilde{r}_S = 0.9$ and for the TFSC area $\tilde{r}_{TF} = 0.4$ [54], Figure 3.2 shows that the maximum cone angle

$\theta_{max} = 61$ deg of the hybrid sail is less than the maximum cone angle 64.15 deg of a pure sail. This is due to the fact that for a hybrid sail $\tilde{r}_{TF} < \tilde{r}_S$.

The non-dimensional acceleration due to the SEP thruster can be obtained from Eq. (3.5) by dividing through by the hybrid sail mass m and reference acceleration a_{ref} as

$$\mathbf{a}_T = \frac{\mathcal{T}/m}{a_{ref}} \mathbf{u}_T = a_T \mathbf{u}_T \quad (3.10)$$

These force models will now be used to define sets of AEP for a hybrid sail.

3.2 Equations of Motion and Artificial Equilibria

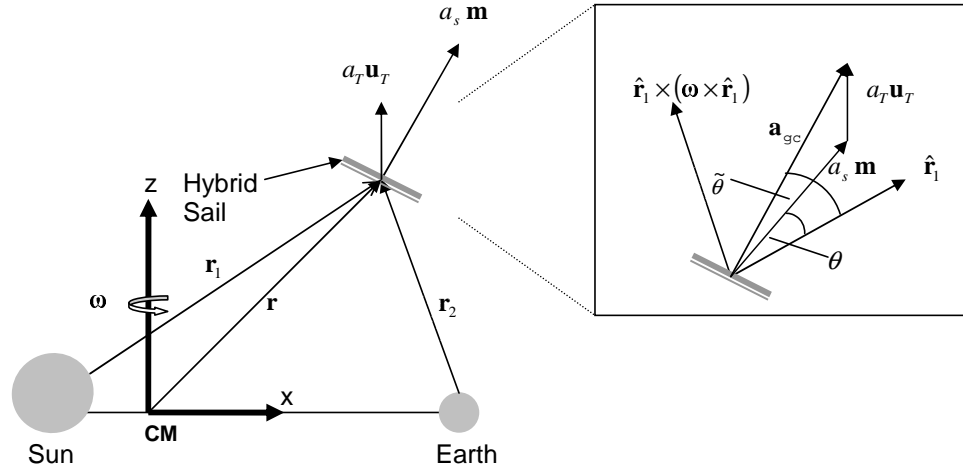


Figure 3.3: Definition of coordinate system and hybrid sail using two low-thrust propulsion systems.

Consider a synodic frame $F_a(x, y, z)$ co-rotating with the two primary masses at constant angular velocity $\boldsymbol{\omega}$ with origin at their center of mass, as shown in Figure 3.3 (see section 1.1.1 for synodic frame discussion). The nondimensional equation of motion of a hybrid sail in the rotating synodic frame of reference F_a is given by

$$\frac{d^2 \mathbf{r}}{dt^2} + 2\boldsymbol{\omega} \times \frac{d\mathbf{r}}{dt} + \nabla U(\mathbf{r}) = \mathbf{a}_S + \mathbf{a}_T \quad (3.11)$$

where $\boldsymbol{\omega} = [0 \ 0 \ 1]^T$. The vectors \mathbf{a}_S and \mathbf{a}_T are the accelerations due to solar radiation pressure and the solar electric propulsion system and may be written in

the frame F_a as

$$\mathbf{a}_S = a_s \mathbf{m}^a, \quad \mathbf{a}_T = a_T \mathbf{u}_T^a \quad (3.12)$$

and scalar potential $U(\mathbf{r}) = -V(\mathbf{r})$ (see Eq. (2.2) for $V(\mathbf{r})$) includes the three-body gravitational potential and centrifugal term i.e.,

$$U(\mathbf{r}) = - \left(\frac{1-\mu}{r_1} + \frac{\mu}{r_2} \right) - \frac{1}{2}(x^2 + y^2) \quad (3.13)$$

where $\mathbf{r}_1 = [x + \mu \quad y \quad z]^T$ and $\mathbf{r}_2 = [x - (1 - \mu) \quad y \quad z]^T$ are the position vectors of the hybrid sail with respect to the primary bodies. An artificial equilibrium point \mathbf{r}_0 in the rotating frame of reference F_a is obtained if the vector sum of the continuous low thrust acceleration from the two propulsion systems satisfies the following equation

$$\nabla U(\mathbf{r}_0) = \mathbf{a}_S + \mathbf{a}_T \triangleq \mathbf{a}_{gc} \quad (3.14)$$

Now $\nabla U(\mathbf{r}_0) = \mathbf{a}_{gc}$ is the required acceleration vector to cancel the gravitational forces of the two primary bodies and the centrifugal force in the rotating frame F_a . It may also be defined as the required acceleration for converting a nonequilibrium point into an AEP at \mathbf{r}_0 . For a pure sail system [68], the required acceleration vector is generated by the SRP acceleration vector alone, while for a pure SEP system [73] it is generated by the acceleration vector from the SEP system alone. For a hybrid sail, Eq. (3.14) shows that the required vector to keep the hybrid sail at AEP \mathbf{r}_0 is generated by the vector sum of the SRP and the SEP acceleration vectors. A new frame F_b is defined that will be useful in the next section to minimise the thrust acceleration from the SEP system. F_b is defined with a set of three orthogonal vectors $\{\mathbf{r}_1, \boldsymbol{\omega} \times \mathbf{r}_1, \mathbf{r}_1 \times (\boldsymbol{\omega} \times \mathbf{r}_1)\}$ and with its origin at the hybrid sail position. The rotation matrix from F_a to F_b can then be written as

$$\mathbf{C}_{b/a}(\mathbf{r}_0) = \begin{bmatrix} \frac{\mathbf{r}_1}{|\mathbf{r}_1|} & \frac{\boldsymbol{\omega} \times \mathbf{r}_1}{|\boldsymbol{\omega} \times \mathbf{r}_1|} & \frac{\mathbf{r}_1 \times (\boldsymbol{\omega} \times \mathbf{r}_1)}{|\mathbf{r}_1 \times (\boldsymbol{\omega} \times \mathbf{r}_1)|} \end{bmatrix}^T \quad (3.15)$$

Therefore, the condition for artificial equilibrium Eq. (3.14), in F_b is given by

$$\mathbf{a}_{gc}^b = a_s \mathbf{m}^b + a_T \mathbf{u}_T^b \quad (3.16)$$

where $\mathbf{a}_{gc}^b = [a_1 \ a_2 \ a_3]^T = \mathbf{C}_{b/a} \nabla U(\mathbf{r}_0)$. Eq. (3.16) can now be rewritten as

$$a_T^2 = a_{gc}^2 - 2a_s \mathbf{m}^b \cdot \mathbf{a}_{gc}^b + a_s^2 \quad (3.17)$$

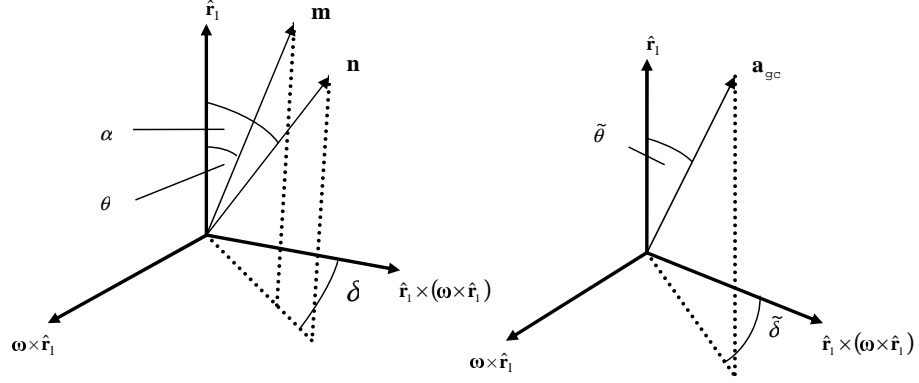


Figure 3.4: Definition of cone and clock angles for vectors \mathbf{n} , \mathbf{m} and \mathbf{a}_{gc} in frame F_b

where $a_{gc} = |\nabla U(\mathbf{r}_0)|$. The required vector \mathbf{a}_{gc} to keep the hybrid sail at an AEP, and the direction \mathbf{m} that defines the direction of the SRP acceleration vector can be expressed in F_b according to Fig. 3.4 as

$$\mathbf{a}_{gc}^b = a_{gc} \begin{bmatrix} \cos \tilde{\theta} \\ \sin \tilde{\theta} \sin \tilde{\delta} \\ \sin \tilde{\theta} \cos \tilde{\delta} \end{bmatrix}, \quad \mathbf{m}^b = \begin{bmatrix} \cos \theta \\ \sin \theta \sin \delta \\ \sin \theta \cos \delta \end{bmatrix} \quad (3.18)$$

where the cone angle $\tilde{\theta}$ and clock angle $\tilde{\delta}$ of \mathbf{a}_{gc} depend upon the AEP \mathbf{r}_0 and can be calculated as

$$\tilde{\theta} = \cos^{-1}\left(\frac{a_1}{a_{gc}}\right) \quad (3.19)$$

$$\tilde{\delta} = \tan^{-1}(a_2, a_3) \quad (3.20)$$

Using Eq. (3.18) in Eq. (3.17), the low thrust acceleration from the SEP system of the hybrid sail can be expressed in terms of the sail pitch angle α and the sail clock angle δ that defines the hybrid sail normal \mathbf{n} as shown in Fig. 3.4 as

$$a_T^2(\alpha, \delta) = a_{gc}^2 - 2a_{gc}a_s \left(\cos \theta \cos \tilde{\theta} + \sin \theta \sin \tilde{\theta} \cos(\delta - \tilde{\delta}) \right) + a_s^2 \quad (3.21)$$

where a_s and θ are functions of the pitch angle α as given by Eqs.(3.7) and (3.9) respectively.

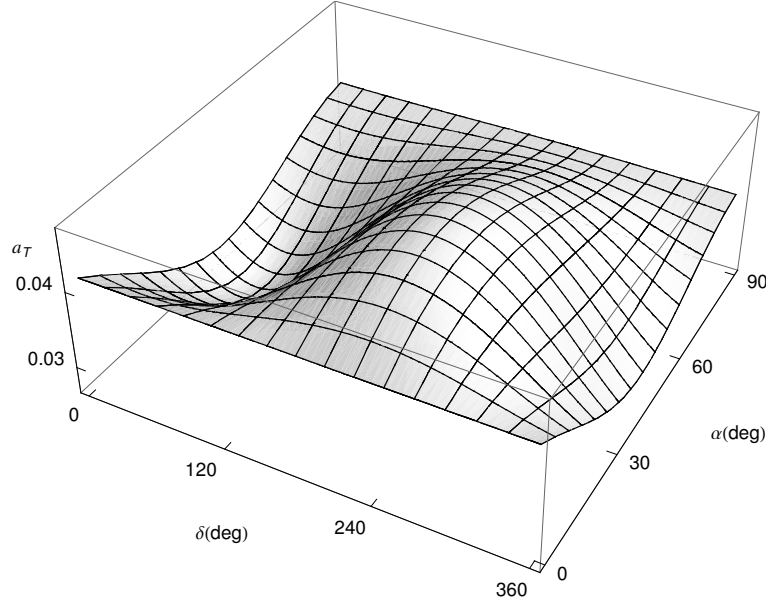


Figure 3.5: Required low thrust acceleration from SEP at $\mathbf{r}_0 = [1.005 \ 0.005 \ 0.005]^T$ as a function of the sail pitch angle α and sail clock angle δ for a sail with $\beta_0 = 0.03$. Minimum $a_T = 0.0269$ at optimal angles $(\alpha^*(0), \delta^*(0)) = (40.23^\circ, 39.46^\circ)$.

For a pure sail or a pure SEP system the required acceleration magnitude and thrust orientation are completely defined by the location of the artificial equilibria \mathbf{r}_0 . For a hybrid sail, the desired acceleration vector to keep the hybrid sail at an AEP is obtained by the sum of the SRP acceleration vector and the SEP acceleration vector, as shown in Fig. 3.3. By fixing β_0 , $m = m_0$, Fig. 3.5 shows that there is freedom in selecting the orientation of the SRP acceleration direction to obtain the desired acceleration vector \mathbf{a}_{gc} whilst minimising the SEP thrust. Once the optimum orientation is selected to obtain the maximum benefit from the SRP, the required orientation for the SEP thruster system \mathbf{u}_T may be determined from condition for artificial equilibria Eq. (3.16).

3.2.1 Minimisation of SEP Acceleration at $t=0$

The problem may now be formulated to determine the optimal hybrid sail cone and clock angles $(\alpha^*(0), \delta^*(0))$ to minimise the thrust acceleration a_T from the SEP system at an AEP \mathbf{r}_0 and for a given sail lightness number β_0 . At initial time $t=0$, $m = m_0$ and Eq. (3.7) becomes

$$a_s = a_s(0) = \frac{1}{2}\beta_0 \frac{1-\mu}{r_1^2} \cos \alpha \sqrt{g^2 \cos^2 \alpha + h^2 \sin^2 \alpha} \quad (3.22)$$

Using Eq. (3.22) in Eq. (3.21) and setting the derivative of a_T with respect to δ to zero yields a stationary point for the optimal clock angle as

$$\frac{\partial a_T}{\partial \delta} = a_{gc} \frac{a_s(0)}{a_T} \sin \theta \sin \tilde{\theta} \sin(\delta - \tilde{\delta}) = 0 \quad (3.23)$$

With $\alpha \neq 90$ deg or $a_s(0) \neq 0$, $\theta \neq 0$ and $\tilde{\theta} \neq 0$, Eq. (3.23) holds if

$$\delta^*(0) = \tilde{\delta} \quad (3.24)$$

This states that the hybrid sail clock angle should be aligned with the clock angle of the vector \mathbf{a}_{gc} in order to minimise the thrust acceleration from the SEP system. Inserting this result into Eq. (3.21) yields

$$a_T^2(\alpha) = a_{gc}^2 - 2a_{gc}a_s(0) \cos(\tilde{\theta} - \theta) + a_s^2(0) \quad (3.25)$$

The above equation can be minimised numerically for $\alpha^*(0)$, and specifying the bounds for $\alpha \in [0, \pi/2]$.

To show the feasibility of the hybrid sail for some practical missions to be discussed in Sec. 3.4, the analysis in the xz -plane will be considered (since $a_2 = 0$ in the xz -plane, so from Eq.(3.20), $\delta^* = \tilde{\delta} = 0$ if $a_3 > 0$, or $\delta^* = \tilde{\delta} = \pi$ if $a_3 < 0$). Fig. 3.6 shows families of acceleration contours near the Earth in the case of pure SEP and a hybrid sail. The shaded area shows the region where the pure sail cannot be placed as the SRP force direction is constrained by the maximum cone angle ($\theta \leq \theta_{max}$) due to the sail film partial reflectivity. The benefit of the hybrid

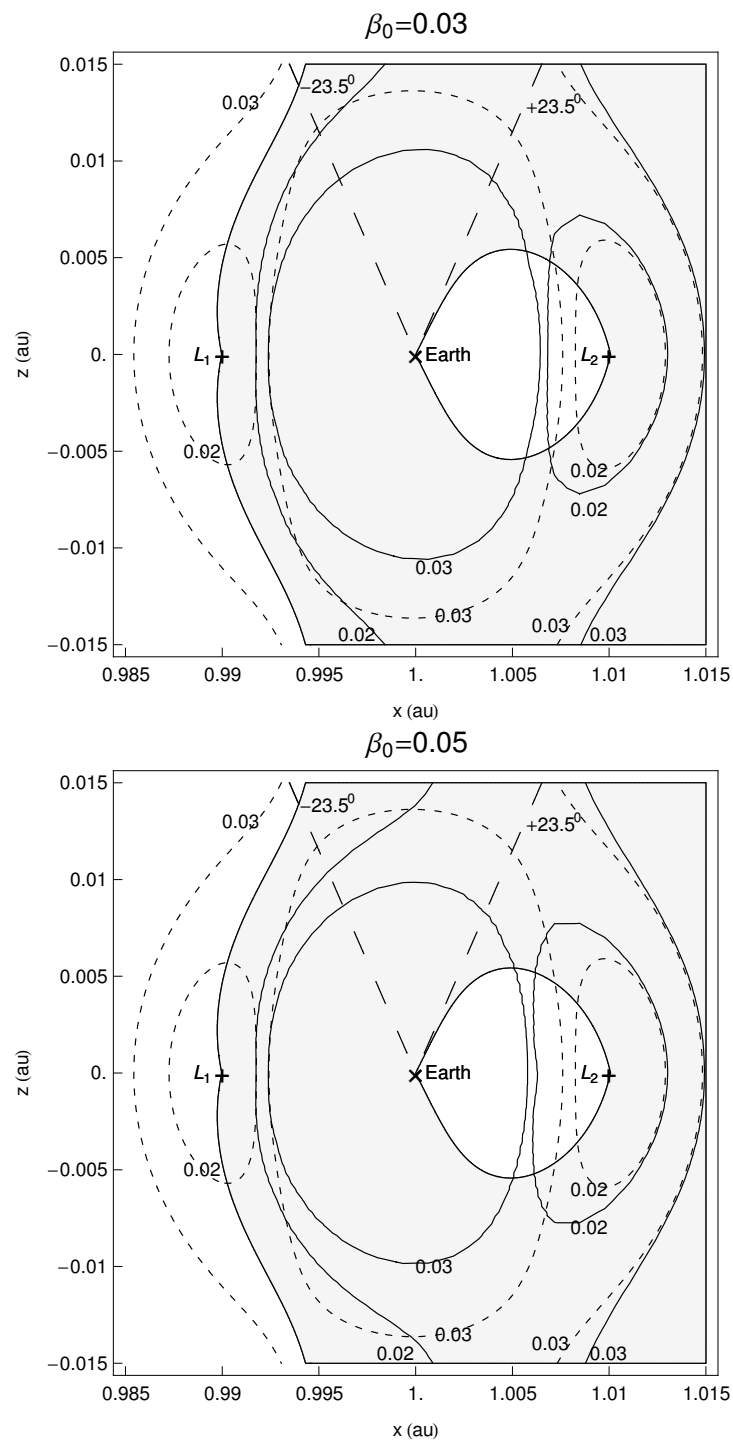


Figure 3.6: Thrust acceleration contours a_T in the xz -plane. Values 0.02, 0.03 shown by dotted lines for the pure SEP system and shown by solid lines for the hybrid sail. ∓ 23.5 deg are the angles of the polar axis of the Earth (dashed lines) with respect to the normal to the ecliptic plane at summer and winter solstices.

sail is clear over the pure sail. The pure sail can be placed in the shaded region by combining it with an electric thruster, since the thrust vector from the SEP system of a hybrid sail can be oriented in any direction. In reality the SEP system direction is limited by solar sail impingement and this will restrict the shaded region for the hybrid sail. Also, the benefit of the hybrid sail is clear over pure SEP, since a larger volume of space is available for artificial equilibrium solutions around L_2 and displaced equilibrium solutions towards Earth near L_1 exist, with the same low thrust acceleration value ($a_T = 0.02$). This is due to part of the total acceleration required to cancel the gravitational acceleration of the two primary bodies and centrifugal force being available from the solar sail. In general, the addition of a small SEP system to a solar sail allows the hybrid sail to be in equilibrium closer the Earth, and in volumes of space inaccessible to a pure sail system.

In Fig. 3.6 the electric thruster acceleration contours can be compared in the case of the pure SEP and the hybrid sail system. The electric thruster acceleration contour of value $a_T = 0.03$ about the Earth in the case of the hybrid system is not symmetric. This depends upon where the hybrid sail can or cannot use SRP effectively. However, the electric thruster acceleration contours of values $|\nabla U| = 0.03$ around the Earth for pure SEP are symmetric due to the near symmetric 3-body potential at the Earth. From Earth towards L_1 along the x -axis, and also in regions beyond L_2 , the acceleration contours of the hybrid sail and pure SEP are identical because at these locations the hybrid sail cannot use SRP effectively. Here the sail pitch angle becomes approximately 90 deg to minimise the required thrust acceleration from the SEP system. At these locations the hybrid sail will not be of use as compared to a pure SEP system.

3.2.2 Equilibria Options During Mission Life

The hybrid sail is a variable mass system, unlike a pure sail which is a constant mass system. As the SEP system consumes propellant, so the magnitude of the SRP

acceleration continuously increases with time due to the decrease of the hybrid sail mass m . In principle, the thrust magnitude needed from the SEP system should decrease with mission lifetime. There are two options to keep the hybrid sail at an AEP \mathbf{r}_0 during its mission life.

3.2.2.1 Option 1

In option 1, a_T can be minimised at $t = 0$ or for initial mass $m = m_0$ as in the previous section, and the hybrid sail can be maintained at this optimum fixed attitude $(\alpha^*(0), \delta^*(0))$ during the whole mission lifetime. Due to the increase of the SRP acceleration a_s , the thrust from the SEP system should be adjusted in magnitude (throttled) and its direction trimmed at each instant to ensure that the equilibrium condition is satisfied. The algorithm works as follows:

- (1) At $t = 0$, $m = m_0$, choose an appropriate β_0 so that the total sail area $A_T = \frac{m_0 \beta_0}{\sigma^*}$.
- (2) In the xz -plane choose an AEP \mathbf{r}_0 which in turn determines the desired acceleration vector \mathbf{a}_{gc} . Calculate the cone angle $\tilde{\theta}$ using Eq. (3.19). However, in the xz -plane $a_2 = 0$, so from Eq. (3.20) $\tilde{\delta} = 0$ or π depending on sign of a_3 , which implies the clock angle $\delta^*(0) = 0$ or π .
- (3) Minimise a_T given in Eq. (3.25) for a hybrid sail of mass m_0 and determine the optimum sail pitch angle $\alpha^*(0)$ and keep it fixed for mission lifetime τ_m i.e., $\alpha^*(t) = \alpha^*(0)$ for $0 \leq t \leq \tau_m$. The normal to the hybrid sail \mathbf{n} , and unit vector \mathbf{m} along the SRP force given in Eq. (3.18) become

$$\begin{aligned} \mathbf{n}^b &= \begin{bmatrix} \cos \alpha^*(0) & 0 & \pm \sin \alpha^*(0) \end{bmatrix}^T \\ \mathbf{m}^b &= \begin{bmatrix} \cos \theta^*(0) & 0 & \pm \sin \theta^*(0) \end{bmatrix}^T \end{aligned} \quad (3.26)$$

where $\theta^*(0)$ is calculated using Eq. (3.9).

- (4) Calculate the SRP acceleration a_s and SEP acceleration a_T for a hybrid sail of mass m from Eqs. (3.7) and (3.21) respectively at the optimum sail pitch angle and clock angle $\delta^*(t) = \tilde{\delta} = 0(\pi)$.
- (5) Calculate the propellant mass $m_{prop}(t)$ consumed up to time t

$$m_{prop}(t) = m_0 \left(1 - \exp \left(-\frac{1}{I_{sp} g_0} \int_0^t \dot{a}_T dt \right) \right) \quad (3.27)$$

so that the instantaneous mass of the hybrid sail $m = m_0 - m_{prop}$.

- (6) Calculate the electric thruster direction at time t

$$\mathbf{u}_T^b = [u_1 \quad 0 \quad u_3]^T = \frac{1}{a_T} [\mathbf{a}_{gc}^b - a_s \mathbf{m}^b] \quad (3.28)$$

- (7) $t = t + \Delta t$. If $t < \tau_m$ go to step 4; otherwise the calculation is over.

3.2.2.2 Option 2

In option 2, the optimum sail pitch angle $\alpha^*(t)$ at each instant t is determined using the instantaneous mass m during the mission lifetime, instead of fixing it at $\alpha^*(0)$. In this case both \mathbf{n} and \mathbf{u}_T will be varied to keep the hybrid sail at an artificial equilibrium point \mathbf{r}_0 . The algorithm in this case works similarly to option 1, except step (3) and step (7) should be replaced accordingly:

- (3) Minimise a_T given in Eq. (3.21) with $\delta^*(t) = \tilde{\delta} = 0$ or π and determine the optimum sail pitch angle $\alpha^*(t)$ using the instantaneous mass m of the hybrid sail. The unit vectors \mathbf{n}^b and so \mathbf{m}^b in this case will vary with time as

$$\begin{aligned} \mathbf{n}^b &= \begin{bmatrix} \cos \alpha^*(t) & 0 & \pm \sin \alpha^*(t) \end{bmatrix}^T \\ \mathbf{m}^b &= \begin{bmatrix} \cos \theta^*(t) & 0 & \pm \sin \theta^*(t) \end{bmatrix}^T \end{aligned} \quad (3.29)$$

where $\theta^*(t)$ is calculated using $\alpha^*(t)$.

(7) $t = t + \Delta t$. If $t < \tau_m$ go to step 3; otherwise the calculation is over.

Note the \pm sign in Eqs. (3.26) and (3.29). The +ve sign is used when $\delta = \delta^* = 0$ and the -ve sign when $\delta = \delta^* = \pi$ (see Eq. (3.18)).

3.3 Linear Stability Analysis for the Hybrid Sail

3.3.1 Linearised System

To determine the local stability property of an AEP \mathbf{r}_0 , the variational equations in the vicinity of an equilibrium point are derived. Such linearised variational equations are obtained by replacing the nonlinear system Eq. (3.11) by a linear system around the equilibrium point \mathbf{r}_0 . Using the transformation $\mathbf{r} = \mathbf{r}_0 + \delta\mathbf{r}$ for linearisation (in the xz-plane) and assuming the attitude of the hybrid sail \mathbf{n}^a and thruster pointing of the SEP system \mathbf{u}_T^a are not perturbed, so as to restrict the stability analysis in the sense of Lyapunov, Eq. (3.11) can be rewritten in the form

$$\frac{d^2\delta\mathbf{r}}{dt^2} + 2\boldsymbol{\omega} \times \frac{d\delta\mathbf{r}}{dt} + \nabla U(\mathbf{r}_0 + \delta\mathbf{r}) = \mathbf{a}_S(\mathbf{r}_0 + \delta\mathbf{r}, \mathbf{n}^a) + \mathbf{a}_T(\mathbf{r}_0 + \delta\mathbf{r}, \mathbf{u}_T^a) \quad (3.30)$$

The gradient of the potential and the acceleration vectors due to SRP and SEP can be expanded in Taylor series about the equilibrium point \mathbf{r}_0 to a first order as

$$\begin{aligned} \nabla U(\mathbf{r}_0 + \delta\mathbf{r}) &= \nabla U(\mathbf{r}_0) + \left[\frac{\partial \nabla U}{\partial \mathbf{r}} \right]_{\mathbf{r}_0} \delta\mathbf{r} + O(|\delta\mathbf{r}|^2) \\ \mathbf{a}_S(\mathbf{r}_0 + \delta\mathbf{r}, \mathbf{n}^a) &= \mathbf{a}_S(\mathbf{r}_0) + \left[\frac{\partial \mathbf{a}_S(\mathbf{r})}{\partial \mathbf{r}} \right]_{(\mathbf{r}_0, \mathbf{n}^a)} \delta\mathbf{r} + O(|\delta\mathbf{r}|^2) \\ \mathbf{a}_T(\mathbf{r}_0 + \delta\mathbf{r}, \mathbf{u}_T^a) &= \mathbf{a}_T(\mathbf{r}_0) + \left[\frac{\partial \mathbf{a}_T}{\partial \mathbf{r}} \right]_{(\mathbf{r}_0, \mathbf{u}_T^a)} \delta\mathbf{r} + O(|\delta\mathbf{r}|^2) \end{aligned} \quad (3.31)$$

Assuming the acceleration \mathbf{a}_T is fixed with respect to the perturbation $\delta\mathbf{r}$, it can be seen that

$$\left[\frac{\partial \mathbf{a}_T}{\partial \mathbf{r}} \right]_{\mathbf{r}_0} = 0 \quad (3.32)$$

Substituting Eqs. (3.31) and (3.32) into Eq. (3.30) and using the artificial equilibrium condition of Eq. (3.14), then the linear variational equation around an AEP \mathbf{r}_0 is obtained as

$$\frac{d^2 \delta \mathbf{r}}{dt^2} + 2\boldsymbol{\omega} \times \frac{d\delta \mathbf{r}}{dt} - K\delta \mathbf{r} = 0 \quad (3.33)$$

where

$$K = - \left[\frac{\partial \nabla U}{\partial \mathbf{r}} \right]_{\mathbf{r}_0} + \left[\frac{\partial \mathbf{a}_S(\mathbf{r})}{\partial \mathbf{r}} \right]_{(\mathbf{r}_0, \mathbf{n}^a)} \quad (3.34)$$

For an artificial equilibrium point \mathbf{r}_0 in the xz -plane, the explicit expression for K is given in the Appendix B.2.

By letting $\delta \mathbf{X} = (\delta \mathbf{r}, \delta \dot{\mathbf{r}})^T$, the linear system is $\delta \dot{\mathbf{X}} = A(t)\delta \mathbf{X}$. The Jacobian matrix $A(t)$ in the neighborhood of \mathbf{r}_0 is given by

$$A(t) = \begin{pmatrix} 0_3 & I_3 \\ K & \Omega \end{pmatrix}, \quad \Omega = \begin{pmatrix} 0 & 2 & 0 \\ -2 & 0 & 0 \\ 0 & 0 & 0 \end{pmatrix} \quad (3.35)$$

The Jacobian matrix is constant when the dynamics of the pure sail are linearised in the CRTBP. However, the linearisation for a hybrid sail in the CRTBP is a time varying system as the matrix K given in Eq. (3.34) contains mass (time) varying parameter. Furthermore, it is well known that if state deviations are known at a time t_0 , then its value at time t is obtained simply from the product [84]

$$\delta \mathbf{X}(t) = \Phi(t, t_0)\delta \mathbf{X}(t_0) \quad (3.36)$$

where $\Phi(t, t_0)$ is the state transition matrix. The determinant of the state transition matrix of the linearised system is

$$|\Phi(t, t_0)| = e^{\int_{t_0}^t \text{tr} A(\tau) d\tau} \quad (3.37)$$

where $\text{tr}A(\tau)$ is the trace of $A(\tau)$. The necessary condition for asymptotic stability of a linear time varying system is that for any $t > t_0$ [103]

$$\int_{t_0}^t \text{tr}A(\tau) d\tau \rightarrow -\infty \quad \text{as } t \rightarrow \infty \quad (3.38)$$

(as $\|\Phi(t, t_0)\| \rightarrow 0 \Rightarrow \Phi(t, t_0) \rightarrow 0$ (a zero matrix) $\Rightarrow |\Phi(t, t_0)| \rightarrow 0$ for $t \rightarrow \infty$).

Since for the hybrid sail

$$\int_{t_0}^t \text{tr}A(\tau) d\tau = 0 \quad (3.39)$$

it can be concluded that the linear time-varying system of the hybrid sail is not asymptotically stable, as is expected since there is no natural dissipation.

One approach to investigate the instability of slowly time-varying linear systems is to employ a freezing-time method [87]. In this approach, the time varying parameters (e.g., mass m for a hybrid system) are fixed at their current values during each instant of time $t_i = t_0, t_1, t_2, \dots, \tau_m$ and the Jacobian matrix $A(t_i)$ will be treated as constant for each interval t_i to t_{i+1} . Then, the eigenvalues of the constant matrix $A(t_i)$ resulting from its characteristic equation are examined for instability. The instability properties of the time-varying system are the same as those of the frozen-time system provided that the eigenvalues of $A(t)$ are bounded away from the imaginary axis for all $t \geq 0$ (i.e., eigenvalues do not cross the imaginary axis) and if $\sup_{t \geq 0} \|\dot{A}(t)\|$ (i.e., the norm of the time derivative of matrix $A(t)$) is sufficiently small [87].

3.3.2 Stability Analysis at $t_0 = 0$

To determine the stability of the linear system $\delta\dot{\mathbf{X}} = A(t_0)\delta\mathbf{X}$, the Jacobian matrix $A(t)$ time dependence is frozen at $t_0 = 0$ by substituting $m = m_0$ in the matrix K of Eq. (3.34), so that K may be written as

$$K(t_0) = \begin{pmatrix} k_1 & 0 & k_3 \\ 0 & k_5 & 0 \\ k_7 & 0 & k_9 \end{pmatrix} \quad (3.40)$$

The characteristic equation of $A(t_0)$ in λ is given by

$$|A(t_0) - \lambda I_6| = \lambda^6 + p_2\lambda^4 + p_1\lambda^2 + p_0 = 0 \quad (3.41)$$

where

$$p_2 = 4 - k_1 - k_5 - k_9 \quad (3.42)$$

$$p_1 = k_1k_5 - k_3k_7 - 4k_9 + k_1k_9 + k_5k_9 \quad (3.43)$$

$$p_0 = k_3k_5k_7 - k_1k_5k_9 \quad (3.44)$$

Defining $\kappa = \lambda^2$, then the characteristic equation becomes cubic in κ such that

$$\kappa^3 + p_2\kappa^2 + p_1\kappa + p_0 = 0 \quad (3.45)$$

The discriminant of the cubic Eq. (3.45) can then be defined as

$$D = 4p_0p_2^3 - p_1^2p_2^2 + 4p_1^3 - 18p_0p_1p_2 + 27p_0^2 \quad (3.46)$$

The roots of the cubic Eq. (3.45) in κ are real if the discriminant $D \leq 0$, or alternatively one real root and a pair of complex conjugate roots if $D > 0$. However, if all the roots of the cubic equation are real i.e., $D \leq 0$, then by *Descartes' rule of signs* [80], the number of positive real roots (including multiplicity) is equal to the number of sign changes of the sequence p_0, p_1, p_2 in Eq. (3.45).

The nature of the artificial equilibria (in the xz -plane) for the Sun-Earth CRTBP, where the third body is a hybrid sail is shown in Fig. 3.7. The regions are labelled as:

- (a) Region I-if the discriminant $D < 0$ and $p_0 > 0, p_1 > 0, p_2 > 0$, then by *Descartes' rule of signs* with no sign change of the coefficient sequence of

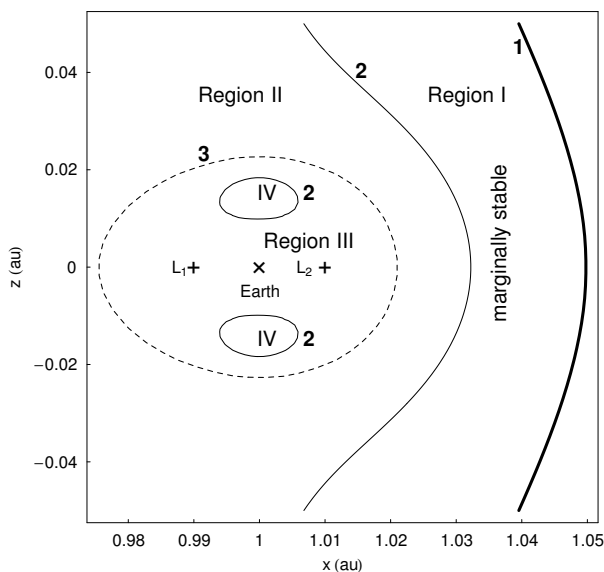


Figure 3.7: Regions I-IV in the Sun-Earth three-body system are classified according to the stability of artificial equilibria for a hybrid sail. 1,2 and 3 represent contours of $D = 0$, $p_0 = 0$ and $p_1 = 0$ respectively.

the cubic equation, all the roots of Eq. (3.45) are negative. Therefore, the spectrum of the Jacobian $A(t_0)$ is centres given by

$$\{\pm i\lambda_1, \pm i\lambda_2, \pm i\lambda_3\} \quad \text{Region I marginally stable}$$

- (b) Region II-if the discriminant $D < 0$ and $p_0 < 0, p_1 > 0, p_2 > 0$ or in Region III-if the discriminant $D < 0$ and $p_0 < 0, p_1 < 0, p_2 > 0$, then by *Descartes' rule of signs* with one sign change of the coefficient sequence of the cubic equation, the spectrum of the Jacobian is centres crossed with saddles

$$\{\pm i\lambda_1, \pm i\lambda_2, \pm\lambda_{r_1}\} \quad \text{Region II and III unstable}$$

- (c) Region IV-if the discriminant $D < 0$ and $p_0 > 0, p_1 < 0, p_2 > 0$, then by *Descartes' rule of signs* with two sign changes of the coefficient sequence of the cubic Eq. (3.45), the spectrum is

$$\{\pm i\lambda_1, \pm\lambda_{r_1}, \pm\lambda_{r_2}\} \quad \text{Region IV unstable}$$

The hybrid sail in Region I does not use SRP as the pitch angle $\alpha^*(0)$ becomes approximately/or equal to 90° to minimise the thrust acceleration a_T from the SEP system. Therefore, in this region the hybrid sail acts as a pure SEP system and the marginally stable region (centers) of the pure SEP system are recovered [73].

During the mission life at an artificial equilibrium location \mathbf{r}_0 , the mass m of the hybrid sail changes according to Eq.(3.27). Hence the matrix $A(t)$, and its eigenvalues, also change with m . Simulations run for different artificial equilibria in Regions II-IV with corresponding mass variation show very slow variation and no sign change in the roots of the cubic Eq.(3.45) during the mission life (see Fig. 3.8). Thus, no eigenvalues cross the imaginary axis and the small parameter variations in $A(t)$ during the mission life implies instability of Regions II-IV.

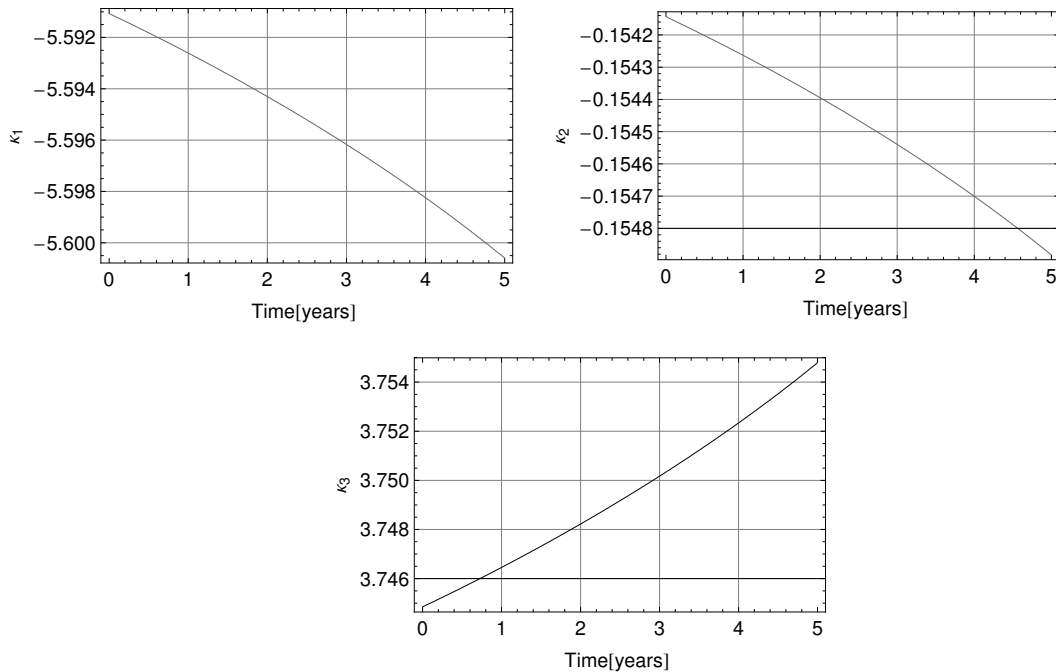


Figure 3.8: Variation in the roots $\kappa_1, \kappa_2, \kappa_3$ of cubic Eq. (3.45) due to decrease of hybrid sail mass. The root κ_3 corresponds to a saddle point. The AEP $\mathbf{r}_0 = [0.99558 \ 0 \ 0.01016]^T$ is chosen for illustration, the hybrid sail has initial mass $m_0 = 500$ kg and $\beta_0 = 0.03$.

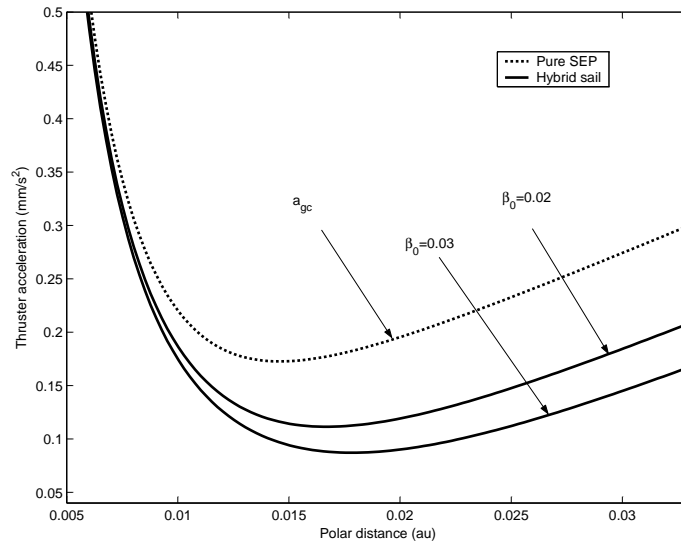


Figure 3.9: Thrust acceleration magnitude required from pure SEP and hybrid sail (at $t = 0$) at artificial equilibrium points above L_1 along the Earth’s polar axis (north pole at summer solstice).

3.4 Evaluation of Hybrid Sail Performance

This section compares the sizing of a hybrid sail, pure SEP system and pure sail system for a polar (Earth) observer mission. In the polar observer mission, AEPs along the polar axis, high above the L_1 side of the Earth are selected in the Sun-Earth system. Such equilibrium locations have been proposed by McInnes and others [21, 67] in the case of a pure sail for continuous, low resolution imaging of high latitude regions of the Earth and for polar telecommunication services at L_2 [29].

The magnitude of the required acceleration a_{gc} for an AEP along the polar axis is shown by the dotted lines in Fig. 3.9. It can be seen that a_{gc} has a minimum value along the polar axis due to the Sun-Earth three body dynamics. To generate an AEP, the pure SEP system alone provides the acceleration a_{gc} . For the hybrid sail, the thruster system provides less acceleration $a_T(\alpha^*(0))$ shown by the solid lines in Fig. 3.9 since part of the acceleration is provided by the SRP to achieve a_{gc} .

The initial (wet) mass for each propulsion system is calculated to position a spacecraft on an AEP with a fixed payload mass m_{pl} and fixed mission life τ_m . The total payload mass (including a small optical imager and spacecraft bus) of 100 kg is assumed for the polar observer mission [67]. The pure sail is a propellantless system, unlike pure SEP and the hybrid sail, and the pure sail mission life is limited only by the sail film. Hence, for the pure sail system only the payload mass m_{pl} is fixed. Some near-term pure sail missions are envisaged with a sail lifetime of at least 5 years [101].

3.4.1 Pure Sail

For a pure sail, the total mass m_0 can be decomposed into the sail assembly mass m_S (sail film, booms and deployment module) and the payload mass m_{pl} . The sail assembly mass m_S is usually written in terms of sail area and sail assembly loading σ_S , a key technology parameter that is a measure of the sail film thickness and lightness of the booms and deployment module (see Sect. 1.3.2). For a fixed m_{pl} and σ_S as given parameters, the initial mass can be calculated for a given equilibrium location \mathbf{r}_0 as

$$m_0 = m_{pl} + m_S = m_{pl} + \sigma_S \left[\frac{m_{pl}}{\sigma_T - \sigma_S} \right] \quad (3.47)$$

where $\sigma_T = \frac{m_0}{A_S}$ is the total (pure) sail loading. It can be calculated from the appropriate sail lightness number which is uniquely determined by the chosen equilibrium location \mathbf{r}_0 and the sail film reflectivity \tilde{r}_S [36].

3.4.2 Pure SEP

The polar observer mission is a long-term and large ΔV mission. To reduce m_0 for a given m_{pl} , in the case of pure SEP and the hybrid sail, the electric thruster selection should be made to reduce the propellant mass m_{prop} and the electric propulsion inert mass. Ion thrusters, among various kinds of electric propulsion

systems, are well-suited because of their potential for providing high $I_{sp} \approx 3200$ s (reduces the propellant requirement), high efficiency and high total impulse (see subsection 1.3.1.2). Higher efficiency for a given I_{sp} and thrust level reduces the input power of the SEP system, while higher total impulse reduces the number of thrusters, and thus also the inert mass of the SEP system. For a pure SEP system with TFSC technology as a power source, the initial mass m_0 breakdown can be written as

$$m_0 = m_{pl} + m_{Tank} + n_{Th} \cdot m_{inert} + m_{prop} + m_{TF} \quad (3.48)$$

where m_{Tank} is the (empty) propellant tank mass, m_{prop} the propellant mass, m_{TF} the TFSC mass and m_{inert} the inert mass of the SEP system including the mass of the thruster, power processor unit (PPU), thermal system for the PPU, Digital Control and Interface unit (DCIU) and cabling/propellant feeding system. n_{Th} is the number of thrusters. Two thrusters are assumed in series, each with an operating life of 2.5 years. In order to maintain the artificial equilibrium \mathbf{r}_0 , a constant acceleration $a_{gc}(\mathbf{r}_0)$ should be provided by the pure SEP system during mission life τ_m , and thus the propellant mass consumed m_{prop} is given by

$$m_{prop} = m_0 \left(1 - \exp \left(\frac{-\dot{a}_{gc} \tau_m}{I_{sp} g_0} \right) \right) \quad (3.49)$$

where \dot{a}_{gc} is the required dimensional acceleration. In the case of ion thrusters the approximate relations in Eq.(3.48) are given by

$$\begin{aligned} m_{Tank} &= 0.1 m_{prop} \\ m_{inert} &= k_e P_{e,max} \\ m_{TF} &= \sigma_{TF} A_{TF} \end{aligned} \quad (3.50)$$

The reasonable assumption is made that the mass of the propellant tank m_{Tank} is 10% of the propellant mass [32]. The specific mass k_e is assumed to be 20 kg/kW (as for the NSTAR class engine [14]). The areal density σ_{TF} of the TFSC is assumed to be 100 g/m² [54]. The thin film solar cell area A_{TF} is selected by using the maximum power level required $P_{e,max}$ (or maximum thrust \mathcal{T}_{max}), W

the solar flux at the AEP \mathbf{r}_0 , and efficiency η_{TF} (i.e., converting solar energy into electrical energy) as follows

$$A_{TF} = \frac{P_{e,max}}{W\eta_{TF}} \quad (3.51)$$

In Eq. (3.51) the TFSC area is assumed to be directed at the Sun while the ion thruster is firing in the desired direction to maintain the artificial equilibrium \mathbf{r}_0 . Although TFSC technology gives larger A_{TF} as compared to wafer based technology for a required $P_{e,max}$, due to its low efficiency $\eta_{TF} = 0.05$, it results in a lower mass m_{TF} due to the small value of σ_{TF} . If $\eta_e = 0.7$ [48] is the efficiency of converting electrical energy into constant exhaust velocity $v_e = I_{sp}g_0$, then

$$P_{e,max} = \frac{\mathcal{T}_{max}v_e}{2\eta_e} = \frac{m_0\dot{a}_{gc}I_{sp}g_0}{2\eta_e} \quad (3.52)$$

The initial (wet) mass m_0 for a pure SEP system then can be written in terms of m_{pl} and τ_m by substituting Eqs. (3.49-3.52) into Eq. (3.48) to obtain

$$m_0 = \frac{m_{pl}}{1 - 1.1 \left(1 - \exp\left(\frac{-\dot{a}_{gc}\tau_m}{I_{sp}g_0}\right) \right) - \frac{\dot{a}_{gc}I_{sp}g_0}{2\eta_e} \left(k_e n_{Th} + \frac{\sigma_{TF}}{W\eta_{TF}} \right)} \quad (3.53)$$

3.4.3 Hybrid Sail

The initial mass breakdown for a hybrid sail is assumed as

$$m_0 = m_{pl} + m_{Tank} + n_{Th}(m_{inert} + m_{gimbal}) + m_{prop} + m_{TF} + m_S \quad (3.54)$$

Here the gimbal mass m_{gimbal} for each engine is assumed to be 30% of the inert mass of the thruster system m_{inert} [32]. A gimbal is required to actuate the thruster relative to the sail assembly to maintain equilibrium. With a given m_0 , the propellant mass m_{prop} required to maintain the artificial equilibrium for a mission life τ_m can be calculated using the algorithms described in section 3.2.2. In Eq. (3.54) for m_{Tank} , m_{inert} and m_{TF} , the same approximate relations for the pure SEP system

given in Eq. (3.50) are assumed. However, for a given m_0 , the maximum thrust level is replaced by $\mathcal{T}_{max} = m_0 a_T(\alpha^*(0))$ in Eq. (3.52) and moreover Eq. (3.51) is divided by $\cos(\alpha^*(0))$, to calculate m_{inert} and m_{TF} respectively since the TFSC is attached to the sail and so is not Sun-pointing. Also, with a given m_0 , the sail mass m_S in Eq.(3.54) is given by

$$m_S = \sigma_S A_T = \sigma_S \left(\frac{m_0 \beta_0}{\sigma^*} \right) \quad (3.55)$$

In summary, for a given β_0 , τ_m , σ_S and an initial guess m_0 , the payload mass m_{pl} can be calculated using Eq. (3.54). A shooting method [6] is used to determine m_0 for different artificial equilibria along the polar axis so that the payload mass m_{pl} becomes 100 kg.

Figure 3.10 shows that the minimum initial mass m_0 along the polar axis is located at 0.0145 AU for a pure SEP, at 0.025 AU for a pure sail with sail film reflectivity $\tilde{r}_S = 0.9$, and at 0.0183 AU for a hybrid sail with $\beta_0 = 0.03$. For the pure SEP system, the minimum m_0 at 0.0145 AU is due to the minimum a_{gc} at 0.0145 AU (see Fig. 3.9). For a pure sail, the minimum is shifted to 0.025 AU due to the variation of SRP acceleration with α . For a hybrid sail, the location for minimum m_0 depends upon the minimum location of $a_T(\alpha^*(0))$ (see Figs. 3.9 and 3.10). Figures 3.10(a-c) also show the dependance of m_0 for the pure sail and hybrid sail systems with the variation of the sail assembly loading. The sail assembly loading of 15 g/m², 10 g/m² and 5 g/m² may be assumed for near, mid-term and far-term sails [32]. Figure 3.10a shows that for a near-term sail assembly loading of 14.1 g/m² equal to that of the Geostorm mission [93], the minimum initial mass m_0 for a pure SEP (with propellant mass 295 kg, maximum power level of 1.5 kW) along polar axis is equal to 500 kg (the effect of SRP on TFSC area is neglected for a pure SEP case), whereas for a pure sail (with sail length of 180 m) is 557 kg, and the hybrid sail clearly has a lower initial mass of 375 kg (with propellant mass 115 kg, sail length of 85 m and maximum power level of 732 W) at an optimum distance of 0.0183 AU, and thus a lower launch mass and higher

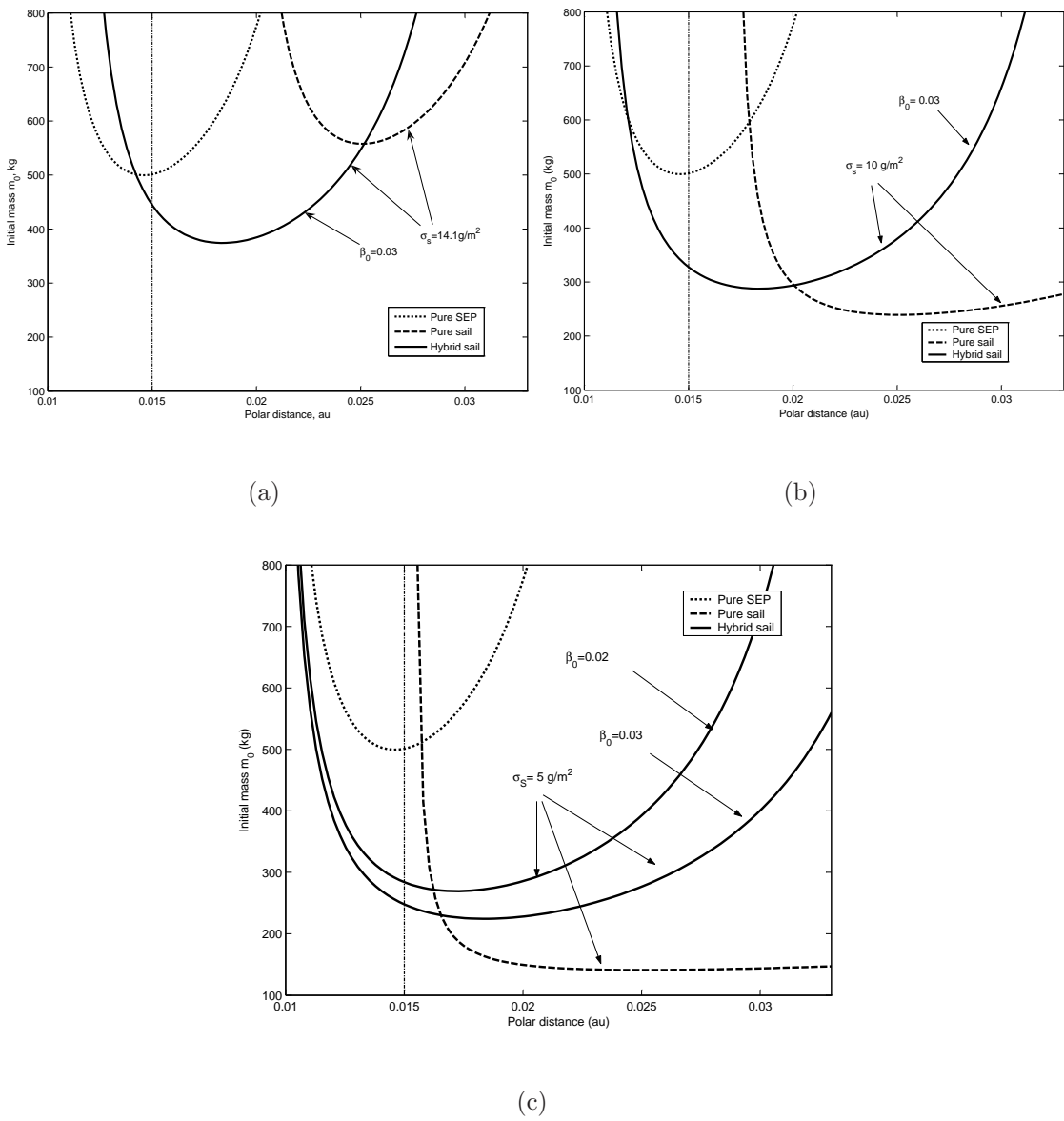


Figure 3.10: Spacecraft initial (wet) mass required for an AEP for a 100 kg payload for a polar observer mission (above L_1). Five-year mission lifetime is considered for a pure SEP and hybrid sail. Initial mass variation for a pure and hybrid sail with sail assembly loading equal to a) 14.1 g/m^2 b) 10 g/m^2 and c) 5 g/m^2 are also shown. The vertical line shows that the pure sail cannot be placed along the polar axis below 0.015 AU.

Table 3.1: Mass breakdown for three different propulsion systems for a spacecraft stationed at a polar distance 0.01831 AU along the polar axis above L_1 . A fixed payload mass and fixed mission life of 5 years is assumed in the case of pure SEP and the hybrid sail.

Subsystem	Pure sail ^a mass budget, kg	Pure SEP mass budget, kg	Hybrid sail ^a mass budget, kg
m_{pl}	100	100	100
m_{prop}	—	376	92
m_{inert} (1st thruster)	—	51.5 ^b	11.3 ^b
m_{gimbal}	—	—	3.4
m_{Tank}	—	37.5	9.2
m_{TF}	—	4.5	1.2
m_{inert} (2nd thruster)	—	51.5	14.7 ^c
m_S	360	—	56.5
m_0 (total initial mass)	460	621	288

^a Pure sail length = 190 m and hybrid sail length = 75 m; sail assembly loading $\sigma_S = 10$ g/m².

^b $P_{e,max} = 564$ W for hybrid sail, $P_{e,max} = 2.58$ kW for pure SEP

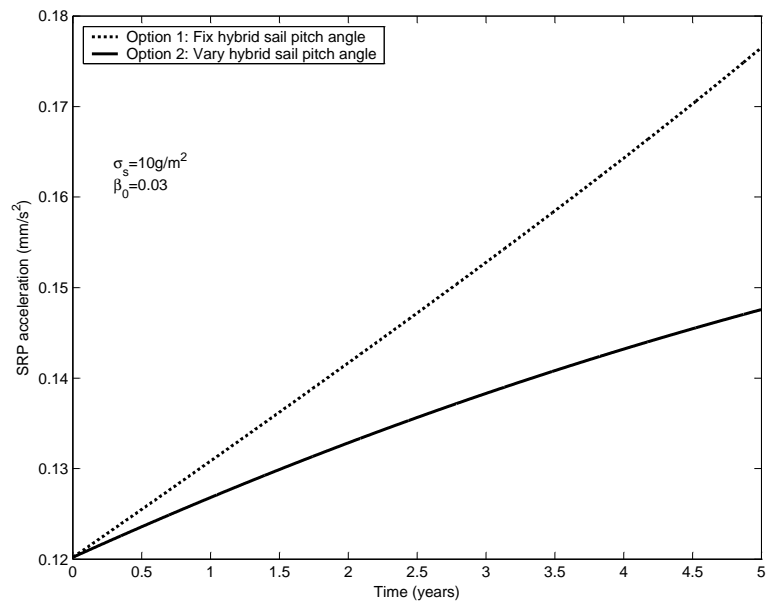
^c Also includes gimbal mass

resolution for imaging than the pure sail. Figure 3.10c shows, that for a far-term sail assembly loading of 5 g/m², the hybrid sail has a significant improvement in payload fraction below 0.015 AU along the polar axis as compared with the pure SEP, and also higher resolution for imaging than a pure sail.

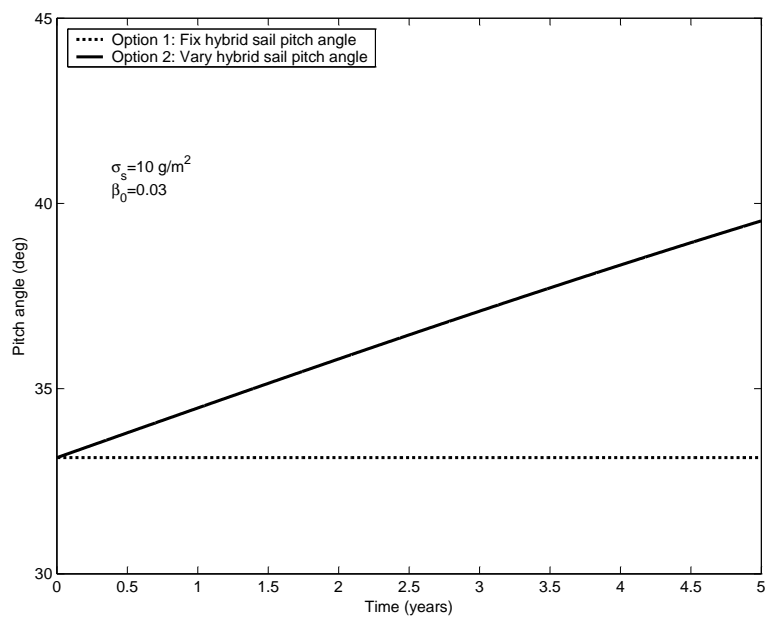
Table 3.1 shows the initial mass breakdown with a mid-term sail assembly loading, for station-keeping a 100 kg payload mass at a polar distance of 0.01831 AU (see Fig. 3.10b). The hybrid sail total initial mass m_0 at this AEP is less than that of the pure SEP and pure sail systems. The hybrid sail total mass is less than the total mass of the pure SEP system as the savings in propellant mass and inert

mass of the thruster system for the hybrid sail, totaling 389 kg, is greater than the additional penalty of the sail assembly mass $m_S = 56.5$ kg compared with the pure SEP. The smaller inert mass of the thruster system for the hybrid sail is due to the lower maximum power required as compared to the maximum power for a pure SEP thruster system. The hybrid sail total mass is less than the total mass of the pure sail as the savings from the sail mass for the hybrid sail, by reducing the sail length, is greater than the penalty of propellant and inert mass of the thruster system needed for the hybrid sail. Table 3.1 shows that the mass of TFSC area is small compared to the inert mass, tank and propellant of SEP system [54].

Figs. (3.11-3.12) shows the hybrid sail parameters during the mission life when it is in a static equilibrium with either of the two equilibria strategies (option 1 and option 2). Figure 3.11a shows the increase of SRP magnitude a_s due to the decrease of mass m during the mission life. For option 2, there is a slow variation in a_s due to the increase of the hybrid sail pitch angle $\alpha^*(t)$ as compared to the fixed pitch angle $\alpha^*(0)$ for option 1 (see Fig. 3.11b). Figures 3.12a and 3.12b show the required force and orientation of the SEP thruster system to maintain the equilibrium condition. Although the same orientation, 52.66 deg for this AEP, is required at the start of the mission in both options, there is less variation in the orientation of the ion thruster system relative to the sail normal for option 2. Option 2 is better than option 1 as the thruster plume does not interact with the sail film during the whole mission life (see Fig. 3.12b). Moreover, in option 2 less thrust is required during the whole mission life (see Fig. 3.12a) with fixed I_{sp} , which suggests less total propellant mass consumption, and hence less total initial mass m_0 . However, for both options, the ion thruster system must have the capability of throttling down, and a gimbal system is required to maintain equilibrium.

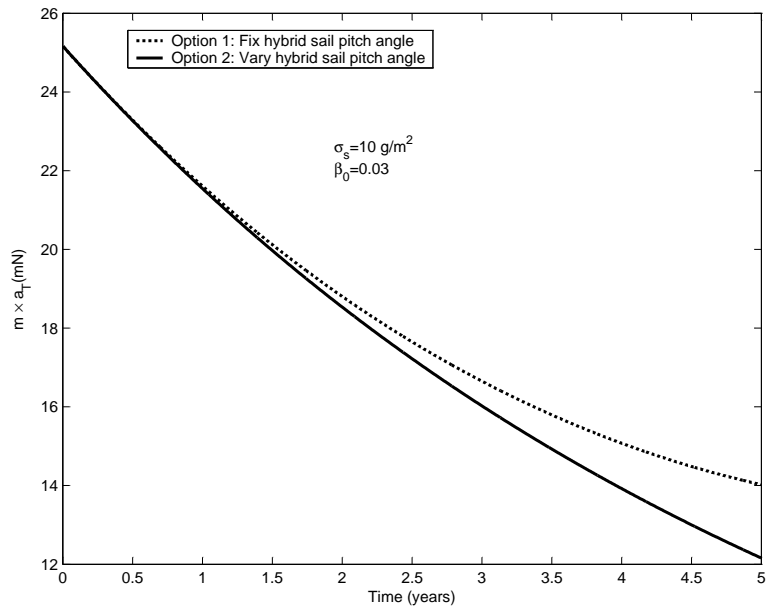


(a)

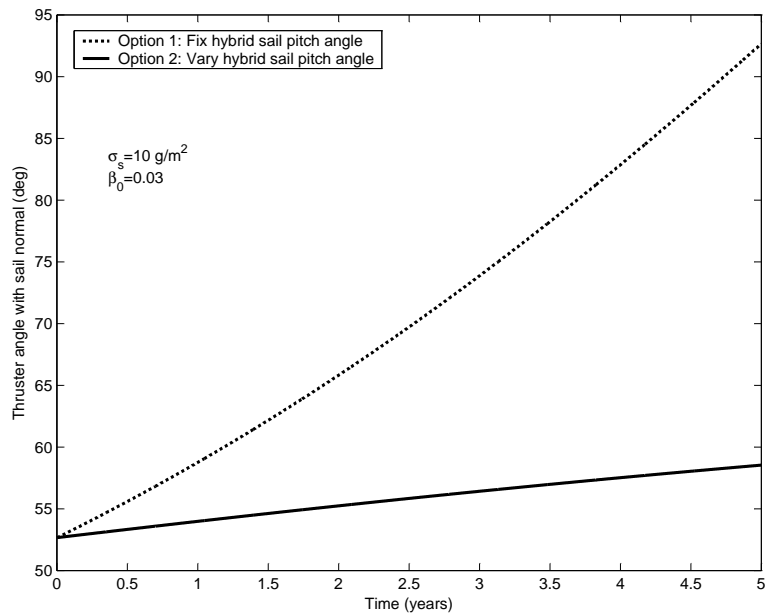


(b)

Figure 3.11: Hybrid sail during mission life stationed at polar distance 0.01831 AU along the polar axis above L_1 : a) SRP acceleration magnitude b) Pitch angle.



(a)



(b)

Figure 3.12: Hybrid sail during mission life stationed at polar distance 0.01831 AU along the polar axis above L_1 : (a) ion thruster force, and b) ion thruster firing angle with respect to the sail normal.

3.5 Conclusions

In this chapter a new concept to generate artificial equilibrium points by using a hybrid solar sail in the circular restricted three-body problem has been analysed. The key idea is that the required acceleration vector to keep the hybrid sail at an artificial equilibrium point is achieved by the vector sum of the solar radiation pressure acceleration and the solar electric propulsion acceleration vectors. We cast the problem to minimise the acceleration from the solar electric propulsion system (SEP) of the hybrid sail for a given sail lightness number. It is shown that the hybrid sail clock angle should be aligned with the clock angle of the required acceleration vector to minimise the acceleration from the SEP system. Finally, the minimisation problem for equilibrium reduces to numerically determining the optimum hybrid sail pitch angle. Notably, it is found that a hybrid sail can be in equilibrium in forbidden regions for a pure sail. A linear stability analysis shows that the artificial equilibrium points for the hybrid sail are unstable in general, apart from some region where the equilibria are marginally stable. Moreover, the time-varying parameter (mass variation) of the hybrid sail does not change the stability properties of the equilibria. It has been shown that the hybrid sail has a potential application of hovering above the L_1 point for real-time, low resolution images of the poles. The hybrid sail along the polar axis is found to have a lower sail length compared to a pure sail, and a lower propellant mass and maximum power level as compared with a pure SEP system. For a near term sail assembly loading (14.1 g/m^2), the hybrid sail for the polar observer mission clearly demonstrates a greater payload mass fraction. Furthermore, the hybrid sail can be used to obtain higher resolution images by hovering in a region which is inaccessible for the pure sail.

Chapter 4

Control of Hybrid Sail at an Equilibrium Point

In the previous chapter, the hybrid sail concept, originally proposed for orbital transfer is extended for use at equilibrium points, and an optimised hybrid sail thrust strategy used to show the feasibility of the hybrid sail in terms of lower initial spacecraft mass for the polar observation mission. However, artificial equilibrium points (AEPs) along the Earth's polar axis (the polar axis lies in Regions II and III of Fig. 3.7) are unstable. Therefore, active control is required to maintain the hybrid sail on unstable AEPs.

This chapter aims to stabilise the hybrid sail onto an unstable AEP. An optimal controller (time-varying Linear Quadratic Regulator (LQR)) is developed to show that equilibria for the hybrid sail can be made stable by using the solar electric propulsion thruster gimbal angles as control parameters, while keeping the large sail in a fixed attitude during the mission lifetime.

Before describing the time varying LQR-controller for the hybrid sail in section 4.2, it is first shown in the next section that the hybrid sail is controllable using the SEP system. The controllability of a hybrid sail (i.e., controllability of a time-varying system [39]) on the finite time-interval $[t_0, t_f]$ means that there exist gimbal angle variations which will drive the hybrid sail from any initial state at t_0

to the equilibrium point at time t_f .

4.1 Controllability of the Hybrid Sail

In this section the controllability of the hybrid sail is demonstrated by gimbaling the SEP thruster while keeping the sail attitude fixed at $\alpha^*(0)$ during the mission life.

The nonlinear dynamics of a hybrid sail in a synodic rotating frame F_a (see Eq. (3.11)) can be re-written as

$$\begin{aligned}\frac{d\mathbf{r}}{dt} &= \mathbf{v} \equiv \mathbf{f}_1 \\ \frac{d\mathbf{v}}{dt} &= -2\boldsymbol{\omega} \times \mathbf{v} - \nabla U(\mathbf{r}) + \mathbf{a}_S + \mathbf{a}_T \equiv \mathbf{f}_2\end{aligned}\quad (4.1)$$

The SEP thruster(s) are mounted on a two degree-of-freedom gimbal allowing pitch and yaw attitude control as shown in Fig. 4.1. The thrust acceleration from the SEP system in Eq. (4.1) can then be written explicitly as

$$\mathbf{a}_T = a_T \mathbf{u}_T^a = a_T \mathbf{C}_{b/a}^T(\mathbf{r}_0) \mathbf{u}_T^b \quad (4.2)$$

where $\mathbf{C}_{b/a}^T$ is the transpose of the matrix given in Eq. (3.15), and

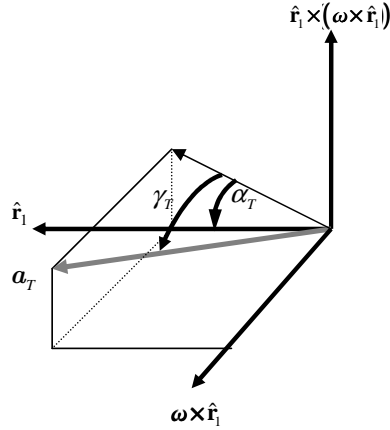


Figure 4.1: SEP system pointing angles α_T and γ_T defined in frame F_b allowing pitch and yaw control. The frame F_b is defined in section 3.2.

$$\mathbf{u}_T^b = \begin{bmatrix} \cos \gamma_T \cos \alpha_T \\ \sin \gamma_T \\ \cos \gamma_T \sin \alpha_T \end{bmatrix}$$

For simplicity consider the nonlinear system in Eq. (4.1) [with Eq.(4.2)] as:

$$\dot{\mathbf{X}}(t) = \mathbf{f}(\mathbf{X}(t), \mathbf{u}(t)) \quad (4.3)$$

where $\mathbf{X} = [\mathbf{r} \quad \mathbf{v}]^T$ is the state vector and $\mathbf{u}(t) = (\alpha_T, \delta_T)$ is an input vector which consists of the gimbal angles. These gimbal angles $\mathbf{u}^*(t)$ vary during the mission life to maintain the equilibrium condition due to mass variation. Now linearise Eq. (4.3) around the nominal (equilibrium) solution, $[\mathbf{X}_e, \mathbf{u}^*(t)]$ that is $\mathbf{f}(\mathbf{X}_e, \mathbf{u}^*(t))=0$. Writing $\delta\mathbf{X}(t) = \mathbf{X}(t) - \mathbf{X}_e$ and $\delta\mathbf{u}(t) = \mathbf{u}(t) - \mathbf{u}^*(t)$, the linearised system can be expressed in the form

$$\delta\dot{\mathbf{X}}(t) = A(t)\delta\mathbf{X}(t) + B(t)\delta\mathbf{u}(t) \quad (4.4)$$

with

$$A(t) = \left[\frac{\partial \mathbf{f}}{\partial \mathbf{X}} \right]_{(\mathbf{X}_e, \mathbf{u}^*(t))} = \begin{pmatrix} \frac{\partial \mathbf{f}_1}{\partial \mathbf{r}} & \frac{\partial \mathbf{f}_1}{\partial \mathbf{v}} \\ \frac{\partial \mathbf{f}_2}{\partial \mathbf{r}} & \frac{\partial \mathbf{f}_2}{\partial \mathbf{v}} \end{pmatrix}_{(\mathbf{X}_e, \mathbf{u}^*(t))} = \begin{pmatrix} 0_{3 \times 3} & I_3 \\ K & \Omega \end{pmatrix}_{(\mathbf{X}_e, \mathbf{u}^*(t))} \quad (4.5)$$

where K and Ω are given in section 3.3, and

$$B(t) = \left[\frac{\partial \mathbf{f}}{\partial \mathbf{u}} \right]_{(\mathbf{X}_e, \mathbf{u}^*(t))} = \begin{pmatrix} \frac{\partial \mathbf{f}_1}{\partial \mathbf{u}} \\ \frac{\partial \mathbf{f}_2}{\partial \mathbf{u}} \end{pmatrix}_{(\mathbf{X}_e, \mathbf{u}^*(t))} = \begin{pmatrix} 0_{3 \times 1} & 0_{3 \times 1} \\ \frac{\partial \mathbf{a}_T}{\partial \alpha_T} & \frac{\partial \mathbf{a}_T}{\partial \gamma_T} \end{pmatrix}_{(\mathbf{X}_e, \mathbf{u}^*(t))} \quad (4.6)$$

and so $\delta\mathbf{u} = (\delta\alpha_T, \delta\gamma_T)$ provides the variation in SEP thrust pointing to correct for position and velocity errors.

If $(A(t), B(t))$ is controllable, then the linear time-varying system given in Eq. (4.4) can be stabilised about an unstable AEP \mathbf{r}_0 by varying the thruster orientation $\delta\mathbf{u}(t)$ around the reference orientation $\mathbf{u}^*(t)$. One of several known controllability tests states that a linear time-varying system is controllable on $[t_0, t_f]$ if and only if the following controllability Gramian $W(t_0, t_f)$ is nonsingular [83]

$$W(t_0, t_f) = \int_{t_0}^{t_f} \Phi(t_0, t)B(t)B^T(t)\Phi^T(t_0, t) dt \quad (4.7)$$

The controllability Gramian (a symmetric and positive definite matrix) can be easily computed by backward integration of the following matrix differential equations with final condition $W(t_f, t_f) = 0$ (a zero matrix) rather than by the definition given in Eq. (4.7)

$$\frac{dW(t, t_f)}{dt} = A(t)W(t, t_f) + W(t, t_f)A^T(t) - B(t)B^T(t) \quad (4.8)$$

If the controllability Gramian is invertible then the open-loop solution that has the least energy among all controls and takes an arbitrary initial condition $\delta\mathbf{X}(t_0)$ to the desired final state $\delta\mathbf{X}(t_f) = 0$ by time t_f is given by

$$\delta\mathbf{u}(t) = -B^T(t)\Phi^T(t_0, t)W^{-1}(t_0, t_f)\delta\mathbf{X}(t_0) \quad (4.9)$$

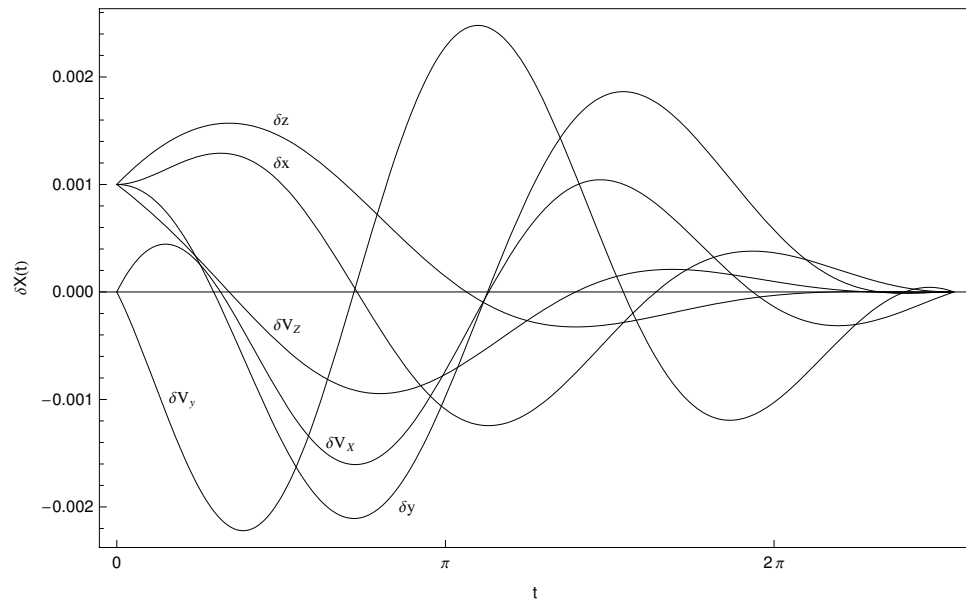
where $\Phi^T(t_0, t)$ is the state-transition matrix of $-A^T(t)$ [46]; i.e.,

$$\frac{d\Phi^T(t_0, t)}{dt} = -A^T(t)\Phi^T(t_0, t), \quad \Phi^T(t_0, t_0) = I \quad (4.10)$$

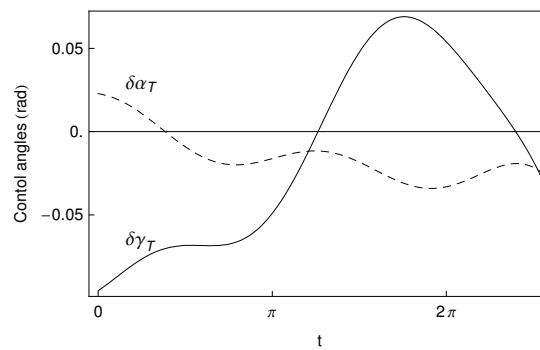
In this chapter $\mathbf{X}_e = (x_e, 0, z_e, 0, 0, 0)$ is chosen, and AEP $x_e = 0.9927$ AU and $z_e = 0.0167888$ AU which corresponds to the minimum mass hybrid sail at a polar distance of 0.018307 AU as shown in Fig. 3.10a. The hybrid sail pitch angle is fixed at $\alpha^*(0) = 33.13$ deg determined by minimising the SEP thrust acceleration at $t = 0$ as described in section 3.2.2.1. Fig. 4.2 shows that the SEP system (gimbal angles) can be used to stabilise the hybrid sail about this unstable AEP. States histories in Fig. 4.2 can be obtained substituting Eq. (4.9) in Eq. (4.4), and then integrating the resulting system for a given $\delta\mathbf{X}(0)$ and t_f . Note that the matrices $W(t_0, t_f)$ and $\Phi^T(t_0, t)$ in Eq. (4.9) are computed by integrating Eqs. (4.8) and (4.10) respectively.

4.2 Linear State-Feedback Control

In this section an optimal state time-varying feedback controller is described to control the hybrid sail about an unstable AEP \mathbf{r}_0 . In optimal control theory [56],



(a)



(b)

Figure 4.2: Open loop control: histories of (a) states and (b) control effort for initial condition $\delta \mathbf{X}(0) = [0.001, 0.001, 0.001, 0.0, 0.0, 0.001]$ and $t_f = 2.55\pi$.

a linear state feedback is sought

$$\delta \mathbf{u}(t) = -G(t)\delta \mathbf{X} \quad (4.11)$$

and choose $\delta \mathbf{u}$ to minimise

$$J = \frac{1}{2}\delta \mathbf{X}^T(t_f)S(t_f)\delta \mathbf{X}(t_f) + \frac{1}{2}\int_{t_0}^{t_f} (\delta \mathbf{X}^T Q \delta \mathbf{X} + \delta \mathbf{u}^T R \delta \mathbf{u}) dt \quad (4.12)$$

subject to the linear dynamical system given in Eq. (4.4) with $\delta \mathbf{X}(t_0) = \delta \mathbf{X}_0$. $S^T(t_f) = S(t_f) \geq 0$, $Q^T = Q \geq 0$ and $R^T = R > 0$ are selected to trade-off requirements on the magnitude of the state $\delta \mathbf{X}$ against requirements on the magnitude of the input $\delta \mathbf{u}$. The required optimal solution for the feedback gain $G(t)$ is given by

$$G_{opt}(t) = R^{-1}B^T(t)P(t) \quad (4.13)$$

where $P(t)$ is the positive semidefinite solution of the matrix differential Riccati equation

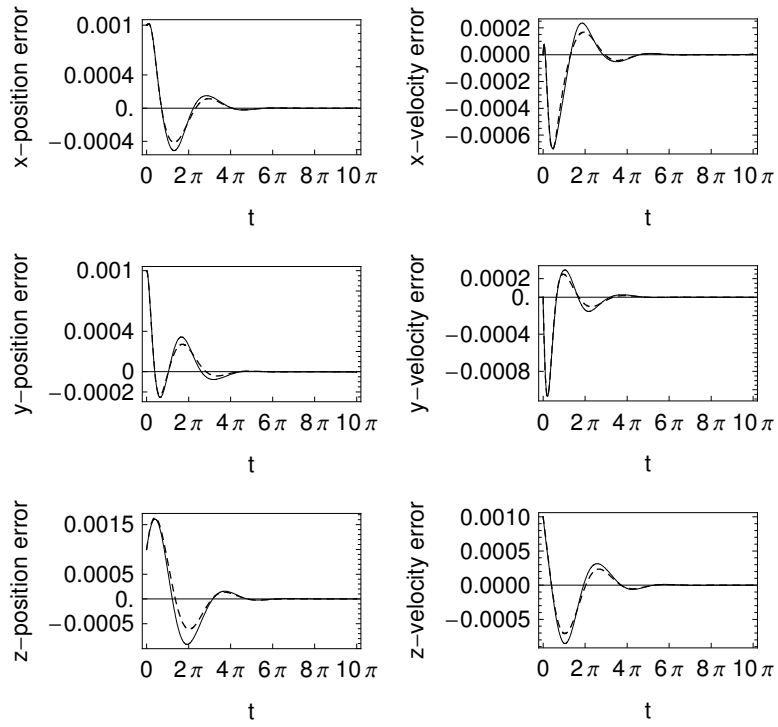
$$\begin{aligned} \frac{dP(t)}{dt} &= -A^T(t)P(t) - P(t)A(t) - Q \\ &+ PB(t)R^{-1}B^T(t)P(t), \quad P(t_f) = S(t_f) \end{aligned} \quad (4.14)$$

The control law given in Eq. (4.11) stabilises the linear system Eq. (4.4). However, the control law Eq. (4.11) will also work with the nonlinear system provided that the linear system is asymptotically and the perturbations are small. The linear control law Eq. (4.11) can be combined with Eq. (4.3), this yields the nonlinear controlled system as

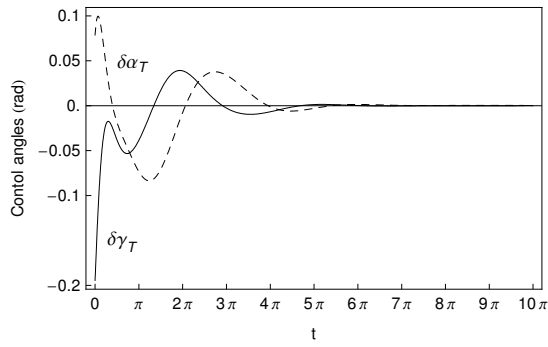
$$\dot{\mathbf{X}}(t) = \mathbf{f}(\mathbf{X}(t), \mathbf{u}^*(t) + \delta \mathbf{u}(t)) \quad (4.15)$$

In the neighborhood of the desired AEP the linear system dominates and trajectories are controlled. The question now reduces to how large is the domain of attraction.

The results for the optimal state-feedback controller (the dashed line is the linearised system of Eq. (4.4) and the solid line is the nonlinear system of Eq. (4.15)) are shown in Fig. 4.3 for the same injection errors as in Fig. 4.2. The control



(a)



(b)

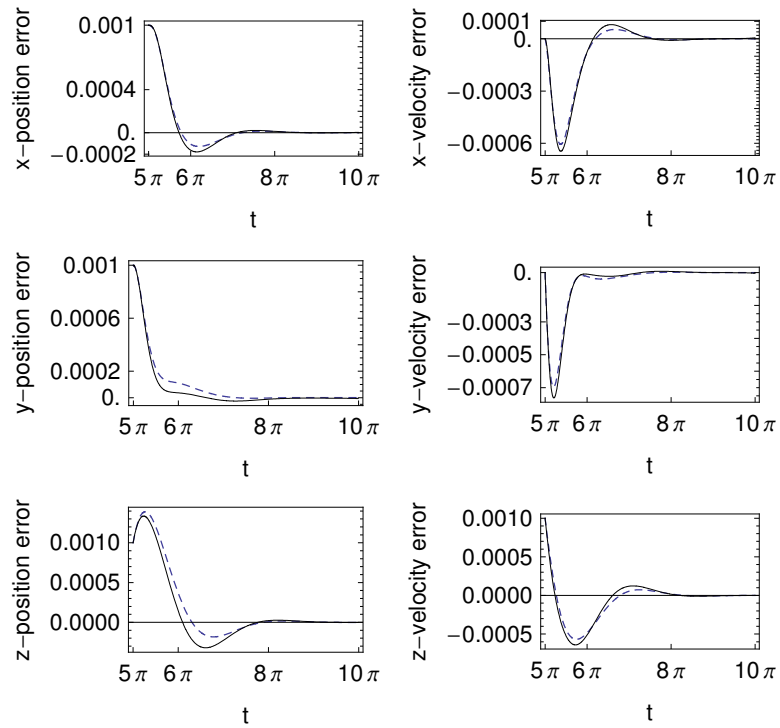
Figure 4.3: Finite horizon LQR control: histories of (a) states (the dashed line is the linear system, and the solid line is the nonlinear system) and (b) control effort for initial condition $\delta\mathbf{X}(0) = [0.001, 0.001, 0.001, 0.0, 0.0, 0.001]$ and $t_f = 10\pi$ (mission lifetime). Weighted matrices $S(t_f) = \rho_1 I_6 = 0_{6 \times 6}$, $Q = I_6$ and $R = \rho_2 I_2 = 10^{-4} I_2$ are chosen.

signal and state response settle to near zero in 4π (2 years) and the state deviation has a good response compared to Fig. 4.2 due to the weight matrix selection Q and R . Fig. 4.3b shows that the largest control signal magnitudes are applied during the initial time interval due to the maximum displacement of hybrid sail.

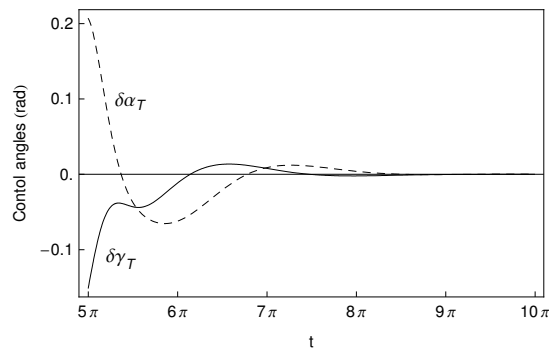
The hybrid sail mass decreases during the mission life due to the decrease of propellant mass. Two SEP thrusters are assumed in series for the whole mission life $t_f = 10\pi$ (5 years). The second thruster should start working at the middle of the mission life at $t = 5\pi$. If for some reason the state is perturbed, Fig. 4.4 shows that the hybrid sail is still stabilised about the AEP but with large control effort $\delta\alpha$ compared to Fig. 4.3. In Fig. 4.5, it is apparent that the maximum control angle deviation norm increases to 0.37 radians for $\delta\mathbf{X}(0) = [0.001, 0.001, 0.001, 0.001, 0.001, 0.001]$ in nondimensional units, which is equal to a position error of 150,000 km and velocity error of 29 m/s in each direction. In summary, the stability of the hybrid sail by the SEP system is robust to large injection errors.

4.3 Conclusions

A simple strategy of controlling the orientation of the SEP gimbal (gimbal angles) is shown to stabilise the hybrid sail, while keeping the large sail at an optimum fixed attitude during the mission lifetime. For an injection error of 0.001 in initial positions and initial velocities (which in dimensional units corresponds to 29 m/s velocity error and 150,000 km position error), the hybrid sail converges to the desired equilibrium point. The control angles settle down to reference values in 4π (2 years). In short, the stability of the hybrid sail using the SEP system alone is robust to injection errors in positions and velocities.

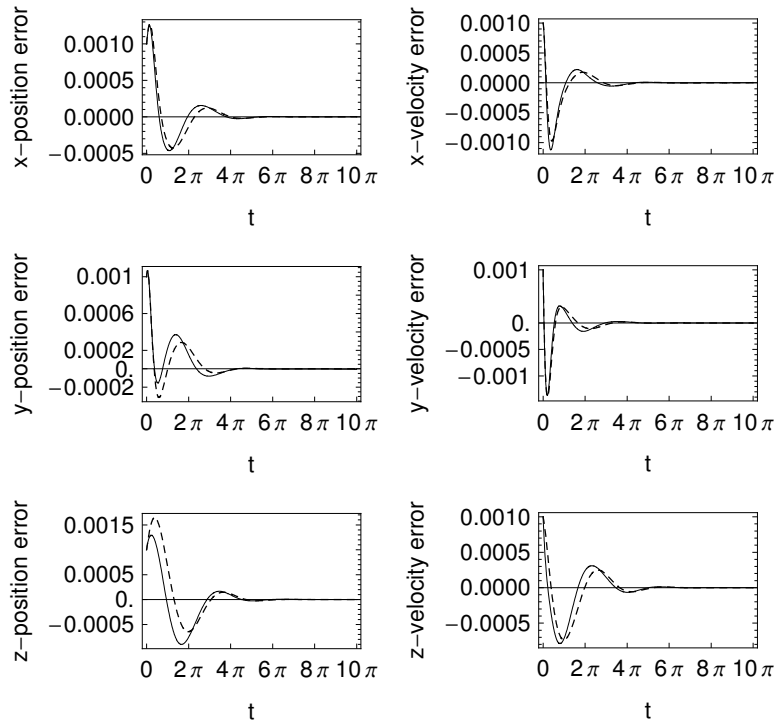


(a)

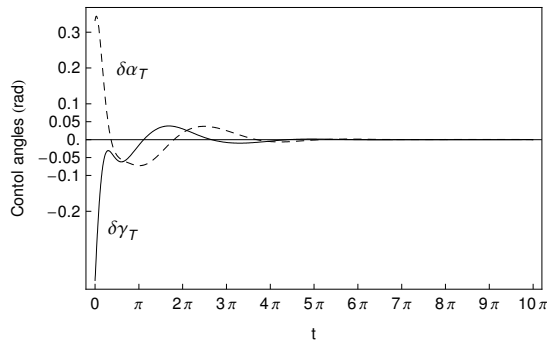


(b)

Figure 4.4: Finite horizon LQR control: histories of (a) states (the dashed line is the linear system, and the solid line is the nonlinear system) and (b) control effort for initial condition $\delta\mathbf{X}(t_0) = [0.001, 0.001, 0.001, 0.0, 0.0, 0.001]$ perturbed at $t_0 = 5\pi$ and $t_f = 10\pi$ (mission lifetime). Weighting matrices are $S(t_f) = \rho_1 I_6 = 0_{6 \times 6}$, $Q = I_6$ and $R = \rho_2 I_2 = 10^{-4} I_2$.



(a)



(b)

Figure 4.5: Finite horizon LQR control: histories of (a) states (the dashed line is the linear system, and the solid line is the nonlinear system) and (b) control effort for initial condition $\delta\mathbf{X}(0) = [0.001, 0.001, 0.001, 0.001, 0.001, 0.001]$ and $t_f = 10\pi$ (mission lifetime). Weighting matrices are $S(t_f) = \rho_1 I_6 = 0_{6 \times 6}$, $Q = I_6$ and $R = \rho_2 I_2 = 10^{-4} I_2$.

Chapter 5

Levitated Geostationary Orbits

In this chapter the Earth-sail system is considered as a two-body problem to investigate light-levitated orbits (i.e., displaced NKO) in an Earth rotating frame at a geostationary point. The chapter aims to prove the assertion by Forward [29] that light-levitated geostationary orbits exist, possibly to increase the number of available slots for geostationary communications satellites. Although, in the literature [26,91], it is claimed that such light-levitation is not possible due to the component of the sail acceleration parallel to the Earth's equatorial plane. In this chapter, this parallel component is used to generate a periodic orbit, thus a NKO for an observer in the Earth fixed rotating frame at a geostationary point exists. However, it is shown that only modest displacements are possible above the Earth's equatorial plane. Light-levitated orbit applications to Space Solar Power are also considered.

It is first shown from linear analysis that such NKO exist. The nonlinear analysis is adopted from Ozimek et al. [58] who find displaced periodic orbits for continuous lunar south pole coverage from a collocation scheme using (partly) a numerical Jacobian matrix and a minimum elevation angle constraint. However, levitated geostationary periodic orbits are computed in the nonlinear analysis using an analytical Jacobian and a box around the linearised NKO as a path constraint. While the existence of levitated geostationary orbits is demonstrated, as proposed

by Forward [27, 28], only modest displacements are found due to the large in-plane component of sail acceleration. Recently, Takeichi et al. [76] proposed a solar power satellite system in which reflectors orbiting in levitated geostationary orbits (typically at ± 2 km levitation) are used to concentrate sunlight onto microwave generator-transmitters orbiting separately at geostationary orbit and in-between the reflectors. It is shown that these orbits are feasible.

The chapter is organised as follows: In section 5.1, the nonlinear equations of motion in the Earth rotating frame are defined for a solar sail above the Earth's equatorial plane with the Sun-line assumed to be in the Earth's equatorial plane. In section 5.2 the solution to the linearised equations of motion around a geostationary point are considered. It is found that NKO exist at linear order. This linear solution acts as an initial guess for finding NKO with the nonlinear equations of motion. In section 5.3 a collocation scheme is described which adjusts the sail orientation for handling the nonlinearities of the Earth's gravity around the geostationary point to give displaced periodic solutions to the full nonlinear non-autonomous system. In section 5.4 a linear analysis is conducted at the summer and winter solstices, when the Sun-line is at maximum excursion from the Earth's equatorial plane. In section 5.5 a collocation scheme is used to generate displaced periodic orbits at the summer solstice. In section 5.6 light-levitated geostationary orbits for the reflectors of solar power satellite systems are shown. In section 5.7, the hybrid sail and pure electric propulsion are investigated to generate such displaced NKO (by generating an artificial equilibrium point in the Earth fixed rotating frame).

5.1 Equations of Motion

A geostationary satellite (shown as geostationary point in Fig. 5.1) orbits the Earth in the equatorial plane at the Earth's rotational angular velocity ω_e , i.e., the geostationary point moves with an orbital period equal to one sidereal day

($\tau_e = 23 \text{ h}, 56 \text{ min}, 4.1 \text{ s} = 86164.1 \text{ s}$). If $\mu_g = 3986004.418 \times 10^8 \text{ m}^3/\text{s}^2$ denotes the gravitational parameter of the Earth, then the radius r_{gs} of the geostationary point follows from

$$\sqrt{\mu_g/r_{gs}^3} = \frac{2\pi}{\tau_e} = \omega_e \tag{5.1}$$

with the result that $r_{gs} = 42164.1696 \text{ km}$. Consider two coordinate systems, Earth-

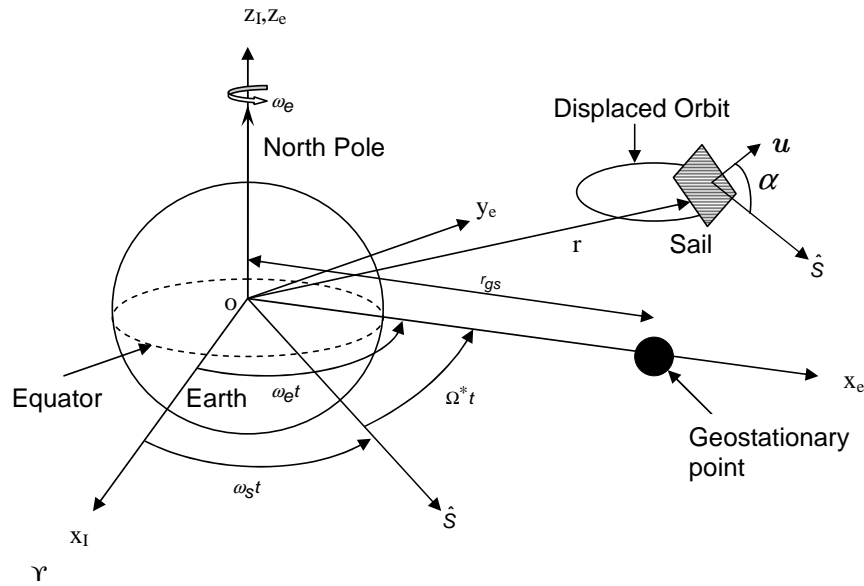


Figure 5.1: Two coordinate systems ECI (x_I, y_I, z_I) and ECEF (x_e, y_e, z_e) are shown. A solar sail on a displaced orbit above the equatorial plane around a geostationary point at r_{gs} , where the sun line \hat{S} is assumed to be in the Earth equatorial plane.

centred inertial (ECI) and Earth-centred, Earth-fixed (ECEF) with common origin ‘o’ at the Earth’s center of mass as shown in Fig. 5.1. The ECI system is an inertial frame with axes x_I, y_I in the equatorial plane and the z_I -axis is directed along the Earth’s spin axis. Furthermore, the x_I -axis is aligned with the vernal equinox. The ECEF system is a rotating frame which is defined by the rotating Earth with axes x_e, y_e in the Earth’s equatorial plane and z_e is directed along the Earth’s spin axis. The angular velocity of this frame is therefore $\boldsymbol{\omega}_e = \omega_e \hat{z}_e$. In addition, the x_e -axis points to the geostationary point and is aligned with the x_I axis at $t = 0$. The units are chosen to set the gravitational parameter μ_g , the distance between the center of the Earth and the geostationary point r_{gs} and the magnitude

of the angular velocity of the rotating frame ω_e to be unity. The unit reference acceleration and unit reference time are then given by

$$a_r = \omega_e^2 r_{gs} = 0.224208 \text{ m/s}^2 \quad (5.2)$$

$$\tau_r = \frac{\tau_e}{2\pi} \text{ sec} \quad (5.3)$$

In this chapter, an ideal solar sail and a spherically symmetric Earth are assumed. Thus, the nondimensional equation of motion in the ECEF system is given by

$$\frac{d^2 \mathbf{r}}{dt^2} + 2\boldsymbol{\omega}_e \times \frac{d\mathbf{r}}{dt} + \nabla \mathcal{U} = \mathbf{a}_{SS} \quad (5.4)$$

where $\mathbf{r} = (x, y, z)^T$ is the position vector of the solar sail with respect to the centre of the Earth in the ECEF frame. The two-body pseudo-potential \mathcal{U} is defined as

$$\mathcal{U} = \mathcal{V} + \varphi$$

where \mathcal{V} is the potential due to the Earth's gravity and φ is the potential due to the centrifugal force in the rotating frame which are given by

$$\mathcal{V} = -1/r \quad (5.5)$$

$$\varphi = -(x^2 + y^2)/2$$

The solar radiation pressure \mathbf{a}_{SS} in Eq. (5.4) is defined by

$$\mathbf{a}_{SS} = a_0 (\hat{\mathbf{S}}(t) \cdot \mathbf{u})^2 \mathbf{u}$$

where a_0 is the sail characteristic acceleration, \mathbf{u} is the sail normal unit vector, and $\hat{\mathbf{S}}(t)$ is the unit-vector in the direction of the Sun-line. Since the objective is to compensate the neglected parallel component of the sail acceleration, so as a starting point the Sun-line will be assumed in the Earth's equatorial plane (which is acceptable in autumn/spring equinoxes only). However, in winter/summer solstice the Sun-line will be assumed 23.5 degree above/below the Earth's equatorial plane (see section 5.4). Now, if the Sun-line direction is assumed to be in the Earth's

equatorial plane, then $\hat{\mathbf{S}}(t)$ is given by

$$\hat{\mathbf{S}}(t) = \begin{pmatrix} \cos(\Omega^*t) \\ -\sin(\Omega^*t) \\ 0 \end{pmatrix} \quad (5.6)$$

where Ω^* is the nondimensional angular velocity of the ECEF-frame relative to the Sun-line and calculated using

$$\Omega^* = \frac{\omega_e - \omega_s}{\omega_e} \quad (5.7)$$

where $\omega_s = 2\pi/(365.25 \times 86400)$ rad/s is the angular velocity of the Sun-line with respect to the inertial frame. Fig. 5.2 describes the sail normal \mathbf{u} using two angles:

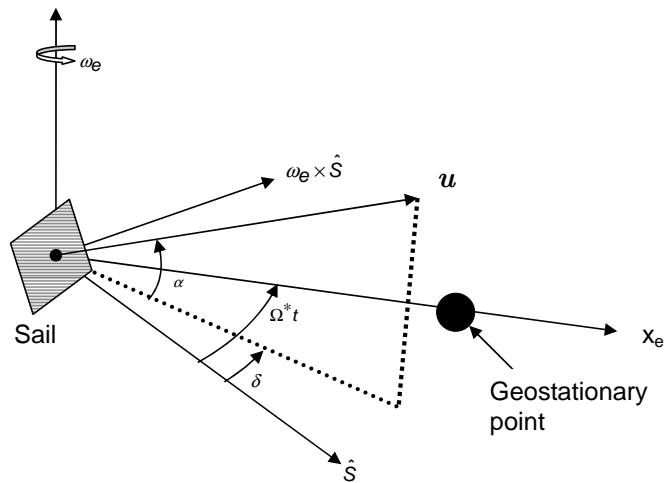


Figure 5.2: The sail pitch α is defined with respect to the Earth equatorial plane, while the yaw angle δ is defined with respect to the Sun-line in the equatorial plane, where the Sun-line $\hat{\mathbf{S}}$ is in the equator plane.

the sail pitch angle α (out of the equatorial plane) and the sail yaw angle δ (in the equatorial plane). Then, the expression for \mathbf{u} in the ECEF-frame is then given by

$$\mathbf{u} = \begin{pmatrix} \cos \alpha \cos(\Omega^*t - \delta) \\ -\cos \alpha \sin(\Omega^*t - \delta) \\ \sin \alpha \end{pmatrix} \quad (5.8)$$

Furthermore, the sail attitude is constrained such that $\hat{\mathbf{S}}(t) \cdot \mathbf{u} \geq 0$, so that the solar radiation pressure acceleration can never be directed towards the Sun ($-90^\circ < \alpha < +90^\circ$). Thus, Eq. (5.4) is nonlinear due to the Earth's gravity ∇V , and nonautonomous system due to the Sun-line direction $\hat{\mathbf{S}}(t)$ changing with time in the rotating ECEF-frame.

5.2 Linearised Equations

In this section, the dynamics of the solar sail in the neighborhood of the geostationary point at $\mathbf{r}_{gs} = (x_e, y_e, z_e)^T = (1, 0, 0)^T$ is investigated. Perturbing Eqs. (5.4) such that $\mathbf{r} \rightarrow \mathbf{r}_{gs} + \delta\mathbf{r}$, it can be seen that

$$\frac{d^2\delta\mathbf{r}}{dt^2} + 2\boldsymbol{\omega}_e \times \frac{d\delta\mathbf{r}}{dt} + \nabla\mathcal{U}(\mathbf{r}_{gs} + \delta\mathbf{r}) = \mathbf{a}_{SS}(\mathbf{r}_{gs} + \delta\mathbf{r}) \quad (5.9)$$

where $\delta\mathbf{r} = (\xi, \eta, \zeta)^T$ denotes a small displacement from the geostationary point in the (x_e, y_e, z_e) directions. Now, since $\nabla U(\mathbf{r}_{gs}) = 0$, and $\frac{\partial \mathbf{a}_{SS}}{\partial \mathbf{r}} = 0$ (the solar radiation field is assumed uniform), expanding in a Taylor series of each term about \mathbf{r}_{gs} in Eq. (5.9) and retaining only the first order term in $\delta\mathbf{r}$, it can be seen that

$$\frac{d^2\delta\mathbf{r}}{dt^2} + 2\boldsymbol{\omega}_e \times \frac{d\delta\mathbf{r}}{dt} + \mathbf{K}\delta\mathbf{r} = \mathbf{a}_{SS} \quad (5.10)$$

where the matrix \mathbf{K} is the partial derivatives of the pseudo-potential given by

$$\mathbf{K} = \left. \frac{\partial \nabla \mathcal{U}}{\partial \mathbf{r}} \right|_{\mathbf{r}=\mathbf{r}_{gs}} = \begin{pmatrix} U_{xx}^0 & 0 & 0 \\ 0 & U_{yy}^0 & 0 \\ 0 & 0 & U_{zz}^0 \end{pmatrix} \quad (5.11)$$

where U_{xx}^0, U_{yy}^0 and U_{zz}^0 are evaluated at the geostationary point. The sail attitude is fixed such that \mathbf{u} points along the Sun-line but is pitched at an angle α only. Substituting $\delta = 0$ in Eq. (5.8), Eq. (5.10) can then be written in component form

as

$$\frac{d^2\xi}{dt^2} - 2\frac{d\eta}{dt} + U_{xx}^0\xi = a_0 \cos^3 \alpha \cos(\Omega^*t) = a_\xi \quad (5.12)$$

$$\frac{d^2\eta}{dt^2} + 2\frac{d\xi}{dt} + U_{yy}^0\eta = -a_0 \cos^3 \alpha \sin(\Omega^*t) = a_\eta \quad (5.13)$$

$$\frac{d^2\zeta}{dt^2} + U_{zz}^0\zeta = a_0 \cos^2 \alpha \sin \alpha = a_\zeta \quad (5.14)$$

Equations (5.12-5.14) define the linearised model for the forced nonlinear system defined by Eq. (5.4). If the input $\mathbf{a}_{SS} = (a_\xi, a_\eta, a_\zeta)^T$ does not drive the system very far from equilibrium, then the linearised model is a valid representation of Eq. (5.4), as the system is then operating in the linear range.

The solution for the uncoupled out-of-plane equation of motion Eq. (5.14) is given by

$$\zeta = \left(\zeta^0 - \frac{a_0 \cos^2 \alpha \sin \alpha}{U_{zz}^0} \right) \cos(\sqrt{U_{zz}^0}t) + \frac{a_0 \cos^2 \alpha \sin \alpha}{U_{zz}^0} \quad (5.15)$$

Therefore, the motion along ζ is a periodic oscillation at an out-of-plane equatorial distance $a_0 \cos^2 \alpha \sin \alpha / U_{zz}^0$. To remove the periodic oscillation, the initial out-of-plane equatorial distance is chosen as

$$\zeta^0 = \frac{a_0 \cos^2 \alpha \sin \alpha}{U_{zz}^0} = \frac{a_\zeta}{U_{zz}^0} \quad (5.16)$$

and so that the sail then remains at this distance. Eq. (5.16) shows that for a fixed ζ^0 , the gravitational acceleration along the z_e -axis (i.e., $\zeta^0 U_{zz}^0$) must be balanced by two parameters a_0 and the pitch angle α . For fixed ζ^0 , the sail characteristic acceleration a_0 can be minimised for an optimal choice of pitch angle determined by

$$\begin{aligned} \frac{d \cos^2 \alpha \sin \alpha}{d\alpha} &= 0 \\ \alpha^* &= \tan^{-1}(2^{-1/2}) \\ \alpha^* &= 35.264^\circ \end{aligned} \quad (5.17)$$

The autonomous (unforced) coupled Eqs. (5.12-5.13) have an eigenvalue spectrum $(\pm i, 0, 0)$. An in-plane solution of Eqs. (5.12-5.13) can be assumed that is

periodic with the same frequency as the sail forcing Ω^* in the rotating frame, that is

$$\begin{aligned}\xi &= A_\xi \cos(\Omega^*t) + B_\xi \sin(\Omega^*t) \\ \eta &= A_\eta \cos(\Omega^*t) + B_\eta \sin(\Omega^*t)\end{aligned}\quad (5.18)$$

Substituting Eq. (5.18) in the Eqs. (5.12-5.13) and equating the coefficients of $\cos(\Omega^*t)$ and $\sin(\Omega^*t)$, the following linear equations for A_ξ , A_η , B_ξ and B_η are obtained

$$\begin{pmatrix} U_{xx}^0 - \Omega^{*2} & 0 & 0 & -2\Omega^* \\ 0 & 2\Omega^* & U_{xx}^0 - \Omega^{*2} & 0 \\ 0 & -\Omega^{*2} + U_{yy}^0 & 2\Omega^* & 0 \\ -2\Omega^* & 0 & 0 & -\Omega^{*2} + U_{yy}^0 \end{pmatrix} \begin{pmatrix} A_\xi \\ A_\eta \\ B_\xi \\ B_\eta \end{pmatrix} = \begin{pmatrix} a_0 \cos^3 \alpha \\ 0 \\ 0 \\ -a_0 \cos^3 \alpha \end{pmatrix}\quad (5.19)$$

so that the coefficients of the particular solution which define the size of the orbit are given by

$$\begin{aligned}A_\xi &= \frac{\sqrt{a_\xi^2 + a_\eta^2}(U_{yy}^0 - 2\Omega^* - \Omega^{*2})}{\Omega^{*4} - \Omega^{*2}(4 + U_{yy}^0 + U_{xx}^0) + U_{xx}^0 U_{yy}^0} = -551.131a_p \\ A_\eta &= 0 \\ B_\xi &= 0 \\ B_\eta &= \frac{-A_\xi(\Omega^{*2} + 2\Omega^* - U_{xx}^0)}{(\Omega^{*2} + 2\Omega^* - U_{yy}^0)} = -2.0036A_\xi = 1104.27a_p\end{aligned}\quad (5.20)$$

where $a_p = \sqrt{a_\xi^2 + a_\eta^2} = a_0 \cos^3 \alpha$. Therefore, the solution to Eqs. (5.12-5.14) can be written as

$$\begin{aligned}\xi(t) &= A_\xi \cos(\Omega^*t) \\ \eta(t) &= B_\eta \sin(\Omega^*t) \\ \zeta(t) &= \zeta^0\end{aligned}\quad (5.21)$$

The component of the sail acceleration parallel to the equatorial plane $a_p = a_0 \cos^3 \alpha$ determines the semi-major and semiminor axes (A_ξ, B_η) of the elliptic

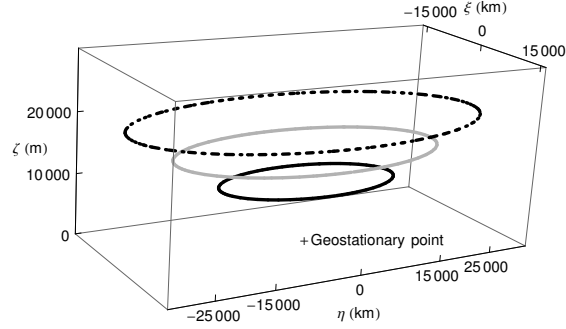


Figure 5.3: Displaced solar sail orbits of period $T = 2\pi/\Omega^*$ around a geostationary point. The solar sails are pitched at $\alpha^* = 35.264^\circ$ on each orbit. For the solid-line orbit at $\zeta^0 = 0.000237168$ (10 km), the gray-line orbit at $\zeta^0 = 0.000355752$ (15 km) and the dashed-line orbit at $\zeta^0 = 0.000474336$ (20 km), the sails require a characteristic acceleration $a_0^* = 0.000616181$ (0.138 mms^{-2}), $a_0^* = 0.000924272$ (0.207 mms^{-2}) and $a_0^* = 0.00123236$ (0.276 mms^{-2}) respectively.

displaced orbit (see Eq. 5.20) while the component out of the equatorial plane $a_\zeta = a_0 \cos^2 \alpha \sin \alpha$ determines the displacement above the equatorial plane (see Eq. 5.16).

Figure 5.3 shows displaced elliptic orbits at displacement ζ^0 (i.e., along the z_e axis) corresponding to 10 km, 15 km, and 20 km. The three sails have a minimum sail characteristic acceleration a_0^* on the displaced orbits corresponding to the optimum sail pitch angle α^* . Figure 5.3 shows that orbits with large displacements ζ^0 above the Earth's equatorial plane need large a_0^* as expected. However, the size A_ξ, B_η of the displaced orbits also increases as the in-plane sail acceleration a_p increases.

Figure 5.4a shows that for a sail with characteristic acceleration $a_0 > a_0^*$, for a given ζ^0 , then two displaced orbits can be generated corresponding to two specific sail pitch angles. These pitch angles α_1 and α_2 can be determined by solving Eq. (5.16) numerically. Thus, for a sail with $a_0 > a_0^*$ at a given ζ^0 , a displaced orbit is parameterised by a_0 and α . Fig. 5.4a also shows that for a larger pitch angle

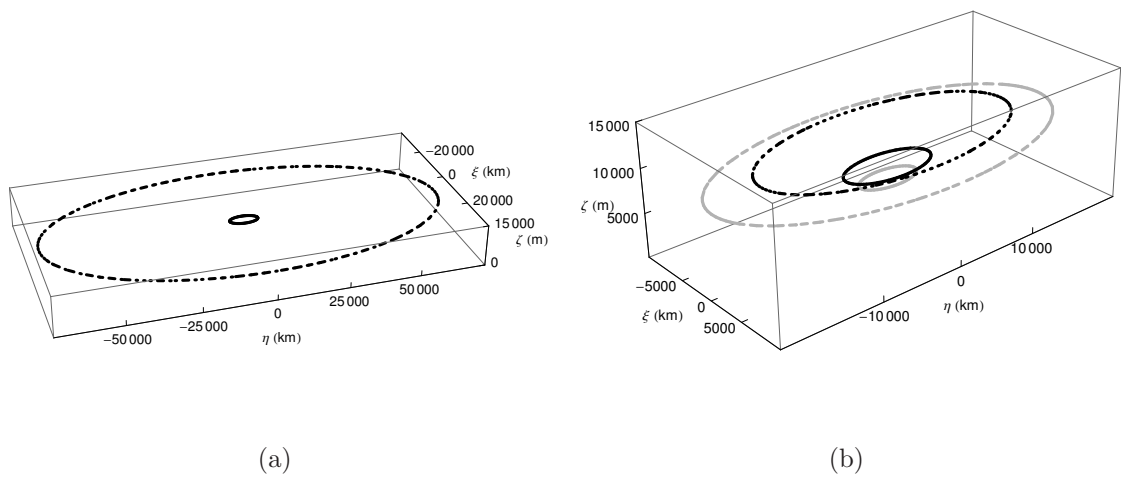


Figure 5.4: Displaced orbits of period $T = 2\pi/\Omega^*$. (a) The two orbits are at the same displacement $\zeta^0 = 0.000237168$ (10 km) for a sail with $a_0 = 0.001561$ (0.35 mms^{-2}). The sail is pitched at angle $\alpha_1 = 8.95^\circ$ for the dashed-line orbit and at an angle $\alpha_2 = 65.92^\circ$ for the solid-line orbit so that $\cos^2 \alpha_1 \sin \alpha_1 = \cos^2 \alpha_2 \sin \alpha_2$ (b) For a sail with a_0 (0.138 mms^{-2}), multiple orbits are shown at different displacements ζ^0 by varying the pitch angle at 60° (the gray solid-line orbit), 55° (the black solid-line orbit), 35.264° (the black dashed-line orbit), 25° (the gray dashed-line orbit).

α_2 , the size A_ξ, B_η of the elliptic displaced orbit decreases due to the decrease of a_p ($a_0 \cos^3 \alpha_2 < a_0 \cos^3 \alpha_1$). Therefore, an orbit with a large pitch angle α_2 does not drive the system far from the geostationary point. Fig. 5.4b shows for a given sail with a_0 (0.138 mms^{-2}), multiple orbits are obtained at different ζ^0 by varying the sail pitch angle α . Note that the maximum displacement ζ^0 orbit, for a given a_0 , also corresponds to $\alpha = 35.264^\circ$.

5.3 Accommodating the Nonlinearities

The linearised model considered in Eqs. (5.12-5.13) is a linear nonautonomous system because the linearised system considers that the Sun-line $\hat{\mathbf{S}}(t)$ is changing direction in the rotating frame, but neglects the effect of the non-linear Earth gravity. Thus, the displaced orbit of the linear system will not be periodic in the nonlinear system Eq.(5.4) due to the non-linear gravitational terms. In this section displaced orbits for the full nonlinear nonautonomous system will be investigated.

If $\mathbf{x}^T = [\mathbf{r}^T, \mathbf{v}^T]$ denotes the state vector then Eq. (5.4) can be rewritten in the rotating frame as

$$\dot{\mathbf{x}} = \mathbf{f}(t, \mathbf{x}, \mathbf{u}) = \begin{pmatrix} \mathbf{v} \\ -2\boldsymbol{\omega}_e \times \frac{d\mathbf{r}}{dt} - \nabla\mathcal{U} + \mathbf{a}_{SS}(t, \mathbf{u}) \end{pmatrix} \quad (5.22)$$

Among the shooting and collocation methods, Ozimek et al. [58] finds that the best method to solve for periodic orbits with path constraints is the collocation method. Furthermore, a larger radius of convergence is expected with the collocation scheme. The use of controls in addition to states as independent parameters allows more flexibility for robust convergence. Therefore, the collocation scheme from reference [58] is adapted to find displaced periodic orbits. However, we implement a pre-defined box around the linear periodic solution Eq. (5.21) as a path constraint and the complete analytical Jacobian matrix (for faster convergence). These will be discussed in subsection 5.3.2, and subsection 5.3.3 respectively.

First, we describe the key idea of the collocation method to transform the differential equations into (nonlinear) algebraic constraints.

5.3.1 Hermite Simpson Method

The transformation of the infinite-dimensional, continuous problem to the finite-dimensional, parameter problem is called transcription. Hargraves and Paris [38] introduced the direct transcription method in which state and control variables are discretised to transform the equations of motion into a set of nonlinear constraints. A discretisation of the time interval

$$0 = t_1 < t_2 < \dots < t_n = T$$

is chosen. Therefore, the time domain $[0 T]$ is divided into n nodes, and $n - 1$ segments whereas the i th segment connects two neighboring nodes at time t_i and t_{i+1} . Within each segment, the state history \mathbf{x} can be approximated by cubic piecewise polynomials (a well known Hermite-simpson method [7]) or higher order polynomials [40]. For a given desired accuracy of the solution, the higher order polynomial approximation reduces the number of nonlinear parameters and execution time. In this chapter, the Hermite-Simpson method is used to investigate the initial feasibility of displaced orbits around geostationary points.

The four coefficients in the cubic polynomial are determined such that states and derivatives at the node points t_i and t_{i+1} of the i^{th} segment match (see Fig. 5.5). The value of the cubic approximation at the midpoint $t_{i,c} = (t_i + t_{i+1})/2$ of the segment is then

$$\mathbf{x}_{i,c} = \frac{1}{2}(\mathbf{x}_i + \mathbf{x}_{i+1}) + \frac{h}{8}\{\mathbf{f}(t_i, \mathbf{x}_i, \mathbf{u}_i) - \mathbf{f}(t_{i+1}, \mathbf{x}_{i+1}, \mathbf{u}_{i+1})\} \quad (5.23)$$

where $h = t_{i+1} - t_i$, and $\mathbf{x}_i, \mathbf{x}_{i+1}, \mathbf{u}_i$, and \mathbf{u}_{i+1} denote the states and controls at node points t_i and t_{i+1} respectively for the i^{th} segment.

The differential equations are automatically satisfied at the node points. In general, they will not be satisfied at the mid point of the segment. The defect

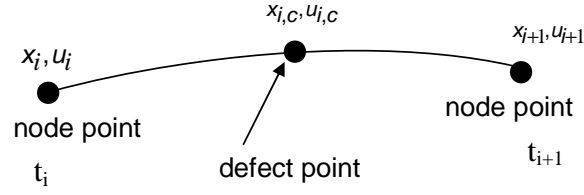


Figure 5.5: i^{th} segment for Hermite-Simpson transcription.

vector is defined as $\Delta = \dot{\mathbf{x}}_{i,c} - \mathbf{f}(t_{i,c}, \mathbf{x}_{i,c}, \mathbf{u}_{i,c})$, so that it can be explicitly written as

$$\begin{aligned} \Delta(t_i, \mathbf{x}_i, \mathbf{u}_i, t_{i+1}, \mathbf{x}_{i+1}, \mathbf{u}_{i+1}) = & \mathbf{x}_{i+1} - \mathbf{x}_i - \frac{h}{6} \{ \mathbf{f}(t_i, \mathbf{x}_i, \mathbf{u}_i) + 4\mathbf{f}(t_{i,c}, \mathbf{x}_{i,c}, \mathbf{u}_{i,c}) \\ & + \mathbf{f}(t_{i+1}, \mathbf{x}_{i+1}, \mathbf{u}_{i+1}) \} \end{aligned} \quad (5.24)$$

where the mid point control $\mathbf{u}_{i,c}$ is linearly interpolated as

$$\mathbf{u}_{i,c} = \frac{1}{2}(\mathbf{u}_i + \mathbf{u}_{i+1}) \quad (5.25)$$

The linear interpolation for control provides a smooth control history and is more computationally efficient. It is through the defect Eq. (5.24) that the equations of motion Eq. (5.22) are transcribed into nonlinear constraints that are driven to zero by selecting $\mathbf{x}_i, \mathbf{x}_{i+1}, \mathbf{u}_i$, and \mathbf{u}_{i+1} such that the equations of motion are satisfied within a specified tolerance.

5.3.2 Statement of Problem

The problem of finding the displaced periodic orbit for the nonlinear nonautonomous system Eq. (5.22) reduces to finding the solution of the (nonlinear) vector constraint. However, the period of the orbit $T = 2\pi/\Omega^*$ is known beforehand since the dynamical system is nonautonomous. The constraints that need to be satisfied for computing the displaced periodic orbits are

- The collocation constraint at $t_{i,c}$

$$\Delta(t_i, \mathbf{x}_i, \mathbf{u}_i, t_{i+1}, \mathbf{x}_{i+1}, \mathbf{u}_{i+1}) = 0, \quad i = 1, 2, \dots, n-1 \quad (5.26)$$

- Equality constraints that satisfy the definition of the periodic orbit. Therefore, the initial and the end point constraint at t_1 and t_n are

$$\begin{aligned} h_1(x_1, x_n) &= x_n - x_1 = 0, & h_2(y_1, y_n) &= y_n - y_1 = 0 \\ h_3(z_1, z_n) &= z_n - z_1 = 0, & h_4(\dot{x}_1, \dot{x}_n) &= \dot{x}_n - \dot{x}_1 = 0 \\ h_5(\dot{y}_1, \dot{y}_n) &= \dot{y}_n - \dot{y}_1 = 0, & h_6(\dot{z}_1, \dot{z}_n) &= \dot{z}_n - \dot{z}_1 = 0 \end{aligned} \quad (5.27)$$

$$\begin{aligned} h_7(u_1^{(1)}, u_n^{(1)}) &= u_n^{(1)} - u_1^{(1)} = 0 \\ h_8(u_1^{(2)}, u_n^{(2)}) &= u_n^{(2)} - u_1^{(2)} = 0 \\ h_9(u_1^{(3)}, u_n^{(3)}) &= u_n^{(3)} - u_1^{(3)} = 0 \end{aligned} \quad (5.28)$$

where $\mathbf{u}_i = (u_i^{(1)}, u_i^{(2)}, u_i^{(3)})^T$.

- Equality constraints at point t_i . This control constraint represents the fact that the sail orientation can be controlled by only two angles i.e., sail pitch angle α and yaw angle δ so that

$$\psi_i(\mathbf{u}_i) = \|\mathbf{u}_i\|^2 - 1, \quad i = 1, 2, \dots, n \quad (5.29)$$

- The inequality path constraints $\tilde{\mathbf{g}}_i(x_i, u_i) < 0$ of the m -element column vector are handled as an equality constraint by using slack variables. The idea is that if $\tilde{\mathbf{g}}_i^{(j)}(x_i, u_i) < 0$, then $\tilde{\mathbf{g}}_i^{(j)}$ plus some positive number (i.e., slack variable) is equal to zero. Let $\mathbf{k}_i^2 = [(k_i^{(1)})^2, (k_i^{(2)})^2, \dots, (k_i^{(m)})^2]^T$ denote the vector i.e., the element-wise square of the m -element slack variable \mathbf{k}_i . Thus, the inequality path constraints $\tilde{\mathbf{g}}_i(x_i, u_i) < 0$ can be written as

$$\mathbf{g}_i(x_i, u_i) = \tilde{\mathbf{g}}_i(x_i, u_i) + \mathbf{k}_i^2 = 0, \quad i = 1, 2, \dots, n \quad (5.30)$$

To find displaced periodic orbits at a given displacement ζ^0 of the nonlinear system Eq. (5.22), the path constraint is applied by choosing a box in the neighborhood of the corresponding linearised displaced periodic orbit to be discussed later in section 5.3.4. The path constraint forces the solution to

remain inside a pre-defined box above the Earth equatorial plane. If $\mathbf{r}_{lb} = (x_{lb}, y_{lb}, z_{lb})^T$ and $\mathbf{r}_{ub} = (x_{ub}, y_{ub}, z_{ub})^T$ denote the lower and upper bounds of the box, then the path constraint can be written as

$$\mathbf{g}_i(\mathbf{r}_i, \mathbf{k}_i) = \begin{pmatrix} \mathbf{r}_{lb} - \mathbf{r}_i \\ \mathbf{r}_i - \mathbf{r}_{ub} \end{pmatrix} + \mathbf{k}_i^2 = 0, \quad i = 1, 2, \dots, n \quad (5.31)$$

The constraints given in Eqs. (5.26-5.29) are necessary constraints for computing a periodic orbit for the solar sail. However, these constraints together with the pre-defined box constraint Eq. (5.31) are necessary to generate an NKO above the Earth equatorial plane with the collocation scheme.

5.3.3 Newton's Method and the Analytical Jacobian Matrix

Newton's method is a recursive method for finding the solutions of the (nonlinear) algebraic equations $\mathbf{C}(\boldsymbol{\mathcal{X}}) = 0$ for the root $\boldsymbol{\mathcal{X}}^* = 0$. For this problem, the single vector $\boldsymbol{\mathcal{X}}$ is defined including all the independent variables i.e., node states and control and slack variables. Therefore

$$\boldsymbol{\mathcal{X}}^T = [\mathbf{x}_1^T, \mathbf{u}_1^T, \mathbf{x}_2^T, \mathbf{u}_2^T, \dots, \mathbf{x}_n^T, \mathbf{u}_n^T, \mathbf{k}_1^T, \mathbf{k}_2^T, \dots, \mathbf{k}_n^T] \quad (5.32)$$

where n is the total number of nodes. Therefore, the total number of free parameters in $\boldsymbol{\mathcal{X}}^T$ is $6n + 3n + nm = n(9 + m)$: $6n$ for the node states, $3n$ for node controls and nm for the slack variables. Then, the full constraint vector \mathbf{C} consists of defect constraints, path constraints, and specific nodal constraints and is defined as

$$\mathbf{C}(\boldsymbol{\mathcal{X}})^T = (\Delta_{1,c}^T, \Delta_{2,c}^T, \dots, \Delta_{n-1,c}^T, \psi_1, \psi_2, \dots, \psi_n, \mathbf{g}_1^T, \mathbf{g}_2^T, \dots, \mathbf{g}_n^T, h_1, h_2, \dots, h_9) = 0 \quad (5.33)$$

Therefore a total of $6(n-1) + n + nm + 9 = n(7+m) + 3$ constraints exist: $6(n-1)$ for the defect, n for the node controls, nm for the path constraints, and 9 for the

node constraints. Note that $m = 6$ for the pre-defined box constraints (see Eq. (5.31)). The linearisation of $\mathbf{C}(\boldsymbol{\mathcal{X}})$ about the point $\boldsymbol{\mathcal{X}}_j$ gives

$$0 = \mathbf{C}(\boldsymbol{\mathcal{X}}_{j+1}) \approx \mathbf{C}(\boldsymbol{\mathcal{X}}_j) + \mathcal{DC}(\boldsymbol{\mathcal{X}}_j)(\boldsymbol{\mathcal{X}}_{j+1} - \boldsymbol{\mathcal{X}}_j)$$

or

$$\mathbf{C}(\boldsymbol{\mathcal{X}}_j) = \mathcal{DC}(\boldsymbol{\mathcal{X}}_j)(\boldsymbol{\mathcal{X}}_j - \boldsymbol{\mathcal{X}}_{j+1}) \quad (5.34)$$

where the Jacobian $\mathcal{DC} \in \mathbb{R}^{(n(7+m)+3) \times (n(9+m))}$ and $\mathbf{C}(\boldsymbol{\mathcal{X}}_j) \in \mathbb{R}^{n(7+m)+3}$. The Jacobian \mathcal{DC} is a rectangular matrix, i.e., there are always fewer constraint equations than unknowns. Therefore, the system of linear equations Eq. (5.34) has an infinite number of solutions. However, the unique solution with minimum norm $\|\boldsymbol{\mathcal{X}}_j - \boldsymbol{\mathcal{X}}_{j+1}\|$ subjected to Eq. (5.34) is called the minimum norm solution [19]. Using the pseudoinverse of $\mathcal{DC}(\boldsymbol{\mathcal{X}}_j)$, then $\boldsymbol{\mathcal{X}}_{j+1}$ closest to $\boldsymbol{\mathcal{X}}_j$ is

$$\boldsymbol{\mathcal{X}}_{j+1} = \boldsymbol{\mathcal{X}}_j - \mathcal{DC}(\boldsymbol{\mathcal{X}}_j)^T [\mathcal{DC}(\boldsymbol{\mathcal{X}}_j) \cdot \mathcal{DC}(\boldsymbol{\mathcal{X}}_j)^T]^{-1} \mathbf{C}(\boldsymbol{\mathcal{X}}_j) \quad (5.35)$$

The algorithm converges quadratically until $\|\mathbf{C}(\boldsymbol{\mathcal{X}}_{j+1})\|$ is satisfied within a prescribed tolerance (within 10^{-10}). In Eq. (5.34), the Jacobian \mathcal{DC} is a very large sparse matrix (see Ozimek et al. [58] for a detailed discussion on calculating $[\mathcal{DC} \cdot \mathcal{DC}^T]^{-1} \mathbf{C}$ that exploits the sparse structure of \mathcal{DC}). In this paper, all the non-zero elements $\mathcal{D}\boldsymbol{\Delta}_{i,c}$, $\mathcal{D}\psi_i$, $\mathcal{D}\mathbf{g}_i$ and $\mathcal{D}h_i$ of the Jacobian \mathcal{DC} are calculated analytically (note that defect derivatives $\mathcal{D}\boldsymbol{\Delta}_{i,c}$ are calculated numerically in reference [58] because a seventh degree polynomial approximation for the states is used therein rather than the Hermite-Simpson method). The 6×18 defect derivatives matrix $\mathcal{D}\boldsymbol{\Delta}_{i,c}$ is computed as

$$\mathcal{D}\boldsymbol{\Delta}_{i,c} = \left\{ \frac{\partial \boldsymbol{\Delta}_{i,c}}{\partial \mathbf{x}_i}, \frac{\partial \boldsymbol{\Delta}_{i,c}}{\partial \mathbf{x}_{i+1}}, \frac{\partial \boldsymbol{\Delta}_{i,c}}{\partial \mathbf{u}_i}, \frac{\partial \boldsymbol{\Delta}_{i,c}}{\partial \mathbf{u}_{i+1}} \right\} \quad (5.36)$$

The derivatives of the defect vector $\boldsymbol{\Delta}_{i,c}$ with respect to states at the node points of the i^{th} segment are obtained from Eqs. (5.23) and (5.24), and are given by

$$\begin{aligned} \frac{\partial \boldsymbol{\Delta}_{i,c}}{\partial \mathbf{x}_i} &= -I_6 - \frac{h}{6} \left[\mathbf{F}(t_i, \mathbf{x}_i, \mathbf{u}_i) + 4\mathbf{F}(t_{i,c}, \mathbf{x}_{i,c}, \mathbf{u}_{i,c}) \frac{\partial \mathbf{x}_{i,c}}{\partial \mathbf{x}_i} \right] \\ \frac{\partial \boldsymbol{\Delta}_{i,c}}{\partial \mathbf{x}_{i+1}} &= I_6 - \frac{h}{6} \left[\mathbf{F}(t_{i+1}, \mathbf{x}_{i+1}, \mathbf{u}_{i+1}) + 4\mathbf{F}(t_{i,c}, \mathbf{x}_{i,c}, \mathbf{u}_{i,c}) \frac{\partial \mathbf{x}_{i,c}}{\partial \mathbf{x}_{i+1}} \right] \end{aligned} \quad (5.37)$$

for $i = 1, 2, \dots, n - 1$, where \mathbf{F} denotes the 6×6 matrix, and results from the differentiation of the right side of the Eq. (5.22) $\mathbf{f}(t, \mathbf{x}, \mathbf{u})$ with respect to states \mathbf{x} . I_6 is the 6×6 identity matrix, and

$$\begin{aligned}\frac{\partial \mathbf{x}_{i,c}}{\partial \mathbf{x}_i} &= \frac{I_6}{2} + \frac{h}{8} \mathbf{F}(t_i, \mathbf{x}_i, \mathbf{u}_i) \\ \frac{\partial \mathbf{x}_{i,c}}{\partial \mathbf{x}_{i+1}} &= \frac{I_6}{2} - \frac{h}{8} \mathbf{F}(t_{i+1}, \mathbf{x}_{i+1}, \mathbf{u}_{i+1})\end{aligned}\quad (5.38)$$

The derivatives with respect to the controls are then found to be

$$\begin{aligned}\frac{\partial \Delta_{i,c}}{\partial \mathbf{u}_i} &= -\frac{h}{3} \left[\mathbf{G}(t_{i,c}, \mathbf{x}_{i,c}, \mathbf{u}_{i,c}) + \left\{ \frac{I_6}{2} + \frac{h}{4} \mathbf{F}(t_{i,c}, \mathbf{x}_{i,c}, \mathbf{u}_{i,c}) \right\} \mathbf{G}(t_i, \mathbf{x}_i, \mathbf{u}_i) \right] \\ \frac{\partial \Delta_{i,c}}{\partial \mathbf{u}_{i+1}} &= -\frac{h}{3} \left[\mathbf{G}(t_{i,c}, \mathbf{x}_{i,c}, \mathbf{u}_{i,c}) + \left\{ \frac{I_6}{2} - \frac{h}{4} \mathbf{F}(t_{i,c}, \mathbf{x}_{i,c}, \mathbf{u}_{i,c}) \right\} \mathbf{G}(t_{i+1}, \mathbf{x}_{i+1}, \mathbf{u}_{i+1}) \right]\end{aligned}\quad (5.39)$$

for $i = 1, 2, \dots, n - 1$, where \mathbf{G} denotes the 6×3 matrix, and results from differentiation of the right side of equation $\mathbf{f}(t, \mathbf{x}, \mathbf{u})$ with respect to the control vector \mathbf{u} . $\mathcal{D}\psi_i, \mathcal{D}\mathbf{g}_i$ and $\mathcal{D}h_l$ are given in the Appendix C.

5.3.4 Illustrative Examples

In this section periodic orbits will be illustrated for Eq. (5.22) using the collocation scheme with inequality path constraints i.e., Eq. (5.31). Again it is assumed that the Sun-line $\hat{\mathbf{S}}(t)$ is in the Earth's equatorial plane. The period of the orbit is known ($T = \frac{2\pi}{\Omega^*}$) and is divided into $n = 100$ node points. Once $\mathbf{u}_i = (u_i^{(1)}, u_i^{(2)}, u_i^{(3)})$ is known from the converged solution $\boldsymbol{\chi}^* = \boldsymbol{\chi}_{j+1}$ of Eq. (5.35), the sail pitch α_i and δ_i angle can be calculated as

$$\alpha_i = \sin^{-1} u_i^{(3)} \quad (5.40)$$

$$\delta_i = \tan^{-1} \left(\frac{u_i^{(1)} \sin \Omega^* t_i + u_i^{(2)} \cos \Omega^* t_i}{u_i^{(1)} \cos \Omega^* t_i - u_i^{(2)} \sin \Omega^* t_i} \right) \quad (5.41)$$

If inequality path constraints are neglected i.e., Eq. (5.31), then the problem for computing periodic orbits reduces to satisfying the defect constraints, periodic orbit definition constraints and the control constraints $\psi_i = 0$. The collocation

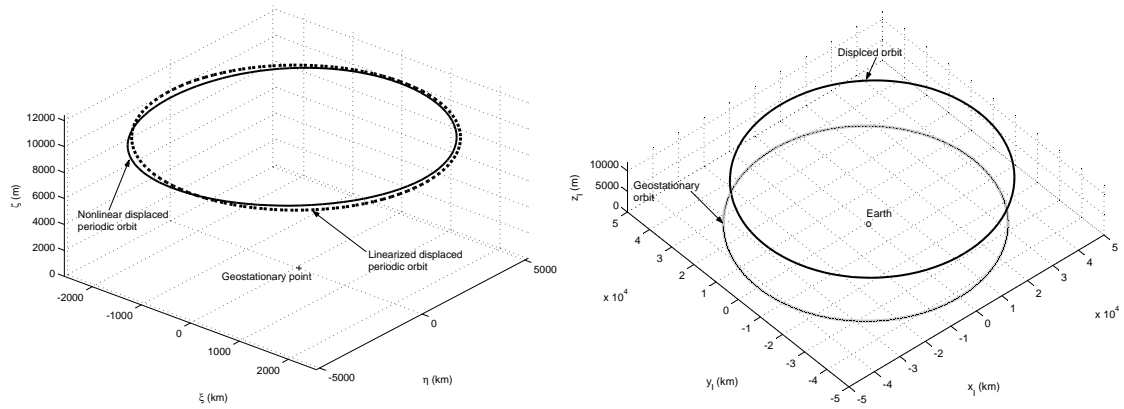
scheme initially generates periodic solutions of period $T = \frac{2\pi}{\Omega^*}$, however, it is not a displaced orbit since it crosses the Earth's equatorial plane (see Sect. 6.1 for such orbits). This result suggests inequality path constraints must be enforced to investigate displaced periodic orbits of Eq. (5.22).

A box in the neighborhood of the linearised forced periodic solution Eq. (5.21) is chosen as an inequality path constraint (see Eq. (5.31)). The lower and upper bounds of the box i.e., $\mathbf{r}_{lb} = (x_{lb}, y_{lb}, z_{lb})^T$ and $\mathbf{r}_{ub} = (x_{ub}, y_{ub}, z_{ub})^T$ are defined as

$$\begin{aligned} x_{lb} &= 1 + \xi_{min} + \nu\xi_{min}, & x_{ub} &= 1 + \xi_{max} + \nu\xi_{max} \\ y_{lb} &= \eta_{min} + \nu\eta_{min}, & y_{ub} &= \eta_{max} + \nu\eta_{max} \\ z_{lb} &= \zeta^0 - \rho\zeta^0, & z_{ub} &= \zeta^0 + \rho\zeta^0 \end{aligned} \quad (5.42)$$

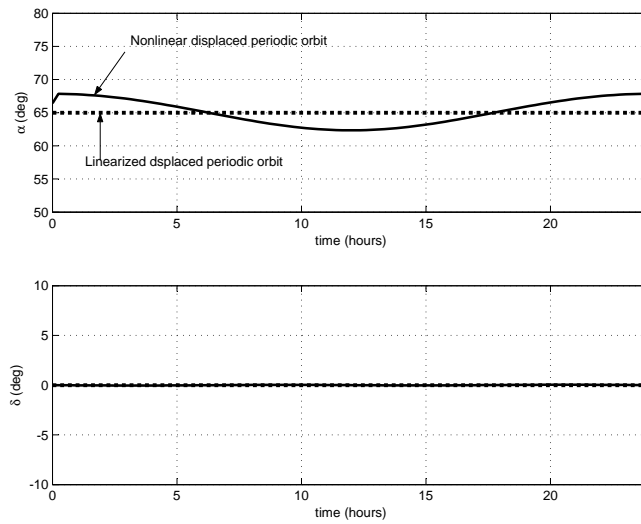
where $\xi_{min} < 0$, $\xi_{max} > 0$, $\eta_{min} < 0$ and $\eta_{max} > 0$ are the minimum and maximum x and y position on the linearised periodic displaced periodic orbit from the geostationary point. $\zeta^0 > 0$ is the desired displacement above the Earth's equatorial plane and ν and ρ are parameters used for sizing the box dimensions.

The sail characteristic acceleration is chosen as $a_0 > a_0^*$ for a given ζ^0 to force the spacecraft in a region above the Earth's equatorial plane. A nearby solution will only exist if the chosen sail characteristic acceleration is sufficient to overcome the non-linearities of the gravitational acceleration near the geostationary point. To compute a displaced periodic orbit at 10 km above the Earth's equatorial plane, a sail characteristic acceleration of 0.328 mms^{-2} is required with the corresponding pitch angle $\alpha = 65^\circ$ determined from Eq. (5.16). A value of $\alpha > \alpha^*$ is required to avoid a large ellipse (see Fig. 5.4a). The vector \mathcal{X} is given by Eq. (5.32). For the initial guess vector \mathcal{X} , the initial state \mathbf{x}_i at all node points is the linearised solution, and the initial guess for \mathbf{u}_i is computed from Eq. (5.8) with $t = t_i$, $\delta(t_i) = 0$ and $\alpha(t_i) = 65^\circ$. The initial guess at all node points for slack variables can be determined by solving Eq. (5.31) for \mathbf{k}_i . For $n = 100$ node points, the size of \mathcal{X} and \mathbf{C} are 1500 and 1303 respectively. Some 99.45% of entries in the matrix \mathbf{DC} are zero because of the sparse structure. With a few iterations of Eq. (5.35), the collocation scheme finds the displaced periodic orbit satisfying the constraints



(a)

(b)



(c)

Figure 5.6: A sail with characteristic acceleration 0.328 mms^{-2} shows a displaced periodic orbits of period $T = 2\pi/\Omega^*$ around a geostationary point (a) in the ECEF frame (b) in the ECI frame (the black solid line orbit is a non-Keplerian orbit from the collocation scheme and the gray solid line orbit is the Keplerian geostationary orbit) and (c) control history.

Eqs. (5.26-5.29) and path constraint Eq. (5.31). $\nu = 0.25$ and $\rho = 0.15$ are chosen in the simulation. The resulting displaced orbit is shown by the solid-line in Fig. 5.6(a). The required sail pitch angle α and yaw angle δ are also shown by the solid-line in Fig. 5.6c. The pitch angle is smooth and slowly varying except at the end points (where only a few degrees per hour slew rate is required). Although the control angles rates are not constrained, they can be easily included in the collocation scheme. No variation of the sail yaw angle δ is seen which suggests that the algorithm averages out the gravitational acceleration along the z axis to generate the displaced periodic orbit 10 km above the Earth's equatorial plane. Fig. 5.6a shows the displaced periodic orbits in the ECEF frame. The displaced periodic orbits computed from the collocation scheme can then be transformed into the ECI frame using

$$\begin{pmatrix} x_I \\ y_I \\ z_I \end{pmatrix} = C_{i/e} \begin{pmatrix} x \\ y \\ z \end{pmatrix} \quad (5.43)$$

Since the Earth's angular velocity ω_e is unity in non-dimensional units, a rotation matrix $C_{i/e}$ from the ECEF to the ECI frame is given by

$$C_{i/e} = \begin{pmatrix} \cos t & -\sin t & 0 \\ \sin t & \cos t & 0 \\ 0 & 0 & 1 \end{pmatrix} \quad (5.44)$$

The displaced periodic orbit is centered around the Earth in the ECI frame and is shown in Fig. 5.6b. Note that the orbit is non-Keplerian as it does not pass through the center of the Earth. Furthermore, the non-Keplerian orbit is pushed slightly away from the Sun by the solar radiation pressure. Such an offset was also suggested by Forward [28].

The possibility of displaced periodic orbits for a high performance solar sail is now investigated with a characteristic acceleration of order 6 mms^{-2} [63]. A linearised displaced periodic orbit at $\zeta^0 = 0.0017788$ ($\simeq 75 \text{ km}$) with a sail characteristic acceleration $a_0 = 0.0268$ ($\simeq 6 \text{ mms}^{-2}$) is chosen as an initial guess for

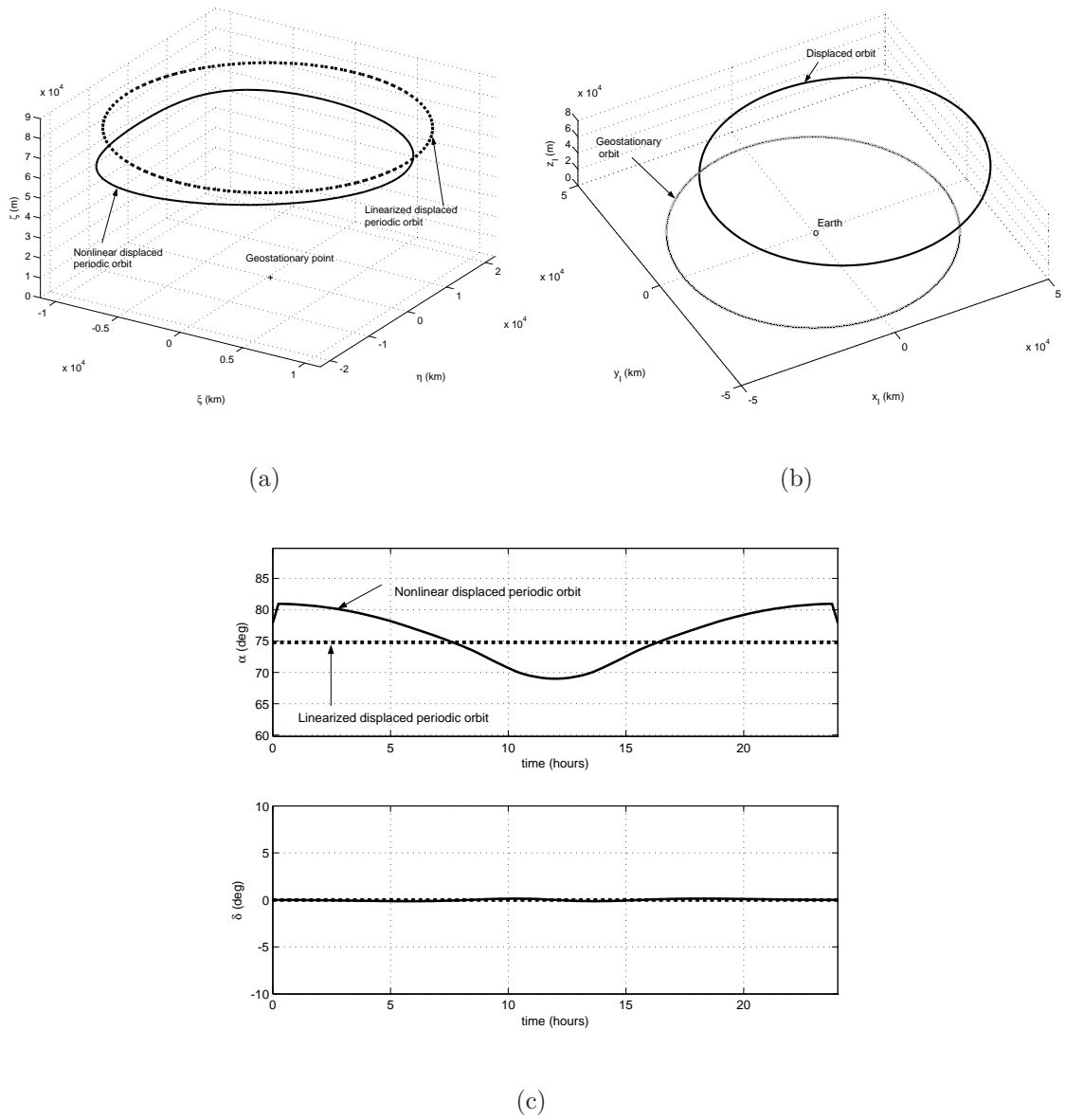


Figure 5.7: Displaced periodic orbits using a high performance sail with a characteristic acceleration of 6 mms^{-2} (a) in the ECEF frame (b) in the ECI frame and (c) the control history.

the collocation scheme (see dashed-line orbit and dashed-line control history in Figs. 5.7a and 5.7c). The large pitch angle $\alpha = 74.8^\circ$ in the control history is due to $a_0 > a_0^*$ for the given ζ^0 (75 km). This large pitch angle reduces the size A_ξ, B_η of the elliptic displaced orbit around the geostationary point (see Sec. 5.2). $\nu = 0.25$ and $\rho = 0.2$ are chosen for the box dimensions. The collocation scheme converges on a solution which is effectively a 62 km displaced periodic orbit with the control time history shown as the solid-line in Fig. 5.7. Fig. 5.7b shows that the offset between the displaced orbit and geostationary orbit increases at higher displacements ζ^0 . A 75×75 km station-keeping box (i.e., $\pm 0.05^\circ$ in longitude and latitude) [59] around a nominal geostationary point has an upper box-face at 37.5 km above the Earth's equatorial plane, so a 62 km displaced orbit is well above the conventional station-keeping box.

5.4 Linear Analysis with Seasonal Effects

So far, it is assumed that the Sun-line is in the Earth's equatorial plane. In reality, depending on the season, the Sun-line moves above and below the Earth's equatorial plane [27, 78]. During the summer solstice (June 21), the Sun-line is 23.5° below the Earth's equatorial plane. During the winter solstice (22 December), the Sun-line is 23.5° above the Earth's equatorial plane. It is only during the equinoxes (March 21, September 23) that the Sun-line is in the Earth's equatorial plane. In this section, a general expression for the forcing term in the linearised model (see Eqs. (5.12-5.14)) will be developed i.e., solar sail acceleration (a_ξ, a_η, a_ζ) in the ECEF frame valid at the solstices and equinoxes. Secondly, the forcing term is used to analyse the linear model at the solstices.

5.4.1 Direction of the Sun-line

Fig. 5.8 shows that the Sun-line $\hat{\mathbf{S}}(t)$ is at an angle ϕ above the Earth's equatorial plane. Although ϕ changes with time, it may be assumed fixed for one orbit period

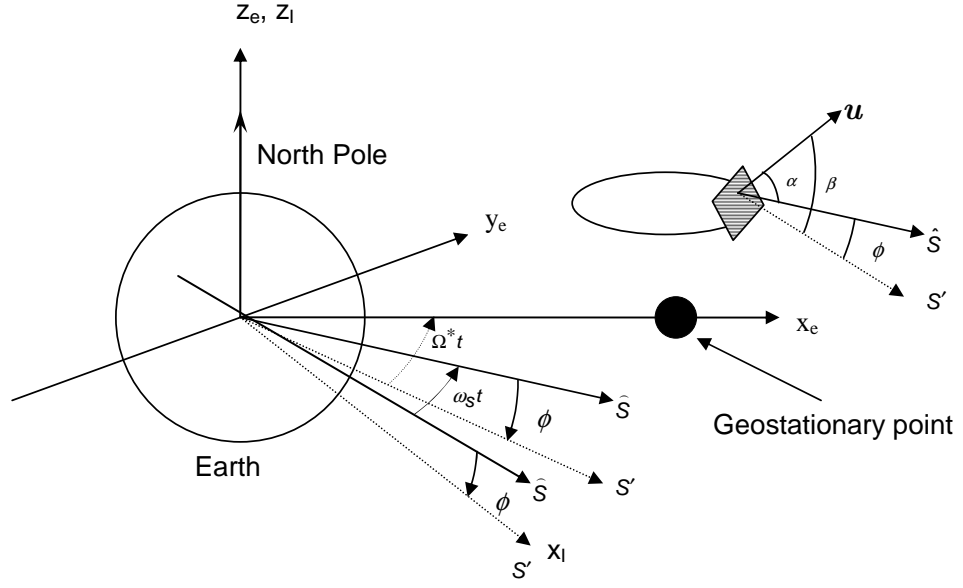


Figure 5.8: The Sun-line $\hat{\mathbf{S}}$ is shown at an arbitrary angle ϕ above the Earth's equatorial plane. $\hat{\mathbf{S}}'$ is the projection of the Sun-line in the Earth's equatorial plane. The angle Ω^*t is in the Earth's equatorial plane and the angle ϕ is out of the Earth's equatorial plane. The angle ϕ is assumed constant over one orbit period.

T . This is a reasonable assumption given the separation of time scales (1 day \ll 1 year). Now re-define the ECI-frame after each period T (since x_e and \mathbf{S}' coincide after one period $T = 2\pi/\Omega^*$) with the x_I -axis now along the projection of the Sun-line $\hat{\mathbf{S}}$ in the equatorial plane i.e., along \mathbf{S}' (see Fig. 5.8, x_I and \mathbf{S}' coincide at $t = 0$ so that time starts from zero for each simulation run). Then, the direction of the Sun-line $\hat{\mathbf{S}}(t)$ and hence the sail normal \mathbf{u} in the ECEF-frame are given by

$$\begin{aligned} \hat{\mathbf{S}} &= \begin{pmatrix} \cos(\Omega^*t) & \sin(\Omega^*t) & 0 \\ -\sin(\Omega^*t) & \cos(\Omega^*t) & 0 \\ 0 & 0 & 1 \end{pmatrix} \begin{pmatrix} \cos \phi & 0 & -\sin \phi \\ 0 & 1 & 0 \\ \sin \phi & 0 & \cos \phi \end{pmatrix} \begin{pmatrix} 1 \\ 0 \\ 0 \end{pmatrix} \\ &= \begin{pmatrix} \cos(\Omega^*t) \cos \phi \\ -\sin(\Omega^*t) \cos \phi \\ \sin \phi \end{pmatrix} \end{aligned} \quad (5.45)$$

$$\mathbf{u} = \begin{pmatrix} \cos \beta \cos(\Omega^*t) \\ -\cos \beta \sin(\Omega^*t) \\ \sin \beta \end{pmatrix} \quad (5.46)$$

Note that in Eq.(5.6), the angle ϕ is constant and equal to zero over the orbit period T . The angle that the sail normal makes with the Earth's equatorial plane is equal to $\beta(= \alpha + \phi)$. It can be shown that $\hat{\mathbf{S}}(t) \cdot \mathbf{u} = \cos \alpha$.

The Sun-line direction $\hat{\mathbf{S}}(t)$ at the autumn/spring equinoxes, the winter and the summer solstices is obtained by substituting $\phi = 0$, $\phi = +\phi_m = +23.5^\circ$ and $\phi = -\phi_m = -23.5^\circ$ respectively in the Eq. (5.45).

5.4.2 Linearised Solution

In summary, the forcing term of the linearised model i.e., \mathbf{a}_{SS} given on the right-side of Eqs. (5.12-5.14)), in the ECEF-frame may be written as

$$\begin{pmatrix} a_\xi \\ a_\eta \\ a_\zeta \end{pmatrix} = a_0 \cos^2 \alpha \begin{pmatrix} \cos \beta \cos(\Omega^*t) \\ -\cos \beta \sin(\Omega^*t) \\ \sin \beta \end{pmatrix} \quad (5.47)$$

where β is given by

$$\begin{aligned} \beta &= \alpha && \text{at autumn/spring equinoxes} \\ \beta &= \alpha - \phi_m && \text{at summer solstice} \\ \beta &= \alpha + \phi_m && \text{at winter solstice} \end{aligned} \quad (5.48)$$

Therefore, the angle β is equal to α at the equinoxes and exactly 23.5° less or greater at the solstices. With the sail forcing term Eq. (5.47), the solution of the linearised Eqs. (5.12-5.14) will still have the same form as Eq. (5.21) except that

A_ξ , B_η and ζ^0 are now replaced by

$$A_\xi = \frac{a_0 \cos^2 \alpha \cos \beta (U_{yy}^0 - 2\Omega^* - \Omega^{*2})}{\Omega^{*4} - \Omega^{*2}(4 + U_{yy}^0 + U_{xx}^0) + U_{xx}^0 U_{yy}^0} \quad (5.49)$$

$$B_\eta = \frac{-A_\xi(\Omega^{*2} + 2\Omega^* - U_{xx}^0)}{(\Omega^{*2} + 2\Omega^* - U_{yy}^0)} \quad (5.50)$$

$$\zeta^0 = \frac{a_0 \cos^2 \alpha \sin \beta}{U_{zz}^0} \quad (5.51)$$

where β is defined by Eq. (5.48). The sail acceleration component in the equatorial-plane $a_p = \sqrt{a_\xi^2 + a_\eta^2} = a_0 \cos^2 \alpha \cos \beta$ determines the size (A_ξ, B_η) of the elliptic displaced orbit, while the component out of the equatorial plane $a_\zeta = a_0 \cos^2 \alpha \sin \beta$ determines the levitation height ζ^0 of the displaced orbit. To size the sail for a mission based on a displaced orbit around a geostationary point, the worst-case scenario should be considered which is the summer solstice (the lowest value of a_ζ in Eq. (5.47)). Therefore, for a given ζ^0 , a_0 could be minimised from the above equation by maximizing $\cos^2 \alpha \sin(\alpha - \phi_m)$, since $\beta = \alpha - \phi_m$ at the summer solstice. Therefore,

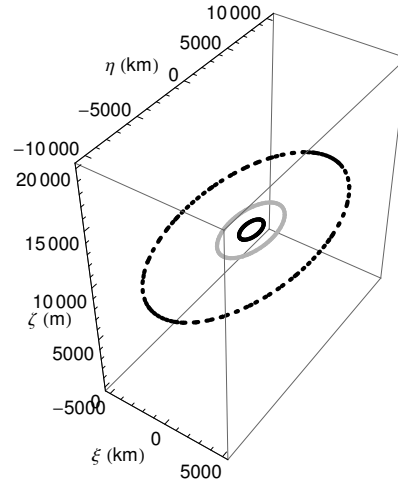


Figure 5.9: 10 km levitated displaced periodic orbits for a sail with characteristic acceleration $a_0 = 0.002795$ (0.626 mms^{-2}) at the summer solstice (dashed-line orbit with $\alpha = 70^\circ$), winter solstice (solid-line black orbit with $\alpha = 73^\circ$) and at autumn/spring equinoxes (gray orbit with $\alpha = 72.65^\circ$).

$$\begin{aligned}
\frac{d \cos^2 \alpha \sin(\alpha - \phi_m)}{d\alpha} &= 0 \\
\tilde{\alpha} &= \frac{1}{2} [\cos^{-1}(1/3 \cos \phi_m) + \phi_m] \\
\tilde{\alpha} &= 47.850^\circ
\end{aligned} \tag{5.52}$$

Denote \tilde{a}_0 as the sail characteristic acceleration determined from Eq. (5.51) corresponding to $\alpha = \tilde{\alpha}$ and $\beta = \tilde{\alpha} - \phi_m$ at a given displacement ζ^0 . Now, in order to compensate for the Earth's non-linear gravity with the collocation scheme the sail characteristic acceleration is chosen as $a_0 > \tilde{a}_0$. Similar to section 5.2, there will be two specific pitch angles α_1 and α_2 for each $a_0 > \tilde{a}_0$. In Fig. 5.9 the outer most dashed-line shows the linearised periodic orbits at displacement ζ^0 (10 km) with a_0 (0.626 mms^{-2}) $>$ \tilde{a}_0 (0.286 mms^{-2}) and a sail pitch angle $\alpha = 70^\circ$ determined from Eq. (5.51) with $\beta = \alpha - \phi_m$ (the worst-case summer solstice). Depending on the season the sun-line angle ϕ will vary. Therefore, for the same sail acceleration and to keep fixed ζ^0 (10 km), the sail pitch angle must vary from $\alpha = 72.6532^\circ$ to $\alpha = 73.008^\circ$ at the equinoxes and winter solstice respectively to form the new linearised displaced periodic orbit. These orbits will act as an initial guess for the collocation scheme to generate the new reference displaced periodic orbits with seasonal effects.

5.5 Illustrative Examples at Summer Solstice

In this section, periodic orbits from the collocation scheme are computed for the configuration at the summer solstice, with the worst-case geometry. For a displacement ζ^0 (32 km), the collocation scheme converges if the linearised periodic orbit is chosen with a sail characteristic acceleration a_0 (6 mms^{-2}) $>$ \tilde{a}_0 (0.916 mms^{-2}), where \tilde{a}_0 is computed from $\tilde{\alpha}$ at ζ^0 (32 km). In the linearised solution (see dashed-line in Fig. 5.10) for a_0 (6 mms^{-2}), the sail pitch angle $\alpha = 79.33^\circ$ is determined from Eq. (5.51) for $\beta = \alpha - \phi_m$ (summer solstice). In the collocation scheme for the initial guess of the vector \mathcal{X} , the \mathbf{x}_i at all node points ($n = 150$ node points)

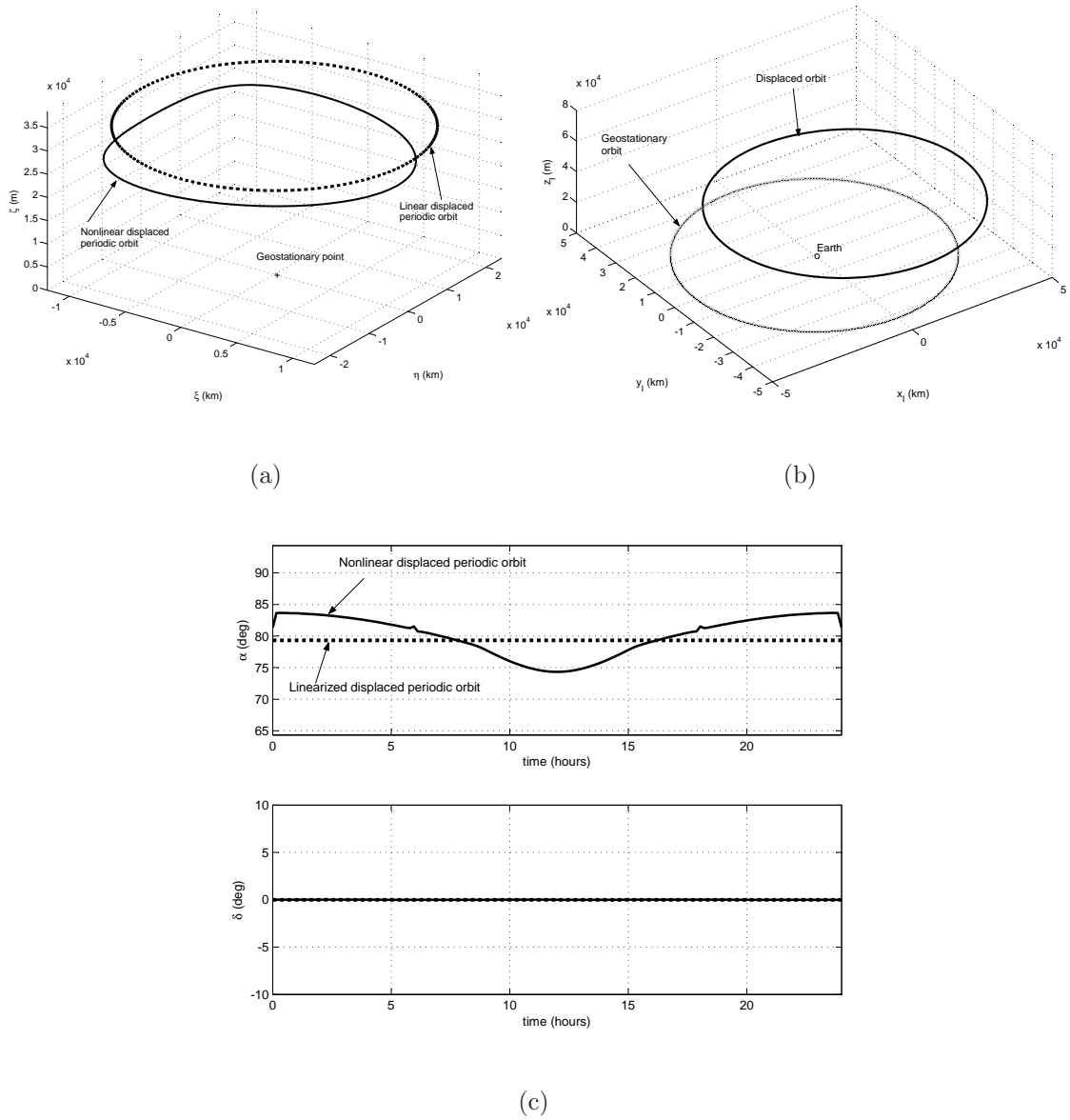


Figure 5.10: At the summer solstice (worst-case scenario), displaced periodic orbits for a sail with a characteristic acceleration 6 mms^{-2} (a) in the ECEF frame (b) in the ECI frame and (c) the control history (right).

are from the linearised solution and the initial guess for the components of \mathbf{u}_i is computed with $\delta = 0$ and $\alpha = 79.33^\circ$ i.e.,

$$\mathbf{u}_i = \begin{pmatrix} \cos(\alpha - \phi_m) \cos(\Omega^* t_i - \delta) \\ -\cos(\alpha - \phi_m) \sin(\Omega^* t_i - \delta) \\ \sin(\alpha - \phi_m) \end{pmatrix} \quad (5.53)$$

$\nu = 0.25$ and $\rho = 0.19$ are chosen for sizing the box in Eq. (5.42) around the linearised solution, and the inequality path constraints Eq. (5.31) are imposed in the collocation scheme. In Eq. (5.22), the expression for the Sun-line $\hat{\mathbf{S}}$ at the summer solstice (i.e., Eq. (5.45) with $\phi = -\phi_m$) is used to compute \mathbf{a}_{SS} . Therefore, \mathbf{G} in Eq. (5.39) should be modified accordingly in this simulation. The size of \mathcal{X} and \mathbf{C} are 1953 and 2250 respectively, and some 99.60% of the entries of the matrix \mathcal{DC} are zero. The collocation scheme converges to a periodic solution, a 25 km displaced periodic orbit with control time history shown in Fig. 5.10 as a solid-line. From \mathcal{X}^* , the angles δ_i are still calculated from Eq. (5.41), but the pitch angle α_i is calculated as

$$\alpha_i = \cos^{-1} \left(\frac{u_i^{(1)}}{\cos(\Omega^* t_i - \delta_i)} \right) + \phi_m \quad (5.54)$$

The Fig. 5.10 shows that the collocation scheme finds a periodic orbit displaced 25 km above the Earth's equatorial plane around a geostationary point with a high performance sail. It is noted that for a realistic sail model the large sail pitch angle will result in significant deviation from an ideal solar sail. With the low and moderate performance sail characteristic acceleration such as 0.9 mms^{-2} and 2.15 mms^{-2} , the displaced periodic orbits at the summer solstice with the collocation scheme are found at displacements of 9.5 km and 16 km respectively. However, a sail with a characteristic acceleration of 60 mms^{-2} (a perforated sail [63]), the collocation scheme converges to a displaced periodic orbit at 37.5 km, which is just above the conventional station-keeping box.

5.6 Application: Solar Power Transmission from Space

The idea of transmitting solar energy from space was first introduced by Glaser [33]. This section describes an example application of light levitated geostationary orbits at $\zeta^0(\pm 2 \text{ km})$ for reflectors (solar sails pitched at $\alpha = \pm 45^\circ$) of a solar power satellite (SPS) system [76]. The two sails are in formation with a microwave energy generator-transmitter which is orbiting around a geostationary point in the Earth's equatorial plane (i.e., $\zeta^0 = 0$) as shown in Fig. 5.11a. Note that the energy generator-transmitter has the same in-plane acceleration a_p as the two displaced orbits in-plane acceleration $a_p = a_0 \cos^3 \alpha$ to ensure that the energy generator-transmitter will always be below/above the pitched sails. The orbits of the SPS system illustrated in Fig. 5.11a are different from reference [76] as the Sun-pointing reflectors and the Earth-pointing transmitter are in orbits around a geostationary point in the ECEF-frame (not stationary in the ECEF-frame). The Sun-light reflected from the levitated sails will fall perpendicularly to the microwave generator-transmitter which will transmit energy to the Earth-receiving antenna.

The dashed-line orbits and the solid-line orbits, shown in Fig. 5.11b, are generated from the linear analysis and the collocation scheme respectively. The corresponding sail pitch angle α on these orbits is shown in Fig. 5.11c. The results from the collocation scheme suggests that the sunlight from the sails on displaced orbits will fall almost perpendicularly on generator-transmitter (see an offset angle within $\pm 5^\circ$ in Fig. 5.11c).

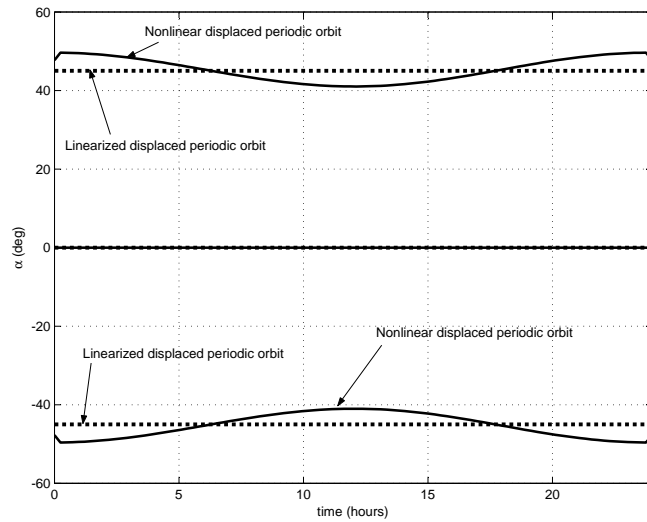
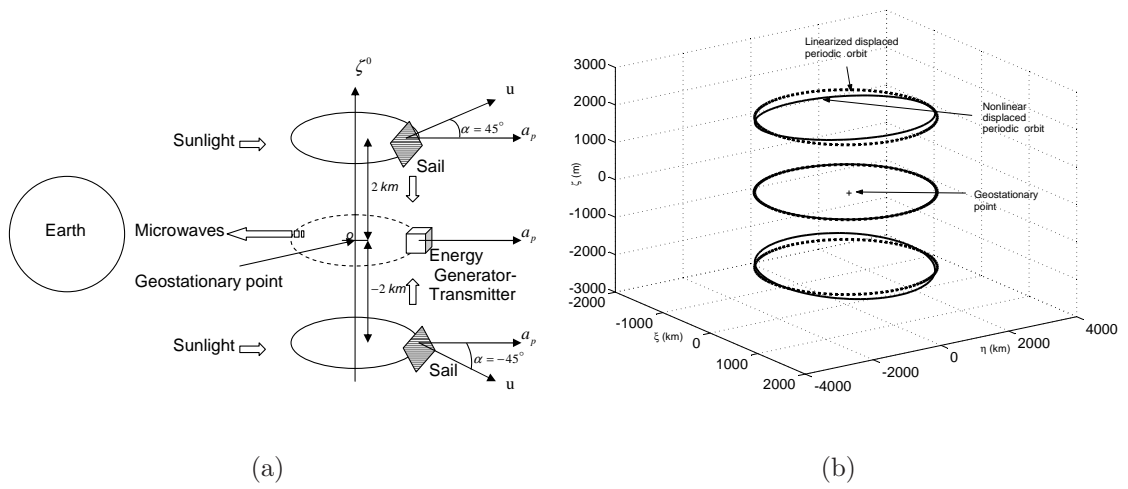


Figure 5.11: (a) The two solar sails are pitched at $\alpha = \pm 45^\circ$ on displaced orbits (the solid-line orbits) at a levitation distance $\zeta^0 = \pm 2$ km. The microwave energy generator-transmitter is orbiting (the dashed-line orbit) in the Earth’s equatorial plane and is placed in centre of the system. All three orbits have the same period $T = 2\pi/\Omega^*$ and in-plane acceleration a_p (b) orbits from the linear analysis (sails on displaced orbits with a_0 (0.03 mms^{-2}) (i.e., a_p ($0.010635 \text{ mms}^{-2}$) on all orbits)) and the non-linear analysis illustrating the SPS concept in ECEF-frame at the equinoxes (c) sail pitch angle history.

5.7 Equilibria in ECEF-Frame and Solar Power Satellite System

In this section, the use of an electric propulsion system to cancel the sail-reflector in-plane acceleration a_p is investigated. The displacement ζ^0 for the reflectors is small (± 2 km), so it will be interesting to calculate the ΔV delivered by the thruster system to cancel a_p for one year duration. This will result in equilibrium in the ECEF-frame and a displaced NKO above the geostationary orbit when viewed in the inertial frame. Moreover, it will be interesting to compare the ΔV per year if a pure SEP spacecraft is levitated at the same displacement ζ^0 (2 km).

Fig. 5.12a shows a light-levitated sail as proposed by Forward [27, 28]. The sail acceleration component a_ζ will provide the levitation and satisfy the relationship

$$a_\zeta = a_0 \cos^2 \alpha \sin(\alpha + \phi) = \frac{\mu_g \zeta^0}{r^2} \quad (5.55)$$

where a_0 (0.06 mms^{-2}) $>$ \tilde{a}_0 (0.0573 mms^{-2}), $r = \sqrt{r_{gs}^2 + (\zeta^0)^2} = \sqrt{1 + (\zeta^0)^2}$, $\mu_g = 1$ and ϕ is the Sun's declination angle that varies over one year as shown in Fig. 5.12b. The sail pitch angle α can be computed from the above equation with time (i.e., for any ϕ). The sail pitch angle α is equal to 65.1° at winter solstice ($\phi = +23.5^\circ$), 53.38° at summer solstice ($\phi = -23.5^\circ$), and 63.58° at equinox ($\phi = 0^\circ$). To maintain equilibrium above geostationary orbit, the sail acceleration component parallel to the equatorial plane a_p must be cancelled out. Fig. 5.12c shows that the sail in-plane acceleration will be maximum at the summer solstice. The required ΔV per year can be computed as

$$\Delta V/\text{year}(\text{m/s}) = \int_0^{1 \text{ year}} |a_p| a_r dt \quad (5.56)$$

where $a_p = a_0 \cos^2 \alpha \cos(\alpha + \phi)$, and a_r is defined in Eq.(5.2). Briefly, the ΔV per year is found to be 271 m/s to levitate at ζ^0 (2 km). Therefore, $\Delta V = 2.71 \text{ km/s}$ for a 10 year mission. This will result in a propellant fraction of 8.27% for the 10 year mission if $I_{sp} = 3200 \text{ s}$ is assumed.

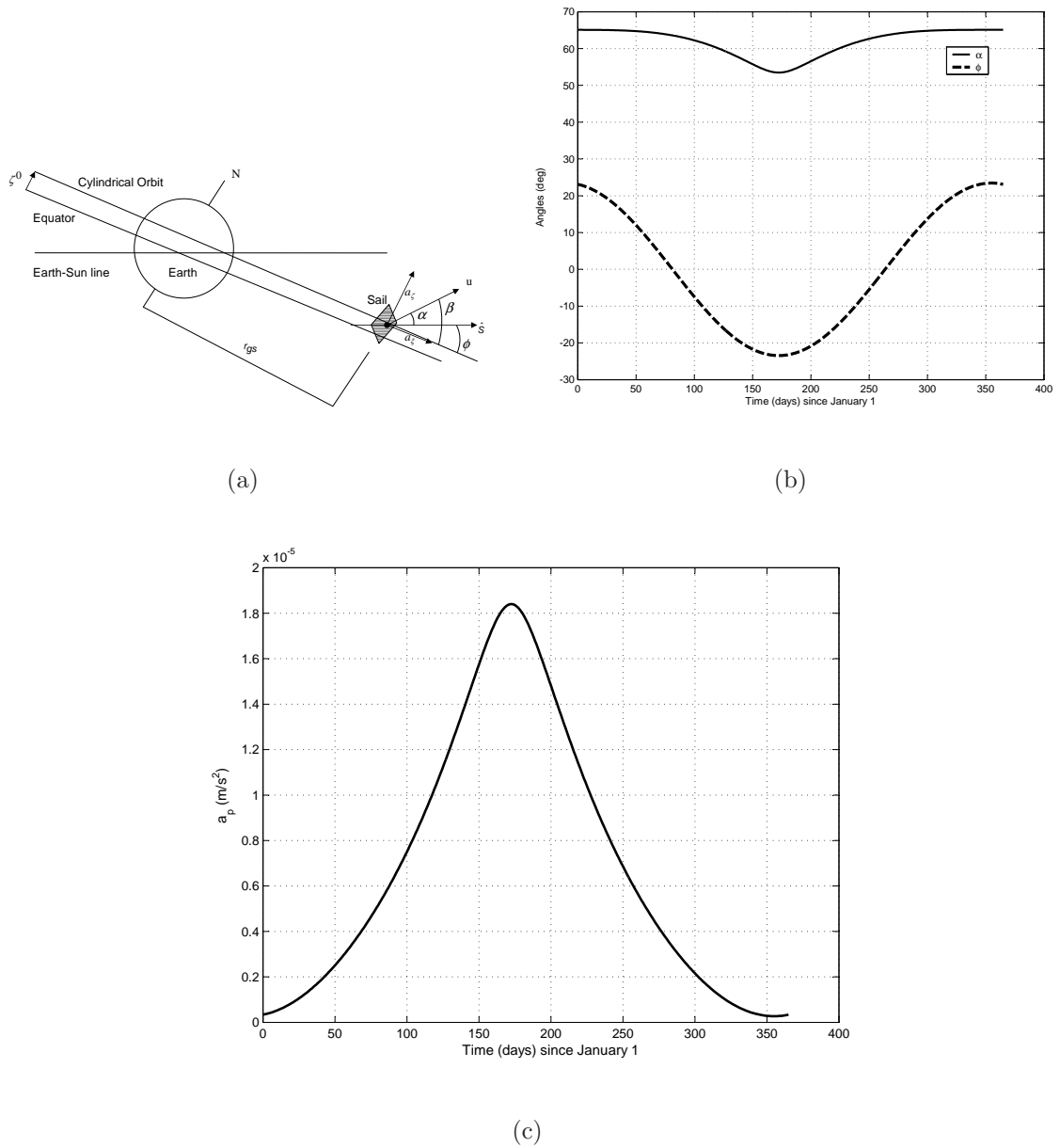


Figure 5.12: (a) Light-levitated cylindrical orbit at +2 km (b) history of sail pitch angle α and Sun's declination angle ϕ over one year (c) component of sail acceleration parallel to Earth's equatorial plane $a_p = a_0 \cos^2 \alpha \cos(\alpha + \phi)$.

Table 5.1: ΔV budget to generate displaced NKO using pure a SEP system. The displaced NKO with period τ_e is chosen above and synchronous with a geostationary point at r_{gs} .

Displacement above the Earth's equatorial plane km	Thrust acceleration from electric propulsion mms ⁻²	ΔV /year (m/s)	ΔV for 10 years (km/s)
2	0.010	335	3.35
4	0.021	670	6.70
6	0.032	1006	10.06

Now consider the ΔV per year for a pure SEP spacecraft to generate an AEP at displacement ζ_0 above the geostationary point. The type II orbit from reference [66] is selected. Table 5.1 shows the constant thrust acceleration and ΔV required to keep equilibrium in the ECEF-frame at different displacements ζ_0 above the Earth's equatorial plane. It can be seen from Table 5.1 that as ζ_0 increases, the ΔV per year increases as expected, but the ΔV is large even for small displacements. Moreover, it can be seen from Table 5.1 that the ΔV per year (335 m/s) for a pure SEP spacecraft is greater than as compared with the ΔV per year (271 m/s) for a hybrid sail at the same levitation distance of 2 km.

5.8 Conclusions

The possibility of generating displaced non-Keplerian periodic orbits around geostationary points in the solar-sail two body problem has been analysed. It has been shown that a family of displaced non-Keplerian orbits exist at linear order around a geostationary point. It has also been demonstrated that the collocation scheme is a promising approach to obtain displaced periodic orbits at non-linear order for this problem as the inequality path constraints can be enforced easily. The collocation scheme converges to a periodic solution provided the sail characteristic acceleration is large enough to counter the variation in the Earth's gravity

on the displaced orbit around the geostationary point. For a high performance sail with a characteristic acceleration of order 6 mms^{-2} and assuming the Sun-line is in the Earth's equatorial plane, a 62 km non-linear displaced orbit is obtained above the Earth's equatorial plane which is well above the station-keeping box of order $75 \times 75 \text{ km}$ of geostationary communication satellites. For the realistic worst-case scenario at the summer solstice, a high performance sail shows a non-linear displaced periodic orbit at 25 km above the Earth's equatorial plane, while a perforated sail is just above the station-keeping box. Displaced orbits at $\pm 2 \text{ km}$ are illustrated for an application to solar space power generation. These results show that Forward's original concept for displaced geostationary orbit is correct, although displacement distances are modest.

Chapter 6

Periodic Orbits Around a Geostationary Point

This chapter will investigate periodic orbits around a geostationary point using a collocation method and differential corrector method respectively. It will be assumed that the Sun-line $\mathcal{S}(t)$ is in the Earth's equatorial plane. Both methods generate families of periodic orbits of period $T = 2\pi/\Omega^*$ and each orbit always crosses the Earth's equatorial plane. Therefore, these orbits are not displaced or 'levitated' above the Earth's equatorial plane. Firstly, the collocation scheme is used (with no inequality path constraints) to generate such orbits. These 2-body orbits have interesting analogies with 3-body halo orbits.

6.1 Collocation Method with no Inequality Path Constraints

Only the defect constraints, periodic orbit definition constraints and the control constraints $\psi_i = 0$ are necessary for computing the periodic orbits for the sail, so the inequality constraints (or Eq. (5.31)) are neglected. Then, the vector \mathcal{X} of

Eq. (5.32) is given by

$$\boldsymbol{\mathcal{X}}^T = [\boldsymbol{x}_1^T, \boldsymbol{u}_1^T, \boldsymbol{x}_2^T, \boldsymbol{u}_2^T, \dots, \boldsymbol{x}_n^T, \boldsymbol{u}_n^T]$$

The initial guess for states \boldsymbol{x}_i at all node points is provided from the linearised solution Eq. (5.21), and the control \boldsymbol{u}_i at all node points is computed from Eq. (5.8) with $t = t_i$ and the sail attitude constraint is fixed i.e., $\delta(t) = 0$, $\alpha(t) = 35.264^\circ$. In particular, the solution of the linearised displaced orbit at $\zeta^0 = 2.37 \times 10^{-4}$ ($\simeq 10$ km) above the Earth's equator plane with sail characteristic acceleration $a_0^* = 0.000616181$ (0.138 mms^{-2}) is chosen as an initial guess for the states \boldsymbol{x}_i (see the dashed-line orbit in Fig. 6.1). For $n = 100$, the size of $\boldsymbol{\mathcal{X}}$ and \boldsymbol{C} are 900 and 703 respectively. The algorithm converges in a few iterations of Eq. (5.35) and finds the periodic solution (see the solid-line periodic orbit in Fig. 6.1) satisfying the nonlinear non-autonomous differential equations and periodic orbit definition constraints.

However, this periodic solution with the nonlinearity of the Earth's gravity is not a displaced periodic orbit since it crosses the Earth's equatorial plane. The control angle history of the sail on this nonlinear periodic orbit is almost constant and is also shown by the solid-line in Fig. 6.2. The identical control history of the linear and nonlinear solution and Fig. 6.1 implies that the collocation scheme adjusts the states \boldsymbol{x}_i (or effectively position and velocity along the z -axis) from the linearised solution Eq. (5.21) to provide a periodic solution of the full nonlinear system. Therefore, it may be anticipated that these nonlinear periodic orbits with a constant control history for the sail can also be obtained by using a shooting/differential corrector method which will effectively fine tune the initial guess of the linear solution Eq. (5.21) to obtain periodic solution of Eq. (5.22). Furthermore, the analysis with no inequality path constraints confirms that inequality path constraints are necessary to investigate the displaced periodic orbits of Eq. (5.22).

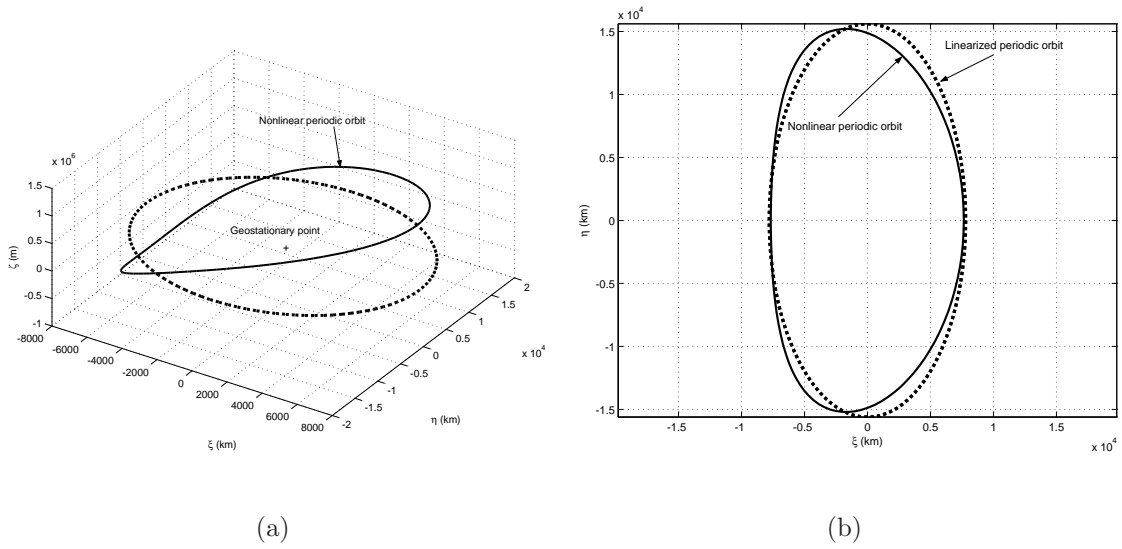


Figure 6.1: (a) Dashed-line represent flat linearised displaced periodic orbit at distance of 10 km above the Earth’s equatorial plane. The solid-line is a periodic solution of Eq. (5.22) around a geostationary point, however it is not a displaced orbit. Both orbits have the same period $T = 2\pi/\Omega^*$ and sail characteristic acceleration 0.138 mms^{-2} (b) periodic orbits x - y projection.

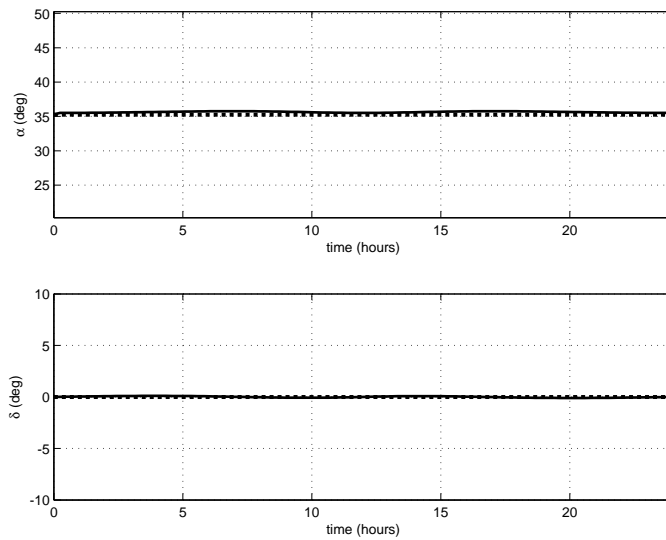


Figure 6.2: The dashed-line and solid line are control history of the linear and nonlinear periodic orbits of Fig. 6.1 respectively.

6.2 Differential Corrector Method

This section evaluates whether the periodic orbits discussed in section 6.1 can also be obtained for the nonlinear system using a differential corrector. The simple case when the solar sail has a constant orientation (i.e., $\alpha(t) = \alpha, \delta(t) = 0$) will be analysed. The nonlinear equation of motion (see Eq. (5.4)), is then given by

$$\frac{d^2 \mathbf{r}}{dt^2} + 2\boldsymbol{\omega}_e \times \frac{d\mathbf{r}}{dt} + \nabla \mathcal{U} = a_0 \cos^2 \alpha \mathbf{u} \quad (6.1)$$

where $\mathbf{u} = (\cos \alpha \cos(\Omega^* t), -\cos \alpha \sin(\Omega^* t), \sin \alpha)^T$.

6.2.1 Linear Periodic Solution for z -Equation

For the nonlinear analysis using the differential corrector method, the information from the linear analysis (Sect. 5.2) with constant sail orientation can be used. The linear solution $\xi(t), \eta(t)$ (see Eq. (5.21)) is periodic with period $T = 2\pi/\Omega^*$. However, Eq.(5.16) is a condition for an NKO, with $\zeta(t) = \zeta^0$. To obtain a periodic solution in the z -equation (or $\zeta(t)$) with frequency Ω^* , it is assumed that the nonlinear terms along with the sail forcing term causes an out of plane frequency equal to the in-plane frequency i.e., Ω^* , so with this assumption the linearised equation in $\zeta(t)$ i.e., Eq. (5.14) can be re-written as

$$\frac{d^2 \zeta}{dt^2} + \Omega^{*2} \zeta = a_0 \cos^2 \alpha \sin \alpha = a_\zeta \quad (6.2)$$

Then, the linearised equation has a periodic solution with frequency Ω^* given by

$$\begin{aligned} \xi(t) &= A_\xi \cos(\Omega^* t) \\ \eta(t) &= B_\eta \sin(\Omega^* t) \\ \zeta(t) &= A_1 \cos(\Omega^* t) + B_1 \sin(\Omega^* t) + a_\zeta / \Omega^{*2} \end{aligned} \quad (6.3)$$

where A_ξ and B_η are given in Eq. (5.20). The constants A_1 and B_1 are yet to be determined. The linearised equation Eq. (5.14) is forced to the form Eq. (6.2),

which can be accomplished by re-writing the z -equation of Eq. (6.2) with the function $\Delta = (\Omega^{*2} - U_{zz}^0)$ and non-linear terms as

$$\frac{d^2\zeta}{dt^2} + \Omega^{*2}\zeta = \Delta\zeta + a_0 \cos^2 \alpha \sin \alpha + (\text{non-linear terms}) \quad (6.4)$$

Assuming weak excitation with the sail forcing term $a_0 = \epsilon \bar{a}_0$ and making the assumption that $\Delta = O(\epsilon)$, the sail characteristic acceleration $a_0 \ll 1$ in non-dimensional units and will act as a small parameter ϵ . Non-linear terms must then be included if a periodic solution with frequency Ω^* is expected for the z -equation.

Linearising Eq. (6.1) about the geostationary point \mathbf{r}_{gs} by making the transformation $\mathbf{r} \rightarrow \mathbf{r}_{gs} + \delta\mathbf{r}$, where $\delta\mathbf{r} = (\xi, \eta, \zeta)$, and Taylor expanding ∇U about \mathbf{r}_{gs} up to second order gives the systems of equations

$$\begin{aligned} \frac{d^2\delta\mathbf{r}}{dt^2} + 2\boldsymbol{\omega}_e \times \frac{d\delta\mathbf{r}}{dt} + \nabla U|_{\mathbf{r}=\mathbf{r}_{gs}} + \delta r^a (\partial_a \nabla U)|_{\mathbf{r}=\mathbf{r}_{gs}} + \frac{1}{2} \delta r^a \delta r^b (\partial_a \partial_b \nabla U)|_{\mathbf{r}=\mathbf{r}_{gs}} \\ + O(\delta\mathbf{r}^3) = \mathbf{a}(\mathbf{r}_{gs} + \delta\mathbf{r}) \end{aligned} \quad (6.5)$$

where tensor notation is used to represent the summation over indices a and b . $\partial_a \nabla U|_{\mathbf{r}=\mathbf{r}_{gs}}$ indicates the linearised matrix given in Eq. (5.11). Substituting $\nabla U|_{\mathbf{r}=\mathbf{r}_{gs}} = 0$ and $\frac{\partial \mathbf{a}_{SS}}{\partial \mathbf{r}} = 0$ in Eq. (6.5), these equations can be written in component form as

$$\begin{aligned} \frac{d^2\xi}{dt^2} - 2\frac{d\eta}{dt} + U_{xx}^0 \xi &= 3C(2\xi^2 - \eta^2 - \zeta^2) + a_0 \cos^3 \alpha \cos(\Omega^* t) \\ \frac{d^2\eta}{dt^2} + 2\frac{d\xi}{dt} + U_{yy}^0 \eta &= -6C\xi\eta - a_0 \cos^3 \alpha \sin(\Omega^* t) \\ \frac{d^2\zeta}{dt^2} + \Omega^{*2}\zeta &= -6C\xi\zeta + a_0 \cos^2 \alpha \sin \alpha + \Delta\zeta \end{aligned} \quad (6.6)$$

where $C = -\frac{\sqrt{x_e^2}}{2x_e^5} = -\frac{1}{2}$. Note that the term $\Delta = O(\epsilon)$ is added in the z -equation as explained in Eq. (6.4). Now let the solution have a particular form of expansion, namely

$$\begin{aligned} \xi(\epsilon) &= \epsilon\xi_1 + \epsilon^2\xi_2 + \dots \\ \eta(\epsilon) &= \epsilon\eta_1 + \epsilon^2\eta_2 + \dots \\ \zeta(\epsilon) &= \epsilon\zeta_1 + \epsilon^2\zeta_2 + \dots \end{aligned} \quad (6.7)$$

Substituting the series Eq. (6.7) into Eqs. (6.6), then assembling and equating powers of ϵ .

At first order the linearised systems of equations Eq. (6.3) are obtained as

$$\begin{aligned}
 O(\epsilon) : \quad \frac{d^2 \xi_1}{dt^2} - 2 \frac{d\eta_1}{dt} + U_{xx}^0 \xi_1 &= \bar{a}_0 \cos^3 \alpha \cos(\Omega^* t) \\
 \frac{d^2 \eta_1}{dt^2} + 2 \frac{d\xi_1}{dt} + U_{yy}^0 \eta_1 &= -\bar{a}_0 \cos^3 \alpha \sin(\Omega^* t) \\
 \frac{d^2 \zeta_1}{dt^2} + \Omega^{*2} \zeta_1 &= \bar{a}_0 \cos^2 \alpha \sin(\alpha) = a_\zeta
 \end{aligned} \tag{6.8}$$

The solution of Eq. (6.8) is then

$$\begin{aligned}
 \xi_1(t) &= A_\xi \cos(\Omega^* t) \\
 \eta_1(t) &= B_\eta \sin(\Omega^* t) \\
 \zeta_1(t) &= A_1 \cos(\Omega^* t) + B_1 \sin(\Omega^* t) + a_\zeta / \Omega^{*2}
 \end{aligned} \tag{6.9}$$

A_1 and B_1 will be determined later when removing the secular terms at higher order. At second order it is found that

$$\begin{aligned}
 O(\epsilon^2) : \quad \frac{d^2 \xi_2}{dt^2} - 2 \frac{d\eta_2}{dt} + U_{xx}^0 \xi_2 &= 3C(2\xi_1^2 - \eta_1^2 - \zeta_1^2) \\
 \frac{d^2 \eta_2}{dt^2} + 2 \frac{d\xi_2}{dt} + U_{yy}^0 \eta_2 &= -6C\xi_1 \eta_1 \\
 \frac{d^2 \zeta_2}{dt^2} + \Omega^{*2} \zeta_2 &= -6C\xi_1 \zeta_1 + \Delta \zeta_1
 \end{aligned} \tag{6.10}$$

Substituting in the ζ_2 -equation the expressions for ξ_1 and ζ_1 i.e., the first order solution from Eq. (6.9), it can be seen that

$$\begin{aligned}
 \frac{d^2 \zeta_2}{dt^2} + \Omega^{*2} \zeta_2 &= \left(\frac{-6CA_\xi a_\zeta}{\Omega^{*2}} + \Delta A_1 \right) \cos(\Omega^* t) + (\Delta B_1) \sin(\Omega^* t) \\
 &\quad + \frac{\Delta a_\zeta}{\Omega^{*2}}
 \end{aligned}$$

The solution ζ_2 is required to have period $\frac{2\pi}{\Omega^*}$, so the coefficients of $\cos(\Omega^* t)$ and $\sin(\Omega^* t)$ must be zero otherwise any solution of ζ_2 would contain the undesirable terms $t \cos(\Omega^* t)$ and $t \sin(\Omega^* t)$, which are secular terms. Thus the coefficients of

$\cos(\Omega^*t)$ and $\sin(\Omega^*t)$ are set to be zero

$$\begin{aligned}\Delta B_1 &= 0 \\ -6CA_\xi \frac{a_\zeta}{\Omega^{*2}} + \Delta A_1 &= 0\end{aligned}$$

which implies constraints on the constants A_1 and B_1

$$\begin{aligned}B_1 &= 0 \\ A_1 &= \frac{1}{\Delta} \left(\frac{6CA_\xi a_\zeta}{\Omega^{*2}} \right)\end{aligned}$$

So ζ_1 in Eq. (6.9) now becomes

$$\zeta_1 = \frac{1}{\Delta} \left(\frac{6CA_\xi a_\zeta}{\Omega^{*2}} \right) \cos(\Omega^*t) + \frac{a_\zeta}{\Omega^{*2}} \quad (6.11)$$

Thus, to order ϵ the expression for the periodic solution (see Eq. (6.7)) is given by

$$\begin{aligned}\xi &= \epsilon(A_\xi \cos(\Omega^*t)) \\ \eta &= \epsilon(B_\eta \sin(\Omega^*t)) \\ \zeta &= \epsilon(\zeta_1)\end{aligned}$$

To remove the ϵ from the solution, apply the mapping $\bar{a}_0 \mapsto \frac{a_0}{\epsilon}$. In short, the complete first order solution is given by

$$\begin{aligned}\xi(t) &= A_\xi \cos(\Omega^*t) \\ \eta(t) &= B_\eta \sin(\Omega^*t) \\ \zeta(t) &= \frac{6CA_\xi}{\Delta} \left(\frac{a_0 \cos^2 \alpha \sin \alpha}{\Omega^{*2}} \right) \cos(\Omega^*t) + \frac{a_0 \cos^2 \alpha \sin \alpha}{\Omega^{*2}}\end{aligned} \quad (6.12)$$

The constant term in $\zeta(t)$ indicates that the solution does not have a mean value of zero in $\zeta(t)$. Setting $t = 0$ in Eq. (6.12) a set of initial conditions are obtained. If this initial condition is used to integrate the nonlinear equations of motion Eq. (6.1), the trajectory corresponding to an almost periodic orbit is found. Then using the differential corrector, the initial conditions can be tuned until the initial conditions for a true periodic orbit are found.

6.2.2 Symmetry in the Equations of Motion

Before applying the differential corrector, it is shown that the nonlinear equations of motion (see Eq. (6.1)) are symmetric with respect to xz -plane under time reversal i.e., $y \rightarrow -y$ and $t \rightarrow -t$. Then, if $(x(t), y(t), z(t))$ is a solution of the equations of motion at time t , $(x(-t), -y(-t), z(-t))$ is also a solution at time $-t$. This symmetry in the equations of motion suggests that the periodic orbit can be found using the differential corrector for the half period $T_{1/2} = \pi/\Omega^*$ only.

The nonlinear equations of motion Eq. (6.1) can be written in component form as

$$\begin{aligned}\ddot{x} - 2\dot{y} &= \Omega_x \\ \ddot{y} + 2\dot{x} &= \Omega_y \\ \ddot{z} &= \Omega_z\end{aligned}\tag{6.13}$$

where

$$\begin{aligned}\Omega_x &\equiv \frac{-x}{r^3} + x + a_\xi \\ \Omega_y &\equiv \frac{-y}{r^3} + y + a_\eta \\ \Omega_z &\equiv \frac{-z}{r^3} + a_\zeta\end{aligned}$$

and $a_\xi = a_0 \cos^3 \alpha \cos(\Omega^*t)$, $a_\eta = -a_0 \cos^3 \alpha \sin(\Omega^*t)$ and $a_\zeta = a_0 \cos^2 \alpha \sin(\alpha)$. Making the transformation $(x(t), y(t), z(t), t) \rightarrow (x(-t), -y(-t), z(-t), -t)$ into Eq. (6.13), it can be seen that

$$\begin{aligned}\ddot{x}(-t) - 2\dot{y}(-t) &= \Omega_x(x(-t), y(-t), z(-t), -t) \\ -\ddot{y}(-t) - 2\dot{x}(-t) &= \Omega_y(x(-t), y(-t), z(-t), -t) \\ \ddot{z}(-t) &= \Omega_z(x(-t), y(-t), z(-t), -t)\end{aligned}$$

Since

$$\begin{aligned}\Omega_x(x(-t), y(-t), z(-t), -t) &= \Omega_x \\ \Omega_y(x(-t), y(-t), z(-t), -t) &= -\Omega_y \\ \Omega_z(x(-t), y(-t), z(-t), -t) &= \Omega_z\end{aligned}$$

which shows the symmetric solution $(x(-t), -y(-t), z(-t), -t)$ also satisfies the equations of motion.

6.2.3 Differential Corrector for Periodic Solution

In this section the differential corrector method is used to find the periodic solution of the nonlinear equations of motion subjected to external excitation [77, 88] i.e., the periodically forced solar sail term. The initial conditions from Eq. (6.12) have the form

$$\mathbf{x}(0) = (1 + \xi(0), 0, \zeta(0), 0, \dot{\eta}(0), 0) = (x_0, 0, z_0, 0, \dot{y}_0, 0)$$

so that the spacecraft leaves the xz -plane perpendicularly. On returning to the xz -plane at time $t = T_{1/2} = \pi/\Omega^*$, the conditions are

$$\mathbf{x}(T_{1/2}) = (\tilde{x}, 0, \tilde{z}, \dot{\tilde{x}}, \dot{\tilde{y}}, \dot{\tilde{z}})$$

Let $\mathbf{x}^T = [\mathbf{r}^T, \mathbf{v}^T]$ and let the non-linear system Eq. (6.1) can be written as $\dot{\mathbf{x}} = \mathbf{f}(t, \mathbf{x}, \mathbf{u})$. To obtain a periodic orbit, the three independent parameters x_0, \dot{y}_0, z_0 can be varied iteratively to make the three parameters $y, \dot{\tilde{x}}, \dot{\tilde{z}}$ zero at $t = T_{1/2}$. The corrections $\Delta x_0, \Delta \dot{y}_0$ and Δz_0 in x_0, \dot{y}_0, z_0 can be calculated from (see Eq. (2.15), whereas in Eq. (2.16) the matrix $A(t) = \frac{\partial \mathbf{f}}{\partial \mathbf{x}}$ is the Jacobian of the nonlinear system $\dot{\mathbf{x}} = \mathbf{f}(t, \mathbf{x}, \mathbf{u})$.

The solid lines in Fig. 6.3 and Fig. 6.4 show the periodic orbits around the geostationary point generated by the differential corrector method (as explained above) with sail characteristic acceleration a_0 (0.05 mms^{-2}) and a_0 (0.1 mms^{-2}) respectively. The dashed lines in Fig. 6.3 and Fig. 6.4 are the corresponding linearised solution from Eq. (6.12). In both figures, the sail is pitched at an angle $\alpha^* = 35.264^\circ$. The linearised solution is in good agreement with the numerically generated differential corrector solution of the non-linear equations of motion. Fig. 6.4 shows that as the sail characteristic acceleration a_0 increases the orbit (see solid line) is shifted upward along the z -axis, however it always crosses the Earth's equatorial plane.

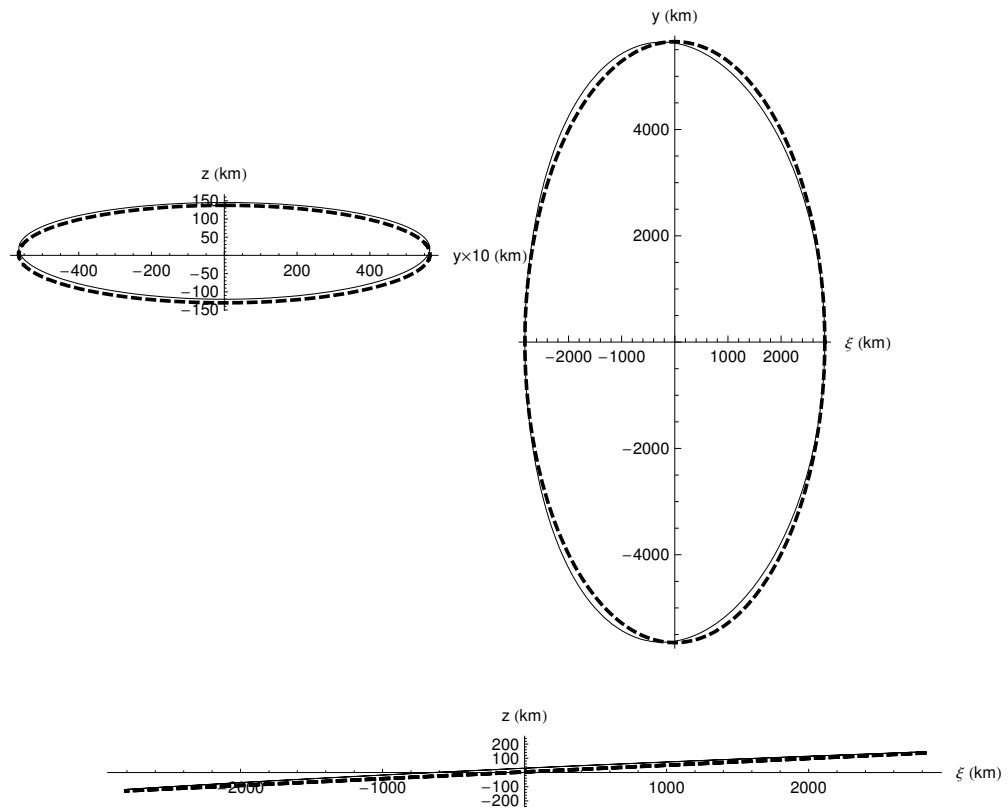


Figure 6.3: Projections of periodic orbits ($a_0(0.05 \text{ mms}^{-2})$) around a geostationary point in the ECEF-rotating frame. Dashed line is the linearised orbit and solid line is the nonlinear orbit from the differential corrector.

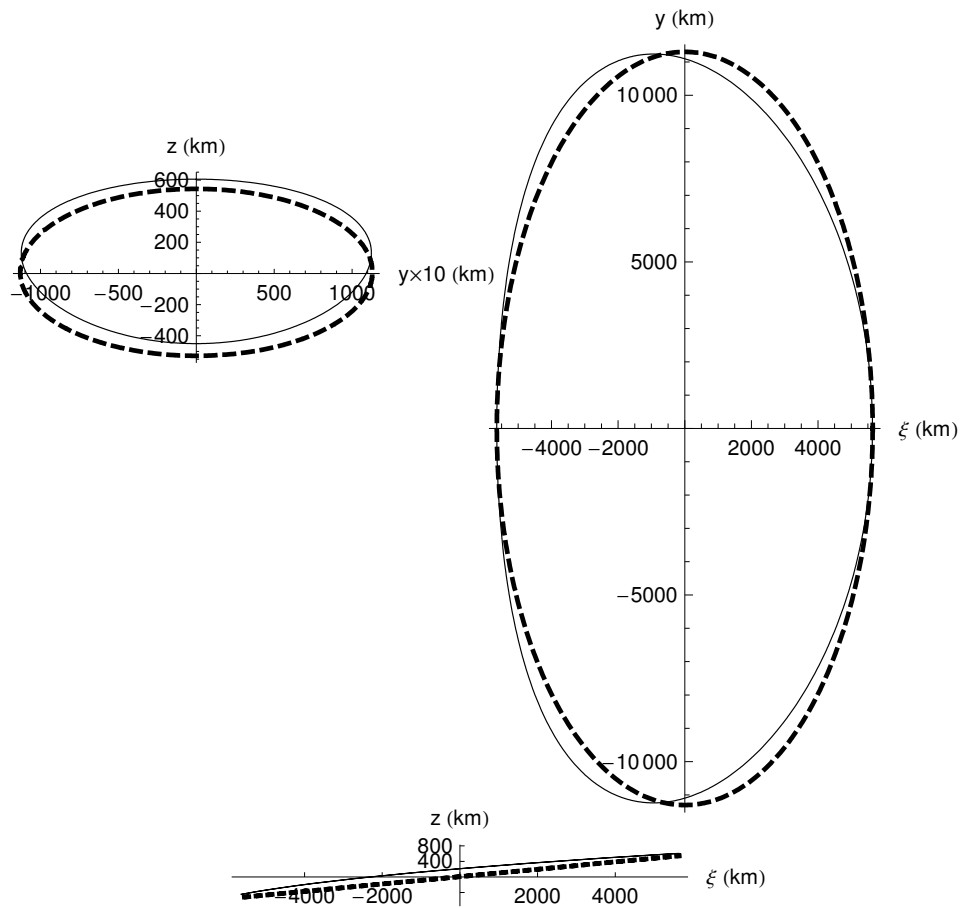


Figure 6.4: Projections of periodic orbits ($a_0(0.1 \text{ mms}^{-2})$) around a geostationary point in the ECEF-rotating frame. Dashed line is the linearised orbit and solid line is the nonlinear orbit from the differential corrector.

The differential corrector algorithm converges up to a_0 (0.3 mms^{-2}) for the initial guess given by Eq. (6.12). For $a_0 > 0.3 \text{ mms}^{-2}$, the continuation method can then be used to find periodic orbits. The sail characteristic acceleration a_0 is used as the continuation parameter. In Fig. 6.5, the thick solid line and dashed-line periodic orbits are generated using the continuation method for a sail with a_0 (0.335 mms^{-2}) and a_0 (0.425 mms^{-2}) respectively. Thus Fig. 6.5 shows that there exists a family of periodic orbits with period $T = \frac{2\pi}{\Omega^*}$ around a geostationary point.

To compare the differential corrector method with the collocation scheme, a periodic orbit is generated using the collocation scheme (see Sect. 6.1) for a sail with characteristic acceleration 0.425 mms^{-2} as shown in Fig. 6.6. The linearised solution given by Eq.(5.21) is used as an initial guess with a fixed $\alpha^* = 35.264^\circ$ and $\delta = 0$. Note that, the corresponding orbit using the differential corrector scheme for a_0 (0.425 mms^{-2}) is shown by the dashed-line in Fig. 6.5. The collocation scheme has a larger radius of convergence since it converges to a periodic orbit for a_0 (0.425 mms^{-2}), while the differential corrector scheme has to go through a continuation method to obtain an orbit for a_0 (0.425 mms^{-2}). However, the differential corrector has a simple (fixed) attitude strategy and the sail has two perpendicular crossings of the xz -plane.

The periodic orbits shown in Fig. 6.5 will be inclined elliptical orbits in the ECI-frame. However, these orbits will be slightly different from Keplerian inclined elliptical orbits, since the sail follows the Sun-line to make an orbit period $T = 2\pi/\Omega^*$.

6.3 Conclusions

A family of periodic orbits of period $T = 2\pi/\Omega^*$ around a geostationary point has been found using the collocation method and the differential corrector method, however all the orbits cross the Earth's equatorial plane. Choosing an initial

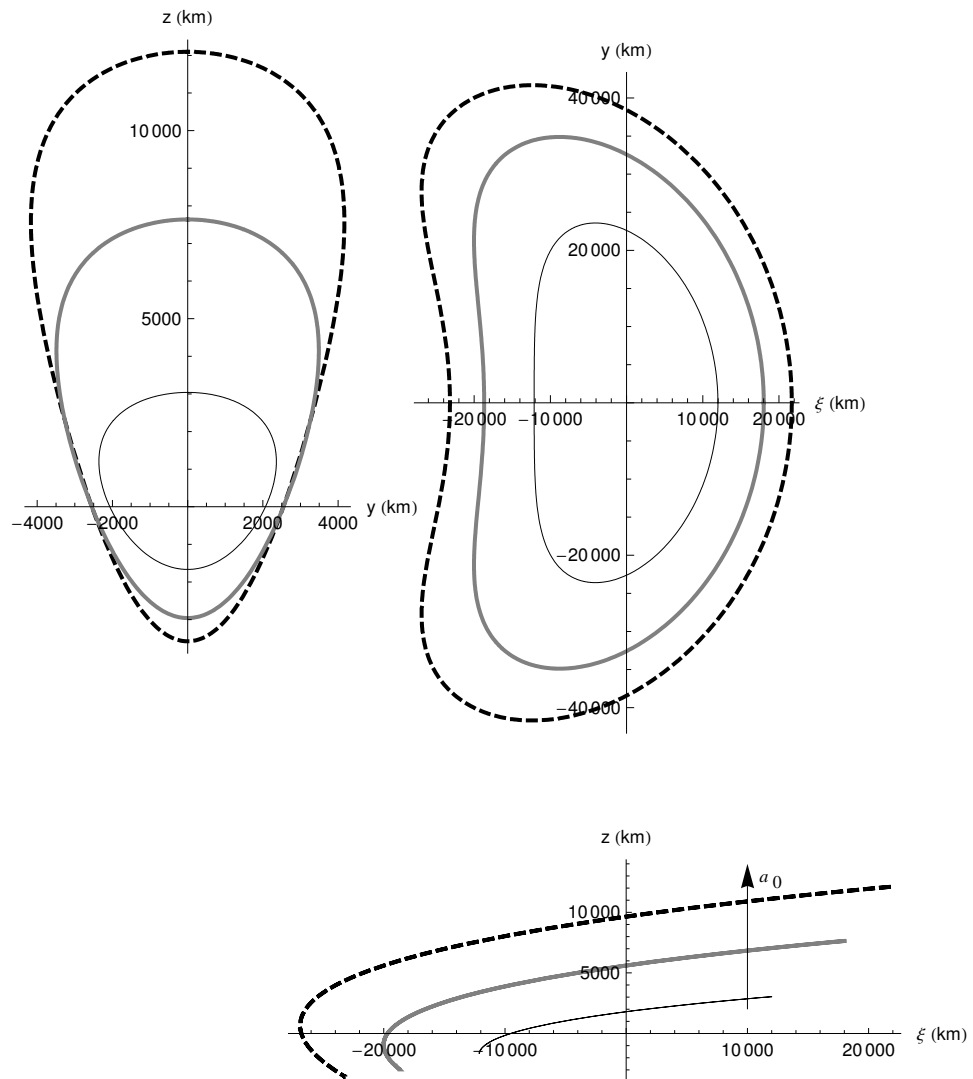
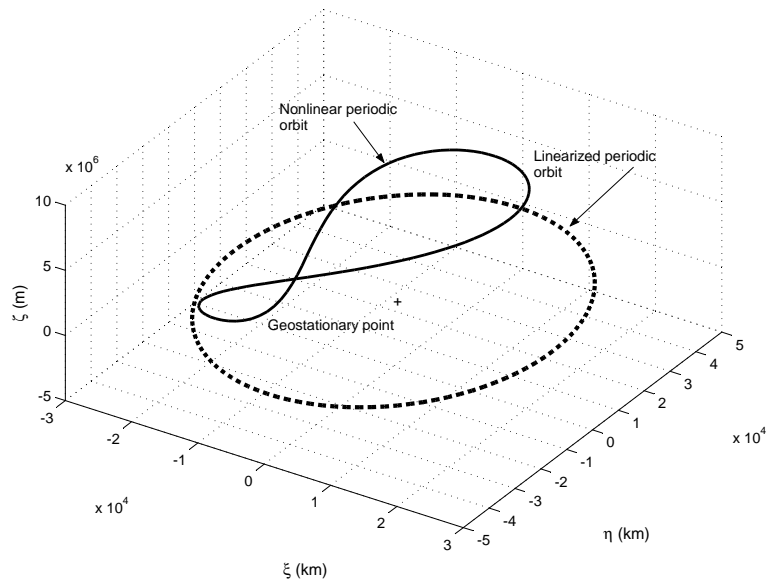
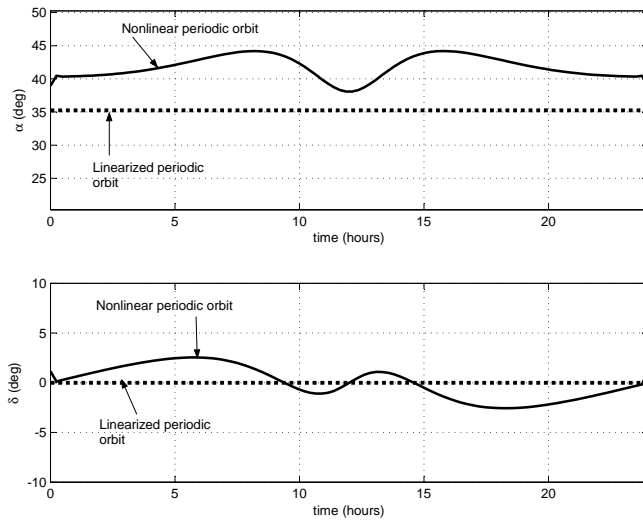


Figure 6.5: Nonlinear periodic orbits of period $T = 2\pi/\Omega^*$ around a geostationary point in the ECEF-rotating frame with $\alpha^* = 35.264^\circ$ and different a_0 parameters: a_0 (0.215 mms^{-2}) for the thin solid-line, a_0 (0.335 mms^{-2}) for the thick solid-line, and a_0 (0.425 mms^{-2}) for the dashed-line. The thick solid-line and dashed-line orbits are generated using the continuation method while the thin solid line orbit is obtained using the differential corrector method.



(a)



(b)

Figure 6.6: A sail with characteristic acceleration 0.425 mms^{-2} (a) the periodic orbit in the ECEF-frame and (b) sail control history obtained using the collocation scheme. The linearised periodic orbit, shown by the dashed-line, is an initial guess for the collocation scheme.

guess from the linear analysis with $\alpha = 35.264^\circ$ and varying the sail characteristic acceleration a_0 , it is demonstrated that the differential scheme converges to the periodic orbits. Starting from the linear solution, the maximum value of a_0 for which the collocation scheme converges to a periodic orbit is higher in value than using the differential corrector method. Therefore, the collocation scheme has a convergence radius greater than the differential corrector method. However, periodic orbits from the differential corrector method (or strictly speaking from the continuation method) have a simple (fixed) attitude strategy. Notably, the analysis of the collocation scheme with no inequality path constraints suggests that inequality path constraints are necessary to generate the displaced NKO of Chapter 5.

Chapter 7

Conclusion

In this thesis new non-Keplerian orbits for solar electric propulsion spacecraft, solar sail propulsion spacecraft and hybrid sail/solar electric propulsion spacecraft have been devised. The appropriate low thrust propulsion system for generating these new non-Keplerian orbits has been identified while considering current and near-term technological constraints for these propulsion systems. The research proposes solar electric propulsion spacecraft for halo orbits around artificial equilibrium points (AEPs) along the Sun-Earth line in the forbidden regions for solar sails, the hybrid sail for displaced non-Keplerian orbits above the ecliptic plane, and solar sails for displaced non-Keplerian orbits above geostationary orbit. The contribution of each chapter to the field is summarised below:

7.1 Chapter 2

In *chapter 2*, the possibility of halo orbits in the Sun-Earth circular restricted three body problem was demonstrated using current and near-term solar electric propulsion technologies. In particular, halo orbits are shown to exist about AEPs at locations where a solar sail cannot generate periodic orbits because of the requirement that the sail thrust cannot be directed towards the Sun i.e., AEPs inside L_1 and beyond L_2 . In addition to unstable halo orbits about these AEPs, it is

also shown that stable halo orbits exist for AEPs beyond L_2 . Such stable halo orbits require thrust acceleration available from current solar electric propulsion technologies. The AEPs are chosen near to the natural Lagrange points L_1 and L_2 to limit the power and thrust level from the solar-electric propulsion system.

7.2 Chapter 3 and Chapter 4

In *chapter 3* a new idea for generating AEPs using a hybrid sail in the Sun-Earth circular restricted three body problem is proposed. The idea extends the hybrid sail concept, originally proposed for orbit transfer, to use at equilibrium points. Notably, it was found that the hybrid sail can be in equilibrium in the forbidden regions for a sail, thereby night-side communication along the polar axis as envisaged by Forward is possible by using a thruster system with a sail. For the Earth polar observer mission, it was found that for a hybrid sail with a given near-term sail assembly loading and 5 year mission life, the sail size is smaller than a pure solar sail and the propellant mass lower than a pure solar electric propulsion spacecraft. In addition, the optimisation of the hybrid sail thrust strategy showed the feasibility of the hybrid sail for the Earth polar observer mission in terms of initial spacecraft mass. Thus, the hybrid sail has advantages for the Earth polar observer mission since a large pure sail is difficult to control and the large propellant mass in the pure solar electric propulsion system is difficult to process with a single thruster.

In *chapter 4* a strategy to stabilise the hybrid sail at artificial equilibria is devised since the AEPs for the Earth polar observer mission are unstable. The simple strategy of orienting the thruster system while keeping the large sail at a fixed attitude is shown to be robust to injection errors and to stabilise the hybrid sail at the desired AEP. An advantage of the hybrid sail is that a simple control strategy is possible since the large sail is at a fixed attitude during whole mission life.

The hybrid sail is not an option to generate halo orbits about AEPs inside L_1 and beyond L_2 (Chapter 2) on the Sun-Earth line since the hybrid sail cannot use solar radiation pressure at these locations, and acts as a pure solar electric propulsion system. Therefore, solar electric propulsion is the only option to generate halo orbits around such AEPs.

7.3 Chapter 5 and Chapter 6

In *chapter 5* an idea first proposed by Forward [27, 28], that light-levitated geostationary orbits (displaced NKO) exist in the solar-sail two-body problem was investigated. However, in the literature [26, 91] it was claimed that such light-levitation is not possible. It was first shown that a family of displaced NKO exist at linear order. Displaced NKO at non-linear order are then obtained using a collocation scheme rather than the usual differential corrector scheme. For the worst-case sail orientation at the summer solstice, it was found that a near term and high performance sail can be displaced between 10 km and 25 km above the Earth's equatorial plane respectively, while a perforated sail can be displaced just above the usual station-keeping box (75×75) km for nominal geostationary satellites. In short, only modest displacements are possible due to the large component of sail acceleration in the equatorial plane.

In *chapter 6*, it was shown that inequality path constraints are necessary to obtain displaced NKO, otherwise all the orbits generated using a differential corrector (or continuation method) intersect the Earth's equatorial plane. Therefore, the collocation scheme is the most promising approach for generating the displaced NKO given in *chapter 5*, as it can handle inequality path constraints.

7.4 Future Work

For chapter 2, future work includes stabilisation of unstable artificial halo orbits about AEPs using the thruster pitch and yaw angles. An in-depth stability analysis of these halo orbits will also be of interest, as mentioned in section 2.5.

For chapter 3 and chapter 4, the possibility of a hybrid sail being used to generate periodic orbits can be investigated. In particular, a one year orbit in the circular restricted three-body problem will be of interest to narrow the angle of elevation of the hybrid sail as viewed from the pole compared to a fixed equilibrium point on the day or night side of the Earth. Periodic orbits with fixed initial mass can be generated and then tracked with the thruster gimbal angle to counter the variation in the hybrid sail mass.

For chapter 5 and chapter 6, the high order Gauss-Lobatto collocation scheme with constraints on the rates of the sail attitude angles can be used to generate displaced NKO above geostationary orbit. The lower-order Hermite-Simpson collocation scheme with larger nodes will accumulate rounding errors. Secondly, the collocation scheme could be used to generate displaced NKO considering changes in the Sun's declination angle over one day, starting from an initial guess of the linearised model with a fixed solar declination.

For a given displacement above the Earth's equatorial plane, the size of the displaced NKO around the equilibrium point and sail characteristic acceleration can be reduced by investigating orbits beyond geostationary radius. Such orbits will be displaced NKO, but the equilibrium point and so the orbit will not be synchronous with the Earth. It will be of interest to investigate if the displacement can become greater than the Earth's radius to allow for polar communications.

Appendix A

Linearized Solution

A.1 Eigenvector for Centre Eigenvalue

The eigenvector $\mathbf{u}_1 + i\mathbf{w}_1$ of the eigenvalue $i\lambda_1$ is determined by

$$\begin{pmatrix} 0 & 0 & 1 & 0 \\ 0 & 0 & 0 & 1 \\ a & 0 & 0 & 2 \\ 0 & b & -2 & 0 \end{pmatrix} \begin{pmatrix} x_1 \\ x_2 \\ x_3 \\ x_4 \end{pmatrix} = i\lambda_1 \begin{pmatrix} x_1 \\ x_2 \\ x_3 \\ x_4 \end{pmatrix} \quad (\text{A.1})$$

Consequently

$$x_3 = i\lambda_1 x_1, \quad x_4 = i\lambda_1 x_2, \quad ax_1 + 2x_4 = i\lambda_1 x_3, \quad bx_2 - 2x_3 = i\lambda_1 x_4 \quad (\text{A.2})$$

Solving this system by choosing $x_2 = (a + \lambda_1^2)$, we find

$$\begin{pmatrix} x_1 \\ x_2 \\ x_3 \\ x_4 \end{pmatrix} = \begin{pmatrix} -2i\lambda_1 \\ (a + \lambda_1^2) \\ 2\lambda_1^2 \\ i\lambda_1(a + \lambda_1^2) \end{pmatrix} = \mathbf{u}_1 + i\mathbf{w}_1 \quad (\text{A.3})$$

Note that $\lambda_1 = w_{xy}$.

A.2 Bounded solution for δx and δy

Substituting $C = D = 0$ in Eq. (2.9), the equations for δx and δy are obtained as

$$\begin{aligned}\delta x &= -2w_{xy}B \cos(w_{xy}t) + 2w_{xy}A \sin(w_{xy}t) \\ \delta y &= A(a + w_{xy}^2) \cos(w_{xy}t) + B(a + w_{xy}^2) \sin(w_{xy}t)\end{aligned}\quad (\text{A.4})$$

The constants A and B can be determined in terms of initial position deviation δx_0 and δy_0 by substituting $t = 0$ in Eq. (A.4) which yields

$$\begin{aligned}A &= \frac{\delta y_0}{a + w_{xy}^2} \\ B &= \frac{\delta x_0}{-2w_{xy}}\end{aligned}\quad (\text{A.5})$$

Substituting Eq. (A.5) in Eq. (A.4) and using the relations $\delta x_0 = A_x \cos \phi$ and $\frac{2w_{xy}\delta y_0}{a + w_{xy}^2} = A_x \sin \phi$, it is found that

$$\begin{aligned}\delta x &= -A_x \cos(w_{xy}t + \phi) \\ \delta y &= \frac{a + w_{xy}^2}{2w_{xy}} A_x \sin(w_{xy}t + \phi)\end{aligned}$$

where A_x is the x -amplitude of the orbit and the phase ϕ corresponds to the starting point on the orbit.

Appendix B

Hybrid sail acceleration due to SRP with TFSC

B.1 Nondimensional solar sail acceleration due to SRP with TFSC

Divide Eq. (3.4) by m and the dimensional reference acceleration $\omega^2 R$, then the hybrid sail acceleration due to SRP is given by

$$\mathbf{a}_S = a_n \mathbf{n} + a_t \mathbf{t} \quad (\text{B.1})$$

where the normal and tangential acceleration components are given by

$$\begin{aligned} a_n &= (\hat{\mathbf{r}}_1 \cdot \mathbf{n})^2 \left[(1 + \tilde{r}_S) \frac{PA_S}{m} \frac{1}{\omega^2 R} + (1 + \tilde{r}_{TF}) \frac{PA_{TF}}{m} \frac{1}{\omega^2 R} \right] \\ a_t &= (\hat{\mathbf{r}}_1 \cdot \mathbf{n})(\hat{\mathbf{r}}_1 \cdot \mathbf{t}) \left[(1 - \tilde{r}_S) \frac{PA_S}{m} \frac{1}{\omega^2 R} + (1 - \tilde{r}_{TF}) \frac{PA_{TF}}{m} \frac{1}{\omega^2 R} \right] \end{aligned}$$

Now, it can be seen that

$$\begin{aligned} \frac{PA_S}{m} \frac{1}{\omega^2 R} &= \left[\frac{L_s}{4\pi R_1^2 c} \right] \frac{A_S}{m} \left[\frac{R^2}{G(m_1 + m_2)} \right] \\ &= \frac{1}{2} \left[\frac{2}{c} \frac{L_s}{4\pi G m_1} \right] \frac{m_1}{(m_1 + m_2)} \frac{1}{\left(\frac{R_1}{R}\right)^2} \frac{A_S}{m} \end{aligned} \quad (\text{B.2})$$

The term $\frac{2}{c} \frac{L_s}{4\pi G m_1}$ is the critical loading parameter σ^* whose value is approximately $1.53 \times 10^{-3} \text{ kg/m}^2$. Denoting $\beta_0 \equiv \frac{\sigma^*}{(\frac{m_0}{A_T})}$, then Eq. (B.2) becomes as

$$\frac{PA_S}{m} \frac{1}{\omega^2 R} = \frac{1}{2} \beta_0 \frac{m_0}{m} \left(1 - \frac{A_{TF}}{A_T}\right) \frac{1 - \mu}{r_1^2} \quad (\text{B.3})$$

Similarly, it can be seen that

$$\frac{PA_{TF}}{m} \frac{1}{\omega^2 R} = \frac{1}{2} \beta_0 \frac{m_0}{m} \frac{A_{TF}}{A_T} \frac{1 - \mu}{r_1^2} \quad (\text{B.4})$$

Substitute Eqs. (B.3) and (B.4) in Eq. (B.1), the SRP acceleration vector for a hybrid sail acting along \mathbf{m} in non-dimensional form is then given by

$$\mathbf{a}_S = a_s \mathbf{m} = \frac{1}{2} \beta_0 \frac{m_0}{m} \frac{1 - \mu}{r_1^2} g (\hat{\mathbf{r}}_1 \cdot \mathbf{n})^2 \mathbf{n} + \frac{1}{2} \beta_0 \frac{m_0}{m} \frac{1 - \mu}{r_1^2} h (\hat{\mathbf{r}}_1 \cdot \mathbf{n}) (\hat{\mathbf{r}}_1 \cdot \mathbf{t}) \mathbf{t} \quad (\text{B.5})$$

where

$$\begin{aligned} g &= (1 + \tilde{r}_S) - \frac{A_{TF}}{A_T} (\tilde{r}_S - \eta_{TF}) \\ h &= (1 - \tilde{r}_S) + \frac{A_{TF}}{A_T} (\tilde{r}_S - \tilde{r}_{TF}) \end{aligned}$$

B.2 Matrix K in Eq.(3.35)

For the matrix $\frac{\partial \nabla U}{\partial \mathbf{r}}$ in Eq. (3.34) the terms are

$$\frac{\partial \nabla U}{\partial \mathbf{r}} = \begin{pmatrix} U_{xx} & U_{xy} & U_{xz} \\ U_{yx} & U_{yy} & U_{yz} \\ U_{zx} & U_{zy} & U_{zz} \end{pmatrix} \quad (\text{B.6})$$

The acceleration due to solar pressure for a hybrid sail can be rewritten using Eqs. (3.12) and (3.7) as

$$\mathbf{a}_S = \frac{1}{2} \beta_0 \frac{m_0}{m} \frac{1 - \mu}{r_1^4} \psi \mathbf{m}^a \quad (\text{B.7})$$

where

$$\psi = [(g^2 - h^2)(\mathbf{r}_1 \cdot \mathbf{n})^4 + h^2 r_1^2 (\mathbf{r}_1 \cdot \mathbf{n})^2]^{1/2}$$

The partial derivatives of Eq. (B.7) can then be obtained as

$$\begin{aligned} \frac{\partial \mathbf{a}_S}{\partial \mathbf{r}} = & -2\beta_0 \frac{m_0}{m} \frac{(1-\mu)}{r_1^5} \psi \begin{pmatrix} \frac{(x+\mu)}{r_1} m_x & \frac{y}{r_1} m_x & \frac{z}{r_1} m_x \\ \frac{(x+\mu)}{r_1} m_y & \frac{y}{r_1} m_y & \frac{z}{r_1} m_y \\ \frac{(x+\mu)}{r_1} m_z & \frac{y}{r_1} m_z & \frac{z}{r_1} m_z \end{pmatrix} \\ & + \frac{1}{2} \beta_0 \frac{m_0}{m} \frac{(1-\mu)}{r_1^4} \begin{pmatrix} \frac{\partial \psi}{\partial x} m_x & \frac{\partial \psi}{\partial y} m_x & \frac{\partial \psi}{\partial z} m_x \\ \frac{\partial \psi}{\partial x} m_y & \frac{\partial \psi}{\partial y} m_y & \frac{\partial \psi}{\partial z} m_y \\ \frac{\partial \psi}{\partial x} m_z & \frac{\partial \psi}{\partial y} m_z & \frac{\partial \psi}{\partial z} m_z \end{pmatrix} \end{aligned} \quad (\text{B.8})$$

where

$$\begin{pmatrix} \frac{\partial \psi}{\partial x} \\ \frac{\partial \psi}{\partial y} \\ \frac{\partial \psi}{\partial z} \end{pmatrix} = \frac{2(g^2 - h^2)(\mathbf{r}_1 \cdot \mathbf{n})^3 + h^2 r_1^2 (\mathbf{r}_1 \cdot \mathbf{n})}{\psi} \begin{pmatrix} n_x \\ n_y \\ n_z \end{pmatrix} + \frac{h^2 (\mathbf{r}_1 \cdot \mathbf{n})^2}{\psi} \begin{pmatrix} x + \mu \\ y \\ z \end{pmatrix}$$

and $\mathbf{m}^a = [m_x \ m_y \ m_z]^T$ and $\mathbf{n}^a = [n_x \ n_y \ n_z]^T$ may be calculated as

$$\begin{aligned} \mathbf{m}^a &= \mathbf{C}_{b/a}^T \mathbf{m}^b \\ \mathbf{n}^a &= \mathbf{C}_{b/a}^T \mathbf{n}^b \end{aligned} \quad (\text{B.9})$$

For an artificial equilibrium point \mathbf{r}_0 is in the xz -plane, \mathbf{m}^b and \mathbf{n}^b are given by Eqs. (3.26) and (3.29) for option 1 and option 2 respectively. Furthermore, for \mathbf{r}_0 in the xz -plane $y = n_y = m_y = 0$, so the two matrices given in Eqs. (B.6) and (B.8) finally reduce to

$$\left[\frac{\partial \nabla U}{\partial \mathbf{r}} \right]_{\mathbf{r}_0} = \begin{pmatrix} U_{xx} & 0 & U_{xz} \\ 0 & U_{yy} & 0 \\ U_{zx} & 0 & U_{zz} \end{pmatrix} \quad (\text{B.10})$$

and

$$\begin{aligned}
\left[\frac{\partial \mathbf{a}_S}{\partial \mathbf{r}} \right]_{(\mathbf{r}_0, \mathbf{n}^a)} &= -2\beta_0 \frac{m_0}{m} \frac{(1-\mu)}{r_1^5} \psi \begin{pmatrix} \frac{(x+\mu)}{r_1} m_x & 0 & \frac{z}{r_1} m_x \\ 0 & 0 & 0 \\ \frac{(x+\mu)}{r_1} m_z & 0 & \frac{z}{r_1} m_z \end{pmatrix} \\
&+ \frac{1}{2} \beta_0 \frac{m_0}{m} \frac{(1-\mu)}{r_1^4} \begin{pmatrix} \frac{\partial \psi}{\partial x} m_x & 0 & \frac{\partial \psi}{\partial z} m_x \\ 0 & 0 & 0 \\ \frac{\partial \psi}{\partial z} m_z & 0 & \frac{\partial \psi}{\partial z} m_z \end{pmatrix}
\end{aligned} \tag{B.11}$$

so that K in Eq. (3.34) can be calculated using Eqs. (B.10) and (B.11).

Appendix C

Jacobian Matrix

Elements of $\mathcal{D}\mathbf{g}_i$ in the Jacobian matrix \mathcal{DC} are given by

$$\left\{ \frac{\partial \mathbf{g}_i}{\partial \mathbf{x}_i}, \frac{\partial \mathbf{g}_i}{\partial \mathbf{u}_i}, \frac{\partial \mathbf{g}_i}{\partial \mathbf{k}_i} \right\} \quad (\text{C.1})$$

for $i = 1, 2, \dots, n$, and

$$\frac{\partial \mathbf{g}_i}{\partial \mathbf{x}_i} = \begin{pmatrix} -I_3 & O_3 \\ I_3 & O_3 \end{pmatrix}$$

where I_3 and O_3 are the 3×3 identity and null matrix, and

$$\frac{\partial \mathbf{g}_i}{\partial \mathbf{u}_i} = O_{6 \times 3}, \quad \frac{\partial \mathbf{g}_i}{\partial \mathbf{k}_i} = 2\mathbf{k}_i^D$$

where \mathbf{k}_i^D is the 6×6 diagonal matrix with entries $k_i^{(1)}, k_i^{(2)}, \dots, k_i^{(6)}$. The non-zero elements in $\mathcal{D}\psi_i$ are $\frac{\partial \psi_i}{\partial \mathbf{u}_i} = 2\mathbf{u}_i^T$ for $i = 1, 2, \dots, n$. The non-zero elements of $\mathcal{D}h_i$ are given by

$$\begin{pmatrix} \frac{\partial h_1}{\partial \mathbf{x}_1} \\ \frac{\partial h_2}{\partial \mathbf{x}_1} \\ \frac{\partial h_3}{\partial \mathbf{x}_1} \\ \frac{\partial h_4}{\partial \mathbf{x}_1} \\ \frac{\partial h_5}{\partial \mathbf{x}_1} \\ \frac{\partial h_6}{\partial \mathbf{x}_1} \end{pmatrix} = -I_6, \quad \begin{pmatrix} \frac{\partial h_1}{\partial \mathbf{x}_n} \\ \frac{\partial h_2}{\partial \mathbf{x}_n} \\ \frac{\partial h_3}{\partial \mathbf{x}_n} \\ \frac{\partial h_4}{\partial \mathbf{x}_n} \\ \frac{\partial h_5}{\partial \mathbf{x}_n} \\ \frac{\partial h_6}{\partial \mathbf{x}_n} \end{pmatrix} = I_6$$

and

$$\begin{pmatrix} \frac{\partial h_7}{\partial \mathbf{u}_1} \\ \frac{\partial h_8}{\partial \mathbf{u}_1} \\ \frac{\partial h_9}{\partial \mathbf{u}_1} \end{pmatrix} = -I_3, \quad \begin{pmatrix} \frac{\partial h_7}{\partial \mathbf{u}_n} \\ \frac{\partial h_8}{\partial \mathbf{u}_n} \\ \frac{\partial h_9}{\partial \mathbf{u}_n} \end{pmatrix} = I_3$$

Bibliography

- [1] H. Baoyin and C. McInnes. Solar sail halo orbits at the Sun-Earth artificial L_1 point. *Celestial Mechanics and Dynamical Astronomy*, (94):155–171, 2006.
- [2] H. Baoyin and C. R. McInnes. Solar sail orbits at artificial Sun-Earth Lagrange points. *Journal of Guidance, Control and Dynamics*, 28(6):1328–1331, 2005.
- [3] H. Baoyin and C. R. McInnes. Solar sail equilibria in the elliptical restricted three-body problem. *Journal of Guidance, Control and Dynamics*, 29(3):538–543, 2006.
- [4] R. H. Battin. *An Introduction to the Mathematics and Methods of Astrodynamics*. AIAA, Reston, VA, rev. edition, 1999, pp. 573.
- [5] D. Betounes. *Differential Equations: theory and applications*. Springer-Verlag, New York, 2001, pp. 200-205.
- [6] John T. Betts. *Practical Methods for Optimal Control and Estimation Using Nonlinear Programming*. SIAM, Philadelphia, 2nd edition, 2001, pp. 93.
- [7] J. Betts. Survey of numerical method for trajectory optimization. *Journal of Guidance, Control and Dynamics*, 21(2):193–207, 1998.
- [8] J. D. Biggs and C. R. McInnes. Solar sail formation flying for deep-space remote sensing. *Journal of Spacecraft and Rockets*, 46(3):670–677, May-June 2009.

- [9] J. D. Biggs, C. R. McInnes, and T. Waters. Control of solar sail periodic orbits in elliptic three body problem. *Journal of Guidance, Control and Dynamics*, 32(1):318–320, January-February 2009.
- [10] J. D. Biggs, C. R. McInnes, and T. Waters. New periodic orbits in the solar sail restricted three body problem. *2nd Conference on Nonlinear Science and Complexity, Porto, Portugal*, 28-31 July, 2008.
- [11] J. D. Biggs, C. R. McInnes, and T. J. Waters. Stabilizing periodic orbits above the ecliptic plane in the solar sail 3-body problem. *59th IAC Congress, Glasgow, Scotland, UK. IAC-08.C1.5.12*, September 29-October 3, 2008.
- [12] J. Bookless and C. McInnes. Control of Lagrange point orbits using solar sail propulsion. *Acta Astronautica*, 62(2-3):159–176, 2008.
- [13] J. V. Breakwell and J. V. Brown. The ‘halo’ family of 3-dimensional periodic orbits in the Earth-Moon restricted 3-body problem. *Celestial Mechanics*, 20:389–404, 1979.
- [14] J. R. Brophy. Advanced ion propulsion systems for affordable deep-space mission. *Acta Astronautica*, 52(2-6):309–316, March 2003.
- [15] R. Broucke, H. Lass, and D. Boggs. A note on the solution of the variational equations of a class of dynamical systems. *Celestial Mechanics and Dynamical Astronomy*, 14(3):383–392, 1976.
- [16] V. Angelopolous C. R. McInnes, M. Macdonald and D. Alexander. Geosail: Exploring the geomagnetic tail using a small solar sail. *Journal of Spacecraft and Rockets*, 38(4):622–629, August 2001.
- [17] R. J. Cassady, R. H. Frisbeeb, J. H. Gillandc, M. G. Houts, M. R. LaPointe, C. M. Reading, S. R. Oleson, J. E. Polk, D. Russell, and A. Sengupta. Recent advances nuclear powered electric propulsion for space exploration. *Acta Astronautica*, 49:412–435, 2008.

- [18] E. Chesta, D. Estublier, B. Fallis, E. Gengembre, J. Gonzalez del Amo, N. Kutufa, D. Nicolini, G. Saccoccia, L. Casalino, P. Dumazert, M. Prioul, J.P. Boeuf, A. Bouchoule, N. Wallace, G. Noci, M. Berti, M. Saverdi, L. Biagioni, S. Marcuccio, and A. Cadiou. Flexible variable-specific-impulse electric propulsion systems for planetary missions. *Acta Astronautica*, 59:931–945, 2006.
- [19] E. K. P. Chong and S.H. Żak. *An Introduction to Optimization*. John Wiley and Sons, New York, 1996, pp. 177-179.
- [20] D. Cielaszyk and B. Wie. New approach to halo orbit determination and control. *Journal of Guidance, Control and Dynamics*, 19(2):266–273, 1996.
- [21] M. Crison and G. Dittberner. Advanced technologies for future environmental satellite systems. *Paper 1.2, 13th Conference on Satellite Meteorology and Oceanography, Norfolk, Virginia, 2004*.
- [22] B. Dachwald. Solar sail performance requirements for missions to the outer solar system and beyond. *59th International Astronautical Congress 2004-Vancouver, Canada, 2004*.
- [23] D. W. Dunham and R. W. Farquhar. Libration point missions, 1978-2002. *Libration point Orbits and Applications, Costa Brava of Girona, Spain, June-10-14 2002*.
- [24] R. W. Farquhar. The control and use of libration point satellites. *Stanford Univ. SUDAR-350 Stanford, CA, July 1968*.
- [25] R. W. Farquhar and A. A. Kamel. Quasi-periodic orbits about the trans-lunar libration point. *Celestial Mechanics*, 7:458–473, 1973.
- [26] H. J. Fischer and A. Haerting. Why light-levitation geostationary cylindrical orbits are not feasible. *Journal of Astronautical Sciences*, 40(3):329–333, September 1992.

- [27] R. L. Forward. Light-levitated geostationary cylindrical orbits. *The Journal of Astronautical Sciences*, XXIX(1):73–80, January-March 1981.
- [28] R. L. Forward. Light-levitated geostationary cylindrical orbits using perforated light sails. *The Journal of Astronautical Sciences*, 32(2):221–226, April-June 1984.
- [29] R. L. Forward. Statite: a spacecraft that does not orbit. *Journal of Spacecraft and Rockets*, 28(5):606–611, 1991.
- [30] R. H. Frisbee. Advanced space propulsion for the 21st century. *Journal of Propulsion and Power*, 19(6):1129–1154, 2003.
- [31] G. Garbe and E. E. Montgomery. An overview of NASA’s solar sail propulsion project. *39th AIAA Joint Propulsion Conference and Exhibit, Huntsville, AL*, (AIAA 2003-5274), July 20-23, 2004.
- [32] R. Gershman and C. Seybold. Propulsion trades for space science missions. *Acta Astronautica*, 45(4-9):541–548, 1999.
- [33] P. E. Glaser. Satellite solar power station. *Solar Energy*, 12:353–361, Pergamon Press, 1969.
- [34] J. E. Granata, P. E. Hausgen, D. Senft, P. Tlomak, and J. Merrill. AFRL thin film solar cell development and upcoming flight experiments. *Proc. 2005 IEEE Aerospace Conference, Big Sky, Montana, No. 1590*, March 5-12 2005.
- [35] D. Grebow, M. Ozimek, and K. Howell. Multi-body orbit architectures for lunar south pole coverage. *Journal of Spacecraft and Rockets*, 45(2):344–358, 2008.
- [36] P. Gurfil. *Modern Astrodynamics*. Elsevier Ltd, London, first edition, 2006, pp. 189-207.

- [37] P. Gurfil and D. Meltzer. Stationkeeping on unstable orbits: Generalization to elliptic restricted three-body problem. *Journal of Astronautical Sciences*, 54(1):29–51, January-March 2006.
- [38] C. R. Hargraves and S. W. Paris. Direct trajectory optimization using nonlinear programming and collocation. *Journal of Guidance, Control and Dynamics*, 10(4):338–342, 1987.
- [39] E. Hendricks, O. Jannerup, and P. H. Sorensen. *Linear Systems Control: Deterministic and Stochastic Methods*. Springer-Verlag, Berlin Heidelberg, 2008, pp. 124-125.
- [40] A. Herman and B. Conway. Direct optimization using collocation based on high-order Gauss-Lobatto quadrature rules. *Journal of Guidance, Control and Dynamics*, 19(3):592–599, 1996.
- [41] K. C. Howell. Three-dimensional, periodic, ‘halo’ orbits. *Celestial Mechanics*, 32:53–71, 1984.
- [42] K. C. Howell and H. J. Pernicka. Numerical determination of lissajous trajectories in the restricted three-body problem. *Celestial Mechanics*, 41:107–124, 1988.
- [43] L. Johnson, L. Alexander, R. M. Baggett, J. A. Bonometti, M. Hermann, B. F. James, and S. E. Montgomery. NASA’s in-space propulsion technology programme: Overview and update. *40th AIAA/ASME/SAE/ASEE Joint Propulsion Conference and Exhibit, Fort Lauderdale, Florida, AIAA 2004-3841*, 11-14 July, 2004.
- [44] L. Johnson, R. M. Young, and E. E. Montgomery. Recent advances in solar sail propulsion systems at NASA. *Acta Astronautica*, 61:376–382, 2007.

- [45] B. G. June. *Poincare and the three-body problem, History of Mathematics (V.11)*. Providence, RI: American Mathematical Society; London, London Mathematical Society, Providence, Rhode Island 02940-6248, 1997.
- [46] T. Kailath. *Linear Systems*. Prentice Hall, New York, 1980, pp. 610-613, 619, 626.
- [47] M. Kim and C.D. Hall. Lyapunov and halo orbits about L_2 . *AAS/AIAA Astrodynamics Specialist Conference, Quebec City, Canada, AAS 01-324*, Jul 30-Aug 2, 2001.
- [48] S. Kitamura, Y. Ohkawa, Y. Hayakawa, H. Yoshida, and K. Miyazaki. Overview and research status of the JAXA 150-mN ion engine. *Acta Astronautica*, 61:360–366, 2007.
- [49] T. Kremic, D. Anderson, and J. W. Dankanich. NASA’s in space propulsion technology project overview and mission applicability. *2008 IEEE Aerospace Conference, Big Sky, MT, USA*, pages 1–10, March 1-8 2008.
- [50] J. E. Kulkarni, M. E. Campbell, and G. E. Dullerud. Stabilization of spacecraft flight in halo orbits: An H_∞ approach. *IEEE Transactions on Control Systems Technology*, 14(3):572–578, 2006.
- [51] M. Lara, R.P Russel, and B. Villac. Fast estimation of stable regions in real mode. *Celestial Mechanics and Dynamical Astronomy*, 42(5):511–515, October 2007.
- [52] M. Leipold, E. Brog, A. Pabsch, R. Sachs, and W. Seboldt. Mercury orbiter with a solar sail spacecraft. *Acta Astronautica*, 35:635–644, 1995.
- [53] M. Leipold, M. Eiden, C.E. Garner, L. Herbeck, D. Kassing, T. Niederstadt, T. Kruger, G. Pagel, M. Rezazad, H. Rozemeijer, W. Seboldt, C. Schoppinger, C. Sickinger, and W. Unckenbold. Solar sail technology development and demonstration. *Acta Astronautica*, 52:317–326, 2003.

- [54] M. Leipold and M. Götz. Hybrid photonic/electric propulsion. *Kayser-Threde, GMBH, Rept. SOL4- TR-KTH-001, Munich, Germany*, Jan. 2002.
- [55] M. E. Leipold and O. Wagner. Mercury sun-synchronous orbits using solar sail propulsion. *Journal of Guidance, Control and Dynamics*, 19(6):1337–1341, 1996.
- [56] F. L. Lewis and Vassils L. Syrmos. *Optimal Control*. John Wiley and Sons, New York, second edition, 1995, pp. 170-172.
- [57] E. T. Lu and S. G. Love. Gravitational tractor for towing asteroids. *Nature*, 438(7065):177–178, 2005.
- [58] D. J. Grebow M. T. Ozimek and K. C. Howell. Solar sails and lunar south pole coverage. *AIAA/AAS Astrodynamics Specialist Conference and Exhibit, Honolulu, Hawaii*, August, 2008.
- [59] G. Maral and M. Bousquet. *Satellite Communications Systems*. John Wiley and Sons Ltd, England, 3rd edition, 1998, pp. 319-322.
- [60] A. I. S. McInnes. Strategies for solar sail mission design in the circular restricted three-body problem. *Masters Thesis, Purdue University*, 2000.
- [61] C. R. McInnes. Solar sail trajectories at the lunar L_2 Lagrange point. *Journal of Spacecraft and Rockets*, 30(6):782–784, 1993.
- [62] C. R. McInnes. Artificial Lagrange points for a non-perfect solar sail. *Journal of Guidance, Control and Dynamics*, 22(1):185–187, 1999.
- [63] C. R. McInnes. Solar sail mission applications for non-Keplerian orbits. *Acta Astronautica*, 45(4-9):567–575, 1999.
- [64] C. R. McInnes. *Solar sailing: technology, dynamics and mission applications*. Springer Praxis, London, 1999.

- [65] C. R. McInnes. Near earth object orbit modification using gravitational coupling. *Journal of Guidance, Control and Dynamics*, 30(3):870–873, May–June 2007.
- [66] C. R. McInnes. Dynamics, stability, and control of displaced non-keplerian orbits. *Journal of Guidance, Control and Dynamics*, 21(5):799–805, September–October 1998.
- [67] C. R. McInnes, M. Eiden, P. Groepper, and T. Peacock. Solar sailing - mission opportunities and innovative technology demonstration. In *ESA Bulletin 108*, pages 58–65, 2001.
- [68] C. R. McInnes, A. J. C. McDonald, J. F. C. Simmons, and E. W. McDonald. Solar sail parking in restricted three-body systems. *Journal of Guidance, Control and Dynamics*, 17(2):399–406, 1994.
- [69] C. R. McInnes and J. F. L. Simmons. Halo orbits for solar sails I-heliocentric case. *Journal of Spacecraft and Rockets*, 29(4):466–471, 1992.
- [70] C. R. McInnes and J. F. L. Simmons. Halo orbits for solar sails II-geocentric case. *Journal of Spacecraft and Rockets*, 29(4):472–479, 1992.
- [71] G. Mengali and A. A. Quarta. Trajectory design with hybrid low-thrust propulsion system. *Journal of Guidance, Control and Dynamics*, 30(2):419–426, March–April 2007.
- [72] M. Y. Morimoto, H. Yamakawa, and K. Uesugi. Periodic orbits with low-thrust propulsion in the restricted three-body problem. *Journal of Guidance, Control and Dynamics*, 29(5):1131–1139, 2006.
- [73] M. Y. Morimoto, H. Yamakawa, and K. Uesugi. Artificial equilibrium points in the low-thrust restricted three-body problem. *Journal of Guidance, Control and Dynamics*, 30(5):1563–1567, 2007.

- [74] E. Morrow, D.J. Scheeres, and D. Lubin. Solar sail orbit operations at asteroids. *Journal of Spacecraft and Rockets*, 38(2):279–286, 2001.
- [75] F. R. Moulton. *An Introduction to Celestial Mechanics*. Macmillan, New York, 1914, pp. 298-300.
- [76] M. Oda N. Takeichi, H. Ueno. Feasibility study of a solar power satellite system configured by formation flying. *Acta Astronautica*, 57:698–706, 2005.
- [77] C. Padmanabhan and R. Singh. Analysis of periodically excited nonlinear systems by a parametric continuation technique. *Journal of Sound and Vibration*, 184(1):35–58, 1995.
- [78] B. Pattan. *Satellite Systems: Principles and Technologies*. Van Nostrand Reinhold, 115 Fifth Avenue, New York, New York 10003, 1993, pp. 177-178, 180.
- [79] M. A. C. Perryman. GAIA: An astrometric and photometric survey of our galaxy. *Astrophysics and Space Science*, 280(1-2):1–10, April 2002.
- [80] L. Råde and B. Westergren. *Mathematics Handbook for Science and Engineering*. Studentlitteratur, Sweden, third edition, 1995, pp. 64-65.
- [81] D. L. Richardson. Analytical construction of periodic orbits about the collinear points. *Celestial Mechanics and Dynamical Astronomy*, 22(3):241–253, 1980.
- [82] D. L. Richardson. Halo orbit formulation for the ISEE-3 mission. *J. Guidance and Control*, 3(6):543–548, 1980.
- [83] W. J. Rugh. *Linear System Theory*. Prentice Hall, New Jersey, 1993, pp. 124-126, 132.
- [84] H. Schaub and J. L. Junkins. *Analytical Mechanics of Space Systems*. AIAA, Reston, VA, 2003, pp. 528-530.

- [85] J. Simo and C. R. McInnes. Displaced periodic orbits with low-thrust propulsion in the Earth-Moon system. *19th AAS/AIAA Space Flight Mechanics Meeting, Georgia, USA, AAS 09-153*, 8-12 February, 2009.
- [86] J. Simo and C. R. McInnes. Solar sail trajectories at the Earth-Moon Lagrange points. *59th IAC Congress, Glasgow, Scotland, UK. IAC-08.C1.3.13*, September 29-October 3, 2008.
- [87] R. A. Skoog and C. G. Y. Lau. Instability of slowly varying systems. *IEEE Transactions on Automatic Control*, 17(1):86–92, 1972.
- [88] P. Sundaraarajan and S. T. Noah. Dynamics of forced nonlinear systems using shooting/arc-length continuation method-application to rotor systems. *ASME Journal of Vibration and Acoustics*, 119(1):9–20, 1997.
- [89] A. Tewari. *Atmospheric and Space Flight Dynamics*. Birkhauser Boston, New York, NY 10013, USA, 2007, pp. 178-191.
- [90] R. Thurman and P. Worfolk. The geometry of halo orbits in the circular restricted three-body problem. *Technical report GCG95, Geometry Center, University of Minnesota*, 1996.
- [91] C. van de Kolk. Stability of levitated cylindrical orbits by using solar sails. *AAS/AIAA Astrodynamics Specialist Conference, Gridwood, Alaska, AAS 99-335*, August 16-19, 1999.
- [92] B. F. Villac. Using FLI maps for preliminary spacecraft trajectory design in multi-body environments. *Celestial Mechanics and Dynamical Astronomy*, 102(1-3):29–48, September 2008.
- [93] C. Wan. Solar sail Geostorm warning mission design. *Proc. AAS/AIAA Spaceflight Mechanics Conference, Maui, Hawaii, No. AAS 04-107*, February, 2004.

- [94] T. J. Waters and C. R. McInnes. Periodic orbits above the ecliptic in the solar sail restricted 3-body problem. *Journal of Guidance, Control and Dynamics*, 30(3):687–693, 2007.
- [95] T. J. Waters and C. R. McInnes. Invariants manifolds and orbit control in the solar sail three-body problem. *Journal of Guidance, Control and Dynamics*, 31(3):554–562, May-June 2008.
- [96] T. J. Waters and C. R. McInnes. Solar sail dynamics in the three-body problem: Homoclinic paths of points and orbits. *International Journal of Non-Linear Mechanics*, 43(6):490–496, 2008.
- [97] T. J. Waters and C. R. McInnes. Periodic orbits high above the ecliptic plane in the solar sail 3-body problem. *AAS/AIAA Space Flight Mechanics Meeting, Sedona, Arizona, USA, AAS 07-232*, January 28-February 1, 2007.
- [98] E. T. Whittaker. *A treatise on the analytical dynamics of particles and rigid bodies*. Cambridge University Press, New York, fourth edition, 1999, pp. 398–399.
- [99] B. Wie. Dynamics and control of gravity tractor spacecraft for asteroid deflection. *Journal of Guidance, Control and Dynamics*, 31(5):1413–1423, September-October 2008.
- [100] B. Wie. *Space Vehicle Dynamics and Control*. AIAA, Reston, VA, 2nd edition, 2008, pp. 800-802.
- [101] B. Wie, D. Murphy, M. Paluszek, and S. Thomas. Robust attitude control systems design for solar sails, part 1: Propellantless primary acs. *AIAA Guidance, Navigation, and Control Conference and Exhibit, Providence, Rhode Island, AIAA-2004-5010*, Aug 16-19, 2004.
- [102] W. E. Wiesel. *Spaceflight Dynamics*. Irwin/McGraw-Hill, New York, USA, second edition, 1997, pp. 284-285.

- [103] M. Y. Wu. On stability of linear time-varying systems. *International Journal of Systems Science*, 15(2):127–150, 1984.